Author:
Budden, Alan Stephen

Title:
Sensorless zero-speed position detection for brushless permanent magnet machines

SENSORLESS ZERO-SPEED POSITION DETECTION FOR BRUSHLESS PERMANENT MAGNET MACHINES

by

Alan Stephen BUDDEN

A dissertation submitted to the University of Bristol in accordance with the requirements of the degree of Doctor of Philosophy in Electrical Engineering

Department of Electrical and Electronic Engineering

UNIVERSITY OF BRISTOL

Merchant Venturers Building

Woodland Road

Bristol BS8 1UB

UNITED KINGDOM

October 2005

Abstract

The work presented in this thesis follows two main themes, both associated with development of accurate zero speed sensorless rotor position estimation for brushless permanent magnet machines. The first of these themes concentrates on the position detection algorithm and the second focuses on machine design.

As a precursor to the development, a detailed literature study is included and comparisons are drawn regarding the state of the art as presented in the published literature. The mathematical basis of the zero speed techniques is then presented, including the derivation of the base technique used throughout this thesis. The technique itself is based on a simple demodulation strategy combined with a machine-specific compensation approach that enables the technique to operate on machines with highly distorted saliency profiles. Simulation results are presented in order to show the development process and confirm the theoretical basis of the approach.

A detailed experimental analysis is also presented, including details of the practical implementation of the test platform. It is shown that the estimation technique operates on a number of different machine topologies and can produce results accurate to only 1° mechanical.

In parallel with the algorithm development, an FEA based tool is developed that provides a means of assessing the form of the saliency of a given machine design. In addition, an analysis of the effect of slot shape variations on the quality of the saliency is presented as an example of the use of this tool. The analysis process gives machine designers the ability to optimise machine designs for simple and accurate zero speed sensorless position estimation as well as for machine performance.

Dedicated to my parents & Carolyn...

Acknowledgements

Firstly, I would like to thank Dr Derrick Holliday for his continuing guidance, support and impartial advice throughout this work. My gratitude also goes to Prof. Phil Mellor for providing direction and application for the project. In addition, I am grateful to Dr Rafal Wrobel for the extensive assistance with FEA, Steve Wilkinson for providing his encyclopædic knowledge of MATLAB, and George Iordanidis and Sam Nall for their similar expertise in AutoCAD.

Special thanks are due to Mike Penney, John Smith and Rob Davies, who contributed greatly to the construction of all of the experimental test platforms used in this development. I would like to thank Goodrich Corporation in general for providing financial and technical support and Dr Andrei Dinu in particular for his support with Goodrich's generic controller platform and with VHDL implementation.

I will always be grateful to my parents for the constant support and encouragement at all stages of my education, without which I would not have had the opportunity to carry out this research and also to Dr Pete Doran, without whom I sincerely believe I would never have been able to reach this point.

Finally, I would like to express my utmost gratitude to Carolyn for all her caring and unconditional support, without which this work would have been infinitely more difficult.

Author's Declaration

I declare that the work in this dissertation was carried out in accordance with the Regulations of the University of Bristol. This work is original except where indicated by special reference in the text and no part of the dissertation has been submitted for any other degree.

Any views expressed in the dissertation are those of the author and in no way represent those of the University of Bristol.

The dissertation has not been presented to any other university for examination either in the United Kingdom or overseas.

Signature : 

Name : Alan Stephen Budden

Date : 31st October 2005

Memorandum

The accompanying thesis "SENSORLESS ZERO-SPEED POSITION DETECTION FOR BRUSHLESS PERMANENT MAGNET MACHINES" is based on work carried out by the author in the Department of Electrical and Electronic Engineering of the University of Bristol.

The main contributions claimed by the author are as follows:

1. A comprehensive review of sensorless techniques for brushless permanent magnet machines with the key features and advantages and disadvantages highlighted.

2. Identification of an appropriate strategy for zero speed operation.

3. Application of the technique to different permanent magnet machine topologies and comparison of the efficacy of the strategy.

4. Analysis of the 'fingerprints' enabling the identification of key issues relating to the applicability of particular machine designs to sensorless position detection.

5. In-depth finite element analysis of slotting effects on sensorless accuracy, highlighting some important requirements for a machine to be suitable for zero speed sensorless position detection and providing a tool for machine designers to optimise machines for zero speed sensorless position detection as well as for performance.

6. Demonstration of an experimental, zero speed sensorless position detection system accurate to less than 1° mechanical.

Publications

1. A. S. Budden, R. Wrobel, D. Holliday, P. H. Mellor and P. Sangha, "Sensorless Control of Permanent Magnet Machine Drives for Aerospace Applications", Proc. IEEE International Conference on Power Electronics and Drives Systems (PEDS), 2005.

2. A. S. Budden, D. Holliday and P. H. Mellor, "A Versatile Zero-Speed Sensorless Position Detection Technique for PMSMs", Proc. European Conference on Power Electronics and Applications (EPE), 2005.

3. A. S. Budden, D. Holliday and P. H. Mellor, "Rotor Position Detection For Permanent Magnet Synchronous Machines without a Mechanical Sensor", Proc. International Universities Power Engineering Conference (UPEC), 2005.

4. A. S. Budden, D. Holliday and P. H. Mellor, "Zero Speed Sensorless Position Detection for Permanent Magnet Synchronous Machine", Proc. IEEE Power Electronics Specialists Conference (PESC), 2005.

5. A. S. Budden, D. M. J. Holliday and P. H. Mellor, "Sensorless Zero Speed Position Detection for Surface Mounted Permanent Magnet Synchronous Machines", Proc. European DSP Education and Research Symposium (EDERS), 2004.

6. A. S. Budden, D. M. J. Holliday and P. H. Mellor, "Effects of Non-Sinusoidal Inductance Variation on Saliency Based Position Detection Techniques in Interior Permanent Magnet Synchronous Machines", Proc. IEE International Conference on Power Electronics, Machines and Drives (PEMD), 2004.

List of Abbreviations

ADC – Analogue-to-Digital Converter

ANN – Artificial Neural Network

CT – Current Transducer

DAC – Digital-to-Analogue Converter

DSP – Digital Signal Processor

EKF – Extended Kalman Filter

EMF – Electro-Motive Force

EMIF – External Memory Interface

FEA – Finite Element Analysis

FFT – Fast Fourier Transform

FPGA – Field Programmable Gate Array

IGBT – Insulated Gate Bipolar Transistor

IPM – Intelligent Power Module

IPMSM – Interior Permanent Magnet Synchronous Machine

MMF – Magneto-Motive Force

PCB – Printed Circuit Board

PMSM – Permanent Magnet Synchronous Machine

PROM – Programmable Read Only Memory

PWM – Pulse Width Modulation

RDC – Resolver-to-Digital Converter

SPMSM – Surface Permanent Magnet Synchronous Machine

VHDL – Very High Speed Integrated Circuit Hardware Description Language

ZCP – Zero Crossing Point

List of Principal Symbols

English

i – Currents

v – Voltages

d – Duty Cycle

x, y – System State and Output Vectors

R_s – Winding Resistance

L_s, L_d, L_q – Synchronous, Direct and Quadrature Inductance

p – Differential Operator

n_p – Number of poles

K_E – Machine EMF Constant

Greek

θ_r – Shaft Electrical Position

$\Delta\theta_r$ – Position Error (Electrical)

ψ_m – Flux in the stator windings due to the permanent magnets

ω_r, $\dot{\theta}_r$ – Shaft Electrical Speed

ψ – Flux Linkage

Subscripts

a, b, c – Three axis stationary reference frame

α, β – Two axis stationary reference frame

d, q – Two axis synchronous (rotor) reference frame

γ, δ – Synchronous (rotor) reference frame based on estimated position

e, m – Electrical / Mechanical quantities (speed or position)

Superscripts

est – Estimated Value

$*$ – Reference Value

$'$ – Reference frame synchronous to injection signal

$''$ – Reference frame synchronous to inverse injection signal

Contents

List of Figures

List of Tables

Chapter 1

Introduction

1.1 Background

The desire to implement machine drives without mechanical position or speed sensors arises primarily from the reduction in cost that results. In addition to this, it provides added advantages in terms of reduced wiring and increased reliability. For different machine topologies and different applications, there are different requirements in terms of sensors. Brushed DC machines do not inherently need position sensors (due to the presence of the mechanical commutator), but either position or speed sensors are often used in position or speed control systems. Induction machines can easily be operated without rotary sensors; however, the use of speed control or field oriented and direct torque control algorithms results in the need being reintroduced. The wound field synchronous machine is generally operated without any rotary sensors, although this results in limited dynamic performance. The introduction of a permanent magnet rotor and the desire for machines that can be easily controlled with a good dynamic response results in the need for electronic commutation, which in turn requires rotor position information.

Permanent Magnet Synchronous Machines (PMSMs) offer many advantages over other machine types, including a high power-to-weight ratio and simplicity of control [1]. Once the electronic commutation has been achieved (using the rotor position

information), it is very straightforward to operate the machine in the same manner as a brushed DC machine, with independent flux and speed control. However, the cost and reliability issues associated with the position sensors is a considerable disadvantage, as is the increased volume and mass that they introduce to the overall system. It is therefore desirable to find a means of measuring the rotor position indirectly, without the use of a mechanical sensor. For speed control applications, the rotor speed can be calculated as the derivative of position. In order to derive the rotor position indirectly, 'sensorless' techniques involve application of signal processing techniques to extract the necessary information from the voltages and/or currents in the machine. These can be measured using simple and rugged transducers at the point of supply and which are already present as a means of detecting machine fault conditions and for use in current control strategies [2].

Two distinct operating modes need to be considered when developing a PMSM drive without mechanical position sensors.

- Medium and High Speed
- Zero and Low Speed

When the machine is driven at a speed that is sufficient to produce a measurable back EMF, the drive currents can be used to detect the rotor position. However, when the machine is stationary, no back EMF is generated and hence an alternative means of position sensing is necessary. To achieve this, there must be some property of the machine that is measurable at zero speed and which varies with rotor position. This is generally the inductance of the stator windings, which varies due to changes in the magnetic circuit, either due to a salient rotor structure or due to saturation of the stator core.

1.2 Permanent Magnet Synchronous Machines

The structure of an interior rotor PMSM is similar in form to that of an exterior rotor permanent magnet brushed DC motor. The stator surrounds the rotor and

contains a number of slots containing (usually three) phase windings. The rotor has a number of permanent magnets mounted on or within the structure. An exterior rotor PMSM has the rotor positioned around the outside of the stator. Figure 1.1 shows a cross section of an example interior rotor PMSM, with magnets mounted on the surface of the rotor.

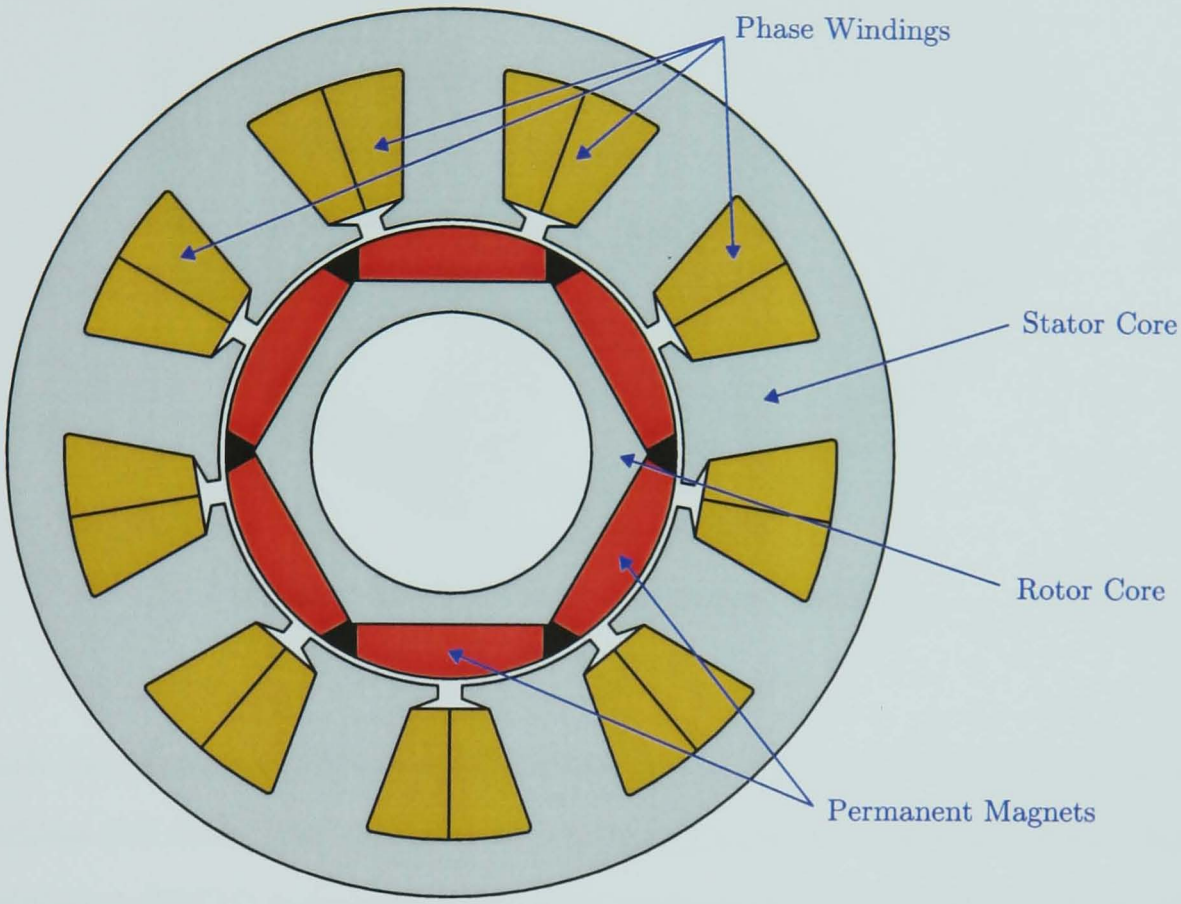

Figure 1.1: Cross Section of Example Motor

The electrical power in the windings is converted to mechanical power through the interaction of the permanent magnet flux (shown in figure 1.2 for an unexcited machine) and the magnetic field produced by the current carrying conductors.

Since there are no electrical connections required for the rotor, a commutator and brushes are not required. Instead, commutation is achieved through the use of an inverter in combination with some form of rotor position measurement system (either a mechanical sensor or a 'sensorless' technique). Depending on the shape of the back EMF in the machine, the commutation is performed in different ways. For machines with approximately trapezoidal back EMF, where the back EMF is constant for approximately 120° electrical, a six-step switching pattern is used to

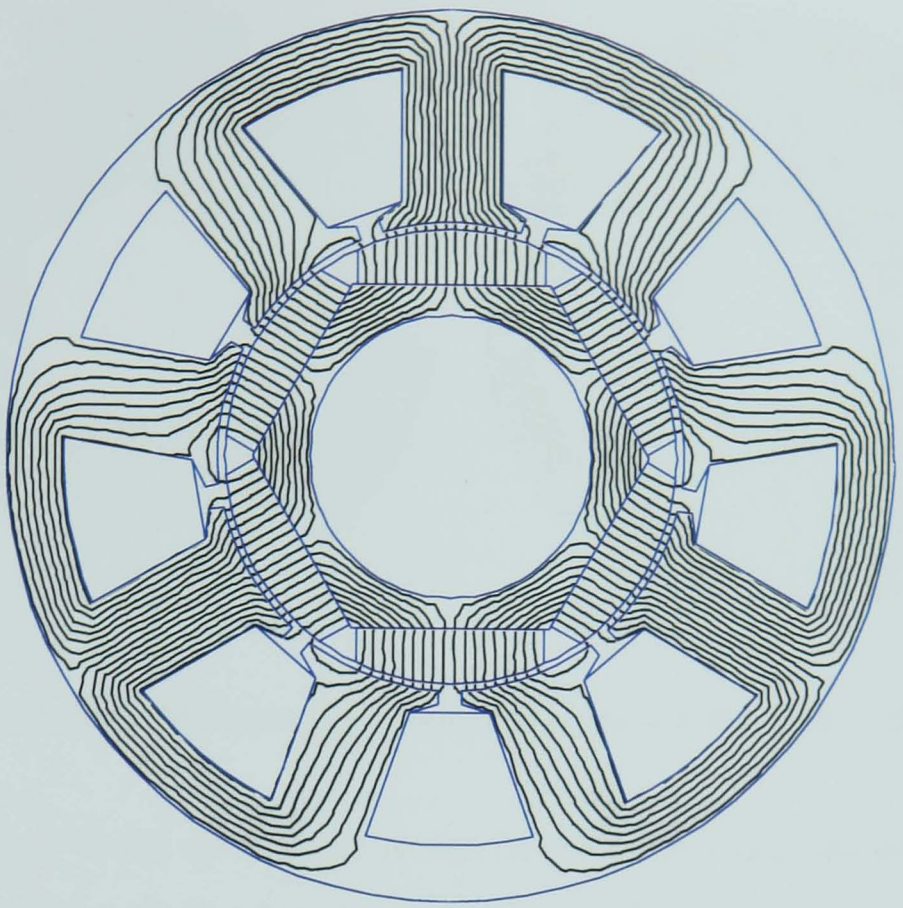

Figure 1.2: Flux Lines for Unexcited Machine

match the operation of brushed DC machines. This type of drive is referred to as a brushless DC drive. For machines with a more sinusoidal back EMF, Pulse Width Modulation (PWM) techniques are used to create sinusoidal currents in the machine windings. This type of drive is known as a brushless AC drive.

It is also possible to operate the machines without any position feedback by maintaining a fixed ratio between terminal voltage and terminal frequency; however, this type of control is only of practical use in constant speed applications or those with limited load variations and where a high accuracy of control is not required.

There are a number of different rotor structures that are used in PMSMs. In addition to surface mounted magnets (shown in figure 1.1), the magnets can either be buried in the rotor structure, as shown in figure 1.3(a), or embedded entirely within it, as shown in figure 1.3(b).

Machines with these rotor topologies are referred to as Interior Permanent Magnet Synchronous Machines (IPMSMs). The salient rotor structure results in a different

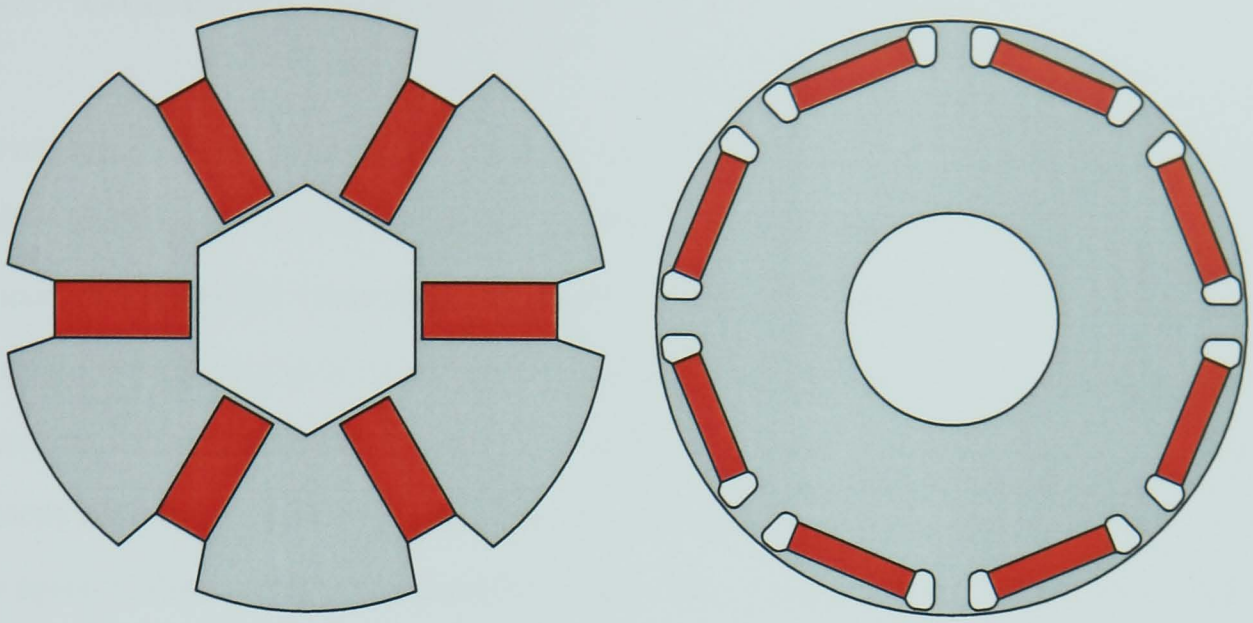

(a) (b)

Figure 1.3: IPMSM Rotors; (a) Buried Magnets; (b) Embedded Magnets

magnetic circuit in the rotor d-axis to that in the rotor q-axis (see Appendix A), resulting in a phase winding inductance that varies with rotor position. This property is used in most low and zero speed sensorless position detection algorithms. In surface magnet machines, it is often still possible to use inductance variation to detect rotor position at zero speed. The inductance variation can either be inherent, due to stator saturation caused by the permanent magnets, or it can be created by applying voltage pulses to saturate the stator iron and detecting the variation in level of saturation caused by the magnets. This is discussed in more detail in chapter 2.

PMSMs are known by a number of different names. Where they are designed for use with a trapezoidal drive, they are often referred to as 'Brushless DC Machines'. When designed for use with sinusoidal drives, they are often referred to as 'Brushless AC Machines'. In addition, since they are generally used with variable speed drives rather than synchronous drives, they are also referred to as 'Brushless Permanent Magnet Machines' in order to avoid confusion. However, since the most common generic term of reference in the literature is 'Permanent Magnet Synchronous Machine', this term has been adopted for the purposes of this thesis.

1.3 Drives

Drives for PMSMs consist of a number of distinct components. These are: a controller, some gate drive circuitry, an inverter and some sensors. The sensors usually consist of Hall-effect Current Transducers (CTs) (to detect the current for torque control, over-current protection and also for position-sensorless techniques) and some form of position sensor (if a position-sensorless technique is not being used or is only present as a backup). There may also be speed sensors in place, but more commonly the speed is derived from the position sensor. The position sensors can be Hall-effect sensors, optical encoders or brushless resolvers. Hall-effect sensors are cheap, but only give sufficient position accuracy for commutation of trapezoidal machines and even then do not allow accurate control at low speed. Relative encoders have a similar disadvantage at low or zero speed. Resolvers can provide accurate rotor position at all speeds, but they contain wound rotor and stator components, leading to high cost and concerns with reliability, especially when operating at high speeds [3].

The inverter is used to provide controlled power to the machine windings. For a three-phase machine, the inverter consists of six power switches (usually MOSFETs or IGBTs) and six power diodes (occasionally the inherent diodes in the MOSFET structure are used). The structure of a three-phase inverter is shown (with IGBT switches) in figure 1.4.

The gate drive circuitry performs a number of roles. Firstly, it is used to isolate the controller from the high potential in the inverter. In addition, it performs level shifting for the top row of inverter switches and amplification in order to turn the switches on and off. This is generally achieved through the use of isolated power supplies coupled with either opto-isolators or high-frequency transformers.

The controller is used to generate the inverter switching signals needed to drive the machine in the desired manner. It can be implemented through analogue comparators and other circuitry, or through discrete logic. However, in modern variable speed drives, it is often implemented through the use of a microprocessor such as a Digital Signal Processor (DSP). In the case of brushless DC drives with Hall-effect

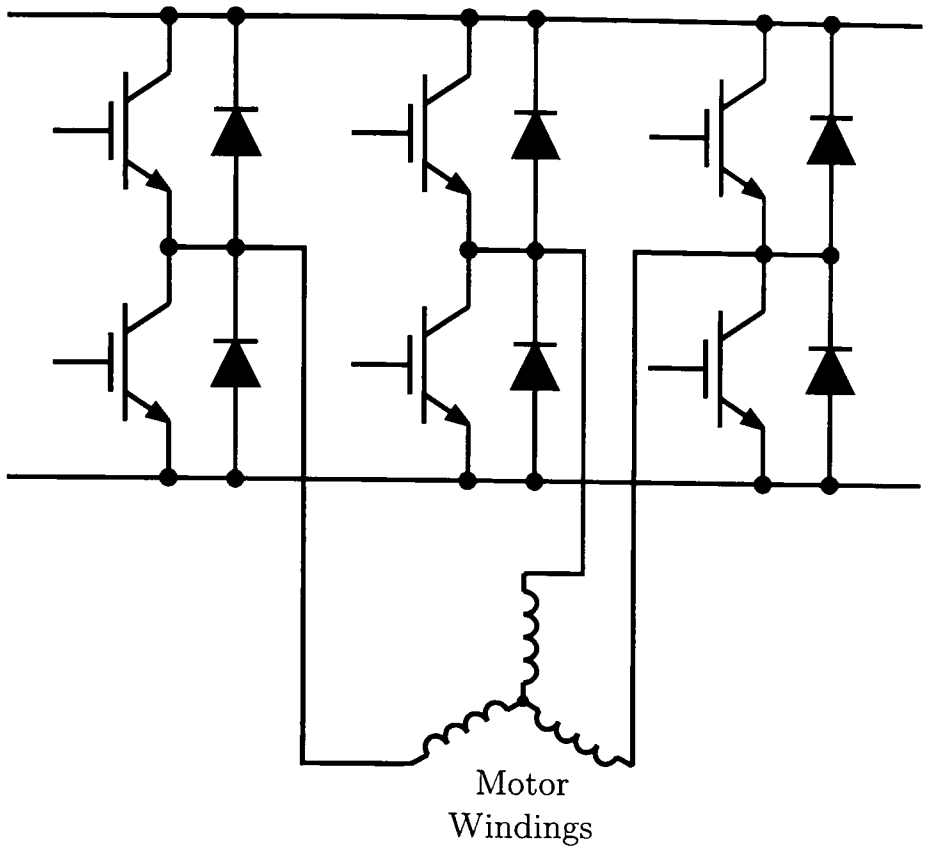

Figure 1.4: Inverter Structure

position sensors, a Programmable Read Only Memory (PROM) based look-up table is sufficient for commutation, although further logic or computation may be used for current, speed or position control.

1.4 Applications

In principle, the applications for which sensorless control of PMSMs is applicable are as wide ranging as the applications of the motors. Generally, however, the areas for which the desire is greatest is those in which the reduction of cost is of prime importance. In addition, there are many systems in which reliability problems with mechanical sensors prevent the use of this type of machine. These systems may benefit from the availability of sensorless control techniques.

The principal applications that the work presented in this thesis focuses upon are traction and aerospace systems. This is primarily due to the availability of test machines, but also due to the safety requirements of systems for these applications and the need to improve reliability as much as possible. There are no application

specific components to the work, however, and therefore it could be applied to PMSMs designed for any application.

1.5 Layout of Thesis

The focus of this thesis is on the development of a position detection algorithm for permanent magnet synchronous machines without a shaft-mounted position sensor. It is specifically aimed at detection at zero speed, where fundamental currents and voltages are not present, resulting in difficulties in position estimation.

There is an impression in some industrial circles that many of the more complex approaches to sensorless control are too complicated for industrial application and are more of purely academic interest. It is therefore desirable to approach the problem of sensorless control with this as a consideration. The algorithm presented in this thesis is therefore intended to be simple to implement in a practical system and, if desired, to customise for a particular machine.

The thesis is set out as follows:

In chapter 2, a detailed review of the approaches to sensorless control that are in the published literature is presented. Details of techniques for high speed detection are discussed and the details of available zero and low speed techniques are then presented. For each approach, advantages and limitations are discussed.

In chapter 3, a purely analytical treatment of the approach is presented. This includes a derivation of the mathematical model of a permanent magnet machine, along with mathematical treatment of the algorithms used to derive the rotor position.

Chapter 4 focuses on the initial practical development and the testing performed on three machines in order to validate the theory. Finite Element Analysis (FEA) techniques are used to confirm the form of the machine saliency and the ability to accurately measure rotor position in these machines. Initial test results are presented

that use linear amplifiers to apply signals to the machines in order to demonstrate that distortion is due to the machine itself, rather than inverter effects. A test system that is similar in form to industrial drives is then used on all three machines to capture the information necessary for off-line testing.

The results captured in the analysis of chapter 4 are assessed in further detail in chapter 5. This involves application of the theoretical analysis to the practical results using the MATLAB platform. Results are presented for the approaches discussed in chapter 3 and comparisons are drawn in order to select an approach for the final system.

A detailed finite element analysis of the effect of slot shape variations is presented in chapter 6. This analysis provides information on the causes of saliency distortion and furnishes machine designers with an additional tool that can be used when designing machines for applications involving zero speed sensorless control.

Chapter 7 presents the development of the final test system on a commercially designed DSP platform. This platform is interfaced with the same power circuit (inverter and gate drivers) as used in chapter 4. Testing of the final system with all three test machines is used to show the validity of the approach. Results are presented and comparisons are drawn with earlier simulation results. The effect of the different machine topologies is discussed.

In chapter 8, a summary of the work documented in this thesis is presented and conclusions are drawn. The innovative aspects of the approach are highlighted and suggestions for future work extending this investigation are given.

Chapter 2

Sensorless Control Review

2.1 Introduction

This chapter provides a brief summary of the literature on sensorless control of permanent magnet synchronous machines that is currently available. It is divided into several sections, each dealing with a particular class of technique. Firstly, there is a discussion of techniques that can only be used at speed (due to the dependence on the back EMF in the machine). Following this, there is a discussion of a technique that is based on monitoring the state of the power inverter used to drive the machine. This enables operation down to lower speeds than many of the back EMF techniques, but is still unable to operate when the machine is stationary. Finally, there is a discussion on saliency based techniques. These techniques allow operation over the entire speed range (although they are often only used at zero and low speed).

2.2 Back EMF Based Techniques

2.2.1 Flux Linkage Based Model

2.2.1a Technique

This type of estimator is based on the principle that as the machine rotates, a back EMF is generated that is related to the electrical angle of the shaft [4]. This is shown in the graph of figure 2.1 for a three-phase machine.

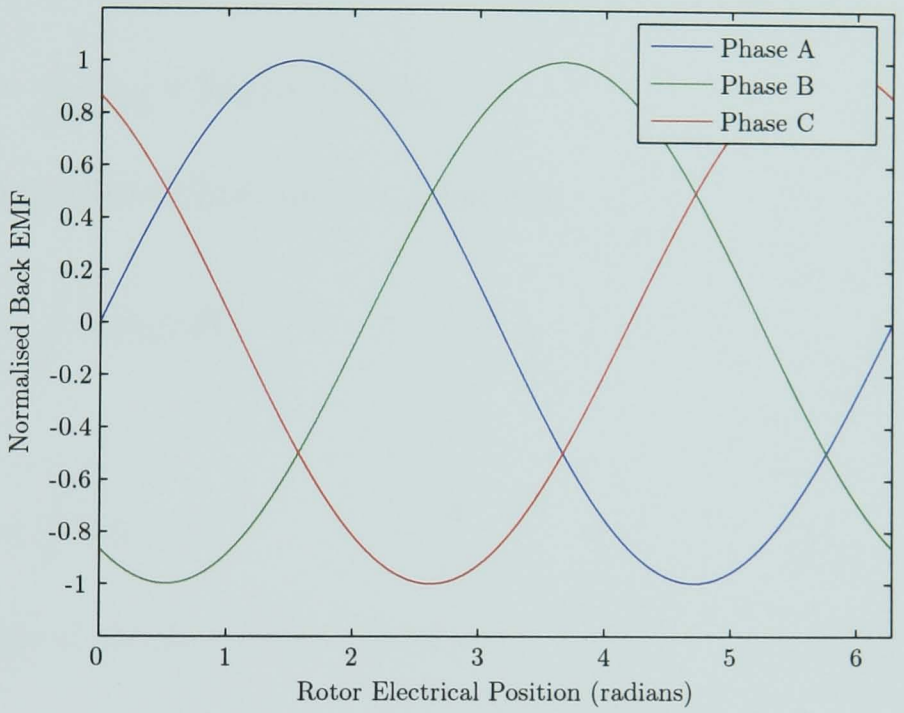

Figure 2.1: Back EMF Waveforms for a PMSM

By monitoring the terminal voltages and currents in the system and applying a motor model to the resulting values, the position on the flux/EMF graph can be estimated.

2.2.1b Algorithm

Firstly, the line-to-line machine voltages must be known, either by direct measurement or from knowledge of the duty cycles. There will be three different duty cycles at any given point, one for each line. These are first translated into the dq axis

reference frame (using the last known position); then the voltages can be calculated from equation (2.1).

$$v_{ab} = V_{dc}\left(d_d - \frac{1}{\sqrt{3}}d_q\right); v_{bc} = V_{dc}\frac{2}{\sqrt{3}}d_q \tag{2.1}$$

From these voltages, the real and imaginary components of the stator line-to-line voltage v_L can be calculated.

$$\Re\left(v_L\right) = v_{ab} - R_s\left(i_a - i_b\right) \tag{2.2}$$

$$\Im\left(v_L\right) = \frac{1}{\sqrt{3}}\left(v_{ab} + 2v_{bc}\right) + \sqrt{3}R_s i_c \tag{2.3}$$

Integration of the line-to-line voltages yields flux.

$$\Re\left(\psi_L\right) = \int \Re\left(v_L\right)\ \mathrm{d}t \tag{2.4}$$

$$\Im\left(\psi_L\right) = \int \Im\left(v_L\right)\ \mathrm{d}t \tag{2.5}$$

The space angle of the flux is then as follows.

$$\theta_{\psi_L} = \tan^{-1}\left(\frac{\Im\left(\psi_L\right)}{\Re\left(\psi_L\right)}\right) \tag{2.6}$$

The line-to-line flux vector ψ_L leads stator flux vector ψ_S by 30°.

$$\theta_{\psi_S} = \theta_{\psi_L} - 30° \tag{2.7}$$

Now, load torque angle δ can be calculated as shown in equation (2.8).

$$\delta = \tan^{-1}\left(\frac{L_q i_q^{est}}{L_d i_d^{est} + \psi_m}\right) \tag{2.8}$$

In equation (2.8), ψ_m is the flux linkage with the stator windings due to the permanent magnets.

The rotor position angle is then,

$$\theta_r = \theta_{\psi_S} - \delta \tag{2.9}$$

One of the major problems associated with this system is drift, due to inaccuracies in the values of inductance and resistance of the windings and in the integral calculation. It is therefore necessary to compensate for this. This is generally done once per cycle [4], by examining the flux values over the last cycle and using the central point as a compensation offset.

$$\text{Drift} = \left(\frac{\Re(\psi_{L(max)}) + \Re(\psi_{L(min)})}{2}\right) + j\left(\frac{\Im(\psi_{L(max)}) + \Im(\psi_{L(min)})}{2}\right) \tag{2.10}$$

The calculated angle then becomes:

$$\theta_{\psi_L} = \tan^{-1}\left(\frac{\Im(\psi_L) - \Im(\text{Drift})}{\Re(\psi_L) - \Re(\text{Drift})}\right) \tag{2.11}$$

2.2.1c Applicability

This system can be used with all permanent magnet synchronous machines, but only functions when the speed is high enough to give a back EMF that is sufficiently above the noise floor.

2.2.2 Zero Crossing Points

2.2.2a Technique

In PMSMs with a trapezoidal EMF, only two phases are ever excited at a given time. This measurement system is based on the monitoring of the unexcited phase and observing the point at which the EMF crosses the zero axis [5,6]. This point is used to control the timing of the switches.

2.2.2b Applicability

This system is only applicable for trapezoidal machines. It functions over a wide speed range, but not at zero speed.

2.2.2c Processing Power

Since this technique simply monitors a signal to find the Zero Crossing Point (ZCP), the processing requirements are minimal.

2.3 Observer Based Techniques

2.3.1 Simplified Observers

2.3.1a Technique

Like most of the observer based techniques, this approach is essentially an enhancement of the back EMF techniques discussed in section 2.2. However, as with all of the observer based systems there exists the availability of self-checking to ensure that parameter variations do not affect the operation of the system.

In the first technique discussed in this section, a mathematical model similar to those used in most techniques is used to estimate the speed, position and voltage in the system [7, 8]. The model used is shown in equation (2.12).

$$\begin{pmatrix} v_\gamma^{est} \\ v_\delta^{est} \end{pmatrix} = \begin{pmatrix} R_s + L_s p & -L_s \omega_r^{est} \\ L_s \omega_r^{est} & R_s + L_s p \end{pmatrix} \begin{pmatrix} i_\gamma \\ i_\delta \end{pmatrix} + K_E \omega_r^{est} \begin{pmatrix} \sin \Delta\theta \\ \cos \Delta\theta \end{pmatrix} \tag{2.12}$$

Under the assumption that the shaft is rotating ($\dot{\theta} \neq 0$) and that the position error is small ($\Delta\theta \approx 0 \therefore \sin \Delta\theta \approx \Delta\theta$), the voltage error (the difference between the

voltage with $\Delta\theta = 0$ and that with $\Delta\theta \neq 0$) becomes

$$\Delta v_\gamma = v_\gamma - v_\gamma^{est} \propto \Delta\theta \tag{2.13}$$

Therefore, if the terminal voltage is measured and compared with the voltage being estimated by the model, the resulting voltage error can be used to correct the position error in the system. However, this ceases to work once the speed becomes close to zero or if the parameter variations are sufficient to invalidate the small value theorem assumption.

2.3.1b Algorithm

The first stage in the process is to measure the three-phase currents and either measure or deduce (from DC link voltage, PWM pattern and dead-band information) the three-phase voltages.

Using the last estimated position value, voltages and currents are then transformed to the $\gamma\delta$ reference frame. The rotor speed is then estimated, using equation (2.14).

$$\omega_r^{est} = \frac{v_\gamma - R_s i_\delta - L_s \frac{\mathrm{d}\, i_\delta}{\mathrm{d}t}}{K_E + L_s i_\gamma} \tag{2.14}$$

Then the hypothetical voltage is calculated using equation (2.12) with $\Delta\theta = 0$. Equation (2.13) is then used to find the angular error. A PI controller is used to find the correction speed, α,

$$\alpha = \left(K_{SP} \Delta v_\gamma + K_{SI} \int \Delta v_\gamma \ \mathrm{d}t \right) \mathrm{sgn}(\omega_r^{est}) \tag{2.15}$$

where K_{SP} is the proportional gain and K_{SI} is the integral gain. The speed and position are then updated and these are used in the controllers for the system.

$$\omega_r = \omega_r^{est} + \alpha \tag{2.16}$$

$$\theta_r = \theta_r^{est} - \Delta\theta \tag{2.17}$$

2.3.1c Applicability

This technique is designed primarily for surface permanent magnet synchronous machines. In principle, it should also work with IPMSMs but due to the interdependence of the two-phase equations, the model becomes significantly more complicated and it is unlikely that it would hold the same simplicity advantages over the more complex observers. It should operate over a good speed range, although not at zero speed.

2.3.1d Processing Power

Since the equations used in this system have been simplified using a number of assumptions, the processing required in this system is reduced to a small number of simple algebraic operations. The processing power required is therefore much less than for the more complex observers discussed in the following sections.

2.3.1e Advantages / Limitations

- Should be capable of dealing with some parameter variations.
- Much simpler than other observers.
- The simulations presented by Matsui [9] show that the system is capable of dealing with initial position errors up to 65° (electrical).

2.3.2 Extended Kalman Filters *et al.*

2.3.2a Introduction

The Extended Kalman Filter (EKF) is an observer designed to estimate the states of a dynamic non-linear system [10]. In simple terms, the operation of the observer is a more advanced version of the self-correcting model discussed in section 2.3.1. The EKF uses system states that are measurable (for example, voltages and currents) and statistical information (of noise and of the states) to estimate the states that are immeasurable [10–17].

There are two main components in the algorithm. The first of these is a prediction stage that uses a mathematical model to estimate states. Following this, there is a filtering stage that corrects the estimates using the weighted (by the 'Kalman Gain') difference between the predicted and actual output vectors. The model used can be in any one of the various reference frames used in these systems; the choice of frame affects the processing speed of the system. This report will concentrate on a model in the two axis stationary reference frame.

2.3.2b Algorithm

Equations (2.18) and (2.19) show the non-linear state equations for the machine [10],

$$\dot{x}(t) = f(x(t)) + Bv(t) + \sigma(t) \tag{2.18}$$

$$y(t) = h(x(t)) + \mu(t) \tag{2.19}$$

where $\sigma(t)$ and $\mu(t)$ are zero mean white Gaussian noise independent of the system state vector x and with covariances of Q and R respectively. Of these, the former deals with system disturbances and model inaccuracies, while the latter represents measurement noise.

In equations (2.18) and (2.19),

$$x = \begin{pmatrix} i_\alpha \\ i_\beta \\ \omega_r \\ \theta_r \end{pmatrix} ; v = \begin{pmatrix} v_\alpha \\ v_\beta \end{pmatrix} ; y = \begin{pmatrix} i_\alpha \\ i_\beta \end{pmatrix} \tag{2.20}$$

$$f(x) = \begin{pmatrix} -\frac{R_s i_\alpha}{L_s} + \frac{\omega_r \lambda}{L_s} \sin\theta_r \\ -\frac{R_s i_\beta}{L_s} - \frac{\omega_r \lambda}{L_s} \cos\theta_r \\ 0 \\ \omega_r \end{pmatrix} \tag{2.21}$$

$$B = \begin{pmatrix} \frac{1}{L_s} & 0 \\ 0 & \frac{1}{L_s} \\ 0 & 0 \\ 0 & 0 \end{pmatrix} ; h(x) = \begin{pmatrix} i_\alpha \\ i_\beta \end{pmatrix} \tag{2.22}$$

The dynamic model of the machine is derived under the 'infinite inertia' hypothesis – i.e. that the rotor speed derivative is negligible compared with the other system variables and that any mechanical load parameter will disappear from the machine equations.

This system is clearly non-linear and hence for accurate control, the estimators must be capable of dealing with non-linear systems. The extended Kalman filter fulfils this requirement.

The first part of the EKF prediction stage calculates initial predictions of the next state of the system assuming that the noise is zero. This is shown in equation (2.23) (in the discrete domain).

$$x_{k+1}^{est} = f(x_k) + Bv_k \tag{2.23}$$

The other part of the prediction stage predicts the next value of the error covariance.

$$P_{k+1}^{est} = A_k P_k A_k^T + W_k Q_k W_k^T \tag{2.24}$$

where A is the Jacobian matrix of partial derivatives of equation (2.18) with respect to x and W is the Jacobian matrix of partial derivatives of equation (2.18) with respect to σ.

Once the prediction stage is complete, the filtering stage (correction stage) begins. Firstly, the Kalman Gain is calculated using equation (2.25),

$$K_k = P_k^{est} H_k^T (H_k P_k^{est} H_k^T + V_k R_k V_k^T)^{-1} \tag{2.25}$$

where H is the Jacobian matrix of partial derivatives of $h(x)$ with respect to x and V is the Jacobian matrix of partial derivatives of $h(x)$ with respect to μ.

The estimate is then updated using the Kalman Gain:

$$x_k = x_k^{est} + K_k(y_k - h(x_k^{est})) \tag{2.26}$$

Finally, the error covariance is updated using equation (2.27) and the process repeats.

$$P_k = (I - K_k H_k) P_k^{est} \tag{2.27}$$

2.3.2c Applicability

This observer can be used with all permanent magnet synchronous machines over a wide range of speed, although not at standstill.

2.3.2d Processing Power

To perform all of the matrix calculations associated with the EKF, there is a very high processing requirement. However, with modern sixth generation floating-point DSPs on the market, it has been shown to be within the capabilities of the processors to perform all of the calculations for the EKF along with the other components of the control system.

2.3.2e Advantages / Limitations

This technique has been shown to produce accurate position sensing at speeds above zero, when provided with a reasonably accurate estimate of the initial state vector and the initial covariance matrices. However, the system requires relatively heavy computation and is unable to operate at zero speed.

2.3.2f Alternatives

Along a similar vein, there exist a variety of other observers, as well as the EKF. These are all based on essentially the same principle, but differ slightly in their operation. They include Luenberger based observers [18] and sliding-mode observers [19–21] among others [22–30].

2.3.3 Artificial Intelligence

2.3.3a Artificial Neural Networks

Artificial Neural Networks (ANNs) can be used to model non-linear systems in a similar way to the EKFs discussed in section 2.3.2 [15]. The ANN is an array of neurons, each of which performs a non-linear function on the weighted sum of its inputs [31]. The array of neurons, like the one shown in figure 2.2, can then be used to produce the desired output.

By appropriate choice of the number of layers, the number of nodes in each layer, the weights of each path and the non-linear function used on each weighted sum, an optimal network can be found to perform the required task. The selection of the various parameters is largely by trial and error.

In a similar manner to the earlier observers, the ANN can be used to calculate measurable states as well as immeasurable ones. The former can be used to adjust the weights dynamically to correct the output. This process is called back-propagation.

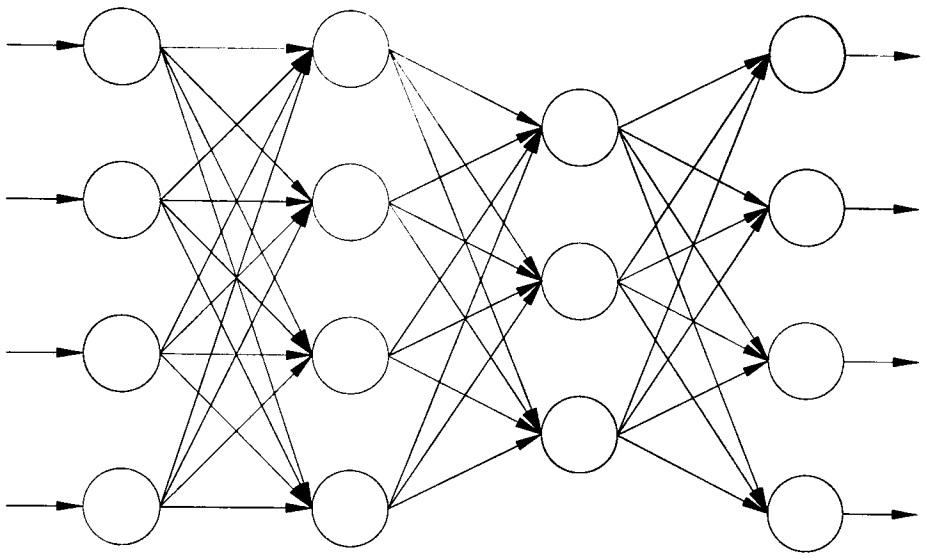

Figure 2.2: Structure of Artificial Neural Network

This technique has been used successfully with reluctance motors [31–33] and using similar principles, it should be applicable to permanent magnet synchronous machines.

2.3.3b Fuzzy Logic

Artificial intelligence controllers can be used to replace most forms of conventional control system. Fuzzy logic controllers offer an intuitive design process to solve particular control problems. Where a heuristic description of a particular control problem can be found, this can be directly translated into a set of fuzzy statements – a far more intuitive process than the design of conventional mathematical controllers [34].

The fuzzy logic controller is composed of three main components. The first of these is known as a 'fuzzifier', in which the input variables are processed using a 'membership function' to determine the degree to which they belong to each of the fuzzy sets [35]. For example, triangular membership functions, as shown in figure 2.3, can be used.

Once the input variables have been fuzzified, if-then-else type rules are applied to the fuzzified input variables and the output fuzzy sets are aggregated into a single set. For example, if this system was used in place of the simplified observer discussed in section 2.3.1, an input variable might be 'voltage error' and a corresponding output

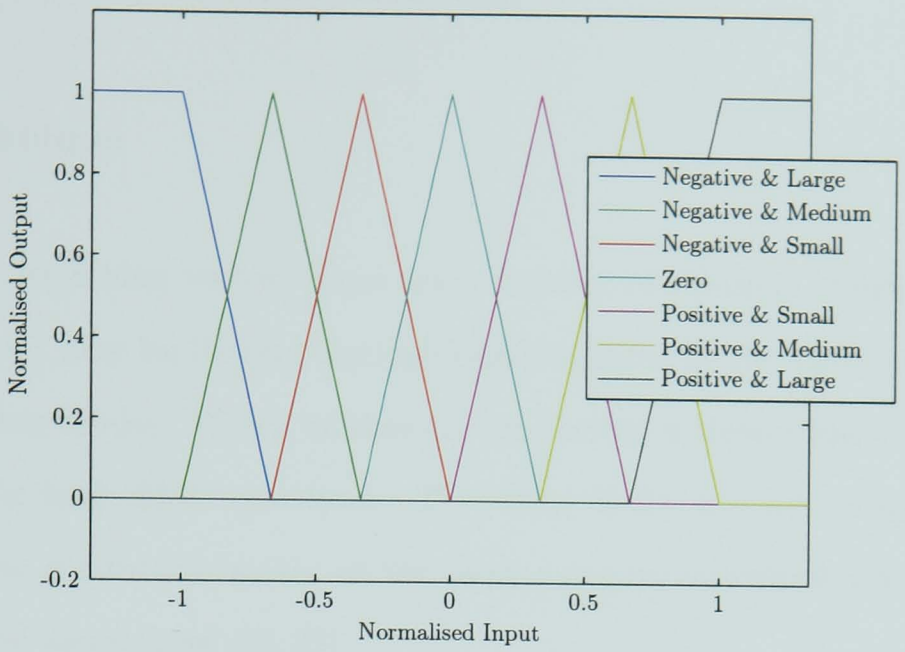

Figure 2.3: Fuzzification Membership Functions

variable might be 'position adjustment'. The corresponding if-then-else statements would be of the form shown below:

if Voltage Error **is** Negative and Large
then Position Adjustment **is** Positive and Large

Once the aggregate output fuzzy set has been compiled, some criteria are defined to produce an output from this set. There are a variety of methods of doing this, such as centre-of-area defuzzification, in which the output value is the geometrical centre of the union of the contributions of each rule. The particular selection of defuzzification method is, like that of the fuzzification method, dependent on the application.

Fuzzy logic controllers have been applied to speed-sensorless induction machine drives [34, 36, 37]. It is believed that they could also be applied, either individually or in combination with other techniques, to develop position-sensorless control systems for permanent magnet synchronous machines.

2.4 Inverter State Monitoring

2.4.1 Technique

For any given switching vector, there are a number of states in which the inverter can be. Current may be flowing through one transistor or through one or other of the freewheeling diodes. Which of these is conducting is dependent on the present segment of the back EMF waveform. Therefore, if the current switching state is known and the conduction states of the diodes can be measured, an approximate position can be ascertained [38, 39].

Since the conduction states cannot be measured directly, an extra circuit must be built to switch with the diodes and thus provide the information.

2.4.2 Applicability

This system only produces segment based position information and hence would only be accurate enough for use with trapezoidal flux distribution machines. However, it does have the advantage over the back EMF techniques that it works at lower speeds since there is no requirement for direct voltage measurements.

2.4.3 Processing Power

This system is extremely simple and once the measuring circuit is implemented, it could be completed either with a very short look-up table or a small number of logic gates or logic instructions.

2.5 Saliency Based Techniques

2.5.1 Introduction

Figure 2.4 shows the structure of an IPMSM. As can be seen, the magnetic circuit along the d-axis is different to that along the q-axis. Each magnet is covered by a steel pole piece and thus high permeance paths are produced for the magnetic fluxes across these poles and in space quadrature to the magnet flux. However, in the magnetic circuit on the q-axis of the rotor there is only iron whereas in the d-axis, a part of the magnetic circuit consists of the magnet, which has a permeance approximately equal to that of air. The reluctance in the d-axis is thus increased and the inductance decreased [15]. More precisely, the inductance is continuously varying with the relative position of the rotor with respect to a particular winding.

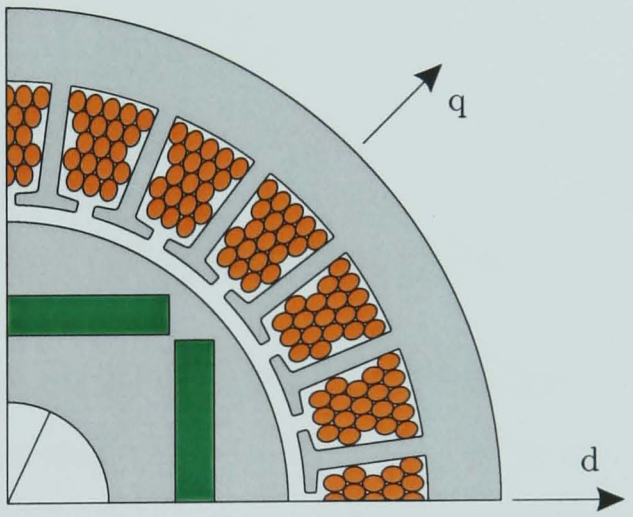

Figure 2.4: Structure of IPMSM

It is important to note that, ignoring any core saturation effects, the magnetic circuit is the same in the positive d-axis as in the negative. Therefore, considering a particular phase, the inductance varies sinusoidally over half an electrical cycle of the rotor. The positions of maximum and minimum inductance in stator phase A are shown in figure 2.5.

From this, it can be seen that in a salient pole machine, the inductance varies with $2\theta_r$, where θ_r is the electrical position of the rotor.

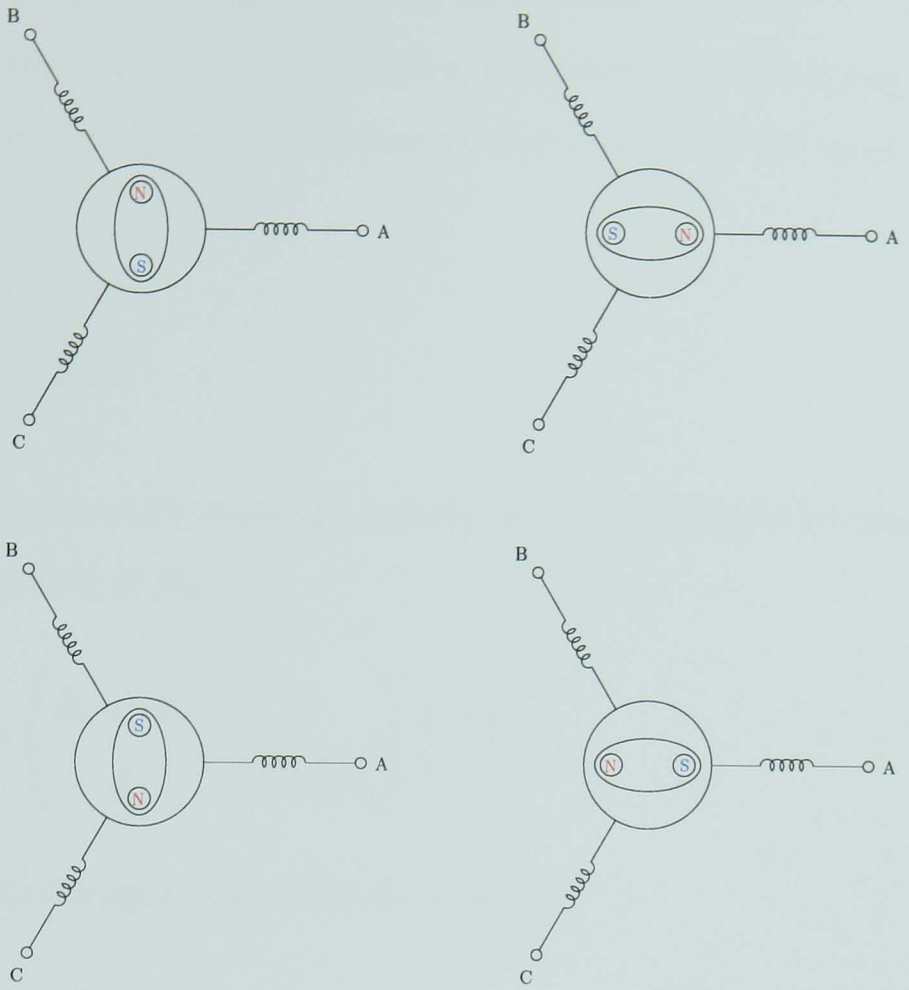

Positions of
Maximum Inductance
in Stator Phase A

Positions of
Minimum Inductance
in Stator Phase A

Figure 2.5: Rotor Positions with Maximum and Minimum Inductance

Since a variation exists in the inductance of the windings according to rotor position, the rotor position can be ascertained as long as the instantaneous inductance can be measured. A number of ways of doing this are discussed in the literature; sections 2.5.2–2.5.5 summarise the main techniques.

2.5.2 Armature Current Locus Based Estimation

2.5.2a Technique

When the shaft is stationary, a three-phase balanced set of sinusoidal voltages is applied to the terminals of an IPMSM. This causes a current to flow. Since the inductance is different in the direct and quadrature axes, the locus of the currents in this reference frame is an ellipse. Similarly, in the two axis phase stationary reference

frame, the locus of the currents is also an ellipse, rotated through an angle equal to the electrical angle of the shaft. Therefore, if the direction of the major axis of the ellipse in the stationary reference frame can be established, the rotor position can be measured.

2.5.2b Algorithm

The voltage equation of a *stationary* interior permanent magnet synchronous motor is given by equation (2.28).

$$\begin{pmatrix} v_d \\ v_q \end{pmatrix} = \begin{pmatrix} R_s + pL_d & 0 \\ 0 & R_s + pL_q \end{pmatrix} \begin{pmatrix} i_d \\ i_q \end{pmatrix} \tag{2.28}$$

A balanced AC voltage is applied to the machine:

$$\begin{pmatrix} v_d \\ v_q \end{pmatrix} = V_i \begin{pmatrix} \cos \omega_i t \\ \sin \omega_i t \end{pmatrix} \tag{2.29}$$

where V_i is the magnitude, and ω_i the frequency, of the injected voltage.

By substituting (2.29) into (2.28), it can be seen that the resulting currents form an ellipse. With $L_d < L_q$ the major axis of the ellipse follows the d-axis [40]. Simulation results for the system have produced figure 2.6, which shows $\alpha\beta$ axis currents with the rotor set at an offset of 0° and 120° (electrical) for a machine with a saliency ratio of 1.5:1.

In order to estimate the rotor position, it is necessary to locate the major axis of the ellipse. The equation of an ellipse rotated from the coordinate axis is a standard equation, in terms of the $\alpha\beta$ coordinate system, given by equation (2.30).

$$Ai_\alpha^2(k) + 2Hi_\alpha(k)i_\beta(k) + Bi_\beta^2(k) + 2Gi_\alpha(k) + 2Fi_\beta(k) + 1 = 0 \tag{2.30}$$

If the effect of magnetic saturation can be neglected, the centre of the ellipse is at

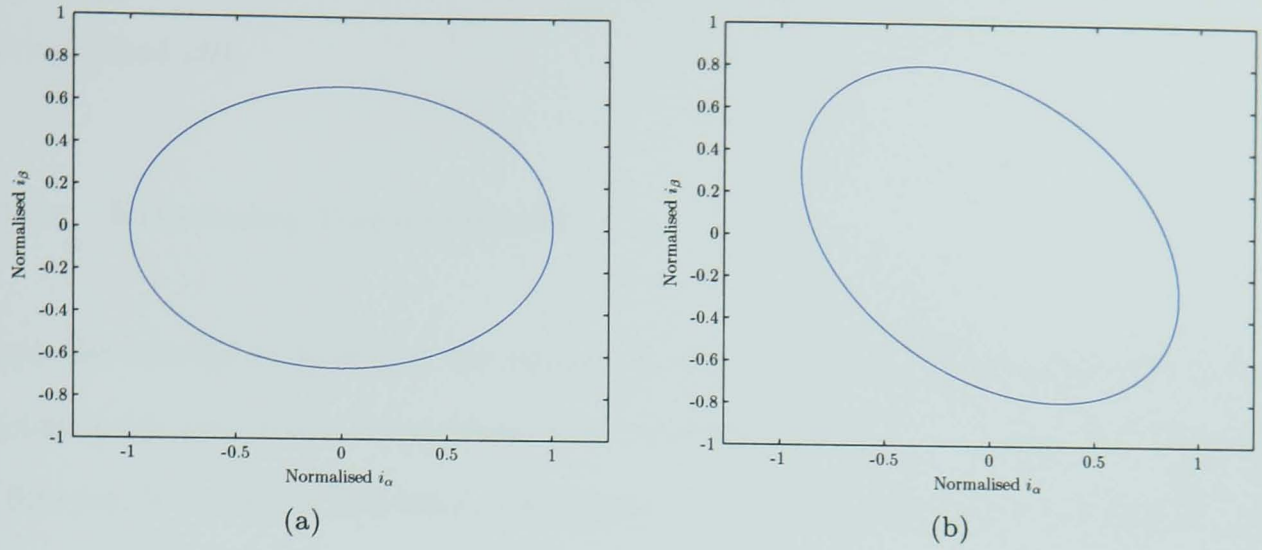

Figure 2.6: Armature Current Locus

the origin and equation (2.30) becomes:

$$Ai_\alpha^2(k) + 2Hi_\alpha(k)i_\beta(k) + Bi_\beta^2(k) + 1 = 0 \tag{2.31}$$

Using Newton-Raphson or a similar curve-fitting algorithm, the coefficients can be found such as to minimise the error between the measured curve and that found using equation (2.31). Once the parameters of equation (2.31) are found, the angle of the major axis of the ellipse is given by equation (2.32) [40].

$$\delta = \frac{1}{2}\tan^{-1}\frac{2H}{A-B} \tag{2.32}$$

For a given input frequency, there is a constant offset between the major axis of the ellipse and the rotor position. This offset is dependent on the impedance of the stator windings and is thus constant if the armature current is kept at a fixed frequency. This can be measured or calculated in advance for a given motor.

Once the rotor axis angle is identified, it is necessary to distinguish between a north and a south pole in the machine. Magnetic saturation has thus far been neglected due to the small effect that it has. However, once the major axis has been identified, the magnetic saturation effects can be examined and from these the north pole can be identified. Due to the magnetic saturation, there is a small offset between the centres of the ellipse and the coordinate axes in the direction of the north pole.

Thus, by examining the data after the ellipse fitting is complete, the poles can be distinguished [40].

2.5.2c Processing Requirements

Since the system is designed for operation at standstill, the real-time processing requirements are reduced compared to a rotating machine. In a machine rotating at 50 rpm, it would be necessary to perform position calculations several thousand times a second, but with a stationary shaft, once is enough. However, to perform the ellipse-fitting algorithm, a reasonable amount of data must be accumulated (figure 7, [40]), which requires sufficient memory in the system.

2.5.2d Applicability

This technique is designed for use on interior permanent magnet synchronous machines only and is only practical at zero speed.

2.5.2e Advantages / Limitations

This system should be relatively simple to implement. There is a certain degree of parameter dependence affecting the offset between the major axis of the ellipse and that of the rotor. However, the system would be practical for providing a good approximation of an initial position that could be used in conjunction with a back EMF or observer based estimator. In addition, the memory requirements are high and the system is impractical above zero speed.

2.5.3 Signal Injection with Observers

2.5.3a Technique

In order to track a saliency present in the IPMSM, high-frequency voltages are injected into the stator and these generate corresponding high-frequency currents that can be detected [41–70]. These currents vary according to the position of the rotor. By detecting the currents and performing appropriate signal processing, a signal is produced that is proportional to the difference between the true rotor position and the estimated one. A tracking observer can then be used to adjust the estimated position.

2.5.3b Algorithm

The injection of a balanced high-frequency voltage component will induce stator currents consisting of spatially variant and invariant components [71].

$$v_{dq} = \begin{pmatrix} v_d \\ v_q \end{pmatrix} = V_i \begin{pmatrix} -\sin\omega_i t \\ \cos\omega_i t \end{pmatrix} \tag{2.33}$$

Equation (2.33) shows the form of the injected components; the currents induced by these are shown in equation (2.34), assuming that the injected signal is of sufficient frequency that the stator transient reactance dominates the stator terminal properties,

$$i_{dq} = \begin{pmatrix} i_d \\ i_q \end{pmatrix} = \begin{pmatrix} I_{i0}\cos\omega_i t - I_{i1}\cos(2\theta_a - \omega_i t) \\ I_{i0}\sin\omega_i t - I_{i1}\sin(2\theta_a - \omega_i t) \end{pmatrix} \tag{2.34}$$

where θ_a is the angular position of the saliency relative to the stator (proportional to the rotor position for a machine with a single saliency) and I_{i0} and I_{i1} are defined in equation (2.35),

$$I_{i0} = \frac{V_i}{\omega_i}\frac{\bar{L}}{\bar{L}^2 - \check{L}^2};\ I_{i1} = \frac{V_i}{\omega_i}\frac{\check{L}}{\bar{L}^2 - \check{L}^2} \tag{2.35}$$

where $\bar{L}$ is the mean of the direct and quadrature axes inductances and $\breve{L}$ is half of the difference between them.

This signal contains two components: one at the frequency of the injection signal and one with an additional position dependent frequency component. Performing a vector rotation by an angle $\omega_i t$ on this signal translates the first component into a steady level that can be filtered out. Practically, this means implementing a low-pass filter in a reference frame synchronous to the injected signal. Once this component has been removed, the signal can be rotated by $-\omega_i t$ and a tracking observer can be used to derive the position.

2.5.3c Extensions

In references [47,52], the effect of multiple saliencies on this form of position detection technique was analysed. Most saliency based sensorless control schemes assume a single, sinusoidally varying, rotor position dependent saliency. However, this is often not the case. There may be multiple saliencies, or the single saliency may be non-sinusoidal (equivalent to multiple saliencies with each corresponding to a Fourier component). Also, there may be stationary saliencies, either due to machine design (for example stator winding asymmetry) or due to unbalanced excitation or scaling differences in the current sensors [47].

A compensation scheme is proposed in these papers, involving decoupling each unwanted saliency using a tracking observer with a model of the saliency. It is necessary to have a reasonable knowledge of the magnitude, phase and position dependence of the saliencies in order to achieve this. A similar technique to that used to detect the rotor position can be used to measure the saliencies. Given a known rotor position (from a resolver or encoder), the algorithm of section 2.5.3b can be used to derive the required saliency information [51]. The principal problem with this approach is one of complexity. For each component of saliency that is present in the machine, an additional observer must be designed to enable correct compensation. The design requirements of this approach are large and once the system has been

designed, the computational complexity of any system restricts its applicability in many applications.

2.5.3d Applicability

This estimator is designed for use with salient machines, specifically the IPMSM. Since it relies on a significant saliency, it could not be used with Surface Permanent Magnet Synchronous Machines (SPMSMs). However, it does hold the significant advantage of working over the full (including zero) speed range of the machine. At higher speeds, however, the requirement for a signal injection signal superimposed on the fundamental will result in a reduction in the maximum available power supply voltage. There is also a requirement for significant spectral separation between the fundamental frequency and the injection frequency [72]. It is therefore desirable to switch from this system to a back EMF or observer based system at higher speeds [72, 73].

2.5.4 Switching Frequency Based Estimation

This technique is based on the same principles as signal injection estimation except that, rather than injecting a fixed frequency signal for the specific purpose of detecting position, it uses the effect of the PWM switching as an injected signal [74–81]. This would suggest similar capabilities in terms of position sensing, as the system is essentially the same apart from operating at a higher frequency. However, at standstill, the inverter would not necessarily be switching and hence there would be no signal to use for a sensorless start. In addition, the frequency spectrum of the PWM "injection" is extremely complex, with a large number of harmonics and sub-harmonics [82]. Therefore, it is difficult to isolate the required components from the other harmonics, which are essentially noise.

2.5.5 Simplified Saturation Based Estimation

2.5.5a Technique

When a short voltage pulse of an appropriate magnitude and duration is applied to the stator windings, the stator iron will saturate, depending on the position of the rotor magnets. This saturated core will cause a variation in the inductance of the windings, which can be measured using the currents produced by the voltage pulse [83–86].

2.5.5b Algorithm

Three positive and three negative voltage pulses (one pair of pulses for each phase) are applied to the stator windings at zero speed. Immediately following the voltage pulse for a given phase, a voltage pulse in the opposite polarity is fired in order to drive the phase currents back to zero. The sinusoidal like behaviour of the phase currents can be modelled as an average value with some offset value, the latter being a function of mechanical position [84].

$$I_A = I_0 + \Delta I_0 \cos(2\theta_r) \tag{2.36}$$

$$I_B = I_0 + \Delta I_0 \cos\left(2\theta_r + \frac{2\pi}{3}\right) \tag{2.37}$$

$$I_C = I_0 + \Delta I_0 \cos\left(2\theta_r - \frac{2\pi}{3}\right) \tag{2.38}$$

By defining the difference between the phase currents and the average value as shown in equation (2.39), these equations can be solved,

$$\Delta I_X = I_X - I_0 \tag{2.39}$$

where the subscript X can be A, B or C.

The phase current that has the largest magnitude change determines the region in which the rotor north pole lies. The remaining two phase-current differences are used to calculate the approximate position. If phase A has the largest difference, then dividing (2.37) by (2.38) and using the relationships given by equation (2.39) results in equation (2.40).

$$\Delta I_B \cos\left(2\theta_r - \frac{2\pi}{3}\right) = \Delta I_C \cos\left(2\theta_r + \frac{2\pi}{3}\right) \tag{2.40}$$

Solving for position gives equation (2.41).

$$\theta_r = \frac{1}{2}\tan^{-1}\left(\frac{\cos\left(\frac{2\pi}{3}\right)(\Delta I_C - \Delta I_B)}{\sin\left(\frac{2\pi}{3}\right)(\Delta I_C + \Delta I_B)}\right) \tag{2.41}$$

2.5.5c Applicability

This type of estimator is the only one found in the literature that allows zero speed position estimation for non-salient machines. It should also be possible to apply this technique to IPMSMs, but considering the number of other possibilities, this would be less preferable than the other options. It is inherently a zero speed only technique, but it could be combined with other techniques designed for different speeds to allow operation over the full range.

2.5.5d Processing Power

If the small angle theorem is used to remove the trigonometric function from equation (2.41), then the only processing required is to calculate a mean and peak value of a sampled waveform. It is then simply a case of calculating the inverse tangent of the result.

2.5.5e Advantages / Limitations

This system does not produce particularly high accuracy, but does enable zero speed sensing in SPMSMs. Therefore, it could be combined with other systems to provide

sensorless control over the full range of speeds. Since it is based on saturation effects in the machine, it is difficult to model.

2.6 Summary

The techniques presented in this literature review fall into two main classifications. The first of these contains the 'at speed' back EMF and observer techniques and the second contains the saliency based techniques. All of these techniques operate effectively when the shaft is rotating at a sufficient speed to overcome measurement noise, but are unable to work when the machine is stationary. However, they are considerably simpler in terms of implementation and computational requirements than the saliency techniques. The back EMF models are the simplest of the 'at speed' techniques, but are more sensitive to parameter variations than the observer techniques. The latter, however, require significantly greater computational capacity and a longer design cycle prior to implementation. Fitting loosely into this classification is also the inverter state monitoring technique, which allows segment based position sensing down to lower speeds than the zero crossing point approach, at the expense of an increase in electronics in the inverter to allow detection of the conduction state of the diodes.

The saliency based techniques have the considerable advantage that they operate at zero speed. Some of these techniques are capable of operating over the full speed range. However, this is unlikely to be desirable in many applications due to the increased computational demand (compared to back EMF or observer techniques), the possibility of torque ripple and the reduction of available DC link voltage, both as a result of the need for a superimposed injection signal.

The work presented in this thesis fits into the second classification, but aims to provide an approach that is simple both in terms of design complexity and computational demand.

Table 2.1 presents a summary of the various techniques discussed in this chapter.

Sensorless Technique	Machine Applicability	Design Complexity	Processing Power	Speed Range
Back EMF				
Flux Linkage Model	Brushless AC	Simple	Low	Med.–High
Zero Crossing Points	Brushless DC	Simple	Low	Med.–High
Observers				
Simple	SPMSMs	Simple	Low	Med.–High
EKF *et al.*	All	Complex	High	Med.–High
Artificial Intelligence	All	Complex	Medium	Med.–High
Inverter State	Brushless DC	Medium	Low	Low–High
Saliency				
Armature Current Locus	IPMSMs	Simple	High	Zero
Tracking Observers	IPMSMs	Complex	High	Zero–Med.
Switching Frequency	IPMSMs	Complex	High	Low–Med.
Saturation Based	SPMSMs	Complex	Low	Zero

Table 2.1: Summary of Sensorless Techniques

Chapter 3

Theoretical Analysis

3.1 Modelling Permanent Magnet Synchronous Machines

Development of sensorless strategies relies on an understanding of the operation of permanent magnet brushless machines. It is therefore instructive to develop a mathematical model of the machine upon which to base the theoretical analysis.

A three-phase permanent magnet brushless machine has three phase windings (usually in slots) on the stator and one or more pairs of permanent magnets mounted on or within the rotor structure. An example of this is shown diagrammatically in figure 3.1.

In modelling the machines mathematically, the following assumptions are made in order to simplify the derivation [87, 88].

1. Magnetic materials are free of eddy current and hysteresis losses.
2. Commutation is ideal; a balanced three-phase supply voltage is considered.
3. Slotting effects are ignored[1]. Distributed windings comprise finely spread conductors of negligible diameter.

[1] However, see section 3.6

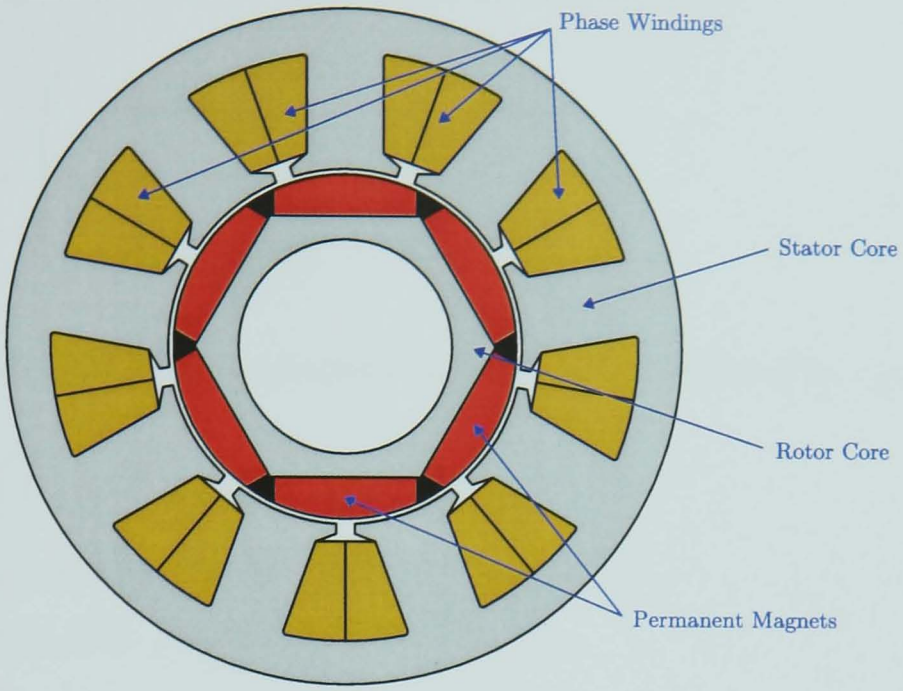

Figure 3.1: Example of PMSM Structure

4. Air-gap reluctance has a constant component as well as a sinusoidally varying component.

5. Stator windings produce a sinusoidal Magneto-Motive Force (MMF) distribution. Space harmonics in the air gaps are negligible.

The electrical equation for the three phases are represented in equations (3.1)–(3.3) [88].

$$v_a = R_s i_a + p\psi_a \tag{3.1}$$

$$v_b = R_s i_b + p\psi_b \tag{3.2}$$

$$v_c = R_s i_c + p\psi_c \tag{3.3}$$

The flux linkages are formed from the interaction of the self and mutual inductances with the winding currents, as well as the flux due to the permanent magnets. The

permanent magnet flux in the winding can be represented as

$$\psi_{m(abc)} = \begin{pmatrix} \cos(\theta_r) \\ \cos(\theta_r - 120°) \\ \cos(\theta_r - 240°) \end{pmatrix} \psi_m \tag{3.4}$$

The three phase flux linkage equations can then be expressed as in equation (3.5),

$$\psi_{abc} = \begin{pmatrix} L_{aa}(\theta_r) & L_{ab}(\theta_r) & L_{ac}(\theta_r) \\ L_{ab}(\theta_r) & L_{bb}(\theta_r) & L_{bc}(\theta_r) \\ L_{ac}(\theta_r) & L_{bc}(\theta_r) & L_{cc}(\theta_r) \end{pmatrix} \psi_{m(abc)} \tag{3.5}$$

where $L_{aa}(\theta_r)$ is the self inductance of phase a, $L_{ab}(\theta_r)$ is the mutual inductance between phases a and b, etc. In the ideal machine, each inductance consists of an average component and a sinusoidally varying component, with the self inductances at a maximum when the rotor q-axis is aligned with the phase and the mutual inductances at a maximum when the q-axis is midway between two phases [88].

Transforming equations (3.1)–(3.5) to the dq reference frame results in equations (3.6) and (3.7),

$$v_d = R_s i_d + p\psi_d - \omega_r \psi_q \tag{3.6}$$

$$v_q = R_s i_q + p\psi_q + \omega_r \psi_d \tag{3.7}$$

where ψ_d and ψ_q are the d- and q-axis flux linkages and are derived from translation of equations (3.4) and (3.5) into the dq reference frame. Representing the dq-axis inductances as L_d and L_q (which are no longer functions of θ_r), ψ_{dq} can be represented as equation (3.8).

$$\psi_{dq} = \begin{pmatrix} L_d & 0 \\ 0 & L_q \end{pmatrix} i_{dq} + \begin{pmatrix} \psi_m \\ 0 \end{pmatrix} \tag{3.8}$$

Combining equations (3.6)–(3.8) results in equation (3.9).

$$v_{dq} = \begin{pmatrix} R_s + pL_d & -\omega_r L_q \\ \omega_r L_d & R_s + pL_q \end{pmatrix} i_{dq} + \begin{pmatrix} 0 \\ \psi_m \omega_r \end{pmatrix} \tag{3.9}$$

3.2 Effect of Injection Signals

To analyse the effect of the application of a balanced set of high-frequency sinusoidal voltages to the terminals of the machine, it is instructive to use the mathematical model developed in §3.1 and reproduced as equation (3.10) to produce a model of the resulting currents.

$$v_{dq} = \begin{pmatrix} R_s + pL_d & -\omega_r L_q \\ \omega_r L_d & R_s + pL_q \end{pmatrix} i_{dq} + \begin{pmatrix} 0 \\ \psi_m \omega_r \end{pmatrix} \tag{3.10}$$

If the angular frequency of the injection signal, ω_i, is sufficient, the resistance of the windings can be considered negligible compared to the reactance. In addition, considering only the high-frequency components of the system, the rotor can be assumed to be effectively stationary. As a result, the machine model may be approximated in the $\alpha\beta$ reference frame by [47]:

$$v_{\alpha\beta} \approx j\omega_i L_{\alpha\beta} i_{\alpha\beta} \tag{3.11}$$

where $L_{\alpha\beta}$ is the result of transforming the dq-axis inductances into the two-phase stationary reference frame [87] as shown in equations (3.12) and (3.13),

$$L_{\alpha\beta} = \begin{pmatrix} \cos\theta_r & -\sin\theta_r \\ \sin\theta_r & \cos\theta_r \end{pmatrix} \begin{pmatrix} L_d & 0 \\ 0 & L_q \end{pmatrix} \begin{pmatrix} \cos\theta_r & \sin\theta_r \\ -\sin\theta_r & \cos\theta_r \end{pmatrix} \tag{3.12}$$

$$= \begin{pmatrix} \bar{L} - \breve{L}\cos 2\theta_r & -\breve{L}\sin 2\theta_r \\ -\breve{L}\sin 2\theta_r & \bar{L} + \breve{L}\cos 2\theta_r \end{pmatrix} \tag{3.13}$$

where,

$$\bar{L} = \frac{1}{2}\left(L_q + L_d\right) \tag{3.14}$$

$$\breve{L} = \frac{1}{2}\left(L_q - L_d\right) \tag{3.15}$$

The high-frequency balanced voltage set that is injected into the windings can be represented by equation (3.16),

$$v_{\alpha\beta} = V_i \begin{pmatrix} -\cos\left(\omega_i t\right) \\ \sin\left(\omega_i t\right) \end{pmatrix} \tag{3.16}$$

where V_i is the magnitude of the injected signal. Combining equations (3.11), (3.13) and (3.16) gives equation (3.17).

$$V_i \begin{pmatrix} -\cos\left(\omega_i t\right) \\ \sin\left(\omega_i t\right) \end{pmatrix} = j\omega_i \begin{pmatrix} \bar{L} - \breve{L}\cos 2\theta_r & -\breve{L}\sin 2\theta_r \\ -\breve{L}\sin 2\theta_r & \bar{L} + \breve{L}\cos 2\theta_r \end{pmatrix} i_{\alpha\beta} \tag{3.17}$$

Breaking this into the two separate components gives equations (3.18) and (3.19).

$$-\frac{V_i}{\omega_i}\cos\left(\omega_i t\right) = j\bar{L}i_\alpha - j\breve{L}\cos\left(2\theta_r\right)i_\alpha - j\breve{L}i_\beta\sin\left(2\theta_r\right) \tag{3.18}$$

$$\frac{V_i}{\omega_i}\sin\left(\omega_i t\right) = j\bar{L}i_\beta + j\breve{L}\cos\left(2\theta_r\right)i_\beta - j\breve{L}i_\alpha\sin\left(2\theta_r\right) \tag{3.19}$$

In order to identify the resulting currents, it is necessary to solve these simultaneous equations for i_α and i_β. A straightforward way to achieve this is to rearrange both equations in terms of either i_α or i_β and then to equate them. Rearrangement of equations (3.18) and (3.19) results in equations (3.20) and (3.21) respectively.

$$i_\beta = \frac{V_i}{\omega_i}\frac{\cos\left(\omega_i t\right)}{j\breve{L}\sin\left(2\theta_r\right)} + \frac{\left(j\bar{L} - j\breve{L}\cos\left(2\theta_r\right)\right)}{j\breve{L}\sin\left(2\theta_r\right)}i_\alpha \tag{3.20}$$

$$i_\beta = \frac{V_i}{\omega_i} \frac{\sin(\omega_i t)}{\left(j\bar{L} + j\breve{L}\cos(2\theta_r)\right)} + \frac{j\breve{L}\cos(2\theta_r)}{\left(j\bar{L} + j\breve{L}\cos(2\theta_r)\right)} i_\alpha \tag{3.21}$$

In order to solve these equations for i_α, it is first necessary to equate them and multiply by (3.22) in order to remove the denominators.

$$\left(j\breve{L}\sin(2\theta_r)\right)\left(j\bar{L} + j\breve{L}\cos(2\theta_r)\right) \tag{3.22}$$

This results in equation (3.23).

$$\begin{aligned} &\frac{V_i}{\omega_i}\left(j\bar{L} + j\breve{L}\cos(2\theta_r)\right)\cos(\omega_i t) \\ &\quad + \left(j\bar{L} - j\breve{L}\cos(2\theta_r)\right)\left(j\bar{L} + j\breve{L}\cos(2\theta_r)\right) i_\alpha \\ &\quad = j\frac{V_i}{\omega_i}\breve{L}\sin(2\theta_r)\sin(\omega_i t) + \left(j\breve{L}\sin(2\theta_r)\right)^2 i_\alpha \end{aligned} \tag{3.23}$$

By grouping terms and using trigonometric identities this can be simplified as shown in equation (3.24).

$$-j\frac{V_i}{\omega_i}\bar{L}\cos(\omega_i t) + j\frac{V_i}{\omega_i}\breve{L}\cos(2\theta_r - \omega_i t) - \left(\bar{L}^2 - \breve{L}^2\right) i_\alpha = 0 \tag{3.24}$$

Rearranging in terms of i_α produces equation (3.25),

$$i_\alpha = -jI_1\cos(\omega_i t) + jI_2\cos(2\theta_r - \omega_i t) \tag{3.25}$$

where,

$$I_1 = \frac{V_i}{\omega_i}\frac{\bar{L}}{\left(\bar{L}^2 - \breve{L}^2\right)} \tag{3.26}$$

$$I_2 = \frac{V_i}{\omega_i}\frac{\breve{L}}{\left(\bar{L}^2 - \breve{L}^2\right)} \tag{3.27}$$

Considering the orthogonal nature of the axes and the phase relationship between sine and cosine, it can be seen that

$$-j\cos x = \sin x \tag{3.28}$$

and therefore

$$i_\alpha = I_1 \sin(\omega_i t) - I_2 \sin(2\theta_r - \omega_i t) \tag{3.29}$$

Following the same process to find i_β as was used for i_α and combining the results produces equation (3.30) [2].

$$i_{\alpha\beta} = I_1 \begin{pmatrix} \sin(\omega_i t) \\ \cos(\omega_i t) \end{pmatrix} - I_2 \begin{pmatrix} \sin(2\theta_r - \omega_i t) \\ \cos(2\theta_r - \omega_i t) \end{pmatrix} \tag{3.30}$$

It can be seen that for any θ_r, this produces an ellipsoidal locus when viewed in the $\alpha\beta$ plane. The ellipse is centred on the origin and the major axis of the ellipse rotates with θ_r. Examples of ellipsoidal current loci produced using equation (3.30) are shown in figures 3.2 and 3.3 for $\theta_r = 0°$ and $\theta_r = 45°$ respectively. It can be

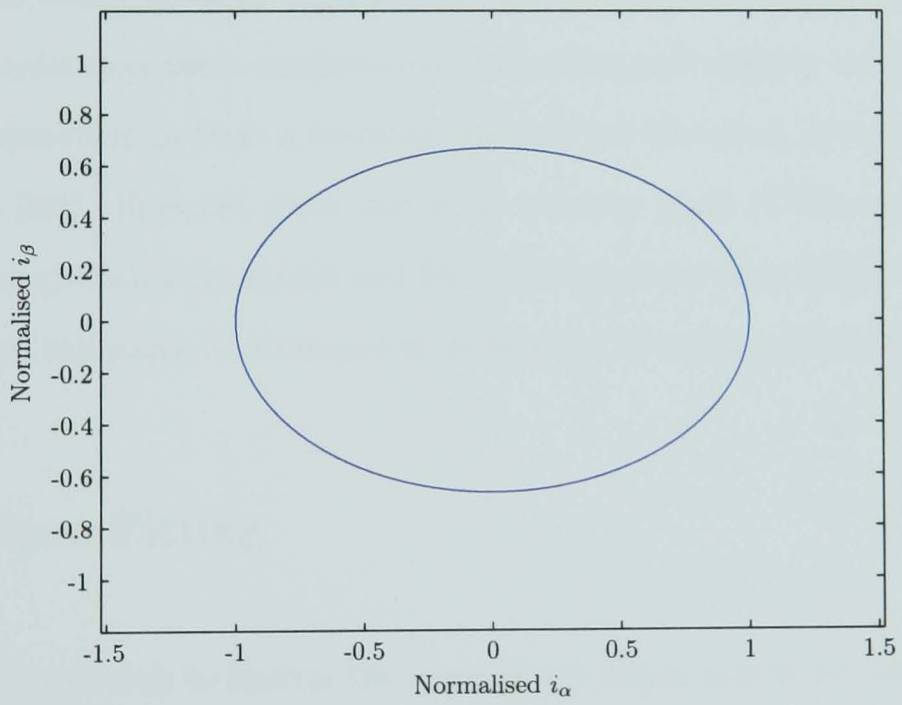

Figure 3.2: Example of Ellipsoidal Current Loci; $\theta_r = 0°$

seen that in theory, since the major axis of the ellipse follows the position of the rotor, if the angle of that major axis can be found then sensorless control can be achieved. This approach was first presented in [40]. However, it can also be seen that any two ellipses at rotor positions separated by 180° electrical will appear identical and thus it is also necessary to identify the magnet polarity in order to distinguish between north and south poles. This is discussed further in section 3.5. In addition

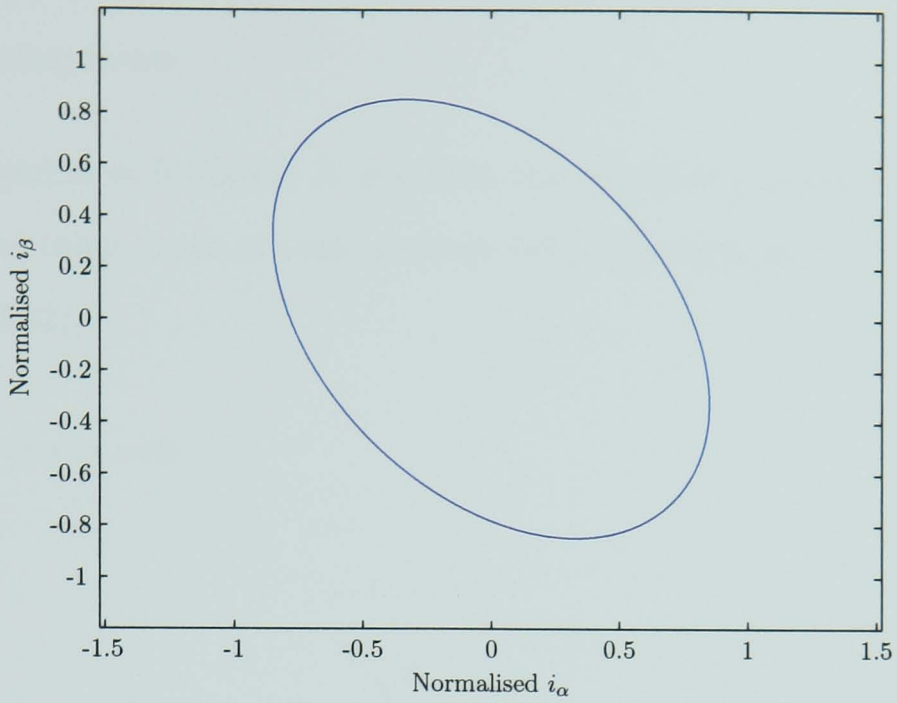

Figure 3.3: Example of Ellipsoidal Current Loci; $\theta_r = 45°$

to the ellipse fitting strategy discussed in further detail in section 3.3, alternative approaches exist that use a combination of machine and saliency models combined with PID controllers to form a tracking observer (as discussed in section 2.5.3 and proposed in [50]). However, since one of the primary goals of this research was to produce a computationally simple and fast and therefore robust technique, a simple demodulation technique is developed in section 3.4 as another alternative.

3.3 Ellipse Fitting

The intuitive approach to finding the angle of the major axis of the ellipse is to use some form of curve fitting algorithm to identify the coefficients of one of the various forms of the standard ellipse equation and to derive the major axis angle from there. Consider the Cartesian equation for a general conic shown in equation (3.31) [89],

$$Ax^2 + 2Hxy + By^2 + 2Gx + 2Fy + C = 0 \tag{3.31}$$

where x and y are the coordinate axes and all other terms are coefficients defining the form of the conic section. In equation (3.31), the A and B coefficients directly affect the minor and major axis length, coefficient H gives the rotation of the ellipse

around the coordinate axis, G and H give the position of the centre of the ellipse and C is a scaling factor.

If $H^2 < AB$ and $A \neq B$ and/or $H \neq 0$ then this equation represents an ellipse (as opposed to the other types of conic section) [89]. Rewriting in vector form results in equation (3.32),

$$f(\mathbf{a}, \mathbf{x}) = \mathbf{a} \cdot \mathbf{x} = 0 \tag{3.32}$$

where,

$$\mathbf{a} = \begin{pmatrix} A & 2H & B & 2G & 2F & C \end{pmatrix}^T \tag{3.33}$$

$$\mathbf{x} = \begin{pmatrix} x^2 & xy & y^2 & x & y & 1 \end{pmatrix}^T \tag{3.34}$$

Due to the zero sum of equations (3.31) and (3.32), the constraint $H^2 < AB \Rightarrow H^2 - AB < 0$ can be arbitrarily scaled and therefore simplified to $H^2 - AB = -\frac{1}{4}$. Removing doubled components with $k_1 = 2H$, $k_2 = 2G$ and $k_3 = 2F$ gives $4AB - k_1^2 = 1$. Expressing this in the matrix form $\mathbf{a}^T\mathbf{C}\mathbf{a} = 1$ as

$$\mathbf{a}^T \begin{pmatrix} 0 & 0 & 2 & 0 & 0 & 0 \\ 0 & -1 & 0 & 0 & 0 & 0 \\ 2 & 0 & 0 & 0 & 0 & 0 \\ 0 & 0 & 0 & 0 & 0 & 0 \\ 0 & 0 & 0 & 0 & 0 & 0 \\ 0 & 0 & 0 & 0 & 0 & 0 \end{pmatrix} \mathbf{a} = 1 \tag{3.35}$$

and following [90] results in the ellipse fitting process being a case of performing a standard least squares minimisation of $E = ||\mathbf{D}\mathbf{a}||^2$ subject to the constraint $\mathbf{a}^T\mathbf{C}\mathbf{a} = 1$ [91], where $\mathbf{D}$ is referred to as the 'design matrix' and contains the vectors corresponding to each measured point on the ellipse circumference.

Once the coefficients in $\mathbf{a}$ have been identified, they can again be scaled arbitrarily

and, since the ellipse is centred on the origin (as discussed in §3.2), it can be seen that $k_2 = k_3 = g = f = 0$. Therefore, the Cartesian ellipse equation is reduced to:

$$Ax^2 + 2Hxy + By^2 + 1 = 0 \tag{3.36}$$

Using these parameters, the angle of the major axis of the ellipse can be found from equation (3.37).

$$\theta_{major} = \frac{1}{2}\tan^{-1}\frac{2H}{A-B} \tag{3.37}$$

However, due to the $\frac{1}{2}\tan^{-1}$ term in equation (3.37), the result is constrained in the region -45° $\rightarrow$ 45°. This does not give sufficient information to derive the absolute position of the major axis. It is therefore necessary to enhance the method shown in [40] to deal with this discrepancy. By rotating equation (3.36) to be aligned with the axis and solving the resulting equation, it is found that in order to determine the absolute position, an additional 90° must be added to the result of equation (3.37) if the sign of (3.38) is negative.

$$(A-B)\cos(2\theta_{major}) + 2H\sin(2\theta_{major}) \tag{3.38}$$

With this addition, the position of the major axis can be found for all rotations of the ellipse. However, due to the symmetrical shape of the ellipse, it is impossible with this position derivation to find whether the top or bottom end of the ellipse corresponds to the north magnetic pole. This issue is discussed in section 3.5.

3.4 Demodulation

Examining the currents resulting from voltage injection shown in equation (3.30) and reproduced here as equation (3.39) it can be seen that there are two main

components.

$$i_{\alpha\beta} = I_1 \begin{pmatrix} \sin(\omega_i t) \\ \cos(\omega_i t) \end{pmatrix} - I_2 \begin{pmatrix} \sin(2\theta_r - \omega_i t) \\ \cos(2\theta_r - \omega_i t) \end{pmatrix} \tag{3.39}$$

The rotor position information is contained only in the second component. Therefore, by isolating this component and removing the injection frequency dependent component, the rotor position can be found. To achieve this, the $\alpha\beta$ reference frame currents are rotated into a reference frame that is synchronous with the injected voltage set as shown in equations (3.40) and (3.41).

$$i' = \begin{pmatrix} \cos(\omega_i t) & \sin(\omega_i t) \\ -\sin(\omega_i t) & \cos(\omega_i t) \end{pmatrix} i_{\alpha\beta} \tag{3.40}$$

$$= I_1 \begin{pmatrix} 1 \\ 0 \end{pmatrix} - I_2 \begin{pmatrix} \sin(2\theta_r - 2\omega_i t) \\ \cos(2\theta_r - 2\omega_i t) \end{pmatrix} \tag{3.41}$$

The first component is thus time invariant and can be removed using a simple high-pass filter. This results in equation (3.42).

$$i' = -I_2 \begin{pmatrix} \sin(2\theta_r - 2\omega_i t) \\ \cos(2\theta_r - 2\omega_i t) \end{pmatrix} \tag{3.42}$$

Removal of the final unwanted component can be achieved by rotating equation (3.42) to a reference frame that is rotating at the same speed as the injection signals but in the opposite direction, as shown in equations (3.43) and (3.44).

$$i'' = \begin{pmatrix} \cos(-2\omega_i t) & \sin(-2\omega_i t) \\ -\sin(-2\omega_i t) & \cos(-2\omega_i t) \end{pmatrix} i' \tag{3.43}$$

$$= -I_2 \begin{pmatrix} \sin(2\theta_r) \\ \cos(2\theta_r) \end{pmatrix} \tag{3.44}$$

A simple Cartesian-to-polar transformation completes the scheme. As with all saliency based techniques, it is then necessary to identify magnetic polarity, as discussed in section 3.5.

3.5 Polarity

Due to the symmetry of the inductance profile in permanent magnet brushless machines, saliency based estimation techniques must be supplemented by a system that identifies the magnetic polarity. In practical systems, this only needs to be performed once at startup as the estimator can simply monitor the position estimation and switch polarity whenever there is a sudden large change in the estimated rotor position.

There are a number of approaches to magnetic polarity detection. The simplest of these (and the one adopted in this thesis) is to simply make an assumption as to the polarity of the machine and then verify that it is correct when power is first applied. Alternatively, it has been reported [40] that it is possible to identify magnetic polarity by applying brief test pulses to each phase individually and deriving the polarity from the rate of change of induced currents. It is also possible to identify magnetic polarity using magnetic saturation effects on the saliency image [92]. Selection of an optimised approach to this, however, is beyond the scope of this thesis.

3.6 Slotting Effects and Saliency Distortion

3.6.1 Introduction

The development of the position sensorless strategy discussed in sections 3.1 to 3.4 has assumed an ideal machine. As discussed in [47] and [93], this is invariably not the case. The ideal machine assumes a single, sinusoidally distributed saliency with a period equal to the pole pitch. Additional distorting components are introduced by stator slotting effects. As a result, the model of the captured currents that the

derivation was based upon is inaccurate. An alternative model, originally presented in [47], is described by equation (3.45),

$$i_{\alpha\beta} = I_1 \begin{pmatrix} \sin(\omega_i t) \\ \cos(\omega_i t) \end{pmatrix} - \sum_{k=2}^{n} I_k \begin{pmatrix} \sin(h_k \theta_r - \omega_i t + \phi_k) \\ \cos(h_k \theta_r - \omega_i t + \phi_k) \end{pmatrix} \tag{3.45}$$

where I_k is the magnitude of the kth component of the saliency, h_k is the harmonic number of that component and ϕ_k is the phase shift of that component relative to the α axis. In this model, the second component of equation (3.30) has been replaced by a Fourier series that can represent any periodic form.

Sections 3.6.2 to 3.6.4 demonstrate simulation results that show the effect of this distortion on the techniques discussed in sections 3.3 and 3.4.

3.6.2 Simulated Currents

The model of equation (3.45) was used with a single additional saliency component to generate a set of simulated currents over one electrical cycle in order to demonstrate the effect of this distortion on the sensorless algorithms. The coefficients were chosen to match test results for a practical machine. The details of the machine and the testing performed are discussed in more detail in chapters 4 and 5. The chosen coefficients are shown in table 3.1.

Parameter	Value
I_1	$\frac{5}{6}$ Vs/rad
I_2	$\frac{1}{6}$ Vs/rad
I_3	$\frac{1}{24}$ Vs/rad
h_2	2
h_3	-4
ϕ_2	0 rad
ϕ_3	3.28 rad

Table 3.1: Coefficients Selected for Slotting Simulation

Examples of the current loci produced at rotor electrical angles of 0° and 60° are shown in figures 3.4 and 3.5 respectively. It can be seen that the currents are

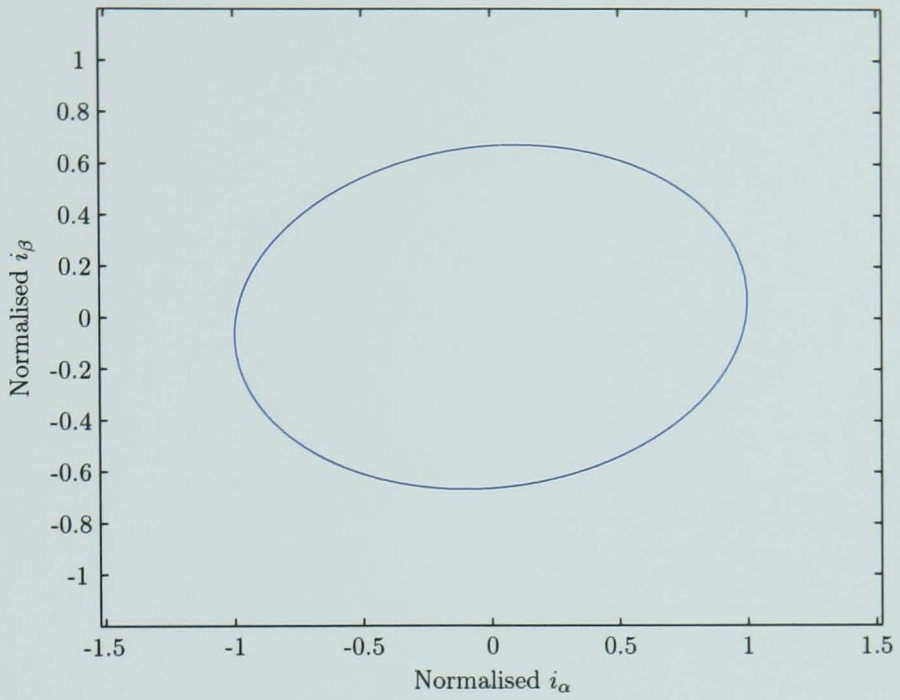

Figure 3.4: Example of Current Loci with Distortion; $\theta_r = 0°$

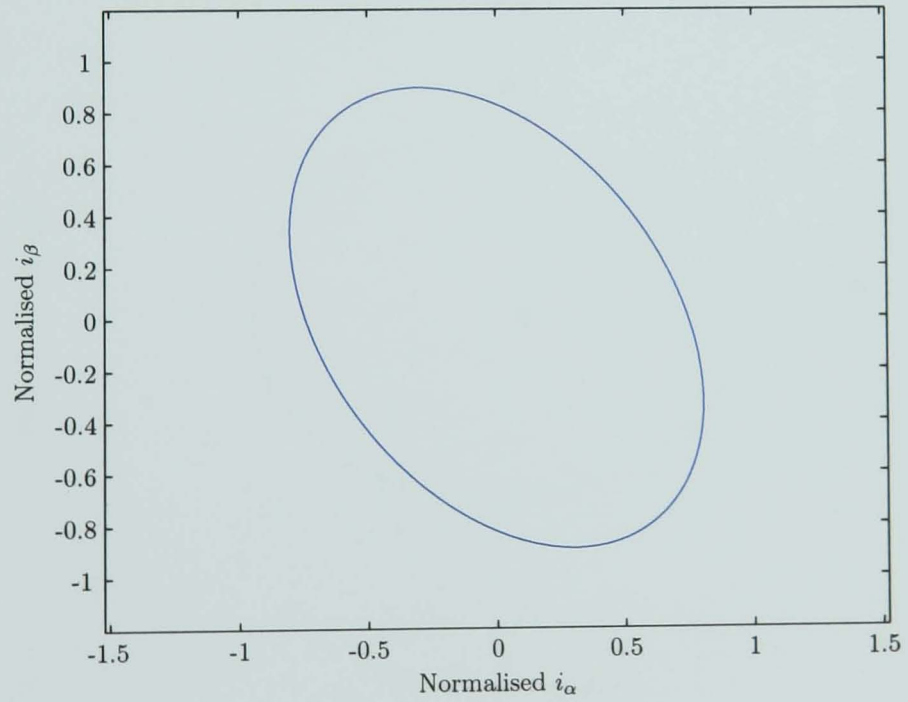

Figure 3.5: Example of Current Loci with Distortion; $\theta_r = 60°$

still ellipsoidal and that the distortion is not obvious, apart from a small deviation from the expected angle. However, comparison of the ellipses for intermediate points makes the effect more distinctive. Viewing each ellipse in a reference frame aligned with its own major axis allows comparison of the shape of the individual

ellipses. Figures 3.6 and 3.7 show these shapes for rotor positions of $-15°$ and $+15°$ respectively. It can be seen that there is a large amount of distortion in the minor

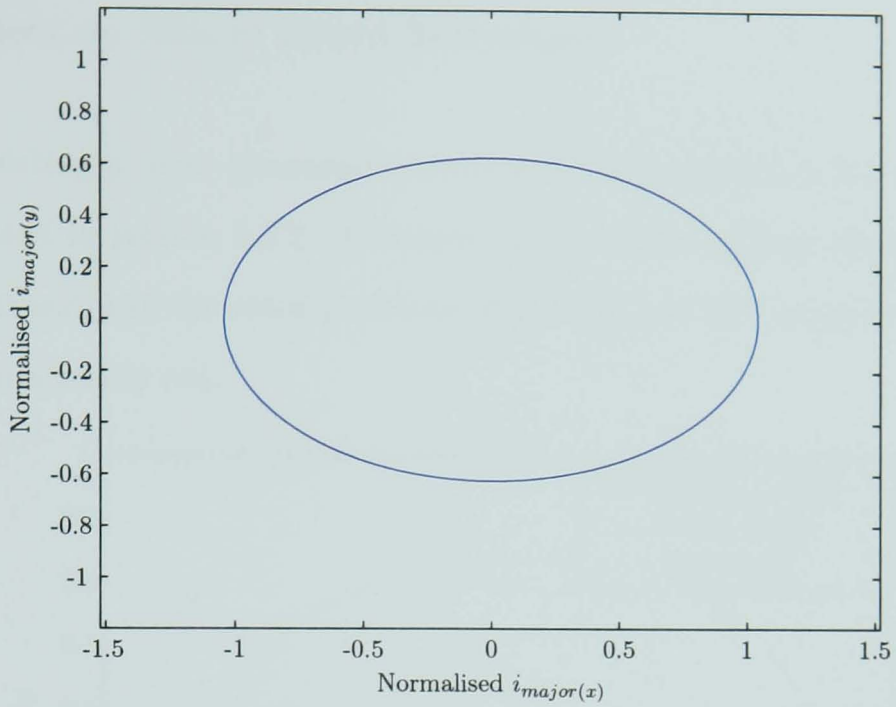

Figure 3.6: Ellipse Aligned with Major Axis, $\theta_r = -15°$

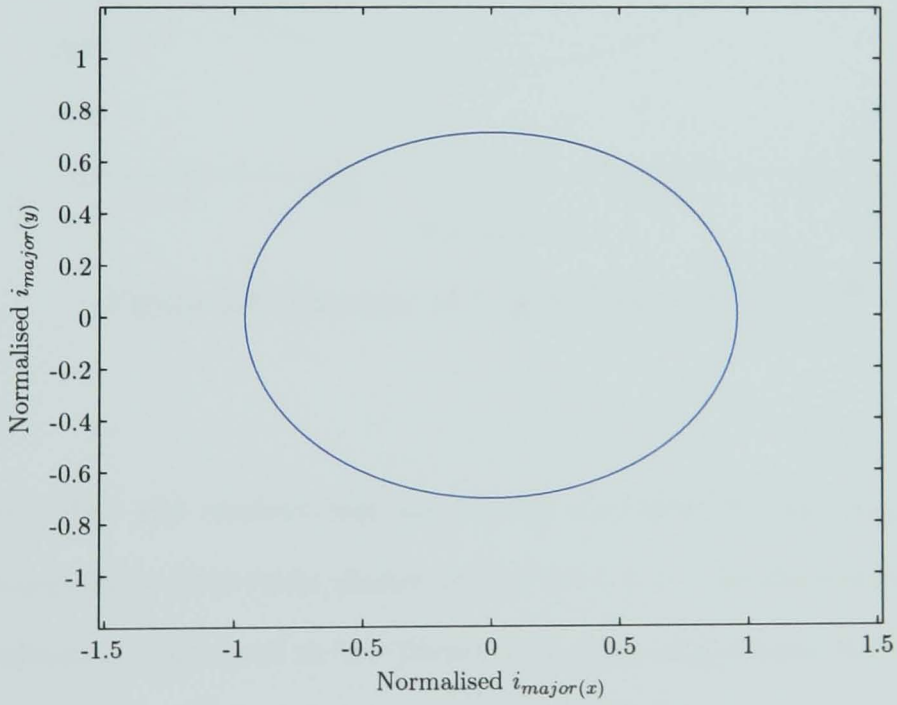

Figure 3.7: Ellipse Aligned with Major Axis, $\theta_r = +15°$

axis length. In comparison to the q-axis, the d-axis offers a very high reluctance comprising the air gaps and the effective magnet length and is therefore relatively insensitive to permeance variation due to slotting. In addition to this magnitude distortion, there is a large degree of phase distortion. This is demonstrated by the

results shown in sections 3.6.3 and 3.6.4.

3.6.3 Effect on Ellipse Based Techniques

The ellipse-fitting process presented in section 3.3 was applied to the currents that were simulated in section 3.6.2. Examples of the fitted ellipses are shown in figures 3.8, 3.9 and 3.10 for rotor positions of 0°, 15° and 60° respectively with the major axis marked in red.

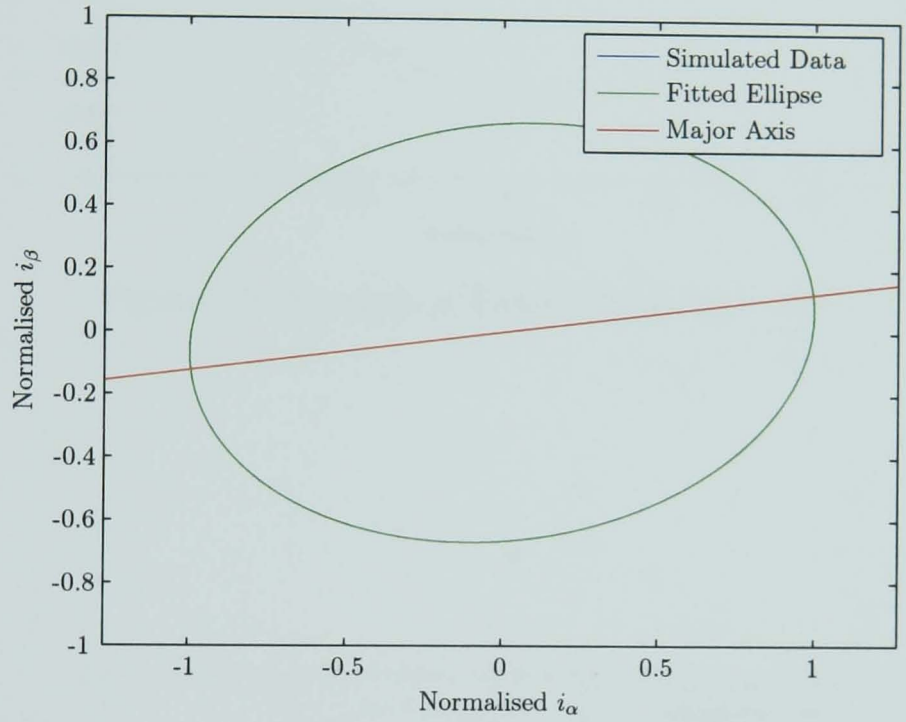

Figure 3.8: Example of Fitted Ellipse; $\theta_r = 0°$

It can be seen that the current loci are closely matched by the modelled ellipses, despite the magnitude distortion shown in section 3.6.2. The information regarding the rotor position is contained in the phase, however, rather than the magnitude of the current loci. It is therefore instructive to plot the position estimate against the actual rotor position in order to see this effect. As can be seen from figure 3.11, there is a large degree of error in the ellipse-fitting results that is introduced by the distortion.

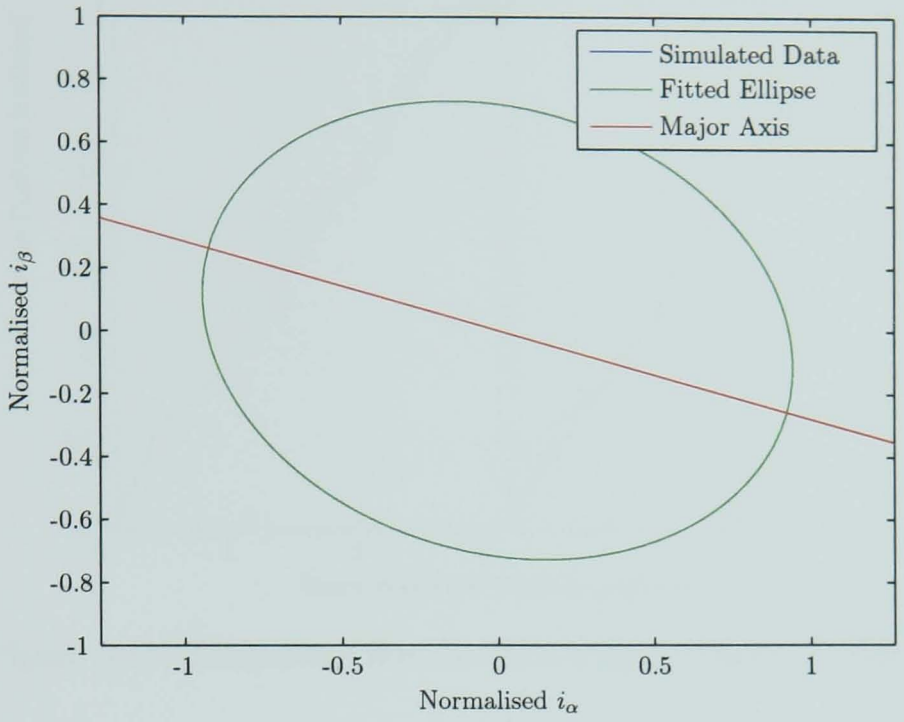

Figure 3.9: Example of Fitted Ellipse; $\theta_r = 15°$

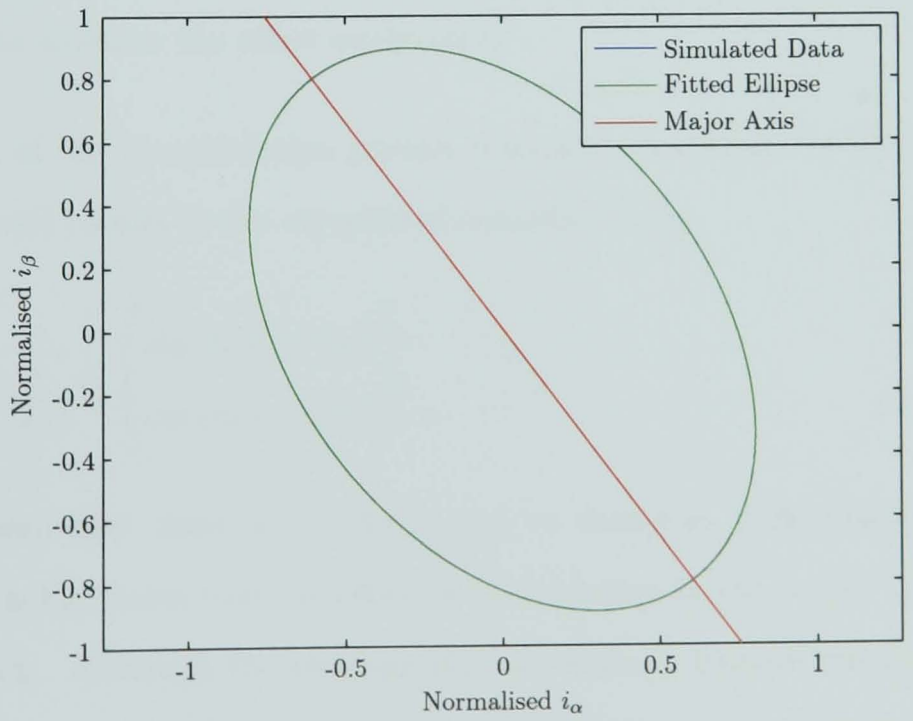

Figure 3.10: Example of Fitted Ellipse; $\theta_r = 60°$

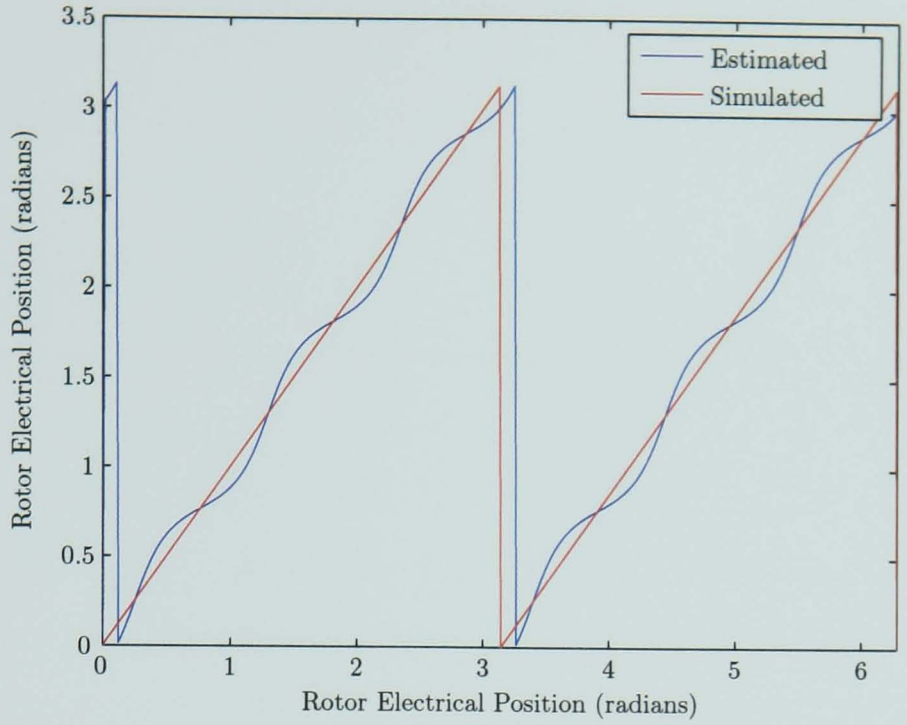

Figure 3.11: Estimation Results with Ellipse-Fitting Strategy

3.6.4 Effect on Demodulation Techniques

Following the analysis of section 3.6.3, the demodulation process was used on the simulated currents of section 3.6.2 in order to discover the effect of the distortion on the demodulation technique. Before showing the results of this, however, it is instructive to consider the effect analytically.

Application of the demodulation process discussed in section 3.4 to the model of equation (3.45) results in the currents of equation (3.46).

$$i'' = -\sum_{k=2}^{n} I_k \begin{pmatrix} \sin(h_k\theta_r + \phi_k) \\ \cos(h_k\theta_r + \phi_k) \end{pmatrix} \tag{3.46}$$

It can be seen that there is no direct way to derive θ_r from this equation and therefore it is inevitable that distortion will be present in the results obtained from this approach. Although the strategy still successfully isolates the time invariant components as expected, it can be seen from figure 3.12 that the distortion affects the demodulation process in a similar manner to the ellipse-fitting strategy. Figure 3.13 shows the 'saliency fingerprint' resulting from this process. This is formed by plotting the point described by equation (3.46) for each rotor position (the blue shape in the

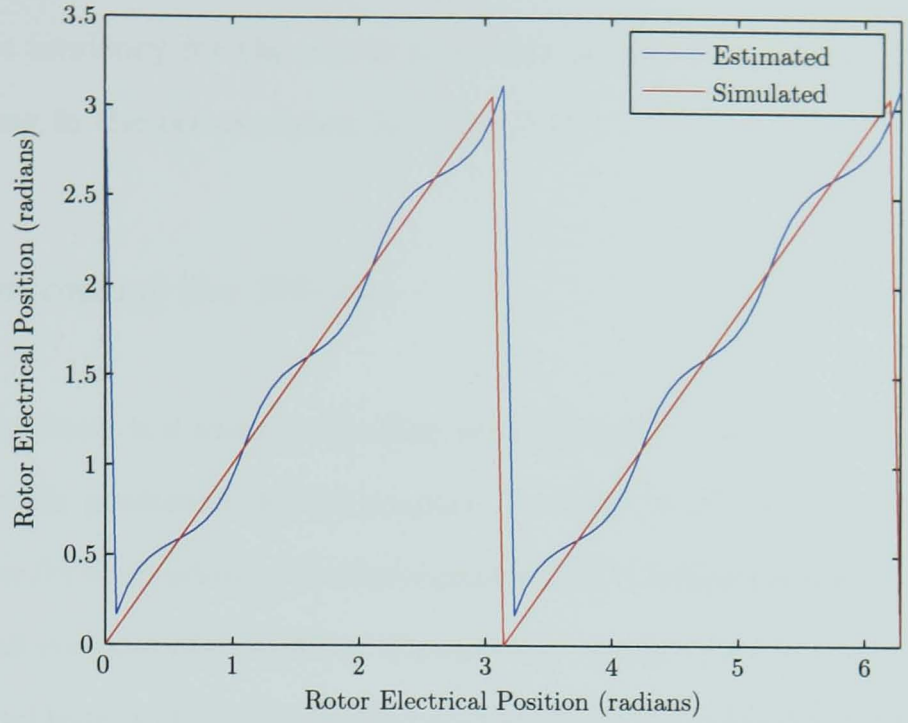

Figure 3.12: Estimation Results with Demodulation Strategy

figure) along with a green circle describing the equivalent points on the 'fingerprint' of an ideal machine. In figure 3.13, the shapes have been scaled for clarity such that the triangle fits within the circle. The red interconnecting lines show the relationship between individual points on each shape. The points are chosen such that the spacing between rotor positions is even and therefore so is the spacing between points on the green circle.

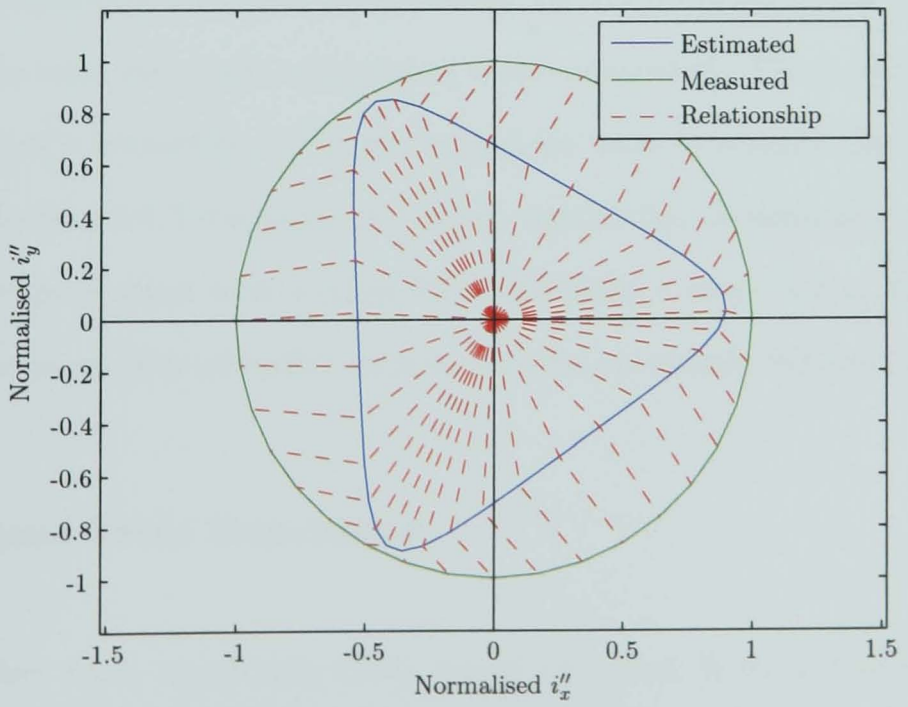

Figure 3.13: 'Saliency Fingerprint' Resulting from Distorted Currents

It can be clearly seen that the ideal circular shape has been severely distorted and that there is a tendency for the points to cluster around the apexes of the distorted shape, resulting in the errors shown in figure 3.12.

3.6.5 Overcoming the Effects

It is clear that there is a need to develop an approach to overcome these distorting effects. The work presented in [47] proposed a solution of implementing additional feedback terms for each additional component to the tracking observer. Each of these feedback terms consists of a model of the saliency component that is being removed. Each additional loop adds considerable complexity to the (already complex) tracking observer structure and it is desirable to explore computationally simpler alternatives for low-cost applications. These are discussed in section 3.7.

3.7 Compensation

3.7.1 Introduction

In order to compensate for the slotting effects discussed in section 3.6 in a computationally simple way, two main approaches were considered. These were both based on generation of a correction table that could be used to remove the distortion on the output. Section 3.7.2 discusses the direct application of manually captured test data for table generation and section 3.7.3 discusses a more automated approach that offers the possibility of online adjustment for parameter variations.

3.7.2 Manual Table Generation

The first option for a correction table based approach is to use static test data captured from the machine. By attaching an accurate mechanical position sensor and a locking gearbox to the shaft of the machine, a detailed characteristic (in the form of a 'saliency fingerprint') can be captured. This is achieved by using the

locking gearbox to rotate the machine through a fixed angle over one half of an electrical cycle (alternatively, more points can be used in order to increase accuracy and resilience to individual test-point noise). At each point, the injection system is used to apply a balanced set of sinusoidal voltages to the machine terminals and either the ellipse-fitting or the demodulation approach is used to generate a position estimate. This estimate is used as the 'input' to the table. The 'output' is read directly from the mechanical position sensor.

This results in a small table size; intermediate positions can be found through linear interpolation. An example of a manually generated correction table is shown graphically in figure 3.14.

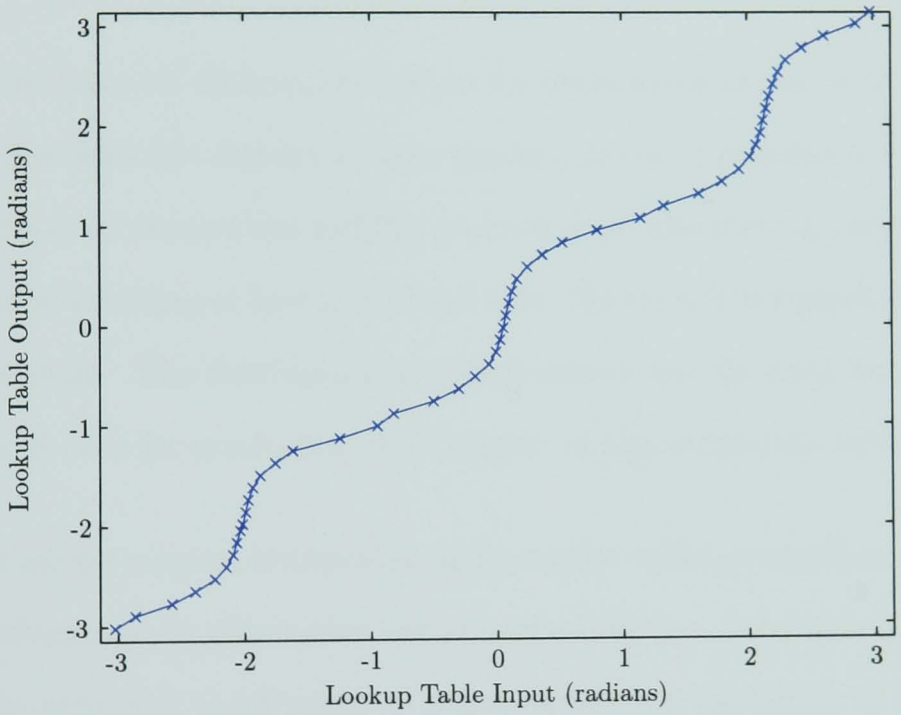

Figure 3.14: Example of Manually Generated Correction Table

The principal advantage of this approach is in terms of simplicity. Although there is a large amount of manual intervention required in order to generate the table for a given machine, the online processing requirements are minimal and hence the technique is ideally suited for the minimal cost applications upon which this investigation has concentrated. It also has minimal memory requirements; in tests carried out in the practical development discussed in chapter 5, only 100 values were required to be stored and this was ample for accurate results. Another possible advantage of this approach is that, assuming parameter invariance and hence stability of the 'fin-

gerprint' form, the approach is very accurate as the information used for correction is based on real captured data.

The latter advantage, however, could also be considered as a significant disadvantage. If the assumption of parameter invariance is invalid and the operating conditions of the machine result in significant variation of the 'fingerprint' form, the accuracy of this approach is likely to diminish. There is also the obvious disadvantage of the large amount of machine-specific testing that is required in order to set up the system.

3.7.3 Automatic Table Generation

It is desirable to have an alternative option for generation of the table discussed in section 3.7.2 that does not require a large amount of user intervention. One obvious approach to this is to remove the locking gearbox from the test rig and perform tests with the machine rotating at low speed and with the injection signals superimposed on the drive signals. The mechanical position sensor can be used both for driving the machine and also for producing the 'output' of the correction table.

Although this allows a more automated approach to table generation, it still maintains the disadvantage of parameter variation sensitivity. In addition, there is the requirement to attach a mechanical position sensor to the shaft of the machine, thereby necessitating undesirable offline testing.

In order to overcome these disadvantages, an alternative solution is proposed. This involves dynamically generating the correction table using the model of the distortion presented in section 3.6. This enables the system to be commissioned without the use of a mechanical position sensor and also makes it possible to dynamically correct the model as the machine is operated.

The model of the distorted currents is reproduced here as equation (3.47).

$$i_{\alpha\beta} = I_1 \begin{pmatrix} \sin(\omega_i t) \\ \cos(\omega_i t) \end{pmatrix} - \sum_{k=2}^{n} I_k \begin{pmatrix} \sin(h_k\theta_r - \omega_i t + \phi_k) \\ \cos(h_k\theta_r - \omega_i t + \phi_k) \end{pmatrix} \tag{3.47}$$

Performing the demodulation processing on these currents will still remove the first component and also the time dependent component of the other parts. Following the same derivation as in section 3.4 results in the currents shown in equation (3.48).

$$i'' = -\sum_{k=2}^{n} I_k \begin{pmatrix} \sin(h_k\theta_r + \phi_k) \\ \cos(h_k\theta_r + \phi_k) \end{pmatrix} \tag{3.48}$$

It can be seen that there is a Fourier series in i''_x and i''_y. Therefore, a complex Fast Fourier Transform (FFT) of these currents can be used to identify the coefficients [51]. However, the calculation can only be performed when the machine is rotating and a number of points can be measured at different rotor positions. There are two options for this (excluding the use of a mechanical position sensor, which would make the modelling process redundant). Firstly, the machine can be gradually accelerated using a fixed $\frac{V}{f}$ drive with a steadily increasing frequency. This will enable an initial measurement to be performed. The second option is to wait until the system is in use and the machine has been accelerated to run either with the signal injection system or, at higher speeds, with a back EMF based approach. Once the machine is running, the injection system can again be used to update the model and correct for parameter variations.

Given the coefficients that are derived using the FFT, a small sample of rotor positions (the 'output') can be applied to the model of the distorted currents to generate the 'input' to the correction table for use in future measurements.

This system has the advantage over the system of section 3.7.2 that the correction table can be automatically generated without user intervention. In addition, the model can be updated while the machine is in use in order to compensate for parameter variations. Because of the fact that the table is based on a model rather than manually captured data, however, the accuracy is expected to be lower.

Although there is a relatively large amount of computation involved in performing the FFT, the processing only has to be performed periodically and there is no firm deadline for completion (unlike the main sensing routine, which would usually have to complete in the PWM period). Therefore, these increased processing requirements are not considered serious in terms of overall system cost.

Chapter 4

Machine Analysis

4.1 Machine Types and Parameters

4.1.1 Introduction

In order to fully validate the technique discussed in chapter 3, testing was carried out on three machines with different topologies and applications. For simplicity and clarity, these machines will be referred to according to application as the 'Actuator' motor, the 'Kart' motor and the 'Traction' motor. The details of the machines are discussed in sections 4.1.2, 4.1.3 and 4.1.4 respectively.

4.1.2 The 'Actuator' Motor

The 'Actuator' motor, shown in figure 4.1, is a six pole PMSM with permanent magnets mounted on the surface of the rotor. The stator of the machine has nine slots.

The intended application of this machine, which is designed to operate in brushless DC mode, is for actuation of an aircraft slat via a lead screw. Due to the short duty-cycle of this application, the machine also has an electromagnetically released mechanical brake to prevent undesired movement of the shaft.

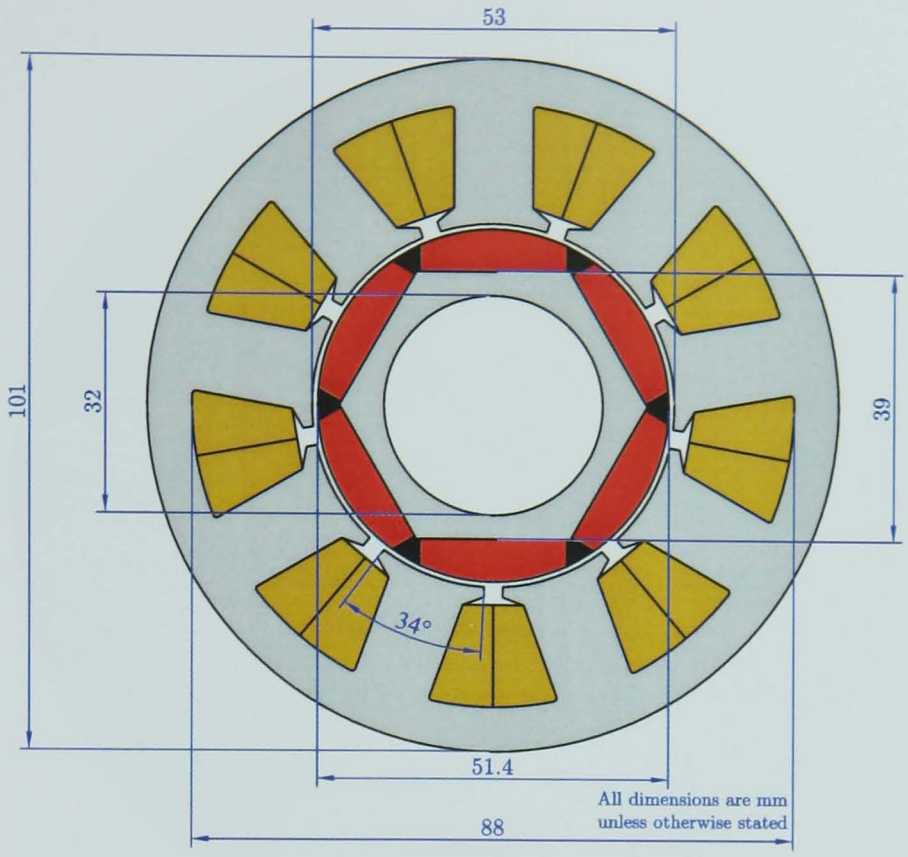

Figure 4.1: Cross Section of 'Actuator' Motor

Despite the non-salient rotor design, the machine exhibits an inductance variation of $L_q : L_d \approx 1.2 : 1$ due to saturation of the stator iron in the region of the poles of the magnets. Flux density plots of the unexcited machine at two different rotor positions (produced using FEA techniques and shown in figures 4.2 and 4.3) clearly demonstrate this effect.

Table 4.1 summarises the key parameters of this machine.

4.1.3 The 'Kart' Motor

The 'Kart' motor is a six pole, eighteen slot PMSM with buried magnets mounted radially and in a spoke formation. The flux induced by the magnets is thus tangential to the rotor. A cross-section of the machine is shown in figure 4.4. This machine was designed to provide power to an electrically propelled 'go-kart' and like the 'Actuator' motor, is designed to operate in brushless DC mode.

Due to the salient rotor design, the magnetic circuit in the d-axis is significantly different to that in the q-axis and hence there is sizeable inductance variation with

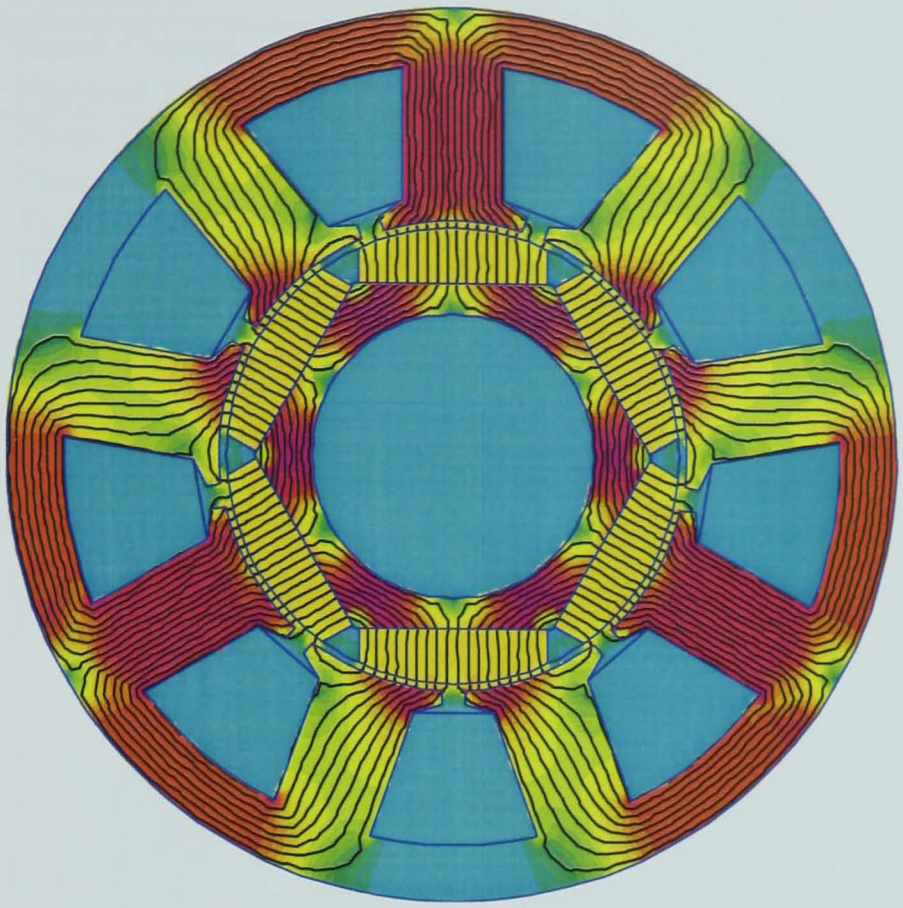

Figure 4.2: Flux Density Plot of Unexcited 'Actuator' Motor, $\theta_r = 0°$

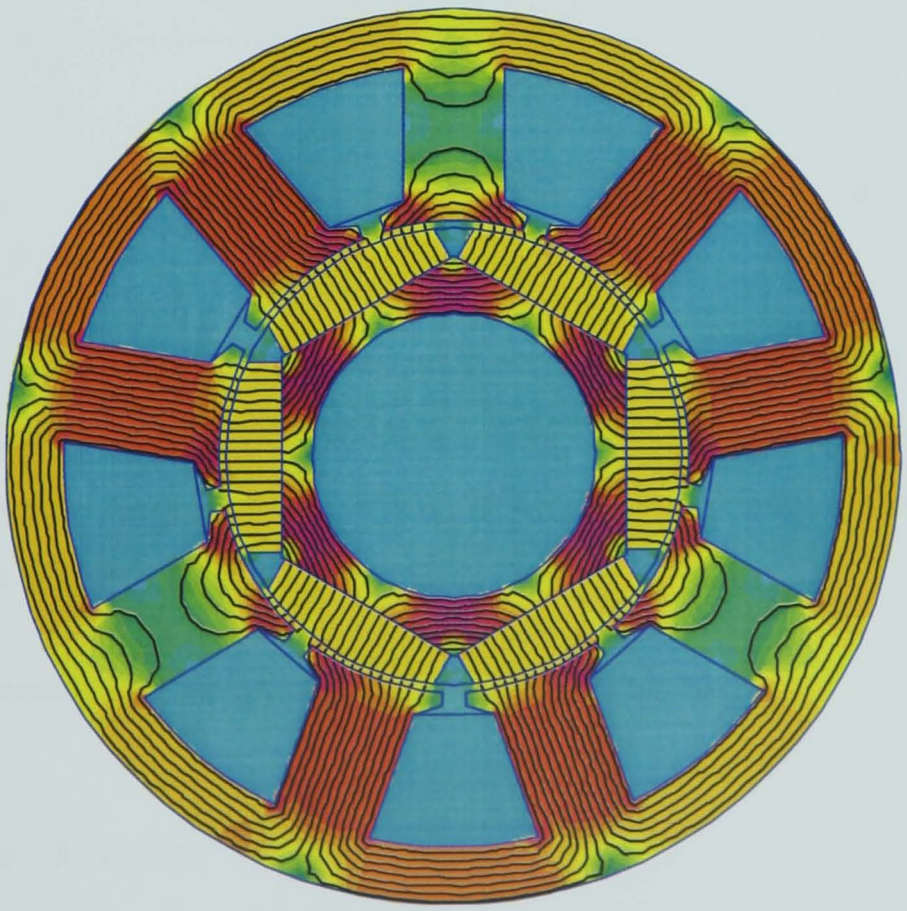

Figure 4.3: Flux Density Plot of Unexcited 'Actuator' Motor, $\theta_r = 30°$

Parameter	Value	
Rated Current	130	A
Nominal Torque	19.8	N m
Phase Resistance	40	mΩ
Phase Inductance	356	μH
Flux Induced By Permanent Magnets	42	mWb
Phase EMF (peak) Constant	0.22	V/rad s^{-1}
Number of Poles	6	
Number of Stator Slots	9	

Table 4.1: Machine Parameters for 'Actuator' Motor

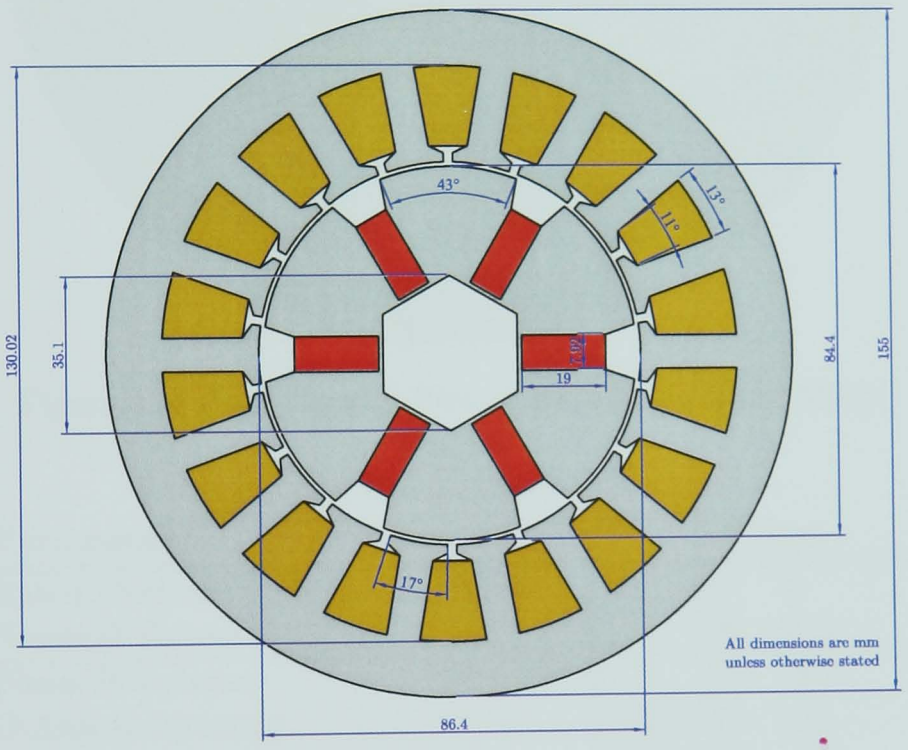

Figure 4.4: Cross Section of 'Kart' Motor

rotor position ($L_q : L_d \approx 1.5 : 1$). As with the 'Actuator' motor, FEA techniques have been used to produce flux density plots of the unexcited machine in order to visualise the differences in the operation of the different machine topologies. An example plot is shown in figure 4.5.

The key parameters of the machine are summarised in table 4.2.

4.1.4 The 'Traction' Motor

The 'Traction' motor is an eight pole, twelve slot PMSM with embedded magnets. As can be seen in the cross-section of figure 4.6, the magnets are mounted tangen-

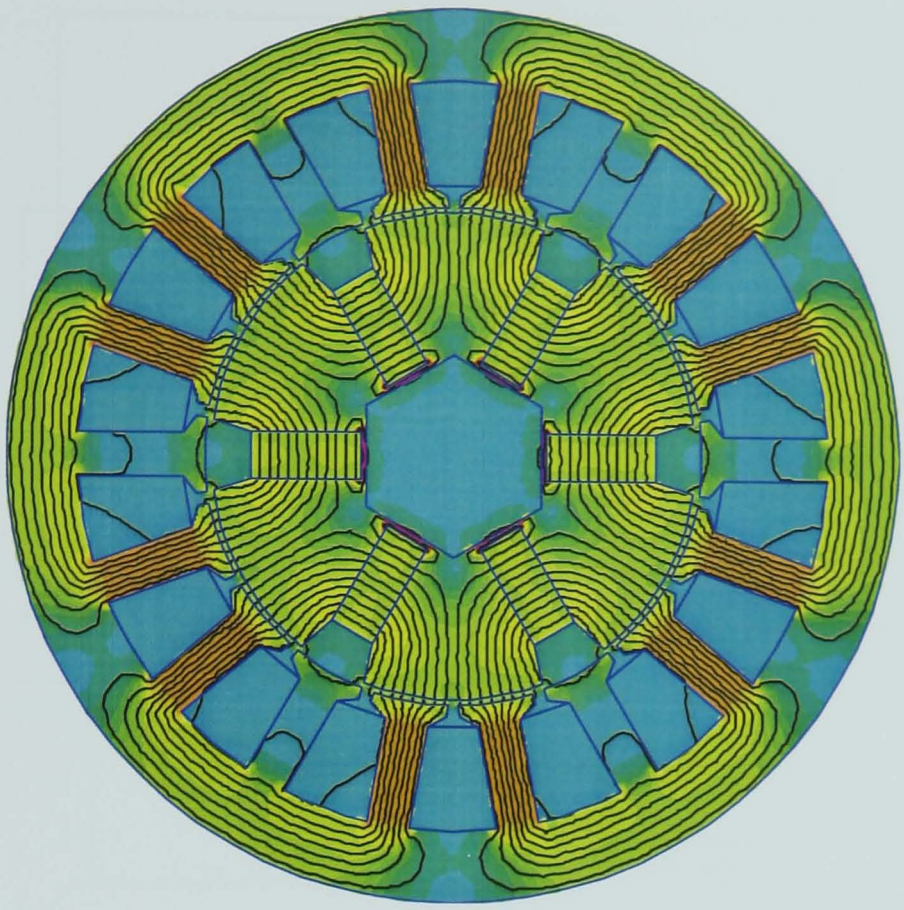

Figure 4.5: Flux Density Plot of Unexcited 'Kart' Motor

Parameter	Value	
Rated Current	100	A
Nominal Torque	20	N m
Phase Resistance	27	mΩ
D-Axis Inductance	190–210	μH
Q-Axis Inductance	290–340	μH
Flux Induced By Permanent Magnets	82.2	mWb
Phase EMF (peak) Constant	0.24	V/rad s^{-1}
Number of Poles	6	
Number of Stator Slots	18	

Table 4.2: Machine Parameters for 'Kart' Motor

tially within the rotor thereby resulting in a radial flux distribution. This machine is designed to operate in brushless AC mode and hence exhibits minimal cogging torque.

The intended application for this machine is to provide power for one of the driving wheels in a full size electric vehicle.

As with the 'Kart' motor, there is a considerable difference between the magnetic paths in the d- and q-axes. As a result, there is a significant inductance variation in

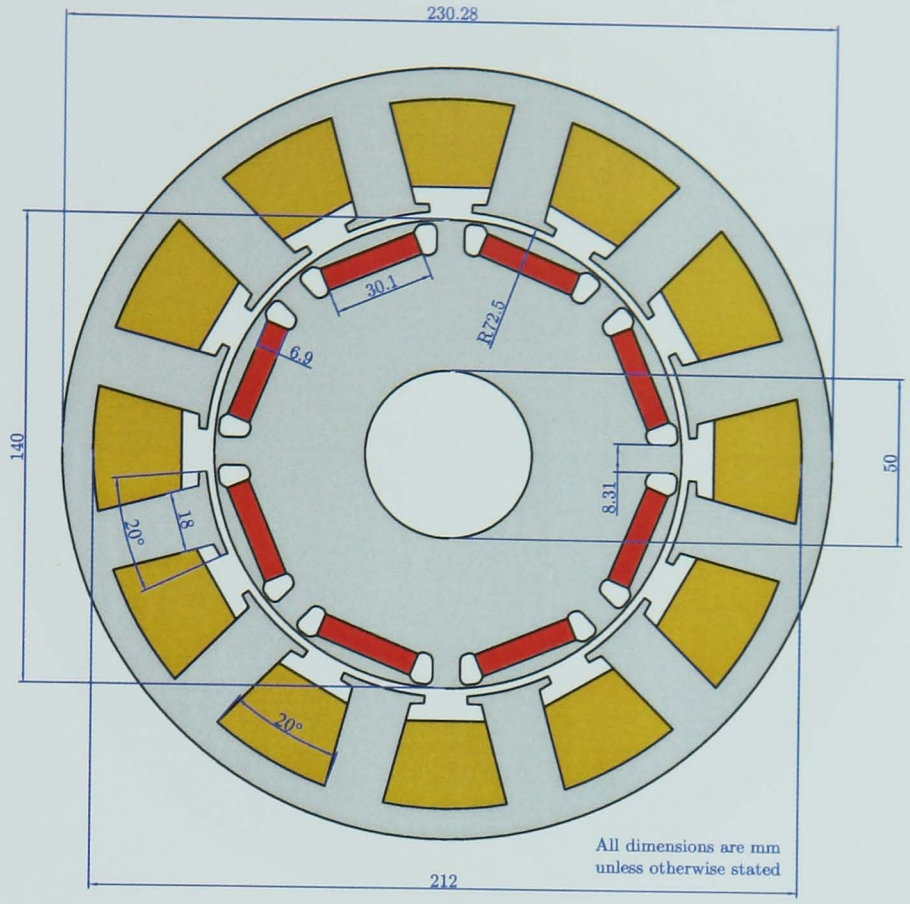

Figure 4.6: Cross Section of 'Traction' Motor

the stator windings ($L_q : L_d \approx 2 : 1$). In order to allow comparison of the flux paths in the different machines, a flux plot for this machine (when unexcited) is shown in figure 4.7 and the key parameters of the motor are summarised in table 4.3.

4.2 Finite Element Analysis

4.2.1 Introduction

In order to confirm the theoretical analysis of chapter 3 in a more comprehensive simulation, FEA techniques were adopted. This has the advantage that a detailed model of the saliency distortion in the test machines can be developed and the effect of this distortion on the accuracy of the technique can be assessed. In addition, the analysis process can be used by machine designers to incorporate sensorless control considerations into the design process, thus providing a valuable tool for optimising a machine design for simple and accurate zero speed sensorless position estimation as well as for machine performance.

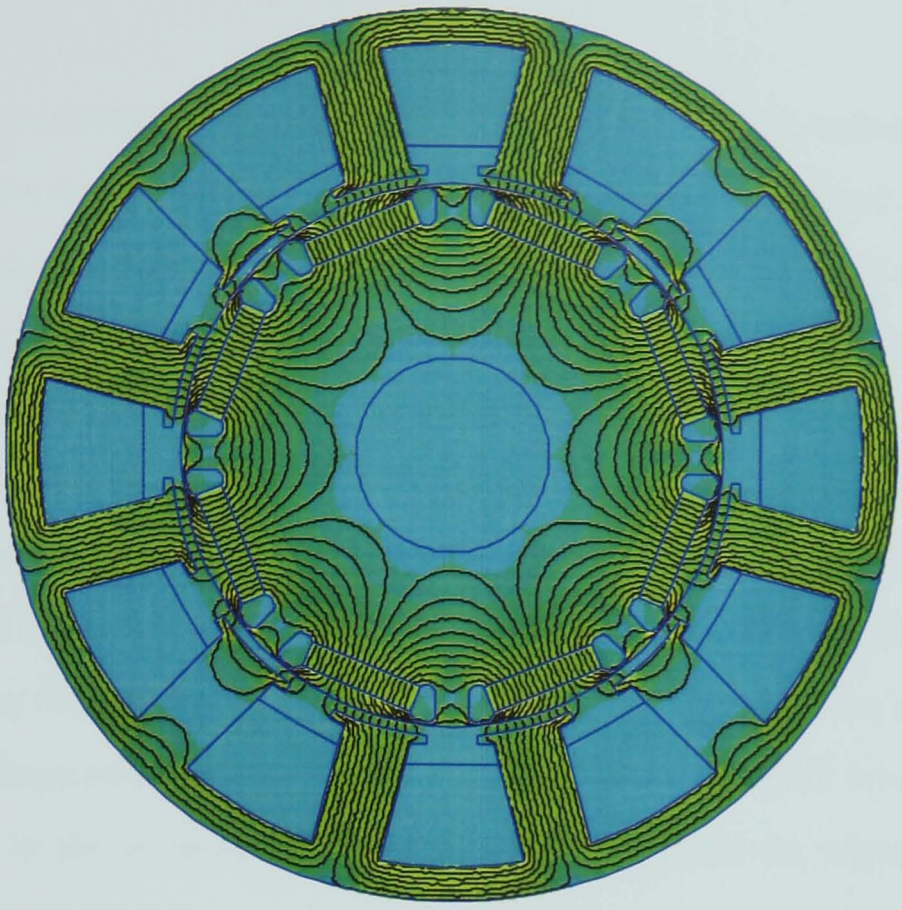

Figure 4.7: Flux Density Plot of Unexcited 'Traction' Motor

Parameter	Value	
Continuous Rated Current	180	A_{RMS}
Nominal Torque	110	N m
Phase Resistance	6.5	mΩ
D-Axis Inductance	170	μH
Q-Axis Inductance	400–300	μH
Flux Induced By Permanent Magnets	65	mWb
Phase EMF (peak) Constant	0.19	V/rad s^{-1}
Number of Poles	8	
Number of Stator Slots	12	

Table 4.3: Machine Parameters for 'Traction' Motor

Section 4.2.2 provides an overview of the methodology adopted in the analysis and section 4.2.3 presents the results for the test machines. Unfortunately, the precise geometries of the 'Kart' motor were unavailable and therefore modelling this machine in this way was impractical. However, detailed schematics were available for both the 'Actuator' motor and the 'Traction' motor and hence these have been used in this analysis.

4.2.2 Analysis Methodology

Due to the computational complexity of FEA techniques, it is undesirable to use voltage injection in the models. It is necessary to define an external circuit when applying voltages to finite element models and this requires additional computation (for modelling of the external circuit). As an alternative, current injection can be used as it produces very similar saliency forms when the injection signals are sinusoidal. This has the advantage that no external circuit needs to be modelled and also that the modelling can be performed in the steady-state rather than carrying out a transient analysis. In order to detect the inductance variation in the machines, the flux linking the phases can be calculated (using the finite element method) and the 'saliency fingerprint' derived therefrom. The Clarke and Park transformations that are used in the demodulation process are equally valid for voltages, currents and fluxes.

In practice, the modelling process begins with the production of a detailed mechanical drawing of the machine to be analysed. The mechanical drawing is provided to the FEA software and the electromagnetic properties of each individual region are identified. For example, each phase winding is identified, as are the strengths and magnetic orientations of the magnets and the B-H curve of the rotor and stator core materials.

The finite element mesh sizes are then defined in order to ensure that a detailed analysis is carried out in small regions where there is a high concentration of field (for example, the air gap and the stator teeth). For each rotor position over one electrical revolution, a set of simulations is then carried out with the current densities in the windings set to vary sinusoidally (as a balanced set) over an electrical cycle. In the simulations carried out for this thesis, the angular step chosen was one mechanical degree. For the six pole 'Actuator' motor, $120 \times 120 = 14400$ simulations were thus required, whilst for the eight pole 'Traction' motor, only $90 \times 90 = 8100$ were used. Due to the predetermined number of simulations required, it was decided that the simulations could use the entire mechanical structure, rather than a segment with rotational symmetry. This simplifies the preparation stage of the simulation, albeit

at the expense of increased (unattended) computation time. If a large number of models were required and computation time a significant issue, the process could easily be accelerated by using a small segment and also by taking into account the symmetry of the 'saliency fingerprint' in order to reduce the number of rotor positions required.

None of the machines used in this development are skewed. It is important to note, however, that if a machine were skewed, it would be important to take this into consideration when modelling the machine. It is also important to note that this approach to finite element modelling ignores frequency effects such as eddy currents and hysteresis losses. However, it will be seen from the experimental analysis of section 5.3 that the finite element models closely match the experimental results, thus validating the method.

4.2.3 FEA Results

The imported mechanical drawing of the 'Actuator' motor is shown in figure 4.8 with the regions defined.

The phase windings are individually labelled to enable simple control of the current densities. In figure 4.8, the phase windings labelled 'A1' refer to the phase A windings on the outward path, while 'A2' refers to those windings on the return path. The same notation is used for phases B and C. The meshed machine is shown in figure 4.9 and the increased mesh density in 'sensitive' areas can be clearly seen. The model is then ready for computation. Once each computation step is complete, the flux density of the machine can be viewed (figure 4.2 in section 4.1.2 gives an example for the unexcited machine). In addition, the flux can be calculated for each set of phase windings. The flux linkage can then be calculated according to

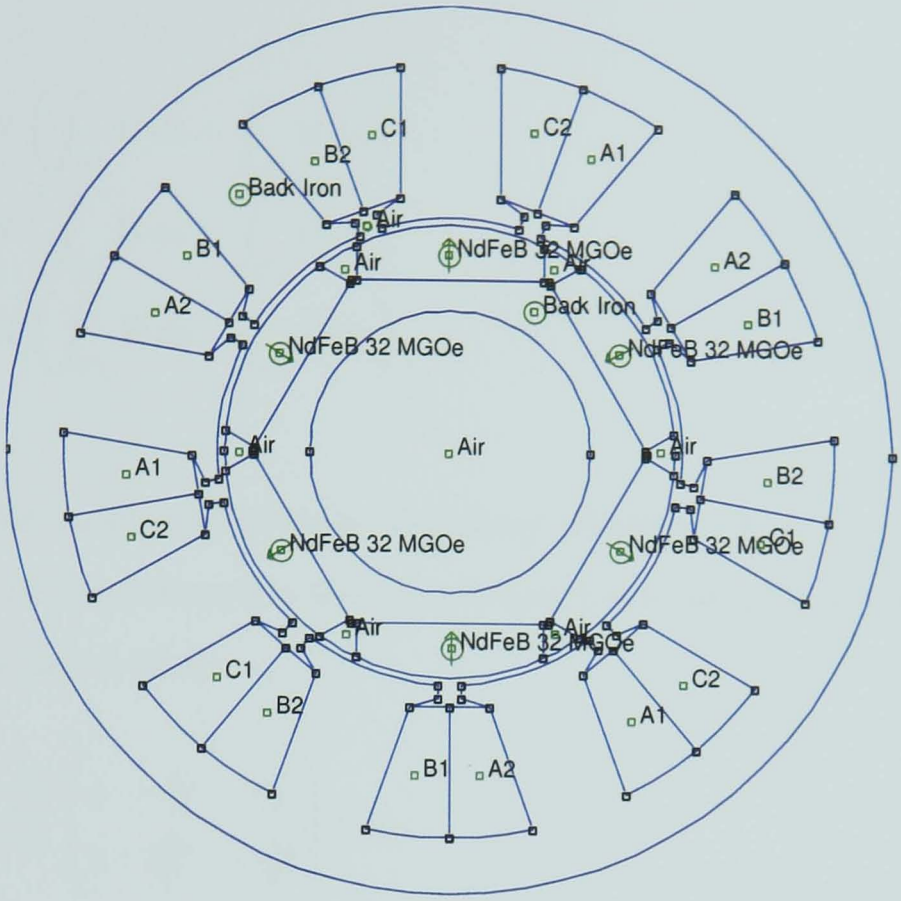

Figure 4.8: Finite Element Model of 'Actuator' Motor

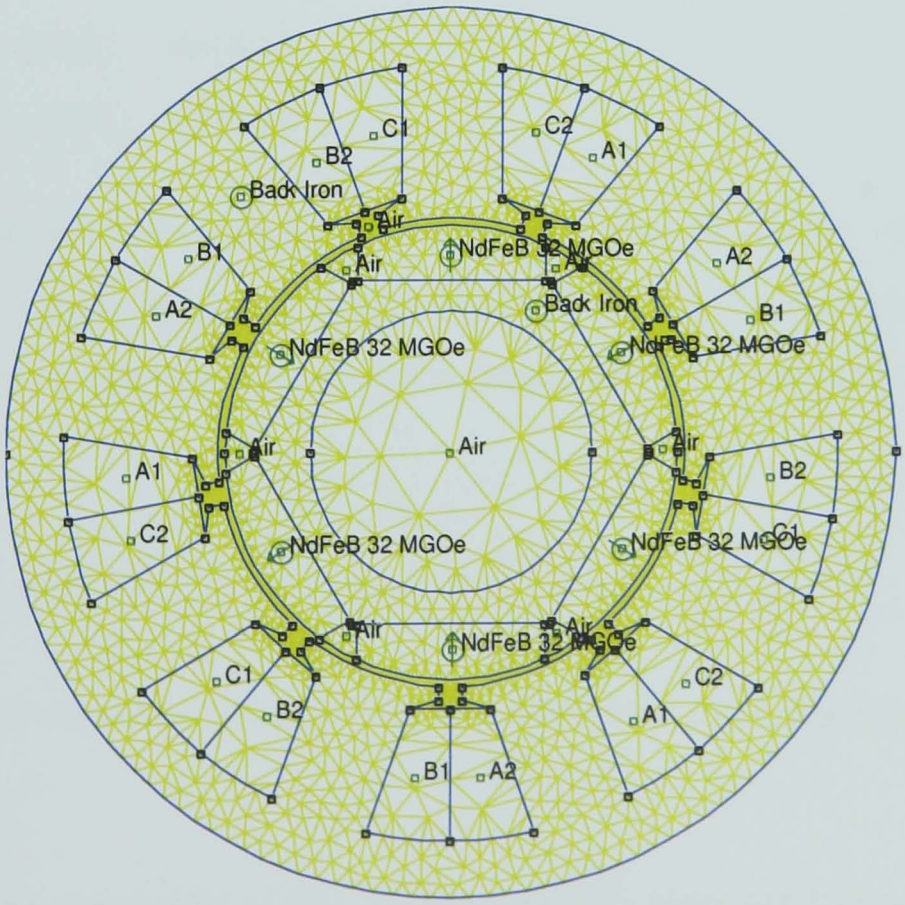

Figure 4.9: Finite Element Mesh for 'Actuator' Motor Model

equations (4.1)–(4.3),

$$\psi_a = 3N\left(\int_{A1}\mathbf{B}\,\mathrm{ds} - \int_{A2}\mathbf{B}\,\mathrm{ds}\right) \tag{4.1}$$

$$\psi_b = 3N\left(\int_{B1}\mathbf{B}\,\mathrm{ds} - \int_{B2}\mathbf{B}\,\mathrm{ds}\right) \tag{4.2}$$

$$\psi_c = 3N\left(\int_{C1}\mathbf{B}\,\mathrm{ds} - \int_{C2}\mathbf{B}\,\mathrm{ds}\right) \tag{4.3}$$

where N is the number of turns in the phase windings. It is then necessary to translate the *abc* flux linkages to the $\alpha\beta$ reference frame using the Clarke transform, as shown in equation (4.4).

$$\psi_{\alpha\beta} = \sqrt{\frac{2}{3}}\begin{pmatrix} 1 & -\frac{1}{2} & -\frac{1}{2} \\ 0 & \frac{\sqrt{3}}{2} & -\frac{\sqrt{3}}{2} \end{pmatrix}\psi_{abc} \tag{4.4}$$

The $\alpha\beta$ flux linkages are then rotated to a reference frame that is synchronous with the injected signal, to give the flux linkages in the ψ' reference frame,

$$\psi' = \begin{pmatrix} \cos(\theta_i) & \sin(\theta_i) \\ -\sin(\theta_i) & \cos(\theta_i) \end{pmatrix}\psi_{\alpha\beta} \tag{4.5}$$

where θ_i is the injection angle corresponding to a given data point. Since the simulations were carried out over exactly one electrical cycle (of injection signal), the high-pass filtering can be replaced with a simple removal of the offset, as shown in equation (4.6).

$$\psi'_{filtered} = \psi' - \bar{\psi}' \tag{4.6}$$

A second Park transform is then used to remove the remaining time dependent components.

When analysing the results of this 'post-processing', there are two main methods that are used to assess the saliency of the machine. Firstly, the 'saliency fingerprint' can be plotted directly from the 'inverse injection' reference frame flux linkages (ψ'')

and compared with idealised results derived from the actual rotor positions. For the 'Actuator' motor, the 'saliency fingerprint' from FEA simulation is shown in figure 4.10. The distortion from the idealised shape (shown in green) can be clearly seen and the red interconnecting lines make clear the phase distortion that results from the non-ideal saliency. It will be seen in section 5.3.1 that the results of the FEA closely match those found experimentally. The other method that is useful for assessing the form of the saliency is to compare the final results of the estimation with the true rotor position.

This comparison is shown in figure 4.11 for the 'Actuator' motor. It can be seen that the large 'fingerprint' distortion is manifested in a large 'ripple' on the measured position. Once again, this distortion will be seen to closely match the experimental test results of section 5.3.1, thus confirming the validity of the approach.

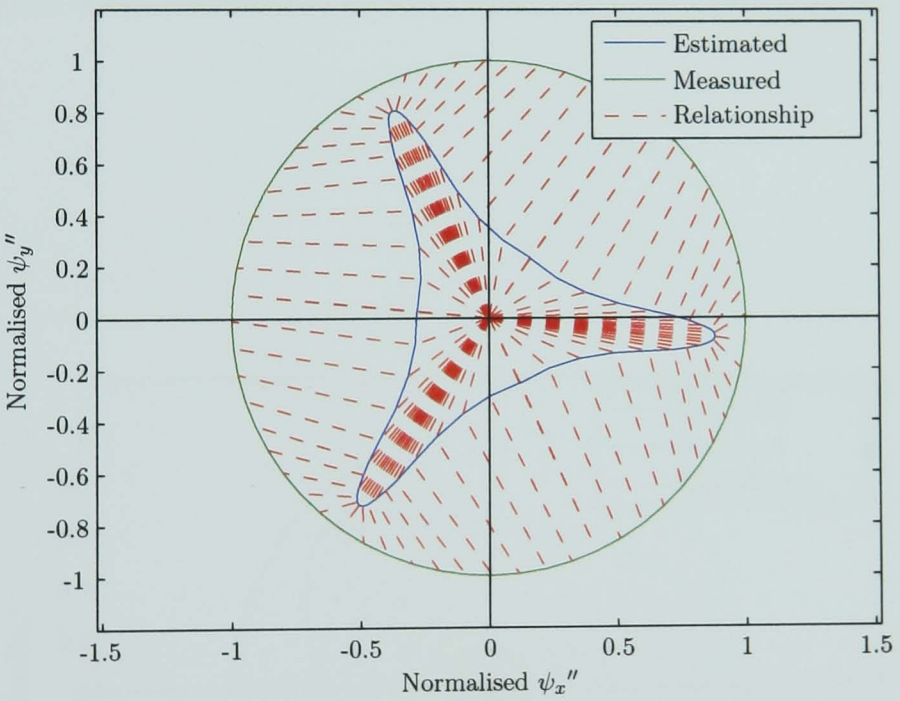

Figure 4.10: 'Saliency Fingerprint' from FEA for 'Actuator' Motor

The same analysis process was also applied to the 'Traction' motor. Structurally, this machine is very different to the 'Actuator' motor. As well as having embedded magnets, the air gap is much larger (as a proportion of the outer diameter), as is the slot opening size. This results in a smoother MMF distribution in the air gap and hence an improved saliency. This is confirmed by the 'saliency fingerprint' produced with FEA, which is shown in figure 4.12. It can be seen that there is

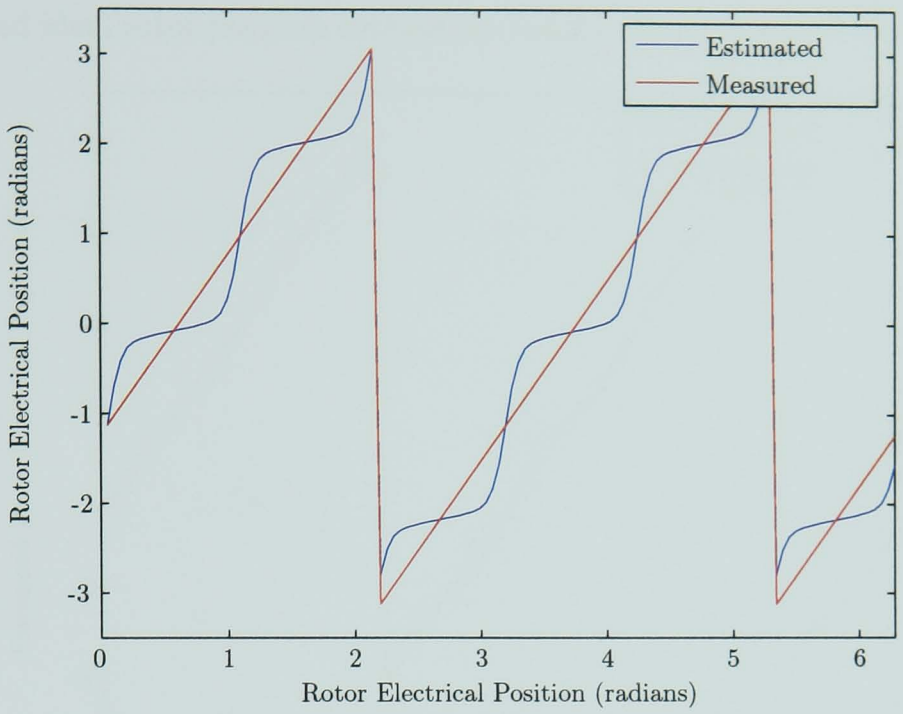

Figure 4.11: Estimation Results from FEA for 'Actuator' Motor

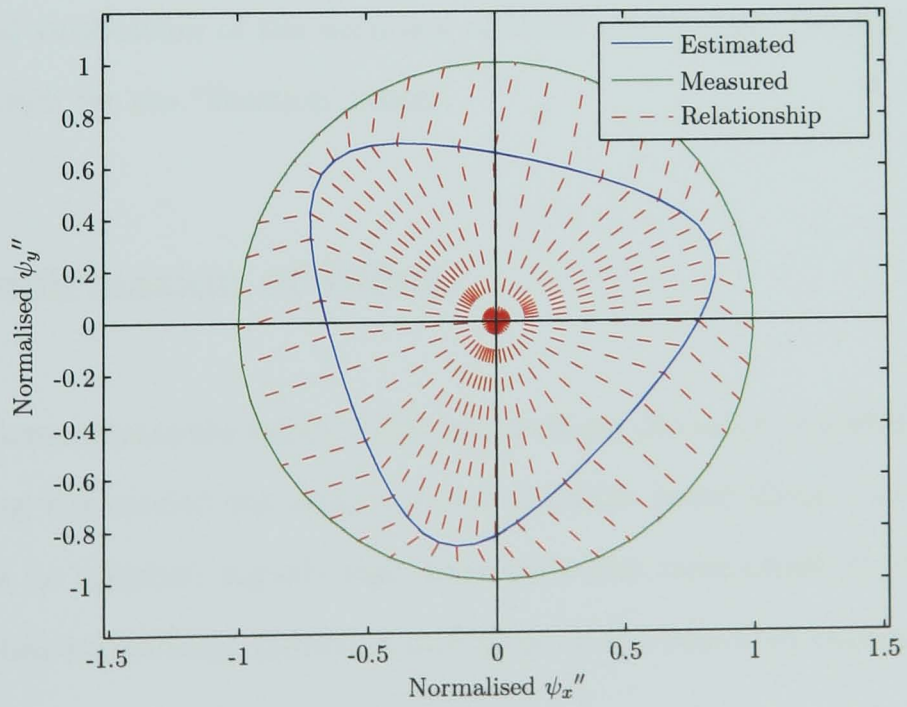

Figure 4.12: 'Saliency Fingerprint' from FEA for 'Traction' Motor

considerably less clustering of points around the apexes of the 'fingerprint'. The magnitude distortion is also reduced. Figure 4.13 shows a direct comparison of the estimated and ideal rotor position estimation results. Once again, it can be seen that

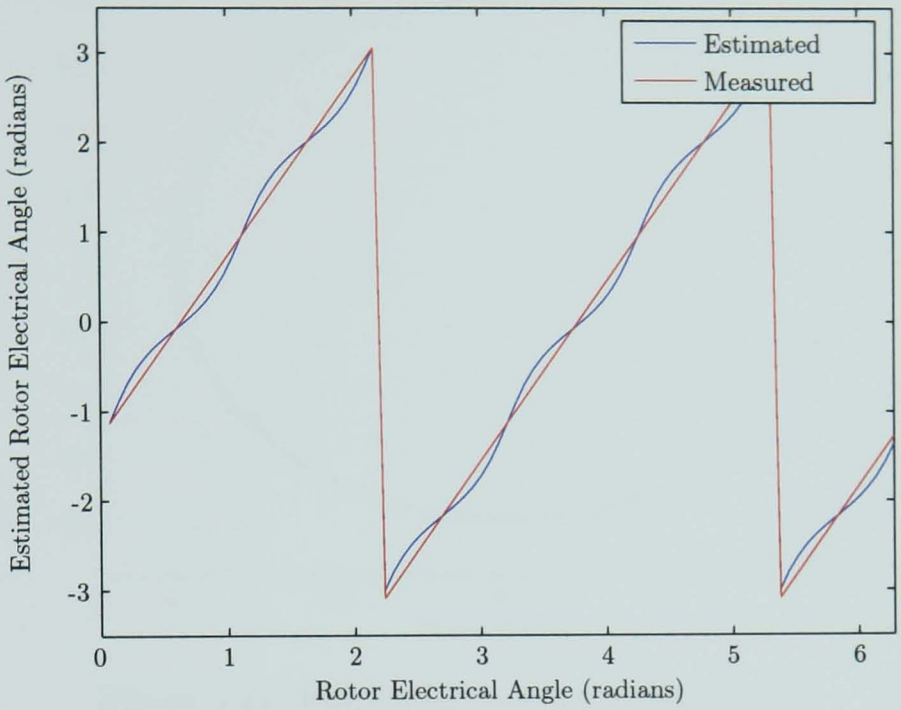

Figure 4.13: Estimation Results from FEA for 'Traction' Motor

there is a 'ripple' on the measured position. However, the magnitude of the ripple is considerably less than that seen in the 'Actuator' motor. Section 5.3.3 includes experimental verification of the accuracy of these results and therefore the validity of the approach for the 'Traction' motor.

4.3 Confirmation of Effect

In order to demonstrate the saliency distortion effects discussed in section 3.6 and 4.2, initial testing was carried out using a power amplifier based signal injection system. This results in injection signals that have only one component in the frequency spectrum, thus minimising distortion and noise in the captured currents.

A signal generator was used to generate three 1 kHz sinusoidal voltages of equal amplitude and with 120° phase difference. Using three 100 W power amplifiers designed for audio applications (and therefore well suited to the injection frequency), initial

tests were carried out to confirm the form of the resulting currents. Figures 4.14 and 4.15 show two examples of captured currents at different rotor positions.

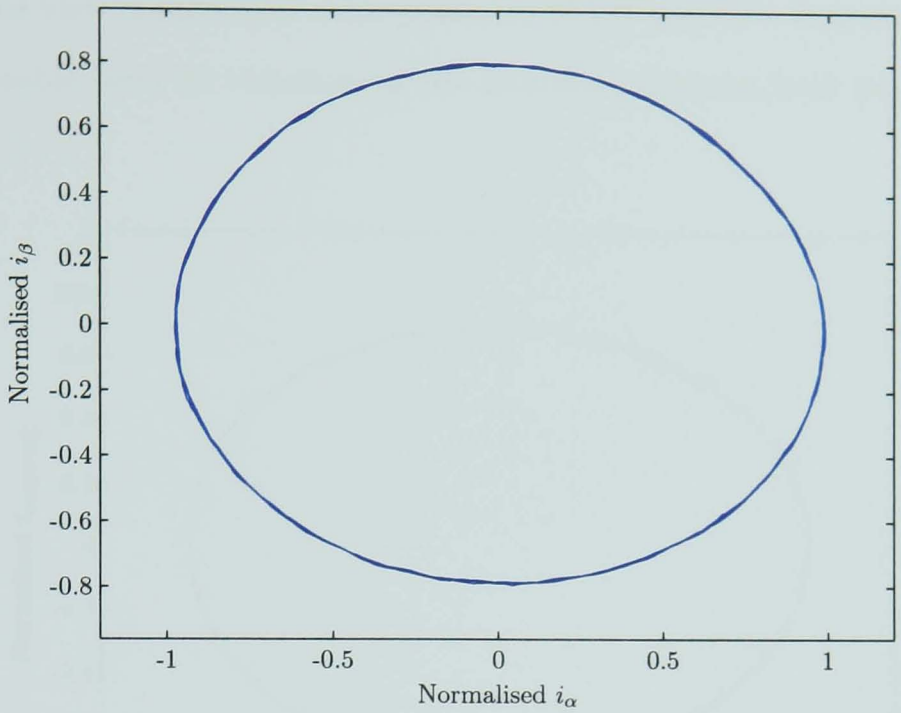

Figure 4.14: Ellipsoidal Current Locus; $\theta_r = 0°$

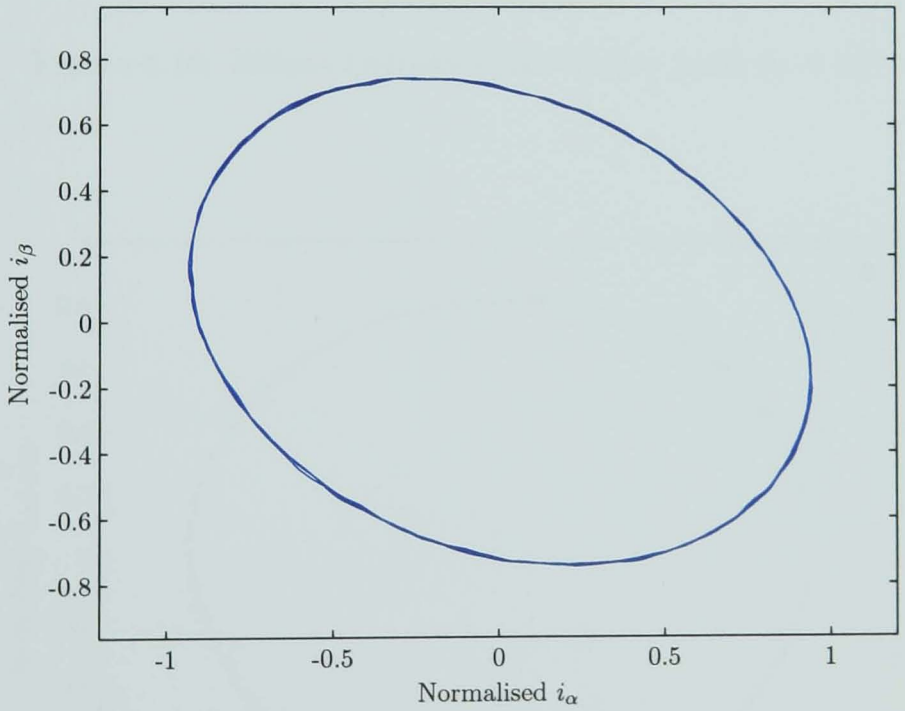

Figure 4.15: Ellipsoidal Current Locus; $\theta_r = 30°$

The rotation of the major axis of the ellipse is clearly visible – for a shaft rotation of θ_r (electrical), the major axis rotates by an angle of θ_r. This confirms the analysis of section 3.2.

In order to demonstrate the effects of slotting in the machine, it is instructive to view the ellipses in a reference frame linked to the major axis. In figures 4.16 and 4.17, this view is shown for rotor positions of 19° and 41°. It is clear that there is a considerable level of variation in the minimum current level (as discussed in section 3.6).

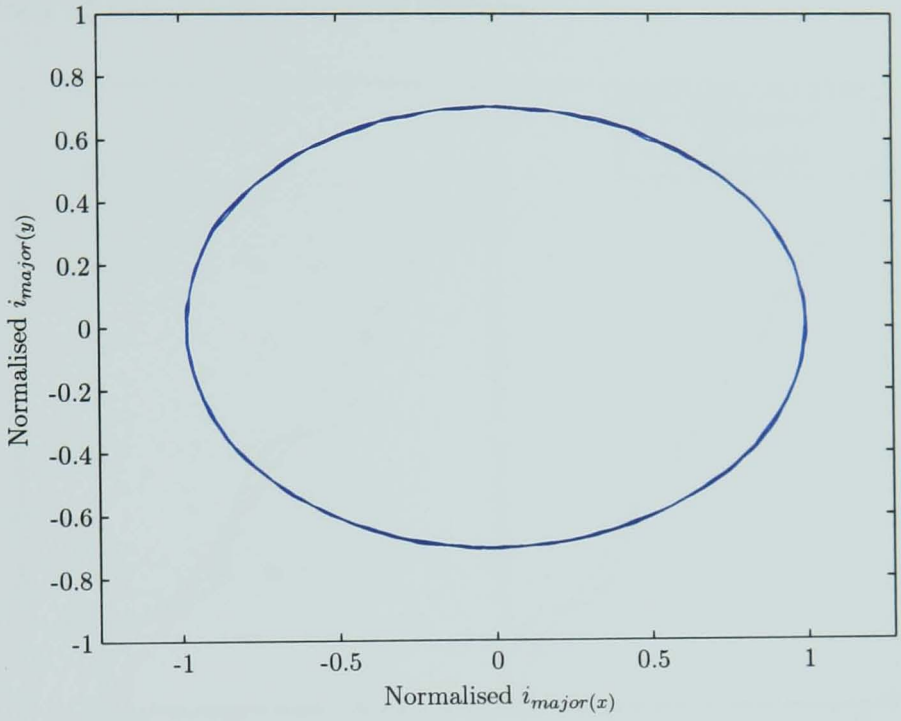

Figure 4.16: Ellipse Orientated to Major Axis; $\theta_r = 19°$

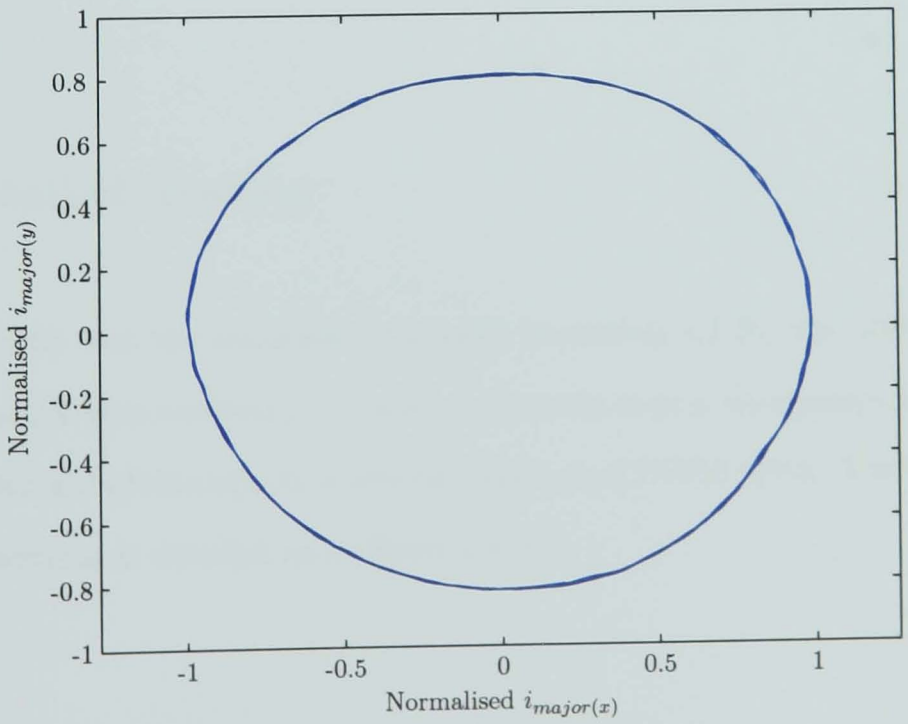

Figure 4.17: Ellipse Orientated to Major Axis; $\theta_r = 41°$

In addition to the magnitude distortion, there is also a significant phase distortion. This phase distortion is the primary reason for errors in position estimation. Using the ellipse fitting technique discussed in section 3.3, the angle of the major axis was found at each rotor position. This resulted in the estimated position information shown in figure 4.18. It can be clearly seen that the distortion has a significant effect on the accuracy of the uncompensated system.

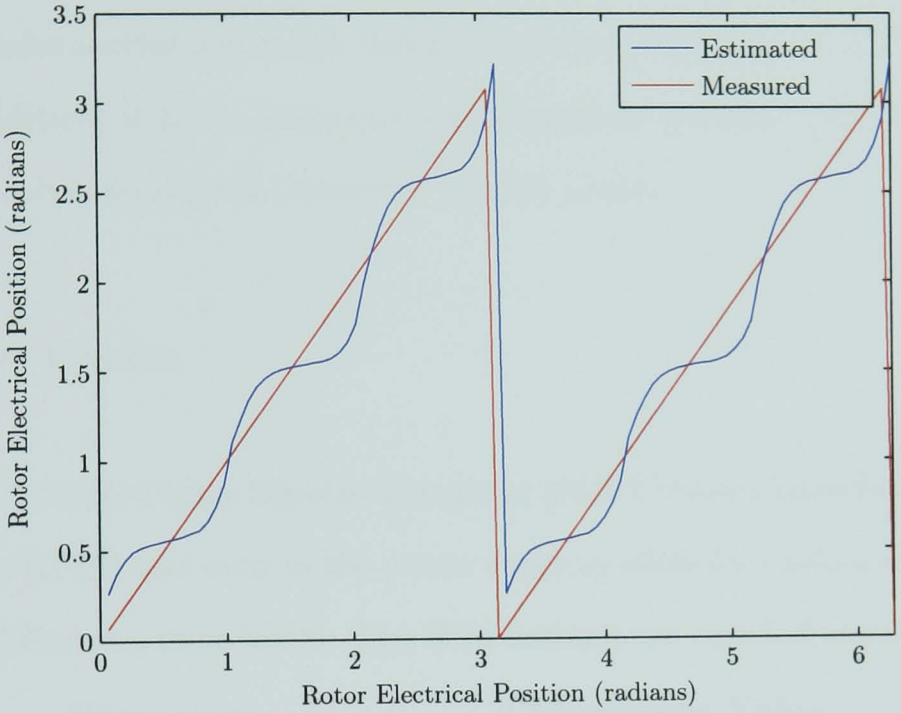

Figure 4.18: Result of Ellipse Fitting

4.4 Detailed Testing

In order to fully test the machines discussed in section 4.1 for the ability to detect rotor position, it was necessary to capture currents over a wide range of rotor positions and with a realistic injection system based on a PWM drive. The development of this test system is detailed in sections 4.5–4.8.

4.5 Hardware

4.5.1 Digital Signal Processor

Due to the low processing requirements of a simple injection system, the Texas Instruments TMS320LF2407 fixed-point DSP starter kit provides a suitable platform for development of the initial test rig. This DSP has built-in PWM generation circuits and includes several automatic timers that can be used for the 1 kHz sinusoidal signals. In addition, it has a large quantity of general purpose I/O pins that were needed for Resolver-to-Digital Converter (RDC) access.

4.5.2 Drive Choice

A high power Insulated Gate Bipolar Transistor (IGBT) based Mitsubishi Intelligent Power Module (IPM) was used as the power stage to allow for testing of the different machines at different power levels. The IPM ratings are detailed in table 4.4.

Parameter	Maximum Value	
Collector-Emitter Voltage	600	V
Collector Current	200	A
Peak Collector Current	400	A
Collector Dissipation	595	W
Switching Frequency	20	kHz

Table 4.4: Power Module Ratings

Three LEM LTA100P/SP1 Hall-effect CTs were used on the output connections from the IPM to enable the line currents to be captured. The IPM is shown (with heatsink attached) in figure 4.19 and the three CTs are shown in figure 4.20.

4.5.3 Mechanical Hardware

The machine under test was coupled to a locking gearbox for static testing and a brushless resolver was used to measure accurately the position of the rotor. This was essential for the verification of the accuracy of the techniques. The same mechanical

Figure 4.19: Photograph of IPM

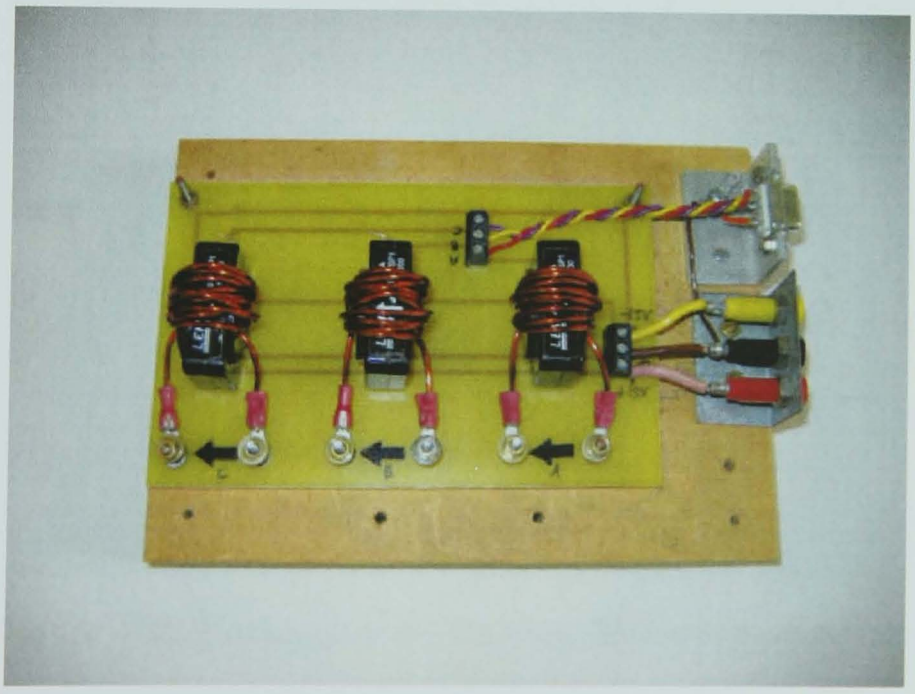

Figure 4.20: Photograph of Current Transducers

rig was used for testing the two smaller machines; a separate resolver and gearbox were mounted on the shaft of the larger 'Traction' motor. Figure 4.21 shows a photograph of the mechanical test rig with the 'Kart' motor attached. The 'Traction' motor is shown with the locking gearbox attached in figure 4.22.

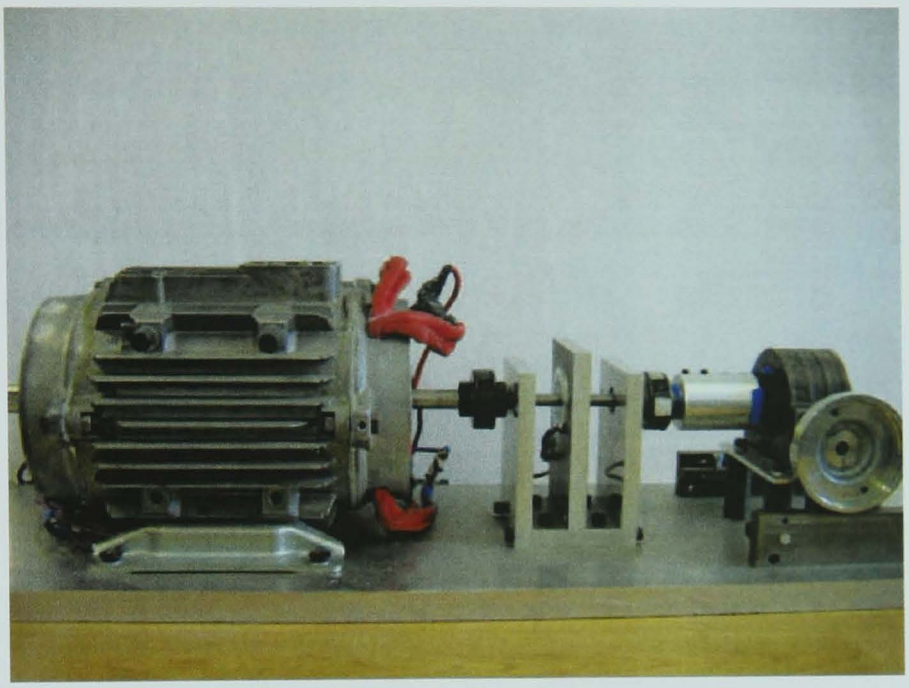

Figure 4.21: Photograph of 'Kart' Motor with Gearbox

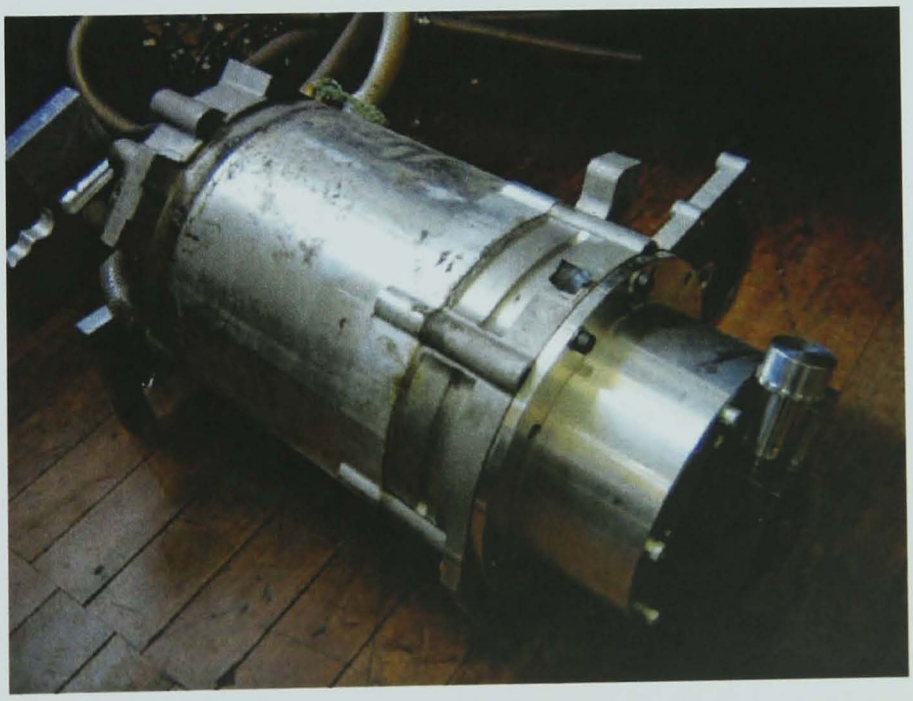

Figure 4.22: Photograph of 'Traction' Motor with Gearbox

4.5.4 Interface Boards

For this implementation, two interface boards were developed. The first of these is the gate drive board for the IPM. This consists of a DC-DC converter that produces four isolated 15 V power supplies (one for the bottom switches of the inverter and one for each of the top switches), and an opto-isolator for each switch to protect the DSP control electronics and to increase the signal voltage to a level sufficient to control the IGBTs in the IPM. Figure 4.23 shows a photograph of the final Printed Circuit Board (PCB).

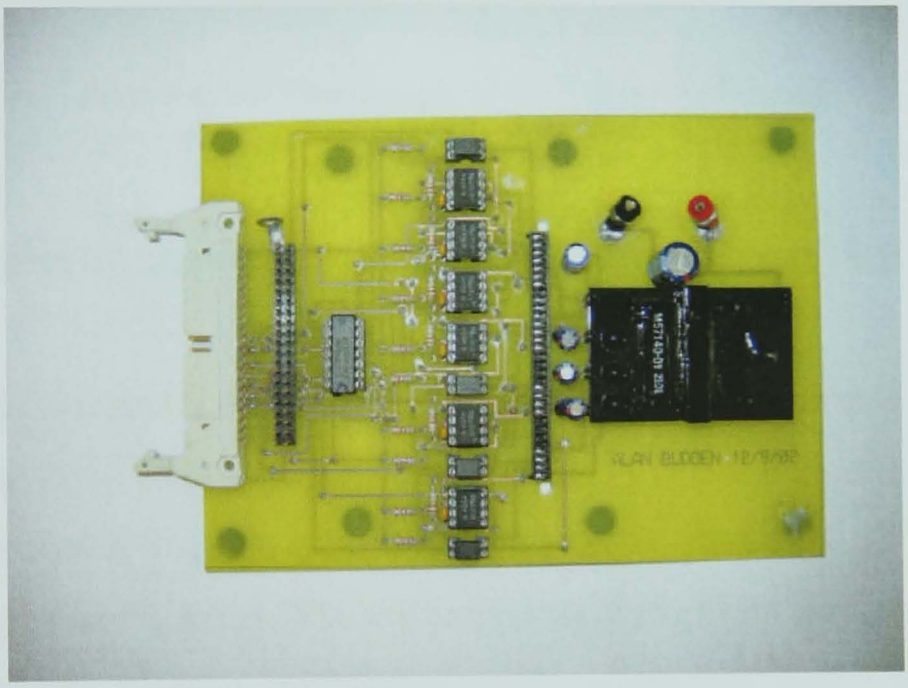

Figure 4.23: Photograph of Gate Drive PCB

The second interface board enables the usage of the DSP with the resolver and drive. In addition to the signal routing and buffering for the connections to the gate drive board, several test points are included to allow oscilloscope access to all of the connections on the DSP board. Finally, an RDC integrated circuit is included (along with all of the necessary auxiliary electronics) in order to capture the accurate rotor position for accuracy checking. A photograph of the final PCB is shown in figure 4.24.

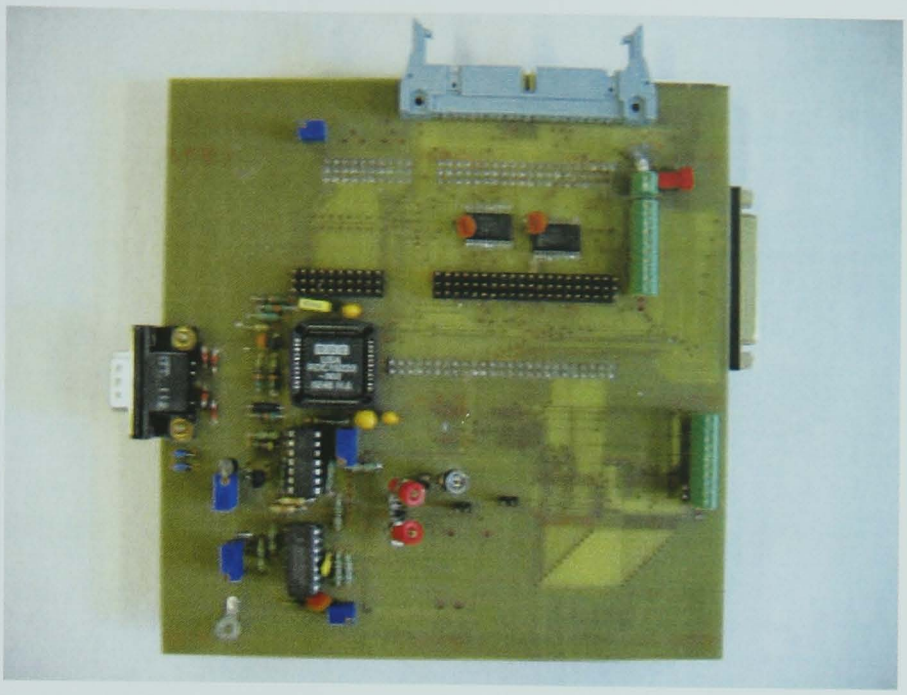

Figure 4.24: Photograph of DSP Interface Board

4.6 Implementation of Static Testing Procedure

To create the required injection signals, the DSP was configured with two timers: one with a period of 50 μs for the PWM and the other with a period of 1 ms for the injection waveforms. On each cycle of the PWM timer, the output of the injection waveform timer was captured. The sine and cosine of this value were then computed using an assembly language (to improve speed) routine that used a short look-up table combined with a simple linear interpolator. The inverse Clarke transform was then used to create three 120° phase displaced sinusoids. These were used in three comparators operating on the PWM timer to produce the switching control signals. The built-in dead-band circuitry was used to generate the switching signals for the gate drive board, whilst ensuring that short circuit conditions did not occur. A flow chart of this functionality is shown in figure 4.25.

4.7 Test Procedure

For each machine, the test rig was connected and the injection voltages applied to give line currents of approximately 1 A. The outputs from the CTs were passed through balanced second order notch filters and connected to the Analogue-to-

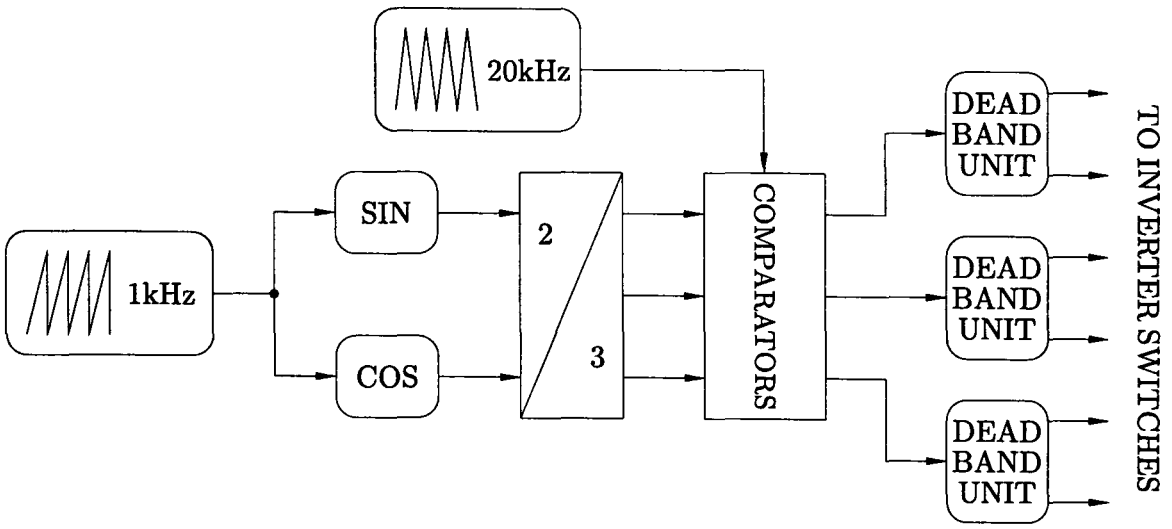

Figure 4.25: Flow Chart Illustrating DSP Functionality

Digital Converter (ADC) converter inputs of the DSP. The DSP was then used to perform the Clarke transform on the captured currents (to convert from the *abc* reference frame to the $\alpha\beta$ frame) and to store a large sample of results. Finally, the Texas Instruments DSP interface software was used to directly access the stored values in the on-board memory on the DSP. In addition, the position reported by the RDC was manually stored.

This approach had the advantage (over oscilloscope based capture) that the results to be processed in MATLAB were of identical accuracy to those that would be used in the final system. This process was repeated at each 'stop' of the locking gearbox – in steps of 1.25° mechanical.

4.8 Results

4.8.1 The 'Actuator' Motor

Figures 4.26 and 4.27 show examples of captured stator currents at rotor positions of 0° electrical and 60° electrical respectively. As expected, there is clear amplitude modulation of the currents. The ellipsoidal current loci discussed in section 3.2 can be seen in figures 4.28 and 4.29 for the same rotor positions as before. The rotation of the major axis is visible despite the low saliency of the machine (which results in the small difference between the major and minor axis length). For direct comparison

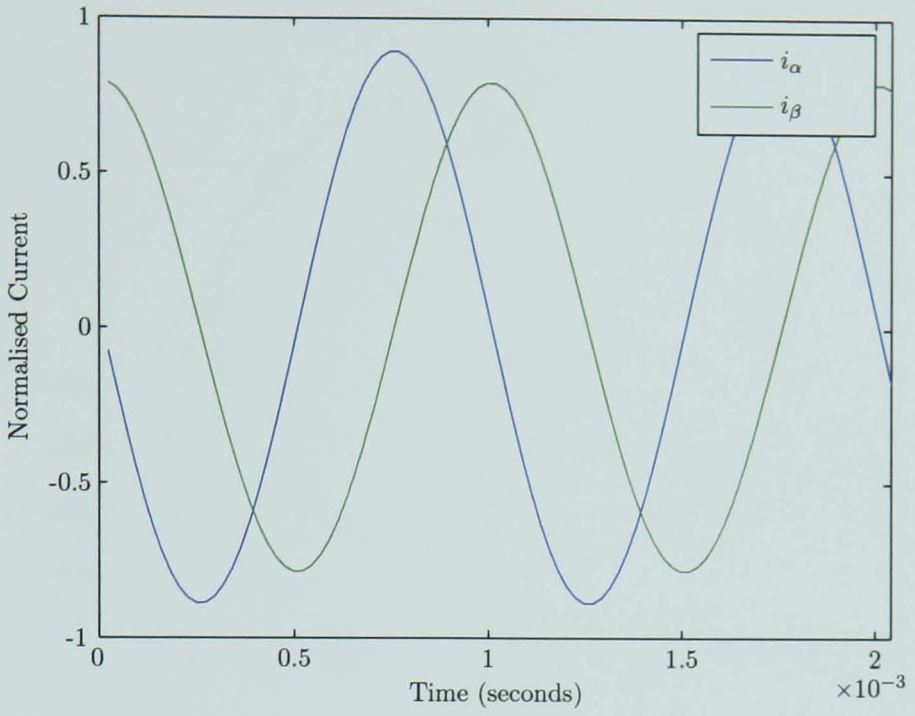

Figure 4.26: Captured Currents – 'Actuator' Motor; $\theta_r = 0°$

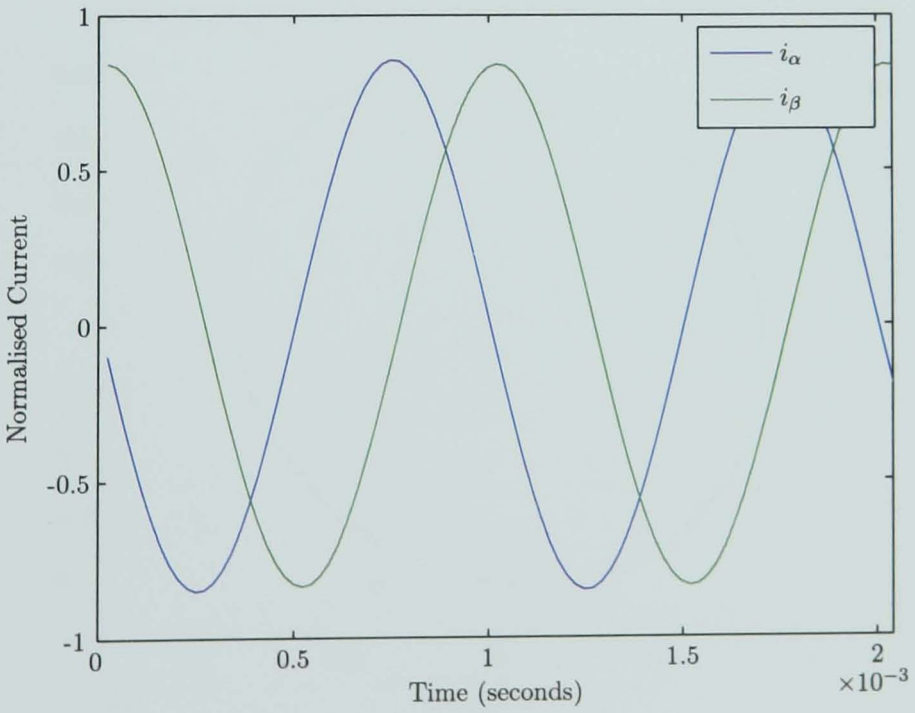

Figure 4.27: Captured Currents – 'Actuator' Motor; $\theta_r = 60°$

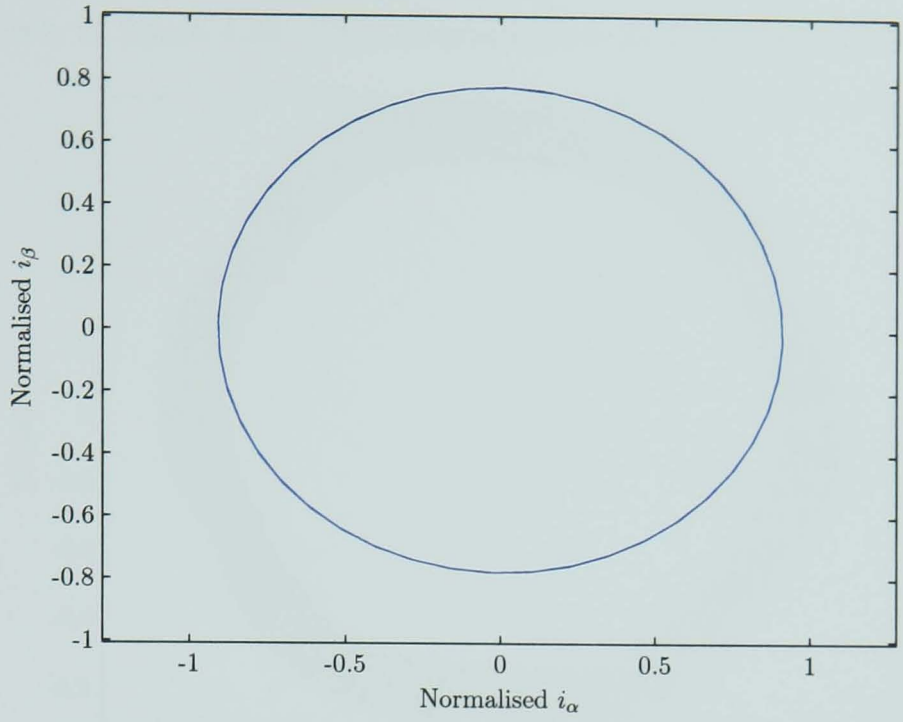

Figure 4.28: Current Locus for 'Actuator' Motor; $\theta_r = 0°$ electrical

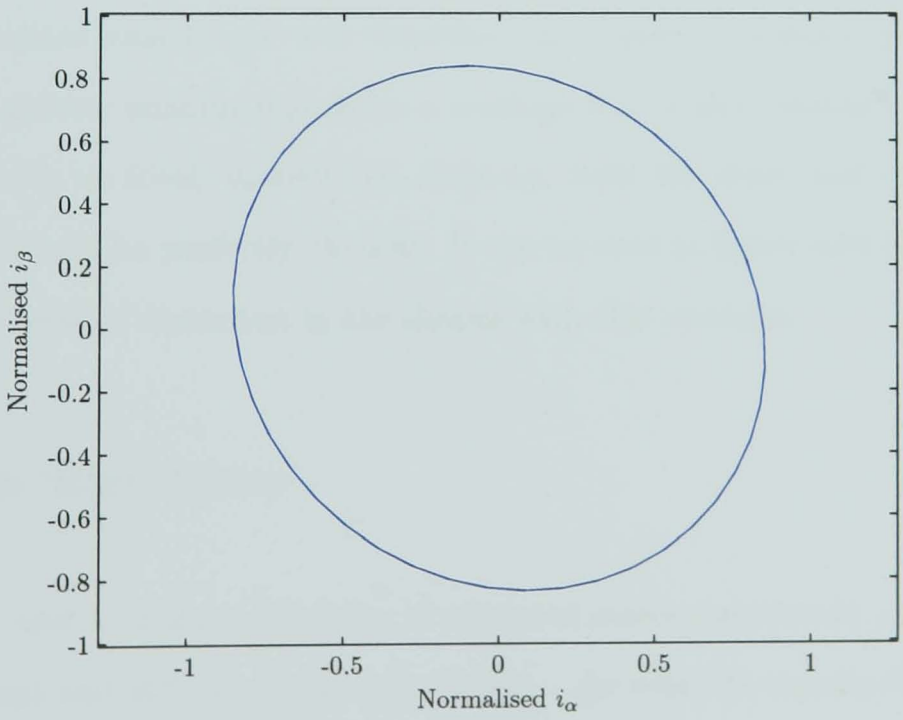

Figure 4.29: Current Locus for 'Actuator' Motor; $\theta_r = 60°$ electrical

of the three machines, it is instructive to superimpose all of the ellipses produced with a given machine (for different rotor positions) on the same graph. The result of this is shown in figure 4.30. This diagram gives an immediate indication of the

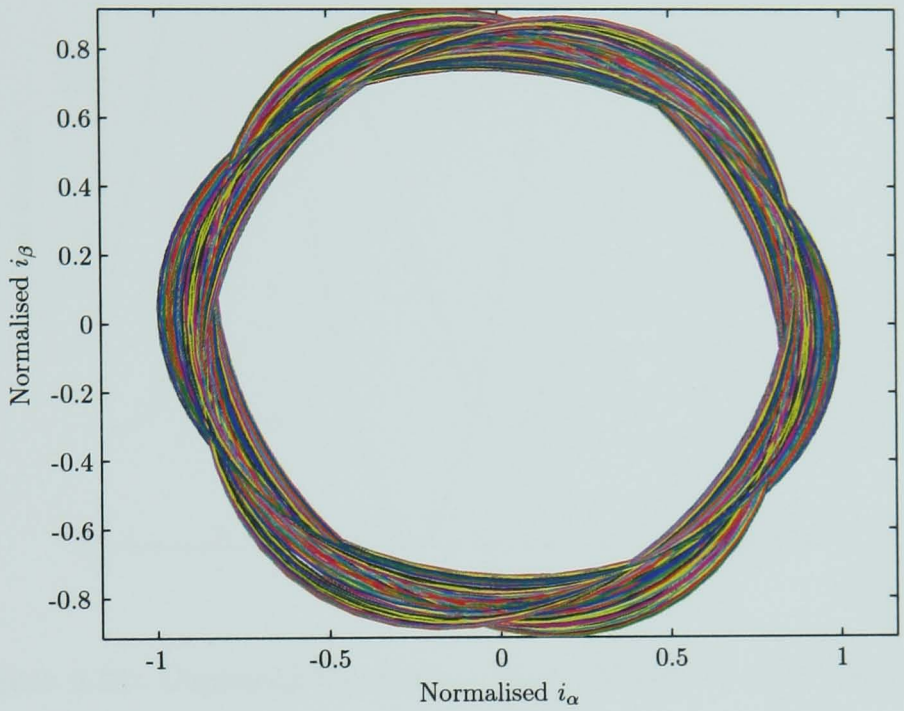

Figure 4.30: Superimposed Ellipses for 'Actuator' Motor

form of the saliency, without the additional steps required to generate a 'saliency fingerprint'. The width of the distorted annulus shows the difference between the major and minor axis length and therefore the degree of saliency present in the machine. A thicker annulus represents a machine with a more distinct saliency. For a machine with an ideal, undistorted, saliency, both the inner and outer edges of the saliency would be perfectly circular. It can be seen in figure 4.30 that there is a considerable level of distortion in the shapes with this machine.

4.8.2 The 'Kart' Motor

Figures 4.31 and 4.32 show examples of captured stator currents at rotor positions of 0° electrical and 60° electrical respectively. As with the results from the 'Actuator' motor, the amplitude modulation can be seen. The ellipsoidal current loci can be seen in figures 4.33 and 4.34 for the same rotor positions as before. The rotation of the major axis of the ellipse is clearly visible. As expected, the ellipsoidal

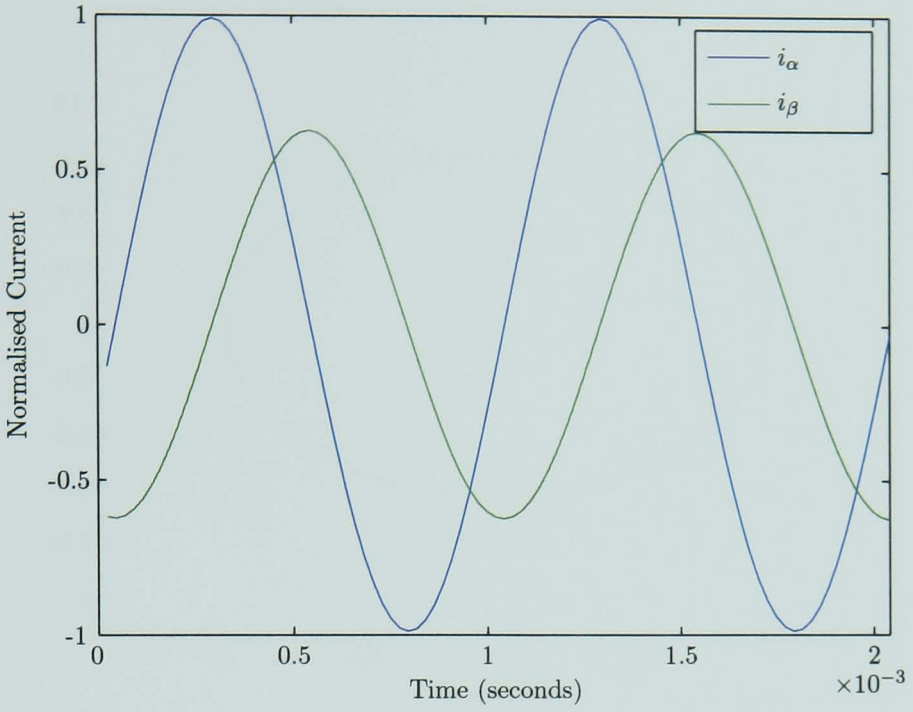

Figure 4.31: Captured Currents – 'Kart' Motor; $\theta_r = 0°$ electrical

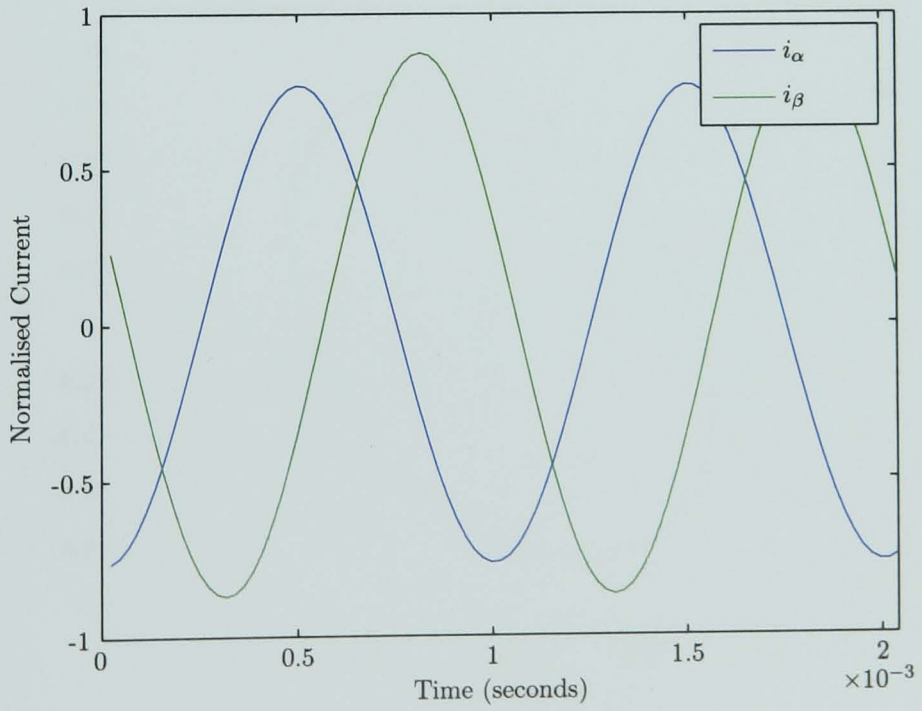

Figure 4.32: Captured Currents – 'Kart' Motor; $\theta_r = 60°$ electrical

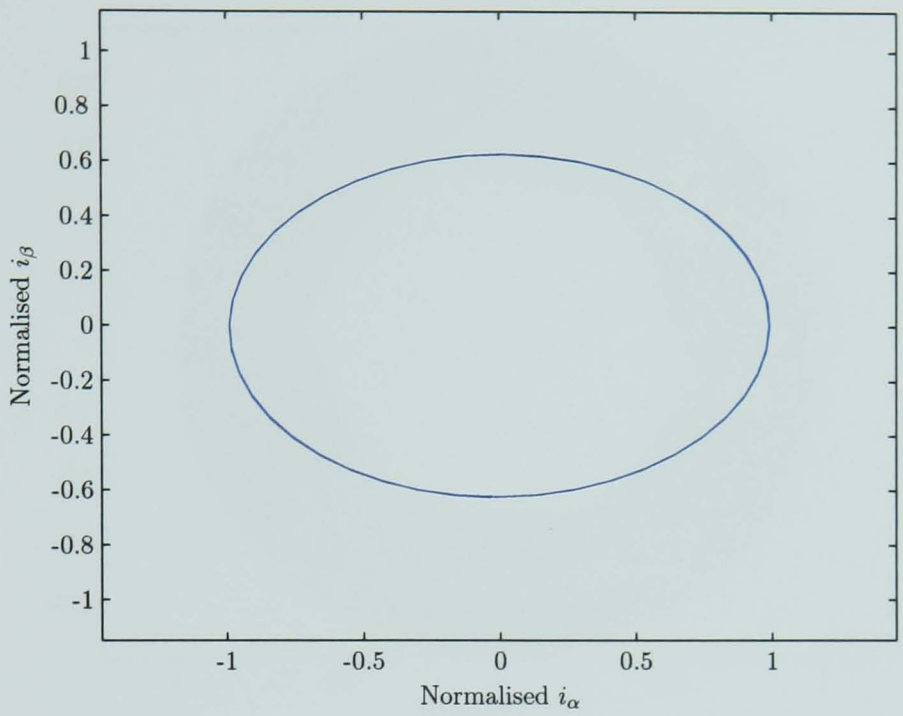

Figure 4.33: Current Locus for 'Kart' Motor; $\theta_r = 0°$ electrical

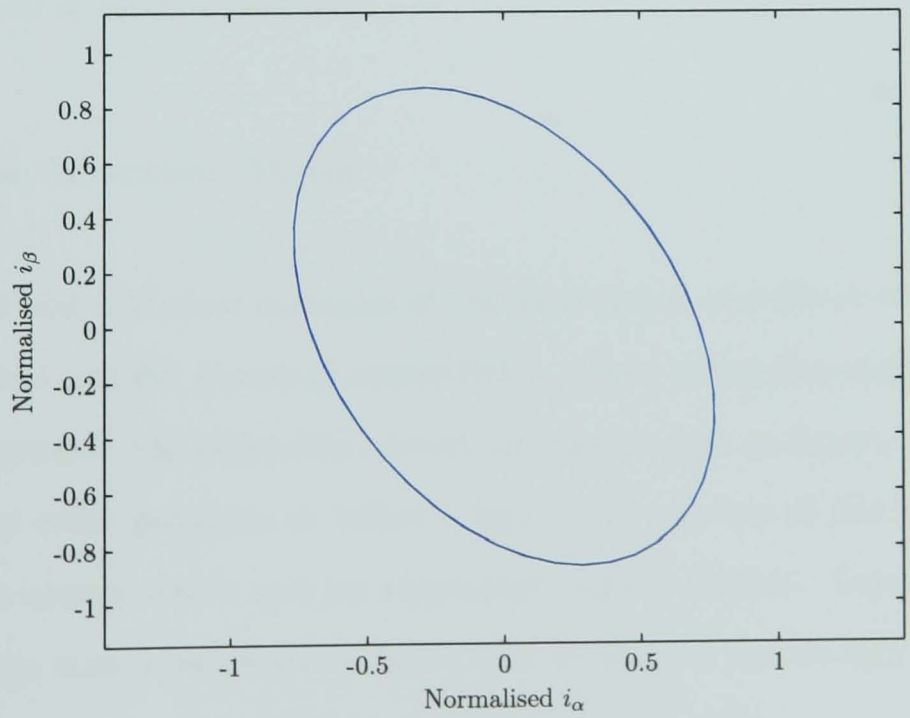

Figure 4.34: Current Locus for 'Kart' Motor; $\theta_r = 60°$ electrical

shape is more distinct due to the higher level of saliency present in the machine. Superimposing all ellipses on the same axes results in figure 4.35.

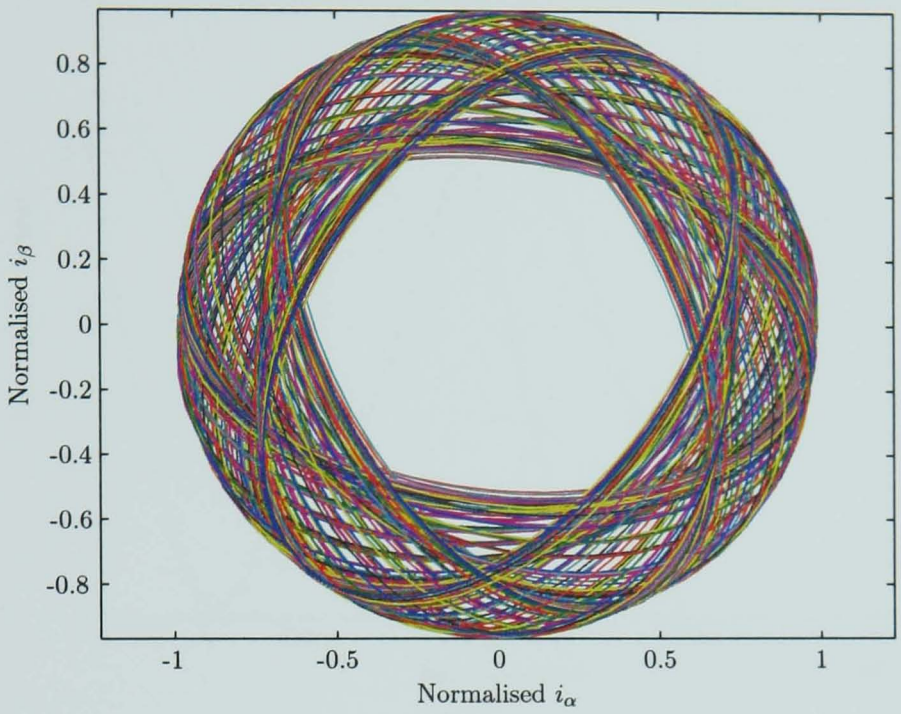

Figure 4.35: Superimposed Ellipses for 'Kart' Motor

The larger saliency in this machine can be clearly seen for this machine. However, there is still a very high level of distortion of the shape of the annulus, corresponding to a high level of saliency distortion.

4.8.3 The 'Traction' Motor

Figures 4.36 and 4.37 show examples of captured stator currents at rotor positions of 0° electrical and 60° electrical respectively. Once again, the amplitude modulation is apparent. The ellipsoidal current loci can be seen in figures 4.38 and 4.39 for the same rotor positions as before. Again, the rotation of the major axis of the ellipse is clearly visible and the ellipsoidal shape is distinct. Superimposing all ellipses on the same axes results in figure 4.40, in which it can be seen that there is a relatively low level of distortion in the shape of the annulus.

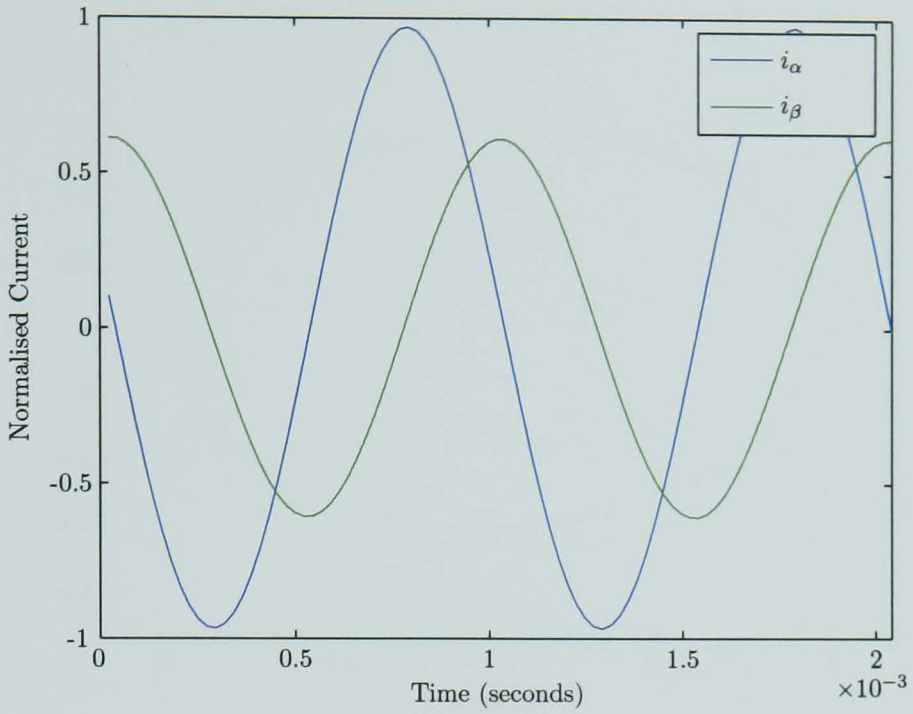

Figure 4.36: Captured Currents – 'Traction' Motor; $\theta_r = 0°$ electrical

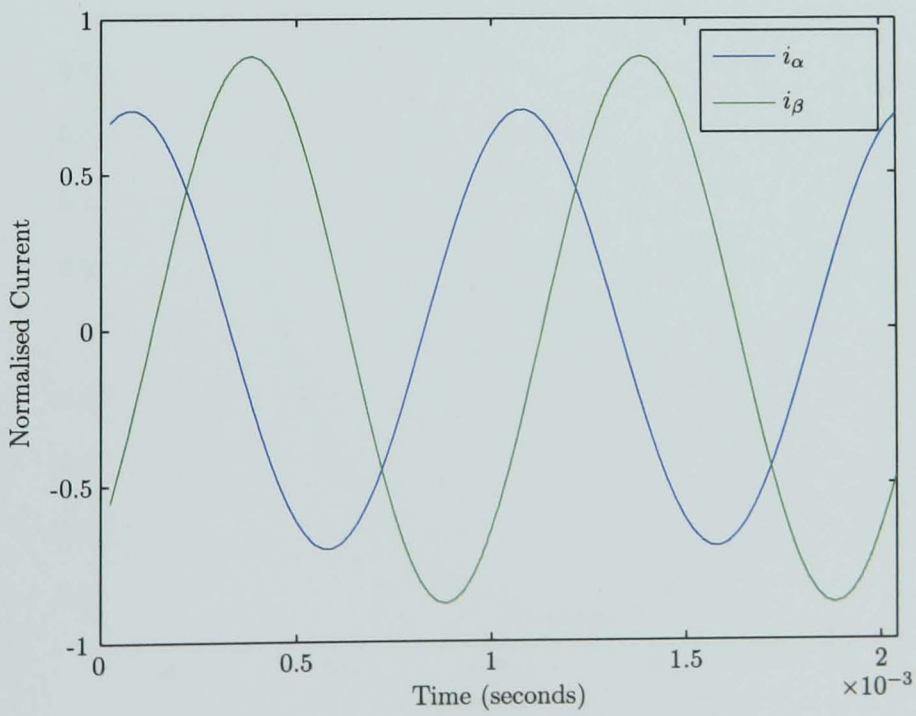

Figure 4.37: Captured Currents – 'Traction' Motor; $\theta_r = 60°$ electrical

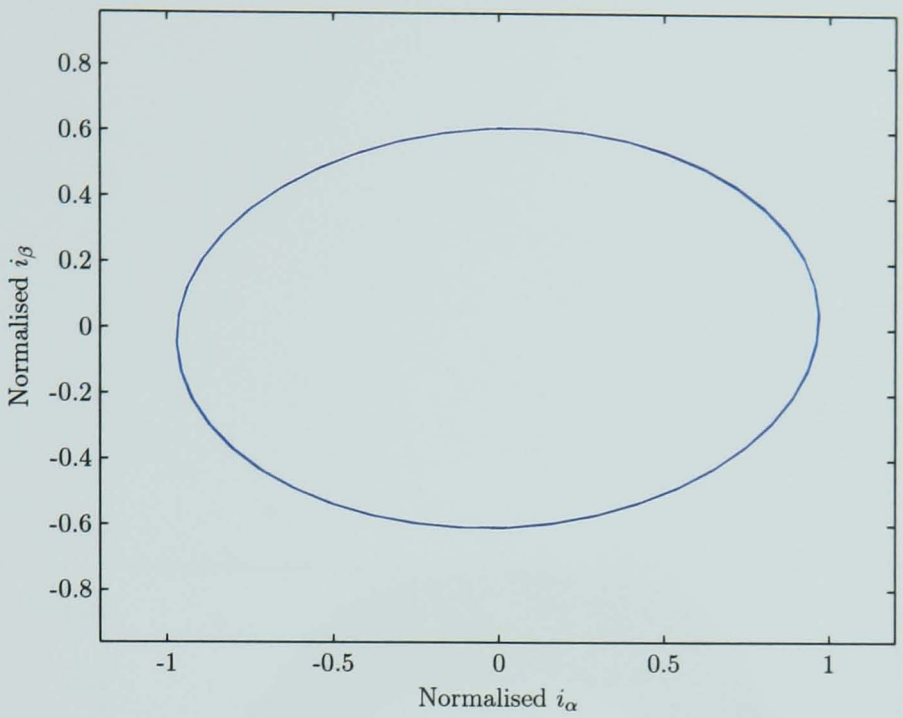

Figure 4.38: Current Locus for 'Traction' Motor; $\theta_r = 0°$ electrical

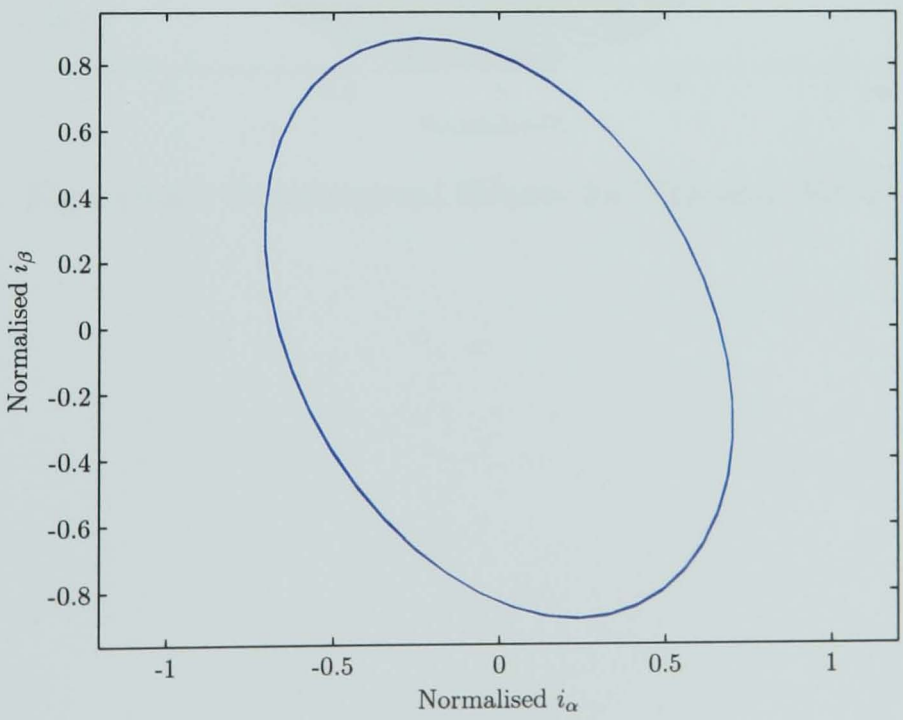

Figure 4.39: Current Locus for 'Traction' Motor; $\theta_r = 60°$ electrical

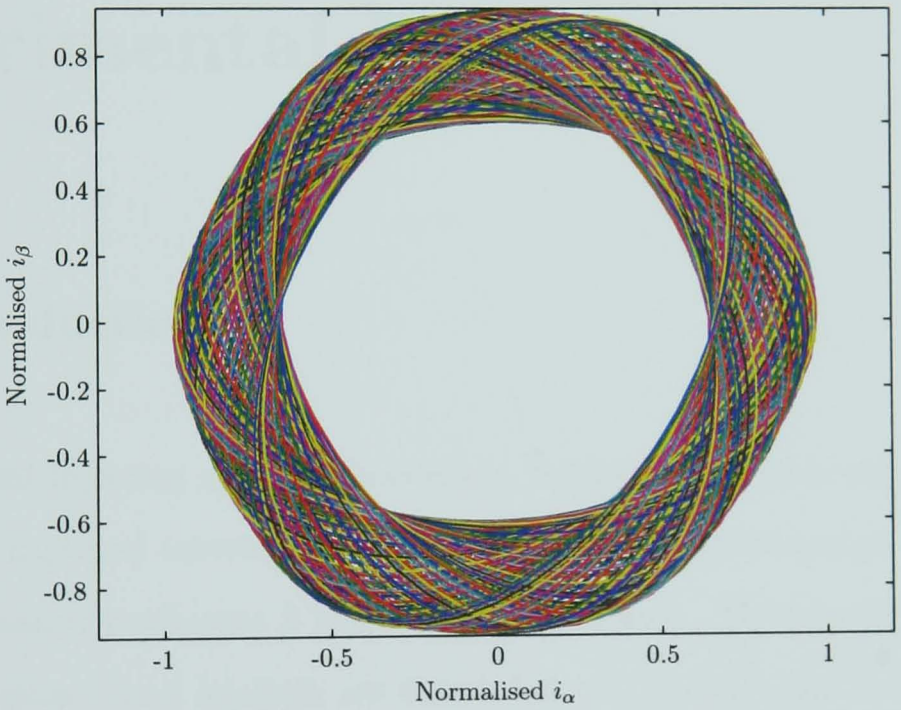

Figure 4.40: Superimposed Ellipses for 'Traction' Motor

Chapter 5

Validation of Techniques with Experimental Results

5.1 Introduction

Once the signal injection system discussed in chapter 4 had been used to produce a large set of captured currents for each machine, it was necessary to simulate the techniques detailed in chapter 3 with experimental data. The results of ellipsoidal and demodulation based analysis are detailed in sections 5.2 and 5.3 respectively. Section 5.4 explains the choice of the demodulation technique over the ellipsoidal approach and section 5.5 gives simulation results from the compensation system.

5.2 MATLAB Analysis of Ellipsoidal Technique

5.2.1 The 'Actuator' Motor

Although the ellipsoidal shape is not as distinctive as that seen in the other machines, the ellipse-fitting routine discussed in section 3.3 was capable of producing an accurate model of the captured ellipsoidal currents at each rotor position. Figures 5.1 and 5.2 show examples of the fitted ellipse at rotor positions of 0° and 60°

respectively. The fitted ellipse equation is of the form shown in equation (3.36) and reproduced here as equation (5.1).

$$Ai_\alpha^2 + 2Hi_\alpha i_\beta + Bi_\beta^2 + 1 = 0 \tag{5.1}$$

Using the coefficients of this equation that were found by the ellipse-fitting routine,

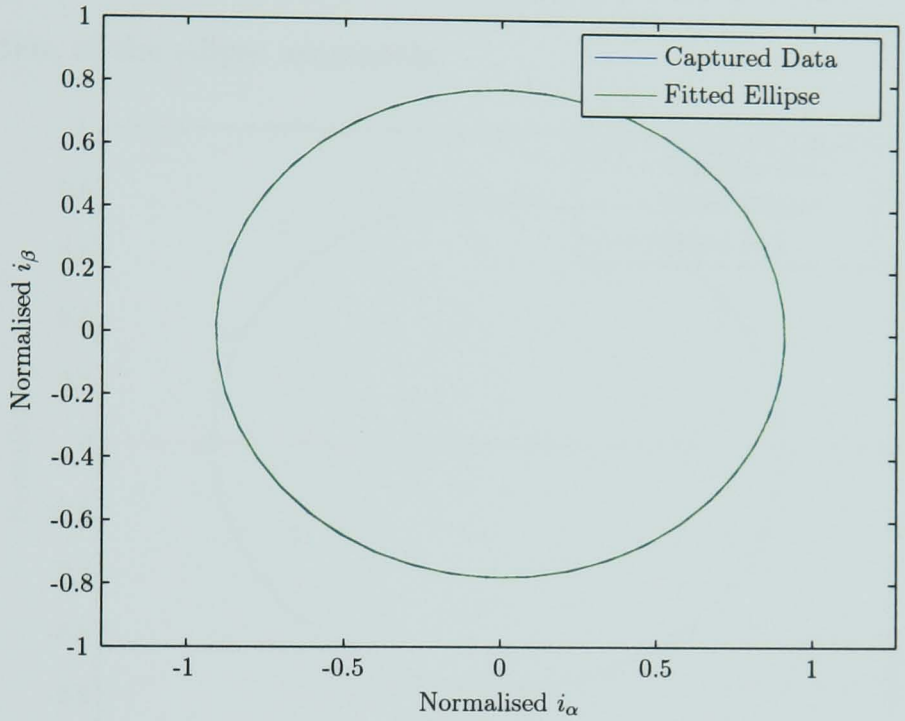

Figure 5.1: Fitted Currents – 'Actuator' Motor; $\theta_r = 0°$

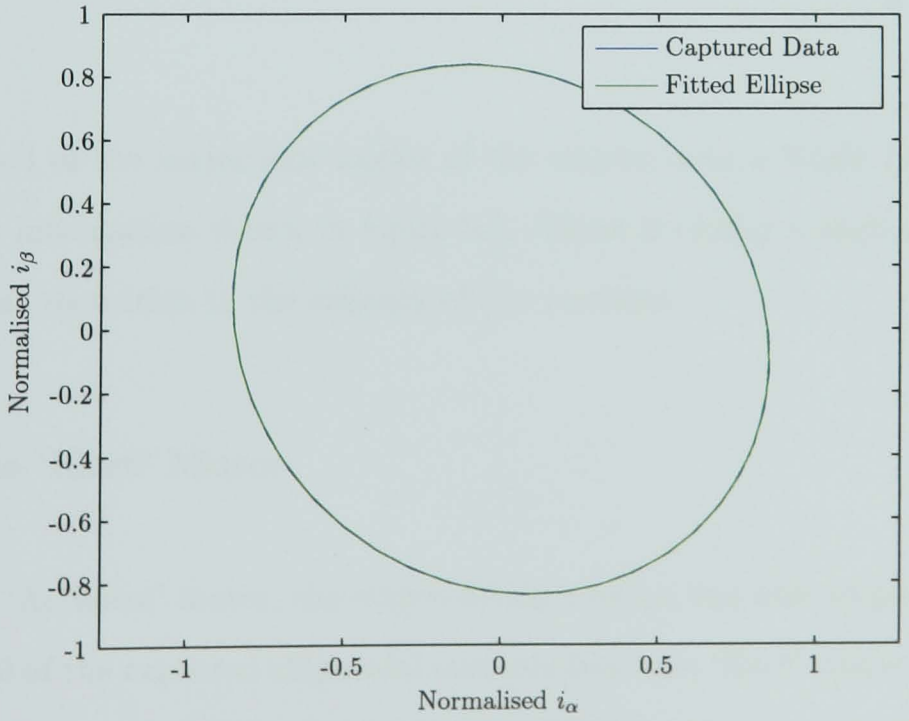

Figure 5.2: Fitted Currents – 'Actuator' Motor; $\theta_r = 60°$

equation (5.2) was used to derive the angle of the major axis of each ellipse.

$$\theta_r^{est} = \frac{1}{2}\tan^{-1}\frac{2H}{A-B} + \begin{cases} 0 & ; \quad (A-B)\cos(2\theta_r^{est}) + 2H\sin(2\theta_r^{est}) \geqslant 0 \\ \frac{\pi}{2} & ; \quad (A-B)\cos(2\theta_r^{est}) + 2H\sin(2\theta_r^{est}) < 0 \end{cases} \tag{5.2}$$

For the rotor positions shown in figures 5.1 and 5.2, this estimated major axis location is shown in figures 5.3 and 5.4 respectively. It can be seen that the estimation fits the position of the ellipse accurately.

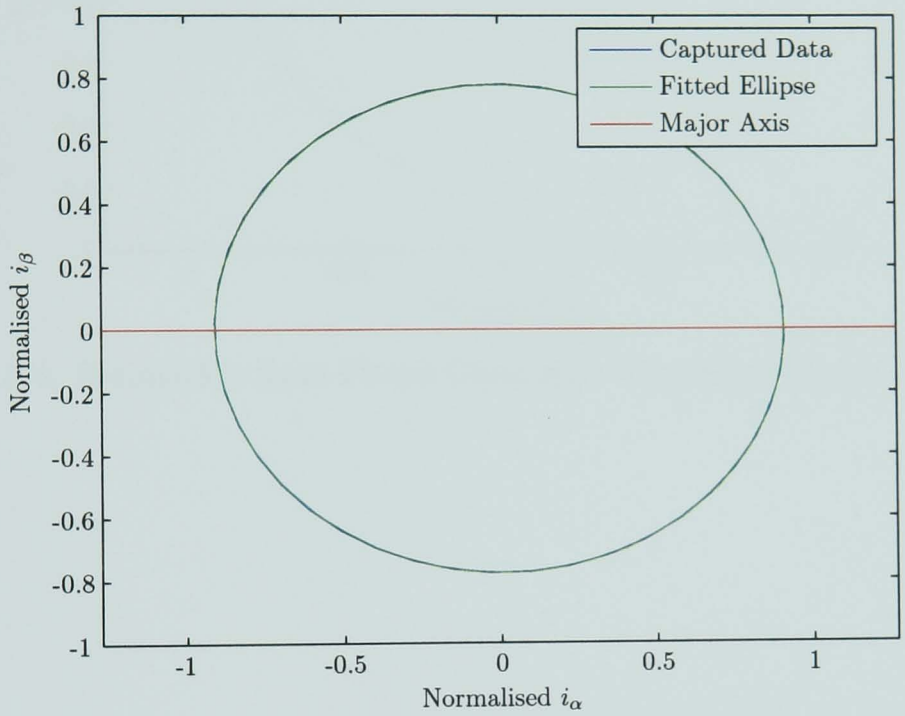

Figure 5.3: Estimation from Fitted Currents – 'Actuator' Motor; $\theta_r = 0°$

Combining all of the major axis angles of the ellipses onto a single plot results in the position information shown in figure 5.5. There is clearly a high level of error resulting from distortion in the saliency of the machine.

5.2.2 The 'Kart' Motor

As with the 'Actuator' motor, the ellipse-fitting routine was able to produce an accurate model of the captured ellipsoidal currents from the 'Kart' motor. Figures 5.6 and 5.7 show examples of the fitted ellipses with the estimated major axis angles marked. Combining all of the results into a position plot results in figure 5.8. Once

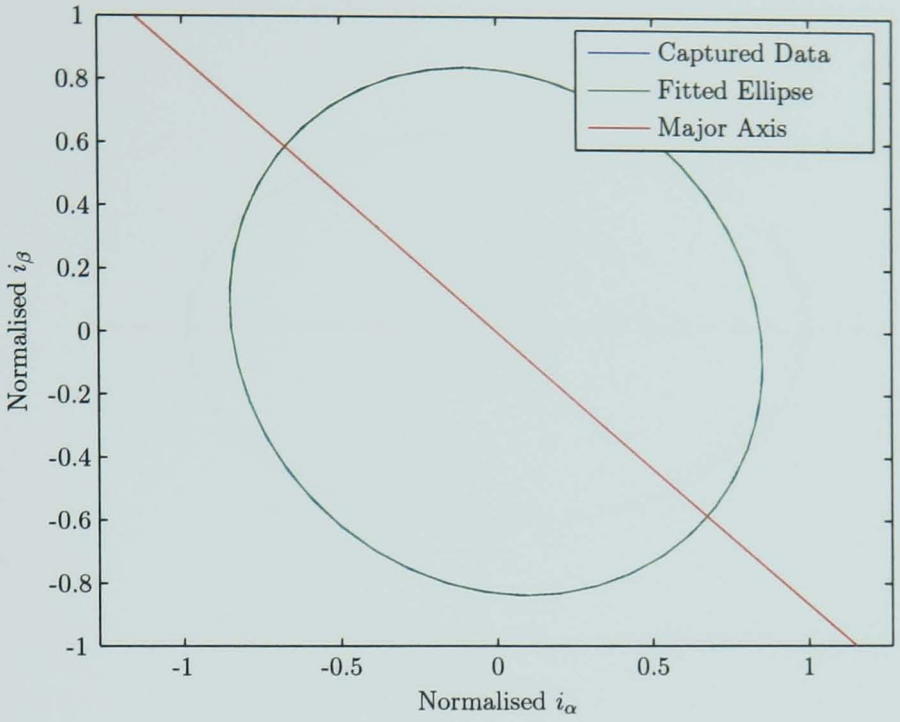

Figure 5.4: Estimation from Fitted Currents – 'Actuator' Motor; $\theta_r = 60°$

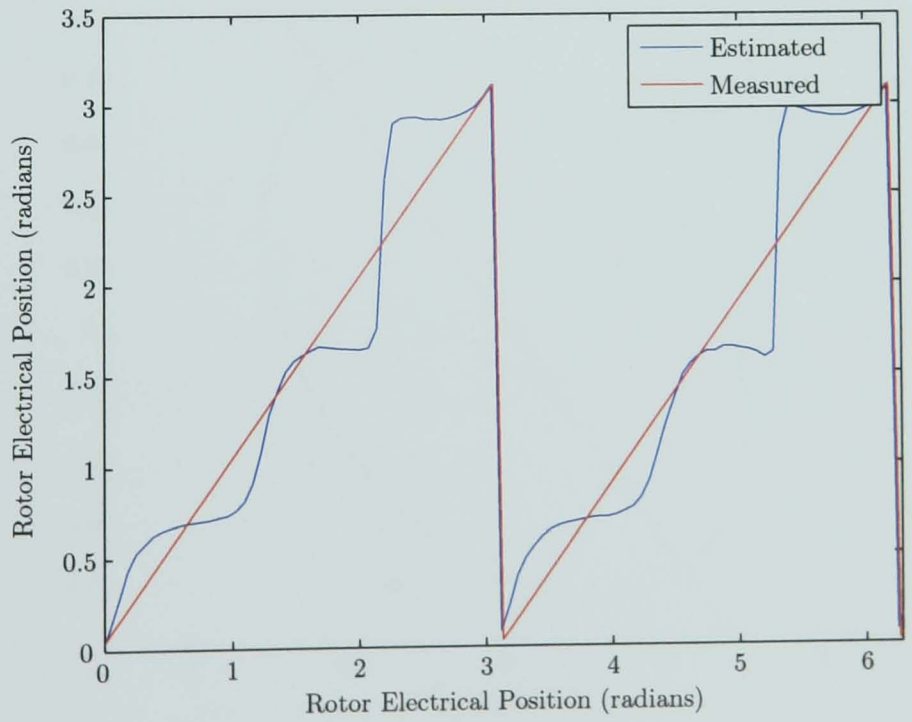

Figure 5.5: Position Estimation Results for 'Actuator' Motor

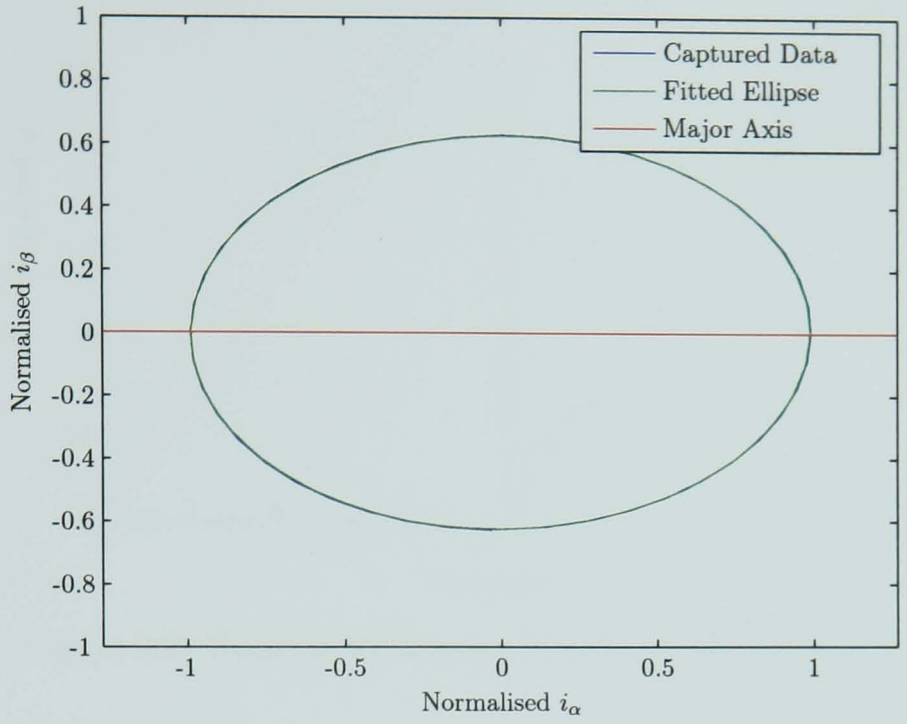

Figure 5.6: Estimation from Fitted Currents – 'Kart' Motor; $\theta_r = 0°$

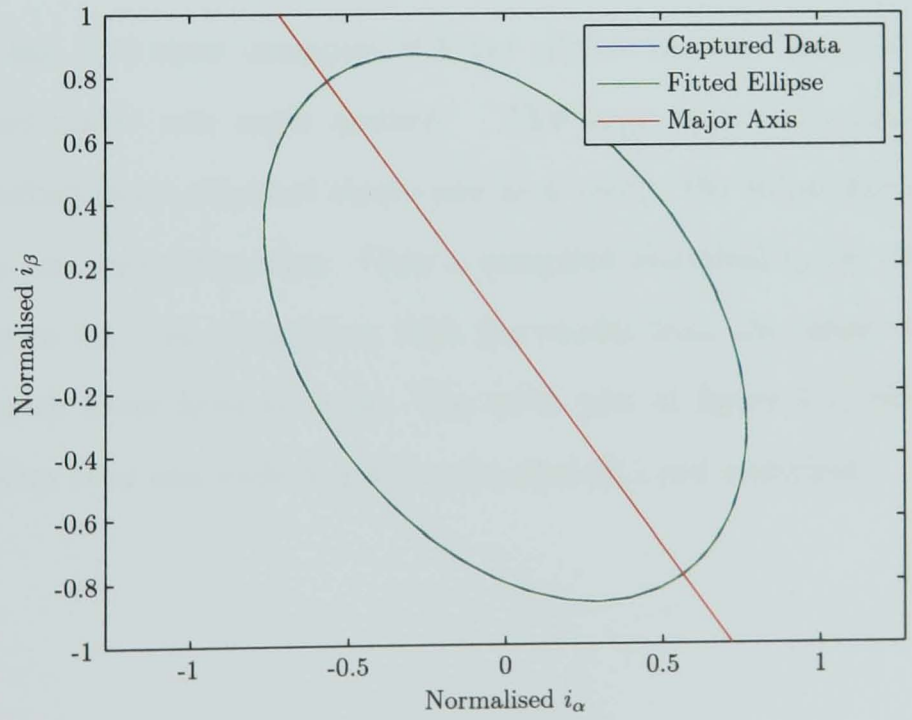

Figure 5.7: Estimation from Fitted Currents – 'Kart' Motor; $\theta_r = 60°$

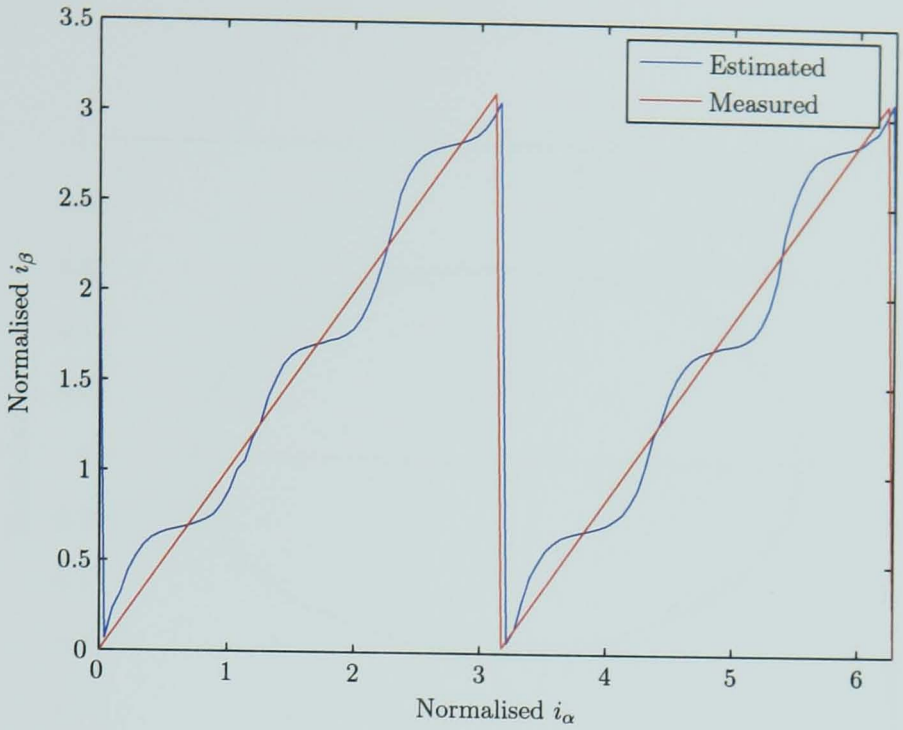

Figure 5.8: Position Estimation Results for 'Kart' Motor

again, a high level of error is present; although there is an increased saliency, it is insufficient to overcome the distortion.

5.2.3 The 'Traction' Motor

Figures 5.9 and 5.10 show examples of fitted ellipses for the 'Traction' motor with the estimated major axis angle marked. The large degree of saliency results in an easily distinguished elliptical shape and as a result, the ellipse-fitting algorithm produces an accurate estimation. Over a complete electrical cycle, the results are shown in figure 5.11. In comparison with the results from the other two machines, there is a much lower level of error. The error plot of figure 5.12 shows that the maximum error over one cycle is 1.4° mechanical (0.1 rad electrical).

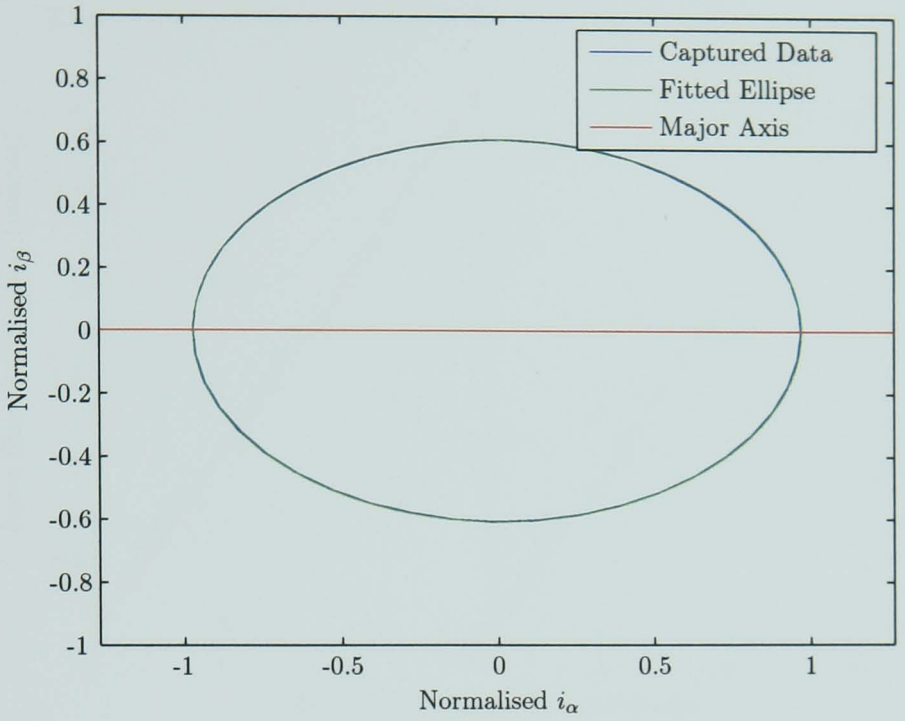

Figure 5.9: Estimation from Fitted Currents – 'Traction' Motor; $\theta_r = 0°$

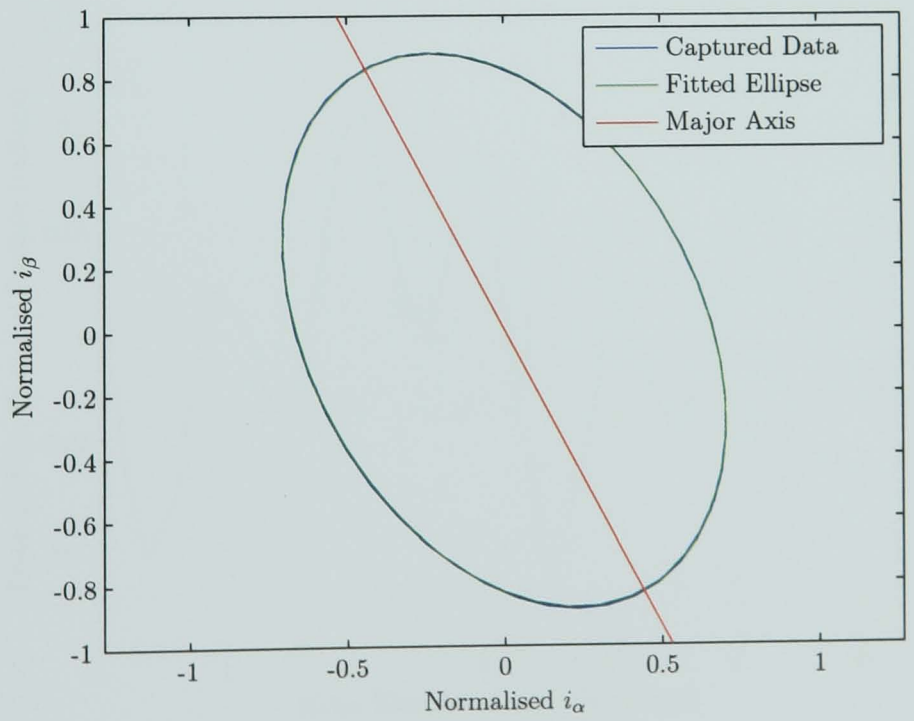

Figure 5.10: Estimation from Fitted Currents – 'Traction' Motor; $\theta_r = 60°$

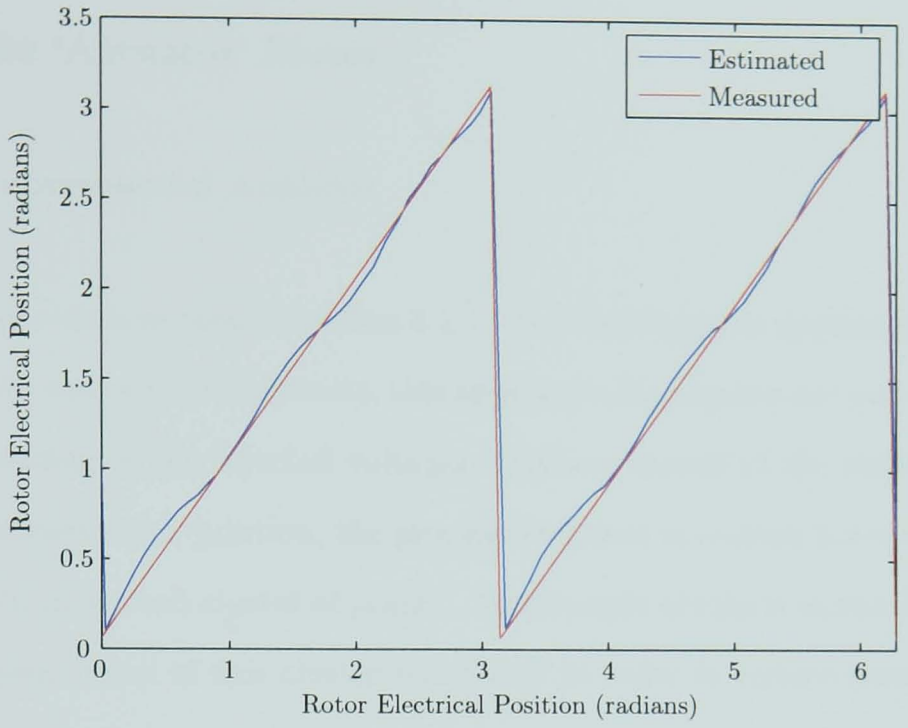

Figure 5.11: Position Estimation Results for 'Traction' Motor

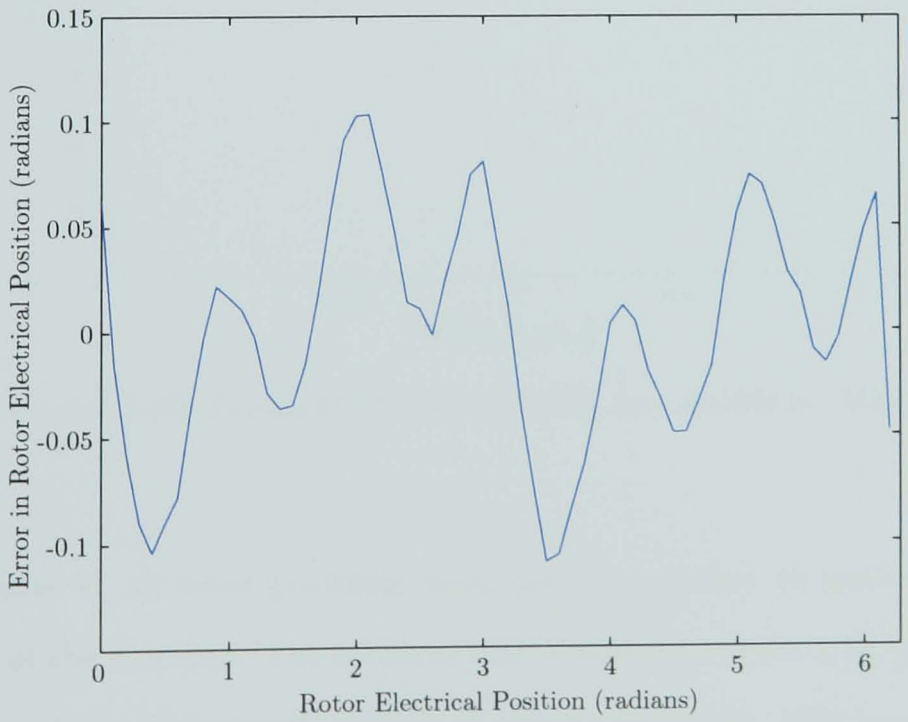

Figure 5.12: Error in Ellipsoidal Estimation Results for 'Traction' Motor

5.3 MATLAB Analysis of Demodulation Technique

5.3.1 The 'Actuator' Motor

5.3.1a Experimental Analysis

With the same data as used in section 5.2.1, the demodulation approach was applied. In addition to the captured currents, this approach also requires accurate information about the timing of the injected voltages; this was stored at the same time as the currents. At each rotor position, the process discussed in section 3.4 was carried out. This resulted in a small cluster of points. An example of this is shown in figure 5.13. The arithmetic mean of this cluster was found in order to reduce errors from noise

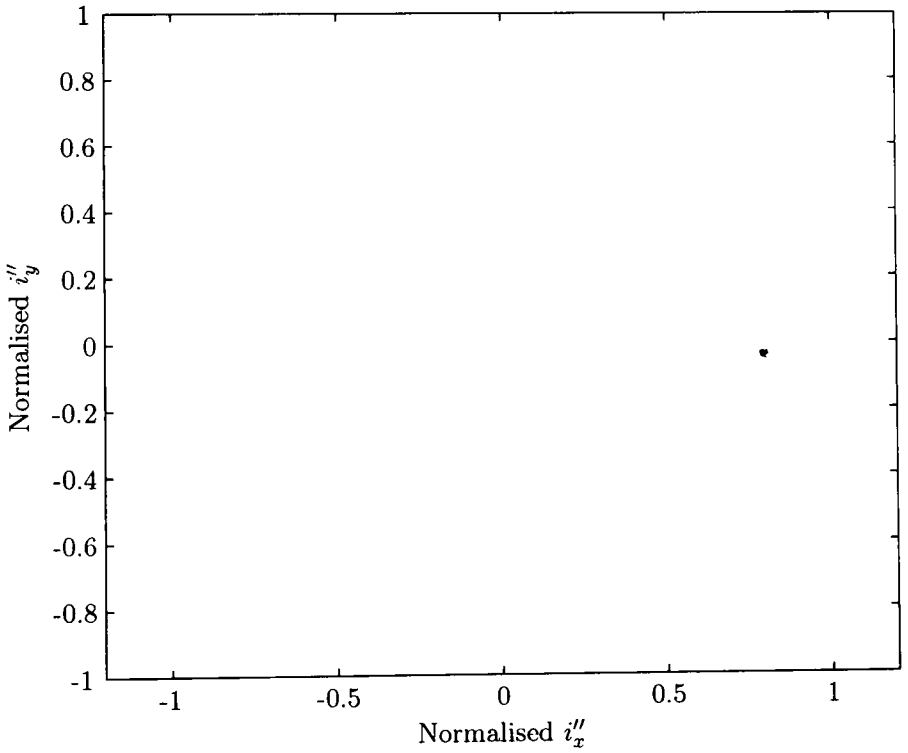

Figure 5.13: Example of Point Cluster for 'Actuator' Motor

and the points at all rotor positions were plotted together to show the 'saliency fingerprint' of the machine. The result of this is shown in figure 5.14 (normalised to the extremes of the 'fingerprint' shape). It can be seen that there is a considerable level of distortion present; the higher order saliencies have resulted in a 'saliency fingerprint' that bears little resemblance to the circular shape of the ideal machine discussed in section 3.4. Figure 5.14 only shows the amplitude component of the

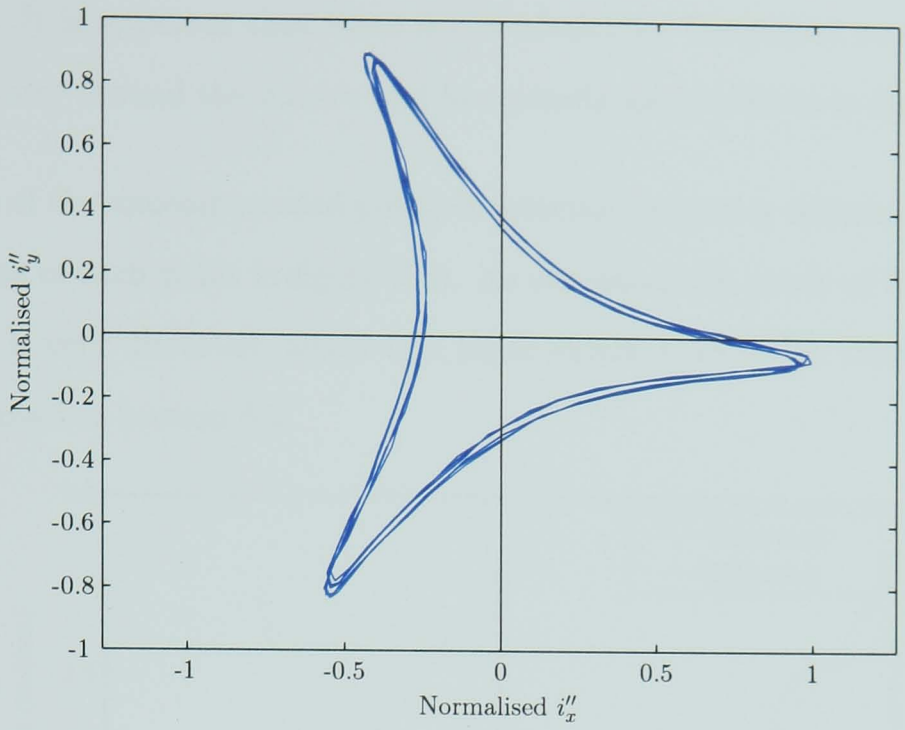

Figure 5.14: 'Saliency Fingerprint' for 'Actuator' Motor

distortion. Since the phase of the result contains the position information, it is instructive to visualise the phase distortion and how it relates to the distorted shape of the 'saliency fingerprint'. Figure 5.15 shows this relationship clearly. The green

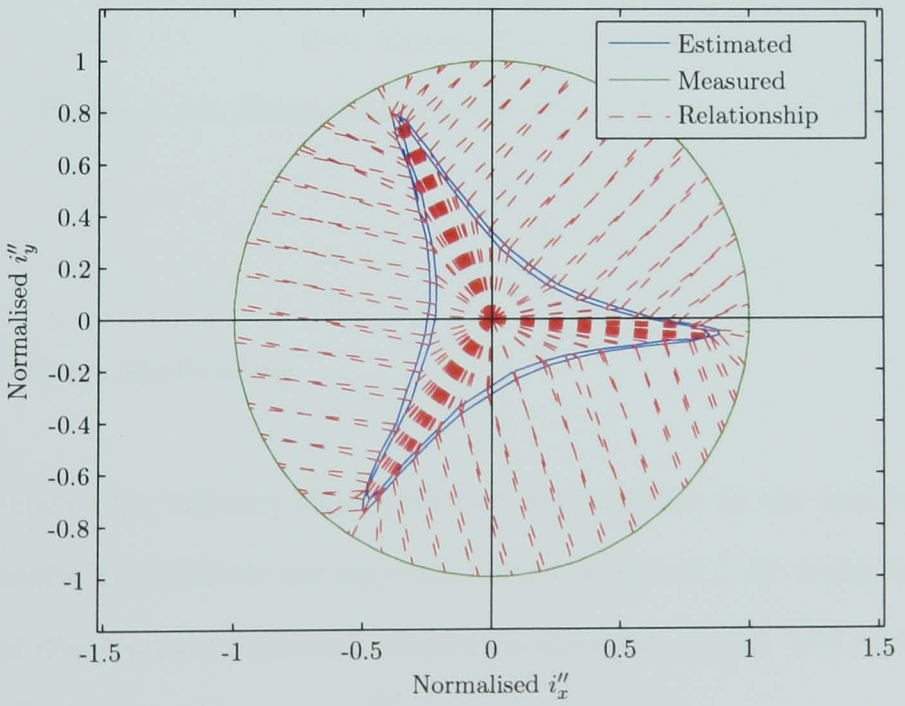

Figure 5.15: Phase Relationship for 'Actuator' Motor

circle is the ideal motor characteristic and the blue shape is a scaled version of the shape from figure 5.14. The red interconnecting lines are used to show which points on the distorted shape correspond to evenly spaced points on the ideal 'saliency

fingerprint'. It is apparent that there is a tendency for the points on the distorted shape to cluster around the apexes and be sparsely spaced between these points.

Completion of the uncompensated position detection system is achieved by calculating the phase of each point in figure 5.14. As expected, the result of this (shown in figure 5.16) is very distorted, albeit to a lesser extent than in the results of ellipse-fitting discussed in section 5.2.

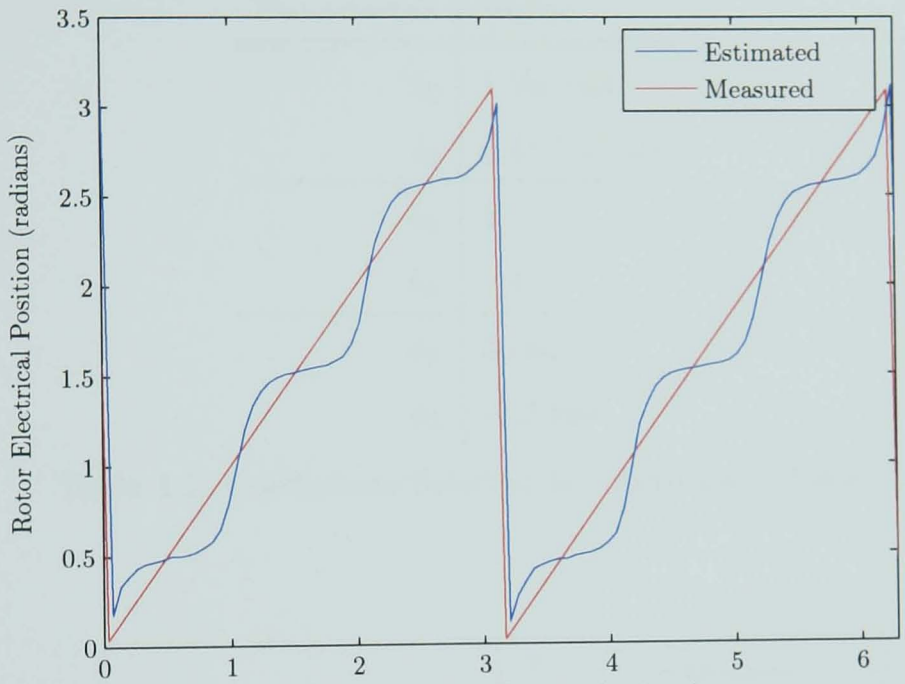

Figure 5.16: Demodulation Results – 'Actuator' Motor

5.3.1b Further Modelling

In order to relate the 'saliency fingerprint' of the machine to the modelling of chapter 3, it is useful to produce an approximation of figure 5.15 using those models. The model of the captured currents shown in equation (3.45) and reproduced here as equation (5.3) was used.

$$i_{\alpha\beta} = I_1 \begin{pmatrix} \sin(\omega_i t) \\ \cos(\omega_i t) \end{pmatrix} - \sum_{k=2}^{n} I_k \begin{pmatrix} \sin(h_k\theta_r - \omega_i t + \phi_k) \\ \cos(h_k\theta_r - \omega_i t + \phi_k) \end{pmatrix} \tag{5.3}$$

After the demodulation process, the position independent component is removed

and this results in equation (5.4).

$$i'' = -\sum_{k=2}^{n} I_k \begin{pmatrix} \sin\left(h_k\theta_r + \phi_k\right) \\ \cos\left(h_k\theta_r + \phi_k\right) \end{pmatrix} \tag{5.4}$$

To match the shape of the 'saliency fingerprint', the parameters shown in table 5.1 were chosen. This resulted in the modelled 'fingerprint' shown in figure 5.17.

Parameter	Value
I_2	1 Vs/rad
I_3	0.45 Vs/rad
h_2	2
h_3	-4
ϕ_2	0 rad
ϕ_3	-1.5 rad

Table 5.1: Coefficients Selected for 'Actuator' Motor

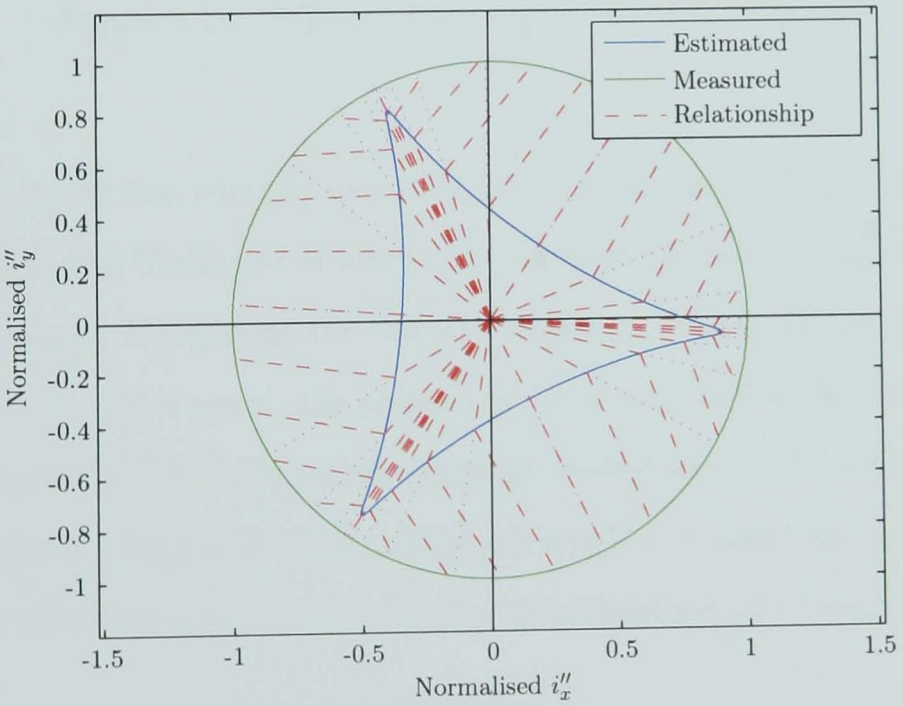

Figure 5.17: Modelled Phase Relationship for 'Actuator' Motor

5.3.2 The 'Kart' Motor

The analysis discussed in detail in section 5.3.1 was repeated using the results captured from the 'Kart' motor. The 'saliency fingerprint' that was produced is shown in figure 5.18. Although there is a significant level of distortion, the higher saliency

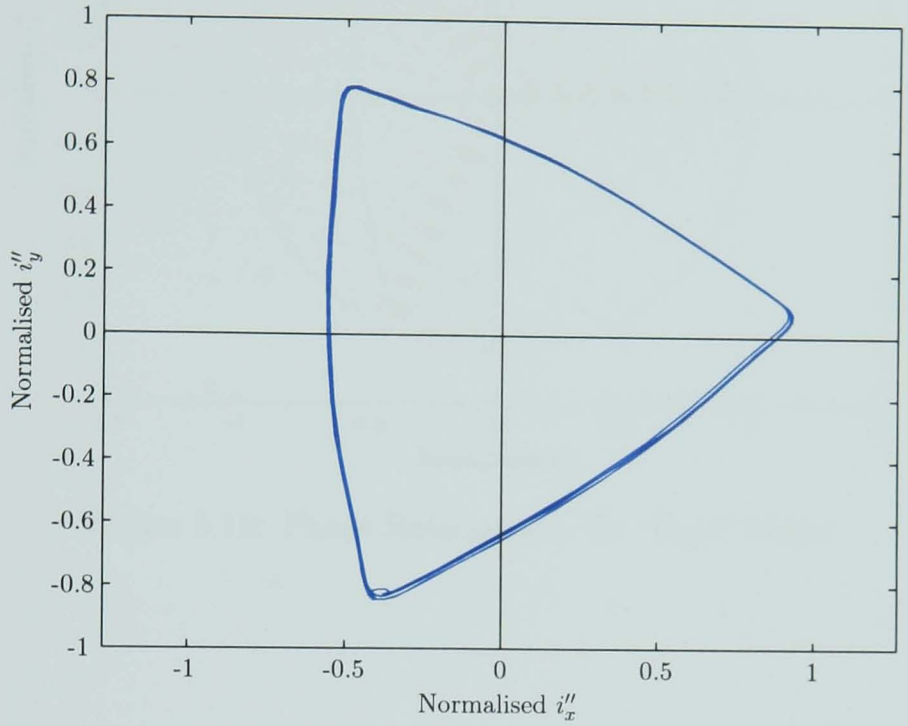

Figure 5.18: 'Saliency Fingerprint' for 'Kart' Motor

of the 'Kart' motor has resulted in a noticeable improvement in the shape. In particular, there is less likelihood of ambiguity between the points immediately either side of the apexes. Comparing the distorted 'saliency fingerprint' to the ideal case gives figure 5.19. Once again, the points can be seen to cluster around the apexes of the 'fingerprint'. Completion of the uncompensated scheme results in figure 5.20. This again shows a high level of distortion, although it is clear that the position information is of sufficient accuracy to allow implementation of a brushless DC drive.

To match the shape of the 'saliency fingerprint', the parameters of equation (5.4) shown in table 5.2 were chosen. The resulting 'fingerprint' is shown in figure 5.21.

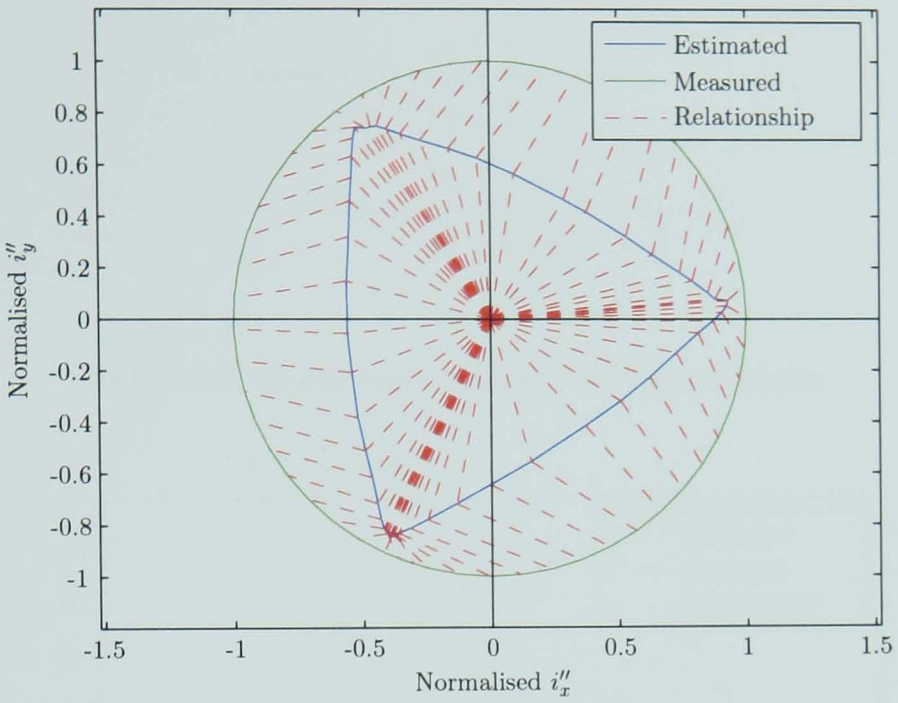

Figure 5.19: Phase Relationship for 'Kart' Motor

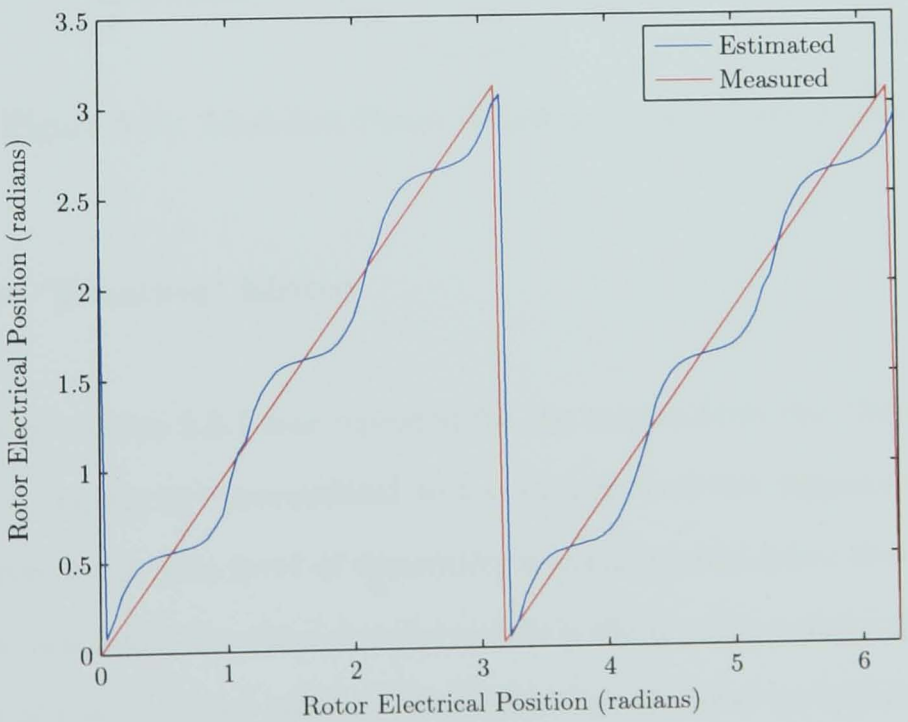

Figure 5.20: Demodulation Results – 'Kart' Motor

Parameter	Value
I_2	1 Vs/rad
I_3	$\frac{1}{4}$ Vs/rad
h_2	2
h_3	-4
ϕ_2	0 rad
ϕ_3	3.28 rad

Table 5.2: Coefficients Selected for 'Kart' Motor

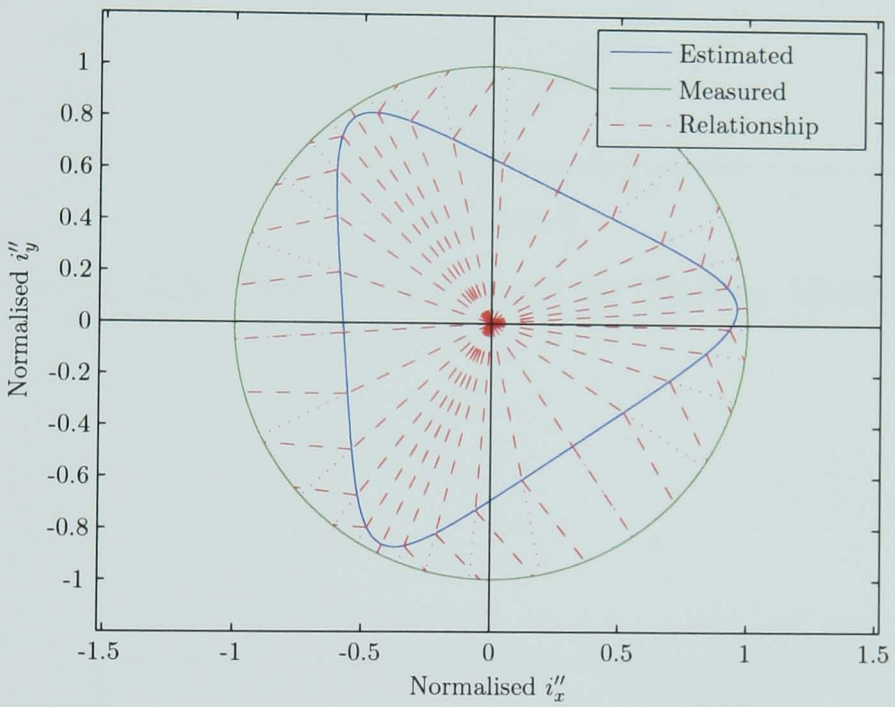

Figure 5.21: Modelled Phase Relationship for 'Kart' Motor

5.3.3 The 'Traction' Motor

The analysis of section 5.3.1 was repeated for the results from the 'Traction' motor. The 'saliency fingerprint' (normalised to the extremes of the 'fingerprint' shape) is shown in figure 5.22. The level of distortion is considerably lower than in either of the other two machines; the ideal circular profile is discernable despite the distortion. Comparison of the distorted 'saliency fingerprint' to the ideal case gives figure 5.23. Although the clustering seen with the 'Actuator' and 'Kart' motors is still present, the effect is considerably less noticeable.

Completion of the uncompensated scheme results in figure 5.24. The level of inaccu-

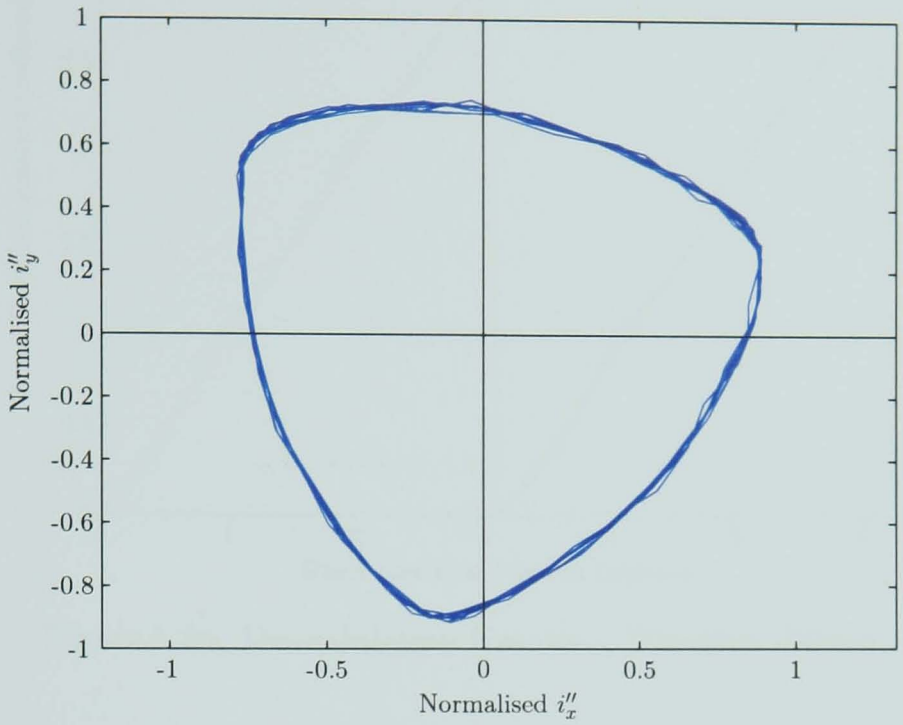

Figure 5.22: 'Saliency Fingerprint' for 'Traction' Motor

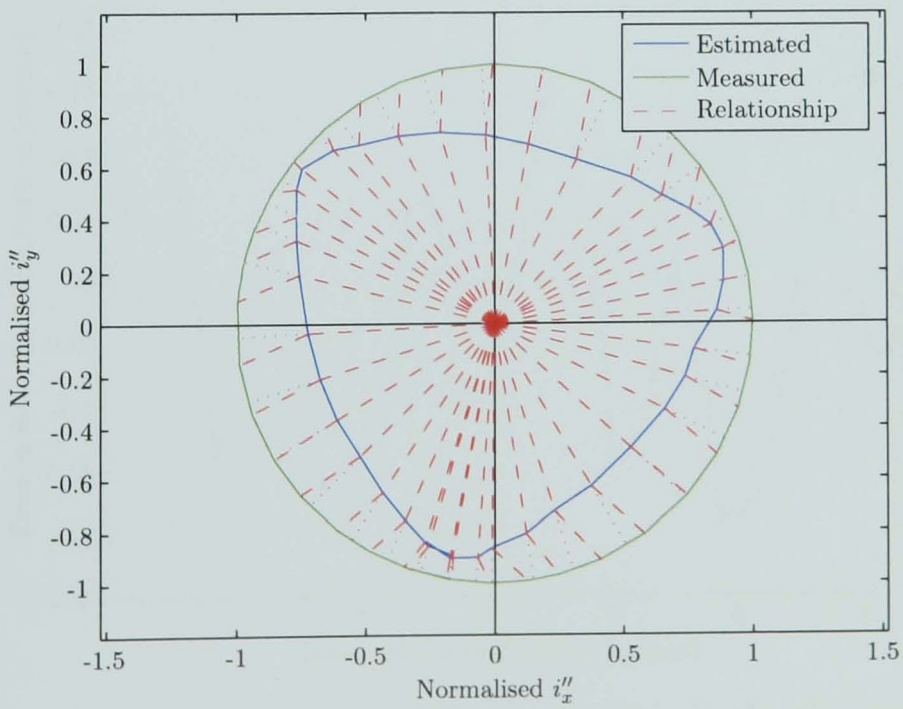

Figure 5.23: Phase Relationship for 'Traction' Motor

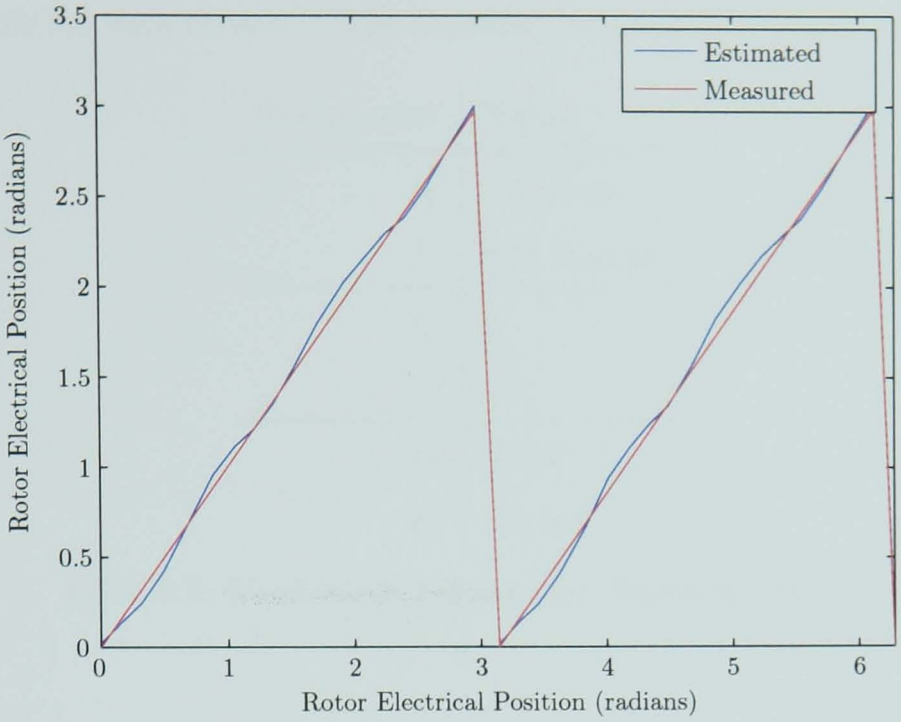

Figure 5.24: Demodulation Results – 'Traction' Motor

racy is much lower than was seen with the other two machines and it is illustrative to examine the error in the position information. This is shown in figure 5.25. The maximum error over a complete electrical cycle is 2.75° mechanical (0.19 rad electrical).

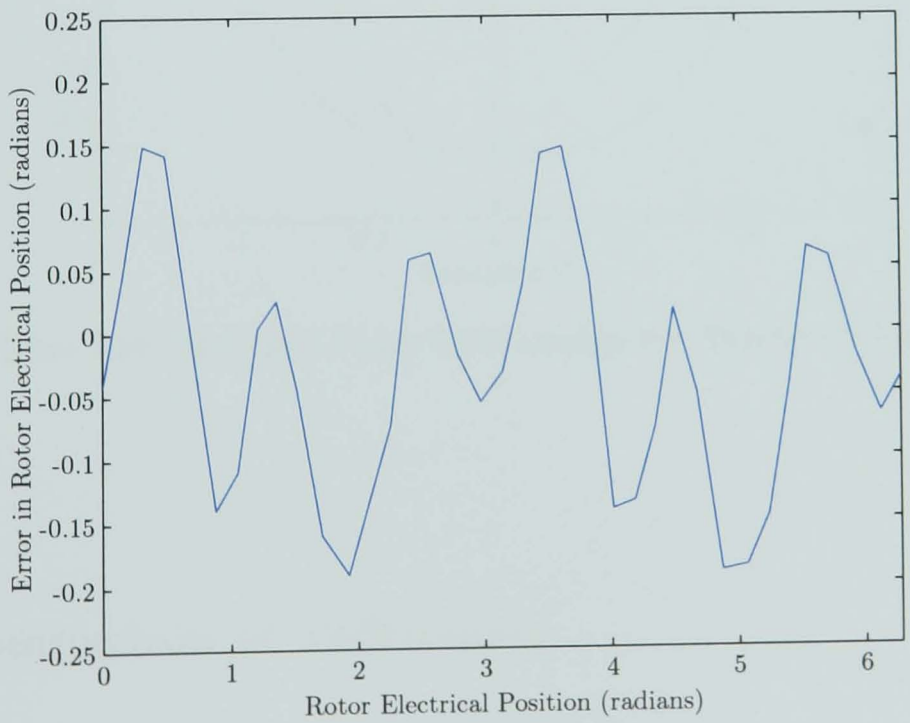

Figure 5.25: Error in Demodulation Estimation Results for 'Traction' Motor

To match the shape of the 'saliency fingerprint', the parameters of equation (5.4)

shown in table 5.3 were chosen. The resulting 'fingerprint' is shown in figure 5.26.

Parameter	Value
I_2	1 Vs/rad
I_3	0.15 Vs/rad
h_2	2
h_3	−4
ϕ_2	0 rad
ϕ_3	2.3 rad

Table 5.3: Coefficients Selected for 'Traction' Motor

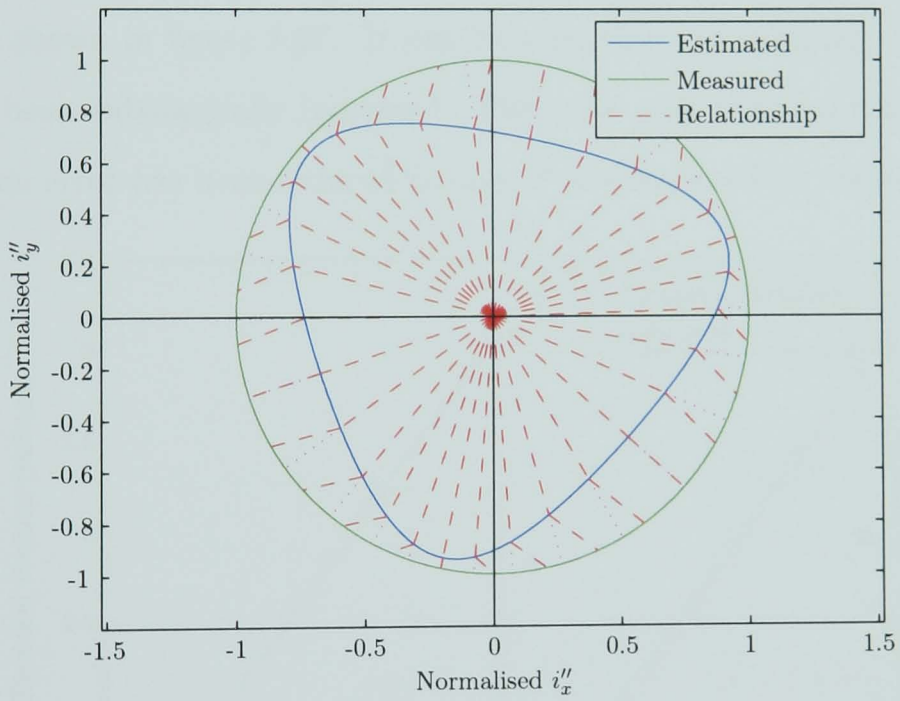

Figure 5.26: Modelled Phase Relationship for 'Traction' Motor

5.4 Comparison of Techniques

Comparing the results from sections 5.2 and 5.3 for each motor, there is little identifiable difference in the accuracy of each technique with the interior magnet machines; the determining factor is the form of the saliency in the machine. Therefore, due to the relative computational simplicity of the demodulation technique (both in terms

of memory requirements and processing load) and the small degree of improvement in accuracy with the 'Actuator' motor, this option was selected for the remainder of the development.

5.5 MATLAB Analysis of Compensation Technique

5.5.1 The 'Actuator' Motor

Through comparison of the distorted and ideal 'fingerprints' shown in figure 5.15, a correction table was generated for the characteristic of the 'Actuator' motor. Using this with a sample of currents over a complete electrical cycle resulted in the position information shown in figure 5.27. It can be seen that the accuracy of the overall system has been substantially increased. The error plot of figure 5.28 shows that the maximum error has been reduced to only 2° mechanical (0.1 rad electrical).

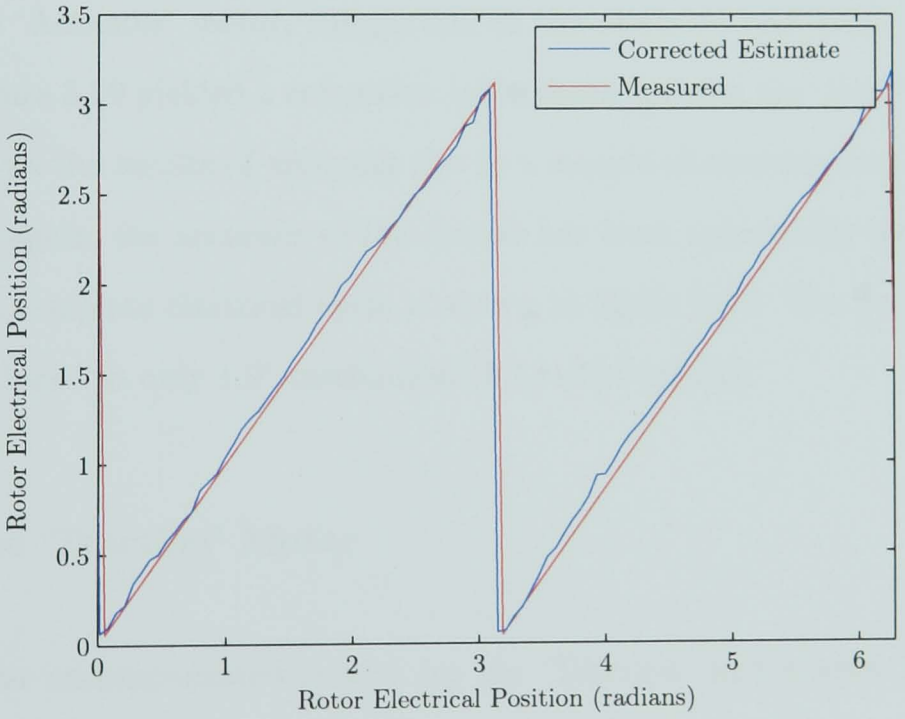

Figure 5.27: Compensated Results – 'Actuator' Motor

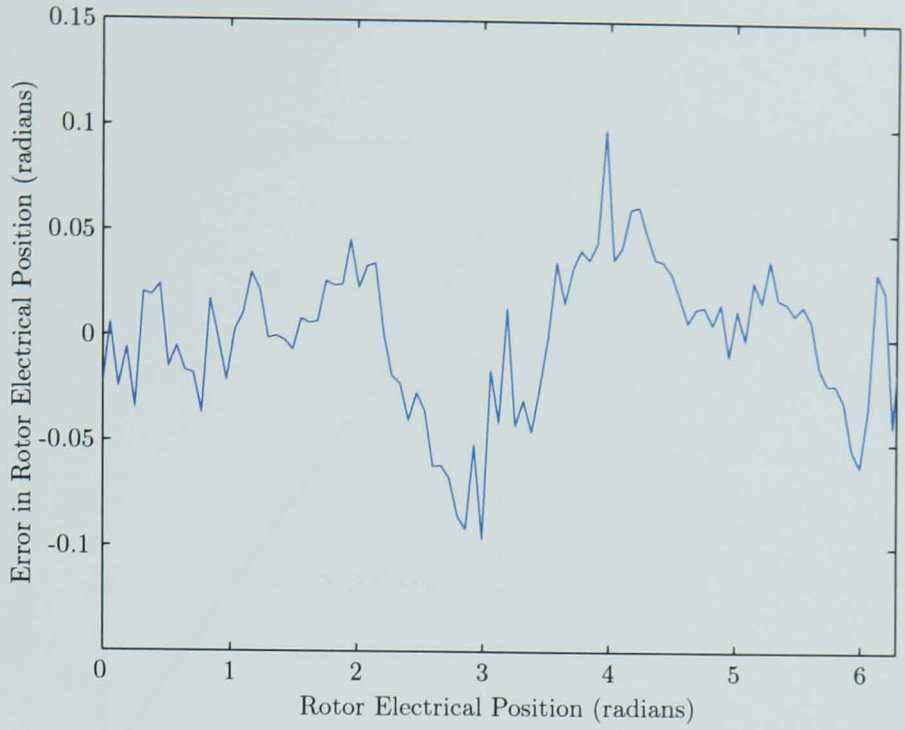

Figure 5.28: Error in Compensated Results – 'Actuator' Motor

5.5.2 The 'Kart' Motor

As with the 'Actuator' motor, comparison of the distorted and ideal 'fingerprints' shown in figure 5.19 yielded a correction table characterising the 'Kart' motor. Figure 5.29 shows the results of applying this to a sample of currents over an electrical cycle. Once again, the accuracy of the system has been appreciably increased. The error over a complete electrical cycle is shown in figure 5.30. The maximum error has been reduced to only 1.9° mechanical (0.1 rad electrical).

5.5.3 The 'Traction' Motor

Although the uncompensated results for the 'Traction' motor show considerably better accuracy than the results from the other machines, it is desirable to improve the accuracy for some applications. For this reason, the compensation process was applied to the captured currents from this motor. Figure 5.31 shows the final position estimation results. The maximum error over one electrical cycle has been reduced to only 0.85° mechanical (0.06 rad electrical). The complete error plot is shown in figure 5.32.

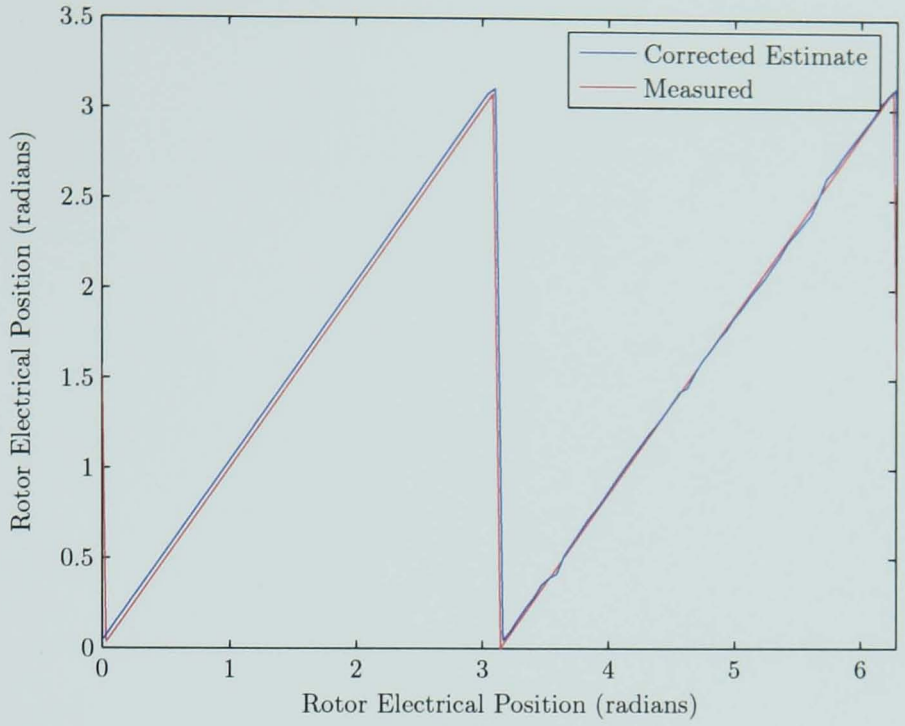

Figure 5.29: Compensated Results – 'Kart' Motor

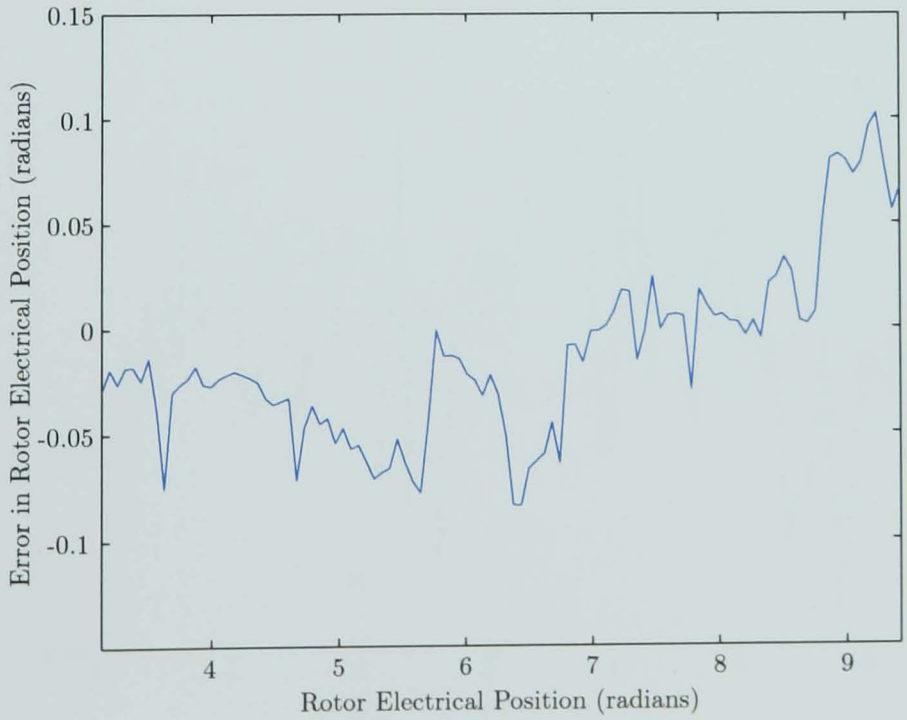

Figure 5.30: Error in Compensated Results – 'Kart' Motor

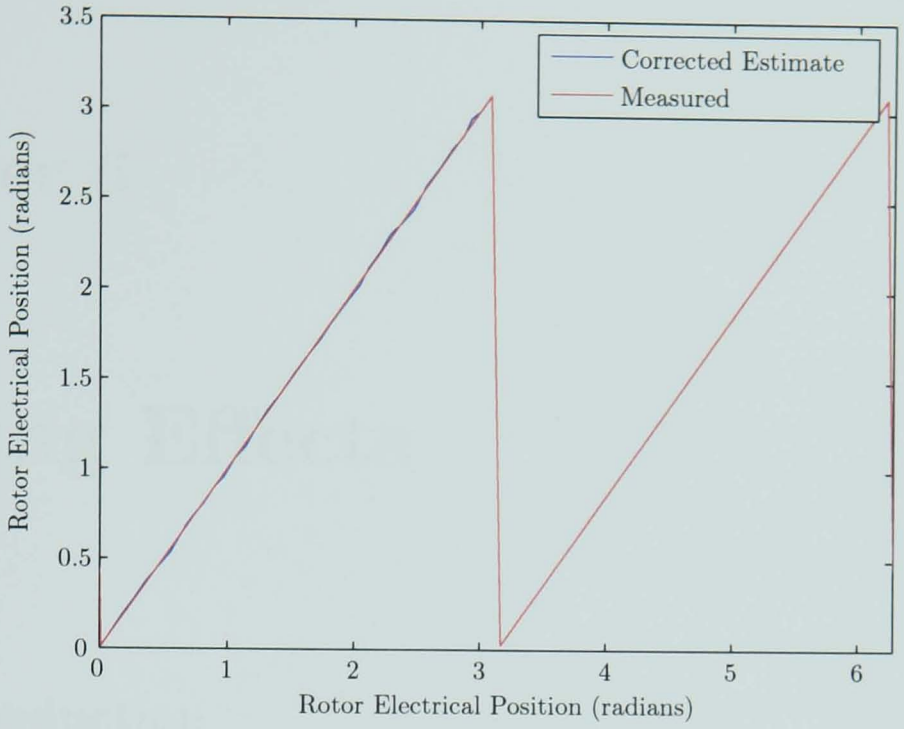

Figure 5.31: Compensated Results – 'Traction' Motor

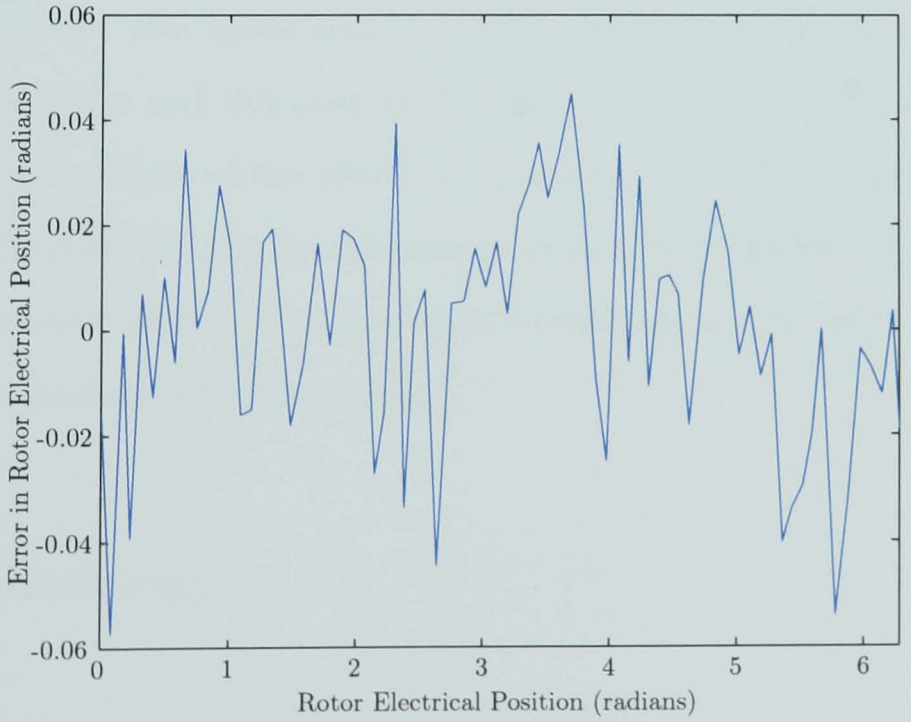

Figure 5.32: Error in Compensated Results – 'Traction' Motor

Chapter 6

Slotting Effects

6.1 Introduction

It is instructive to analyse the effects of slotting in more detail, in order to provide machine designers with information relating to the effect of variations in the physical structure of a machine on the saliency profile. The FEA approach to saliency analysis discussed in section 4.2 provides a valuable tool for optimising machine designs for simple and accurate zero speed sensorless rotor position estimation in addition to machine performance and this chapter provides an example of the use of the tool by providing an analysis of the effect of variations in the slot shape for the test machines. Although the precise dimensions of the 'Kart' motor are unavailable, approximate measurements are used in order to demonstrate the effect of slot shape variation on a machine with this topology.

6.2 Methodology

The approach used to analyse the effect of slot shape on saliency distortion is based on the approach used in section 4.2. However, due to the larger number of simulations required, the symmetry of the physical machine and its saliency was used in order to reduce the computation time. For an n_p pole machine, the model can be

divided into $\frac{n_p}{2}$ sections, with rotational symmetry. Periodic boundary conditions can then be used to ensure that the FEA results are accurate. In addition, the symmetry of the 'saliency fingerprint' can be used to further reduce the number of computational steps in the finite element analysis. For the six-pole machines, for example, the number of required simulations steps is reduced from 14400 to only 2520. The results obtained for the unaltered machines confirm the validity of this approach.

In order to develop an understanding of the effect of slot shape variations, two key slot parameters were analysed: slot opening, s_i, and tooth tip thickness, t_i. These dimensions are shown diagrammatically for a single slot in figure 6.1. It is important

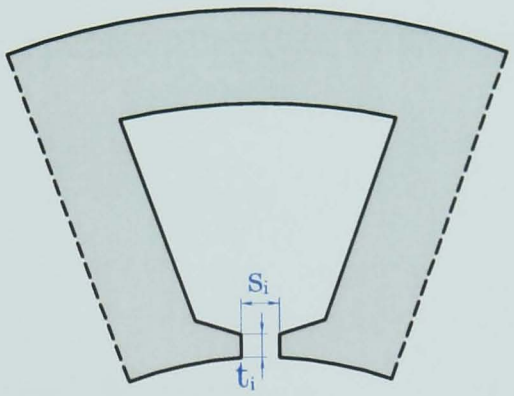

Figure 6.1: Layout of a Single Stator Slot

to note that changes to the slot opening size have a considerable effect on the size of the tooth tip; increasing the slot opening results in a reduction in the width of the tooth tip. The dimensions were changed relative to the original machine design; for all machines, the same alterations were performed. These are summarised in table 6.1, where s and t are the original machine's slot opening size and tooth tip thickness respectively.

It is expected that reductions in the size of the tooth tip (either through a reduction of the tooth tip thickness or an increase in the slot opening size) would produce a greater degree of error in the estimation results due to an increased level of saturation in the tooth tip.

Section 6.3 discusses the results obtained for the 'Actuator' motor, section 6.4 discusses the approximate model of the 'Kart' motor and section 6.5 discusses the

Machine Version	Slot Opening Ratio $\frac{s_i}{s}$	Tooth Tip Ratio $\frac{t_i}{t}$
01	11/11	6/6
02	11/11	5/6
03	11/11	4/6
04	11/11	3/6
05	9/11	6/6
06	9/11	5/6
07	9/11	4/6
08	9/11	3/6
09	7/11	6/6
10	7/11	5/6
11	7/11	4/6
12	7/11	3/6
13	5/11	6/6
14	5/11	5/6
15	5/11	4/6
16	5/11	3/6

Table 6.1: Machine Alterations for Slotting Analysis

'Traction' motor.

6.3 The 'Actuator' Motor

The model of the structure of the 'Actuator' motor used in this analysis is shown in figure 6.2. The dimensions of the slot opening, s, and tooth tip thickness, t, are

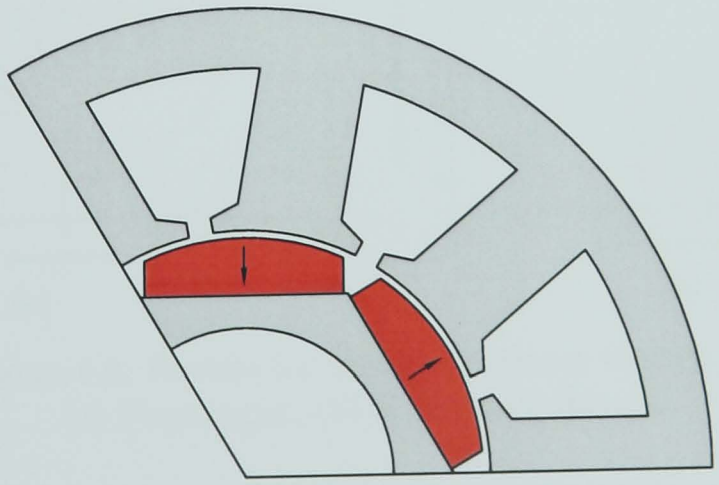

Figure 6.2: Model of 'Actuator' Motor

2.75 mm and 1.5 mm respectively. Combining these with table 6.1 results in the simulation set shown in table 6.2. For each slot opening size, every tooth tip size is

Machine Version	Slot Opening Size (mm)	Tooth Tip Thickness (mm)
01	2.75	1.50
02	2.75	1.25
03	2.75	1.00
04	2.75	0.75
05	2.25	1.50
06	2.25	1.25
07	2.25	1.00
08	2.25	0.75
09	1.75	1.50
10	1.75	1.25
11	1.75	1.00
12	1.75	0.75
13	1.25	1.50
14	1.25	1.25
15	1.25	1.00
16	1.25	0.75

Table 6.2: 'Actuator' Motor Alterations for Slotting Analysis

analysed and thus the trends can be properly assessed.

Figure 6.3 shows the results of the finite element analysis of the original machine. It can be seen that the segmented approach to modelling produces results that are

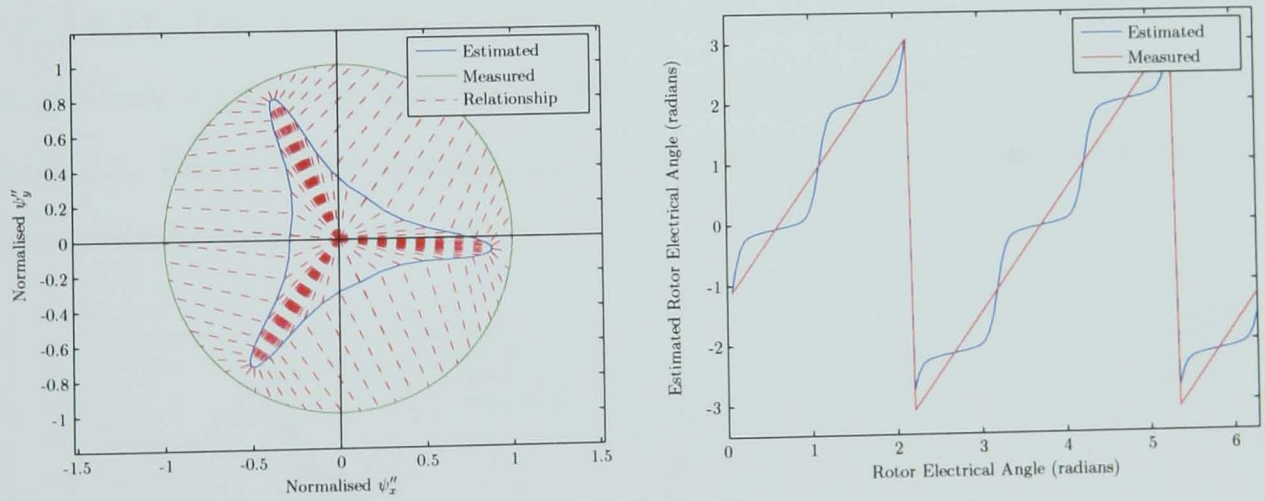

(a) (b)

Figure 6.3: Results for 'Actuator' Motor Version 01
(a) Fingerprint, (b) Estimation Results

identical to those produced by the full model. Figures 6.4–6.6 show the effect of reducing the size of the tooth tip whilst maintaining a constant slot opening size. It can be clearly seen that the size of the tooth tip has a significant effect on the magnitude of the distorting components. There is also clearly a level below which

the distorting component is larger than the principal saliency. At this point, it is difficult to identify the rotor position.

The results from the original machine are reproduced as figure 6.7. Figures 6.8–6.10 show the effect of reducing the size of the slot opening whilst maintaining the thickness of the tooth tip. It can be seen that the size reduction again produces an increased level of distortion; however, the effect is less significant than that of the tooth tip thickness.

The results of the remaining slot opening configurations are included in Appendix B. Figure 6.11 shows a surface plot that summarises the results of the complete analysis. The results with a tooth tip thickness of 0.75 mm have been omitted as the error with this thickness is too large to be meaningful.

6.4 The 'Kart' Motor

The model of the structure of the 'Kart' motor used in this analysis is shown in figure 6.12. The dimensions of the slot opening, s, and tooth tip thickness, t, are both 2 mm. Combining these with table 6.1 results in the simulation set shown in table 6.3. For each slot opening size, every tooth tip size is assessed and thus the trends can be properly assessed.

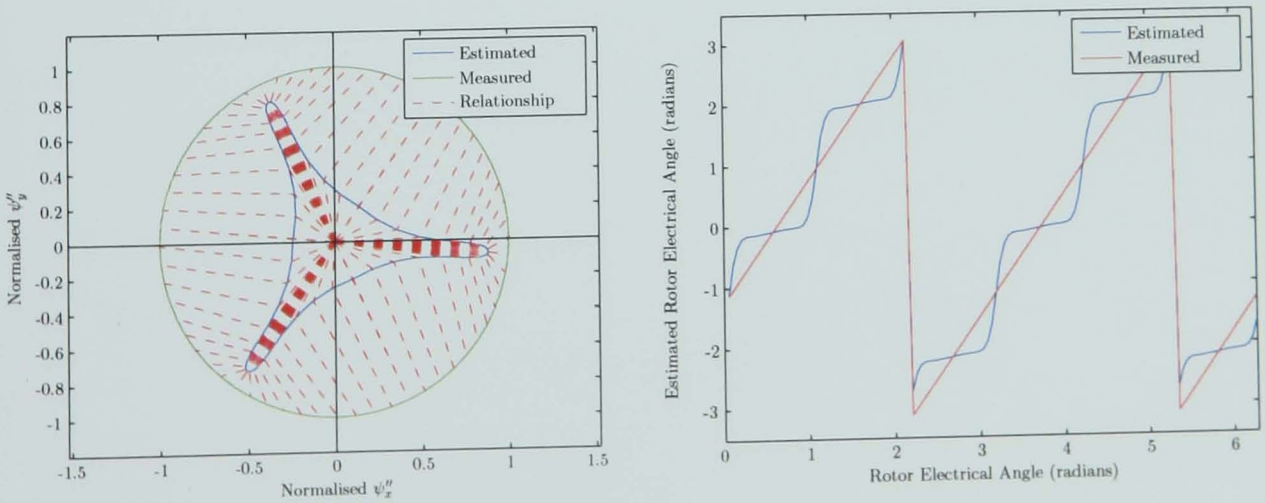

(a) (b)

Figure 6.4: Results for 'Actuator' Motor Version 02
(a) Fingerprint, (b) Estimation Results

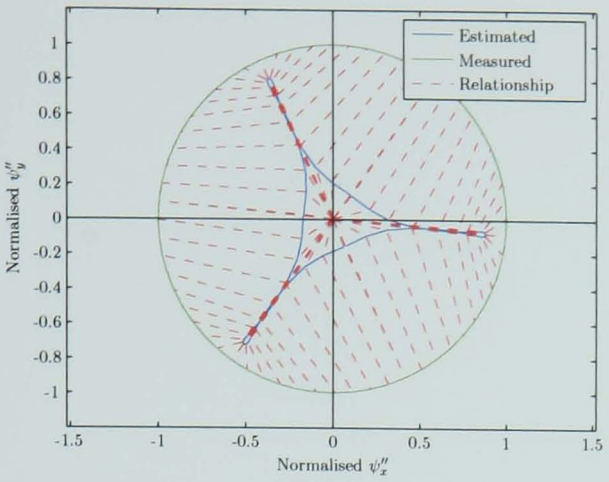

(a)

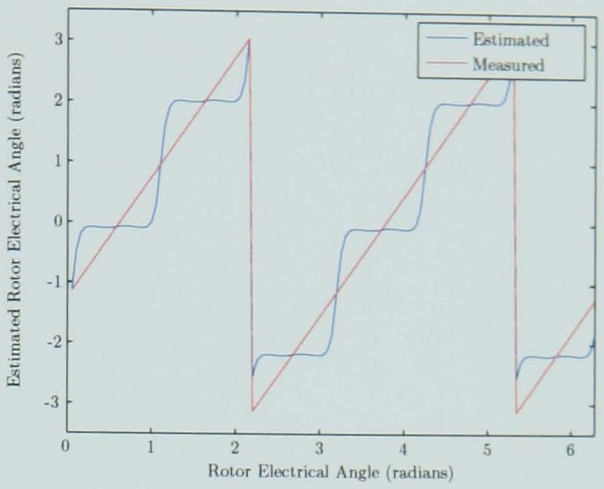

(b)

Figure 6.5: Results for 'Actuator' Motor Version 03
(a) Fingerprint, (b) Estimation Results

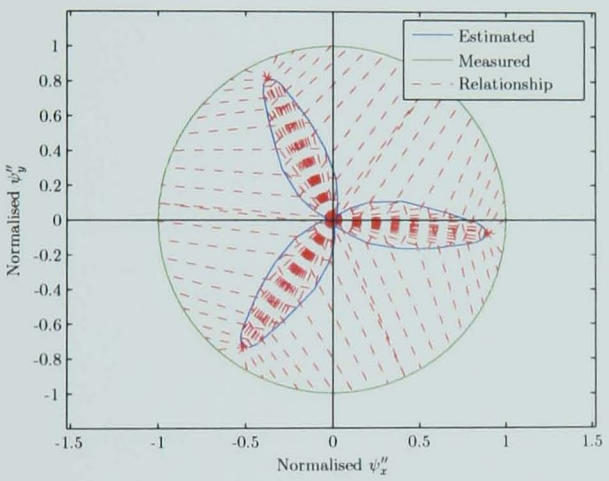

(a)

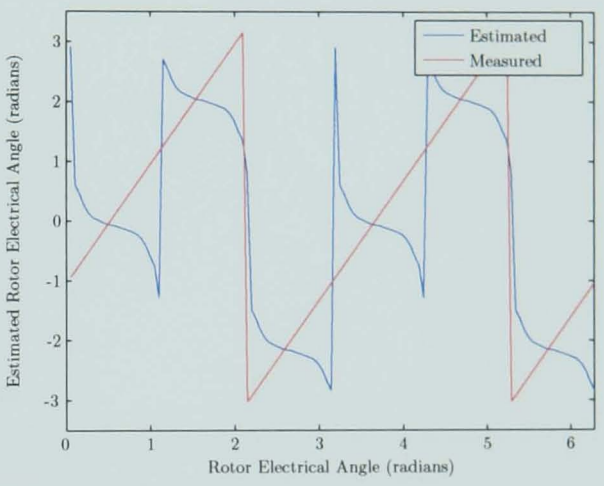

(b)

Figure 6.6: Results for 'Actuator' Motor Version 04
(a) Fingerprint, (b) Estimation Results

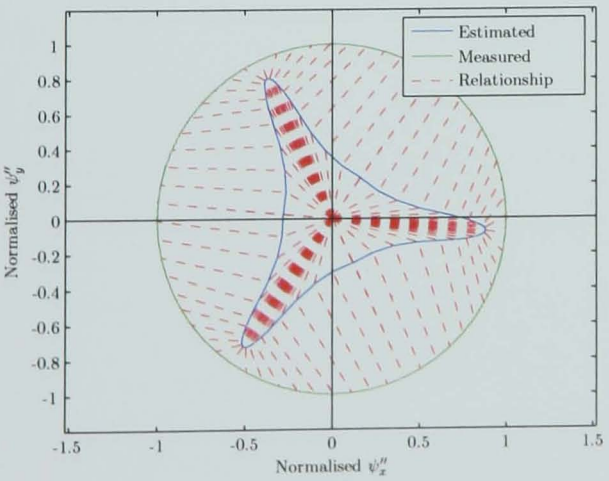

(a)

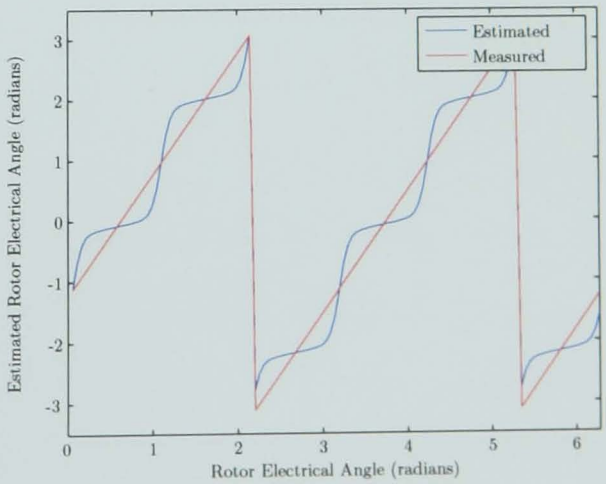

(b)

Figure 6.7: Results for 'Actuator' Motor Version 01
(a) Fingerprint, (b) Estimation Results

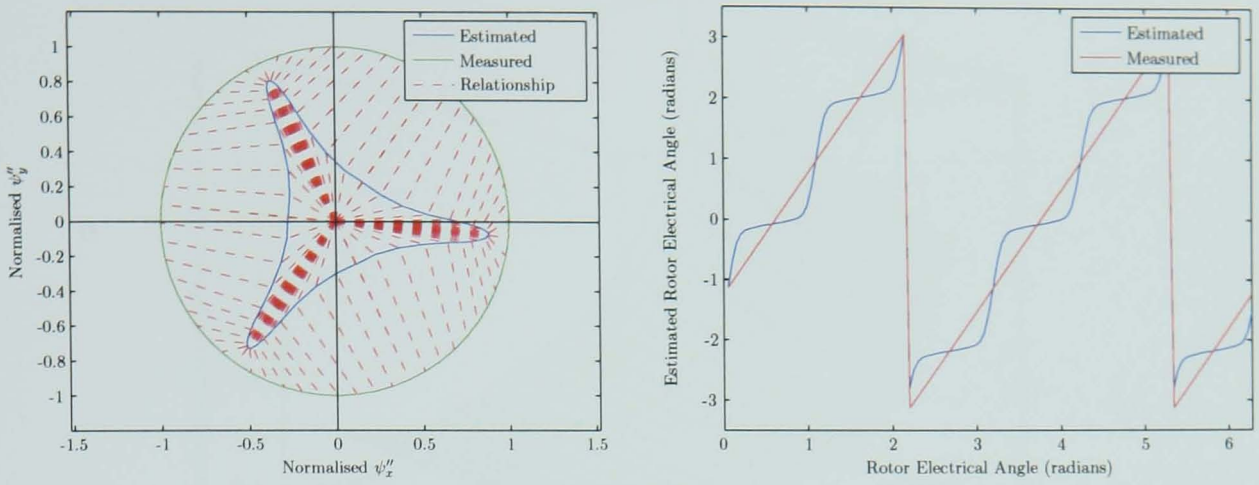

(a) (b)

Figure 6.8: Results for 'Actuator' Motor Version 05
(a) Fingerprint, (b) Estimation Results

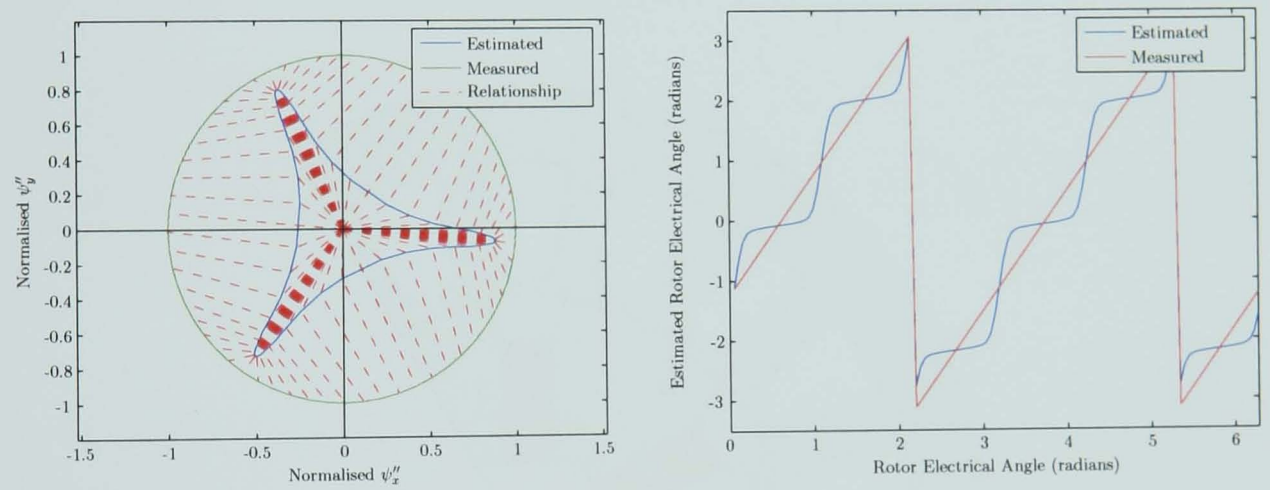

(a) (b)

Figure 6.9: Results for 'Actuator' Motor Version 09
(a) Fingerprint, (b) Estimation Results

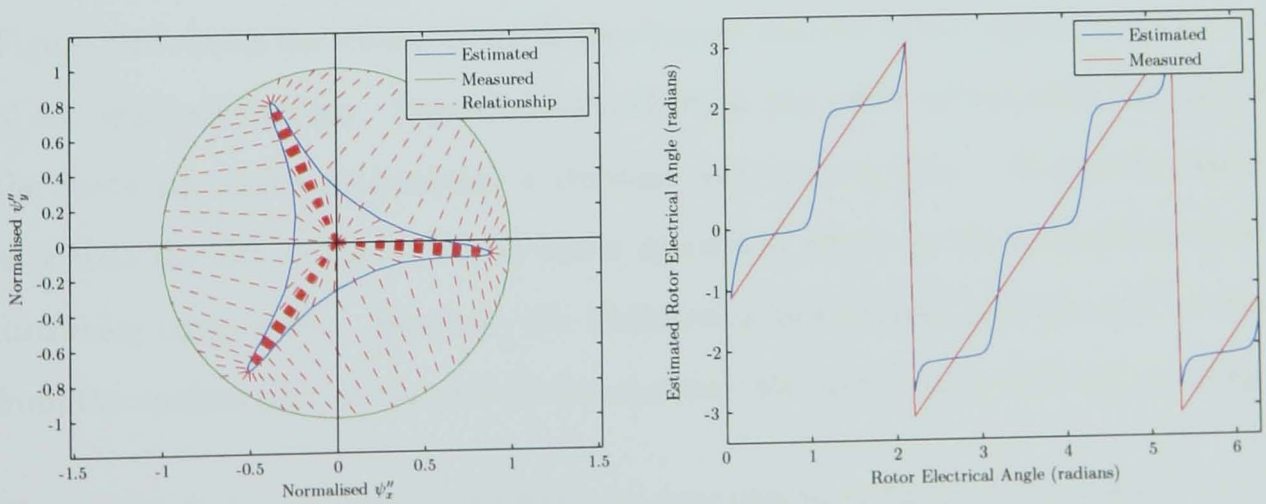

(a) (b)

Figure 6.10: Results for 'Actuator' Motor Version 13
(a) Fingerprint, (b) Estimation Results

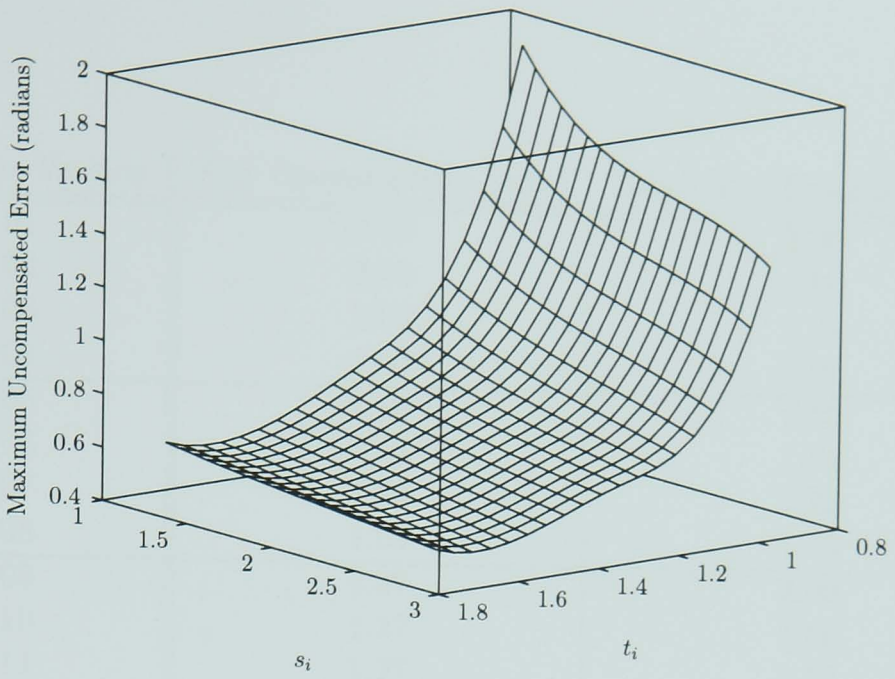

Figure 6.11: Error Surface for 'Actuator' Motor

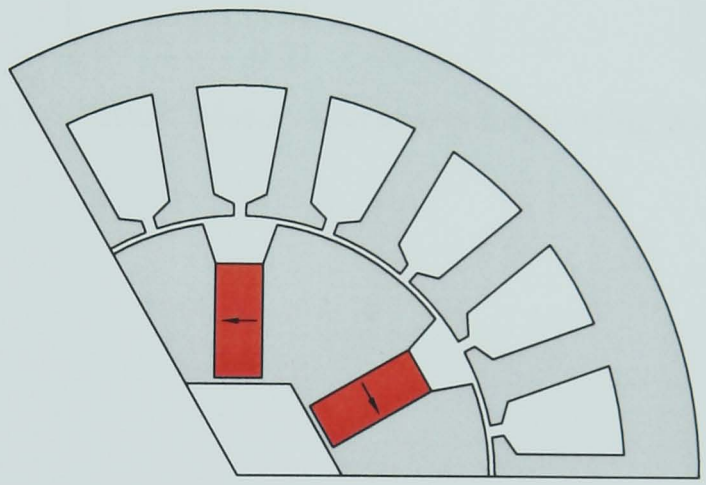

Figure 6.12: Model of 'Kart' Motor

Figure 6.13 shows the results of the finite element analysis of the approximate model of the original machine. Figures 6.14–6.16 show the effect of reducing the size of the tooth tip whilst maintaining a constant slot opening size. It can be clearly seen that the size of the tooth tip has a significant effect on the magnitude of the distorting components. However, the variation is inconsistent and (as will be seen from the surface plot at the end of this section), the form varies with slot opening.

The results from the original machine are reproduced as figure 6.17. Figures 6.18–6.20 show the effect of reducing the size of the slot opening whilst maintaining the thickness of the tooth tip. It can be seen that the size reduction produces a reduction in the level of distortion for the original tooth tip size.

Machine Version	Slot Opening Size (mm)	Tooth Tip Thickness (mm)
01	2.00	2.00
02	2.00	1.66
03	2.00	1.33
04	2.00	1.00
05	1.64	2.00
06	1.64	1.66
07	1.64	1.33
08	1.64	1.00
09	1.27	2.00
10	1.27	1.66
11	1.27	1.33
12	1.27	1.00
13	0.91	2.00
14	0.91	1.66
15	0.91	1.33
16	0.91	1.00

Table 6.3: 'Kart' Motor Alterations for Slotting Analysis

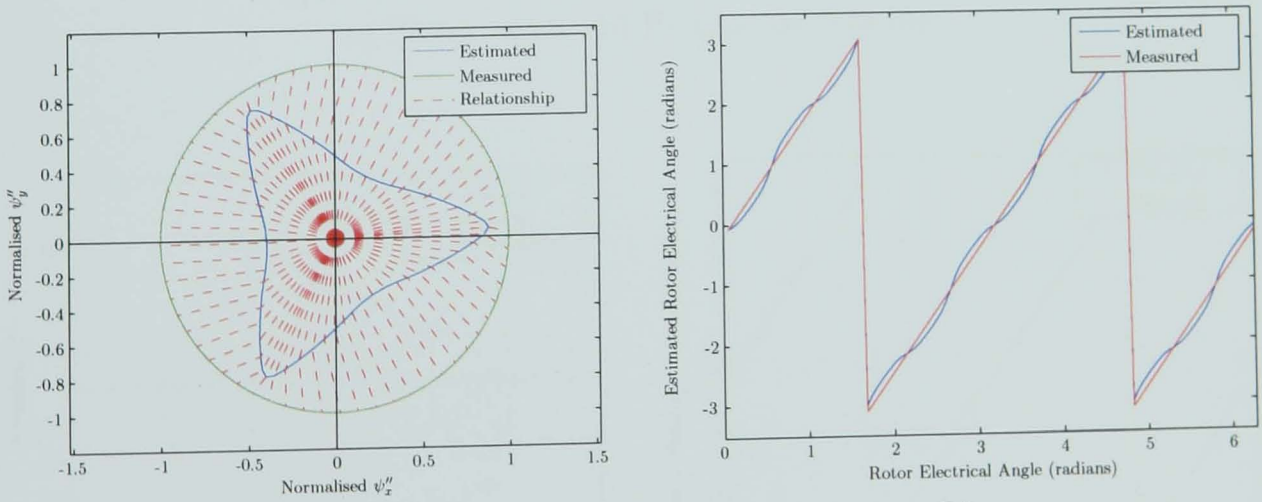

(a) (b)

Figure 6.13: Results for 'Kart' Motor Version 01
(a) Fingerprint, (b) Estimation Results

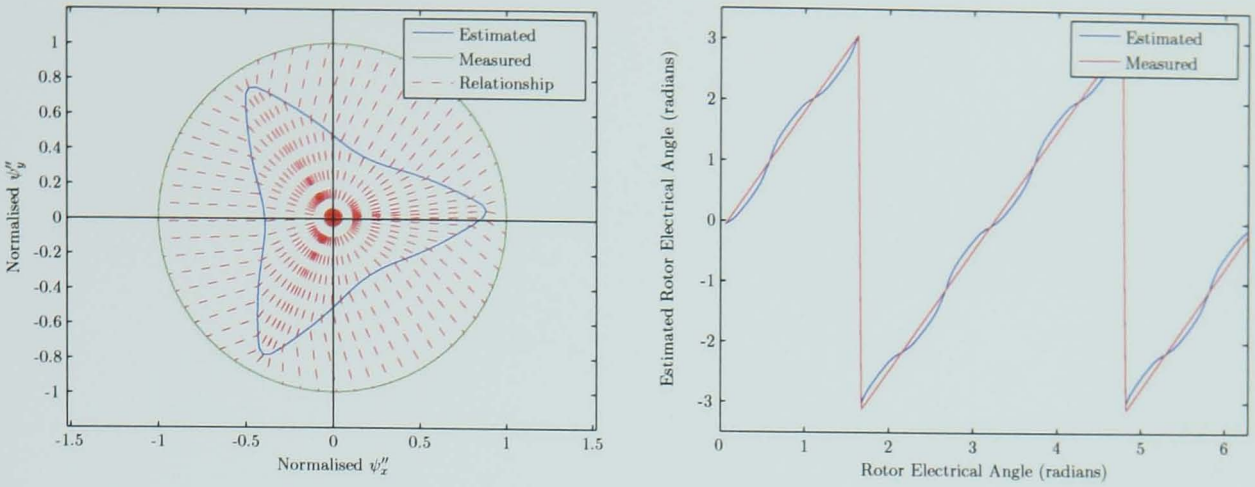

(a) (b)

Figure 6.14: Results for 'Kart' Motor Version 02
(a) Fingerprint, (b) Estimation Results

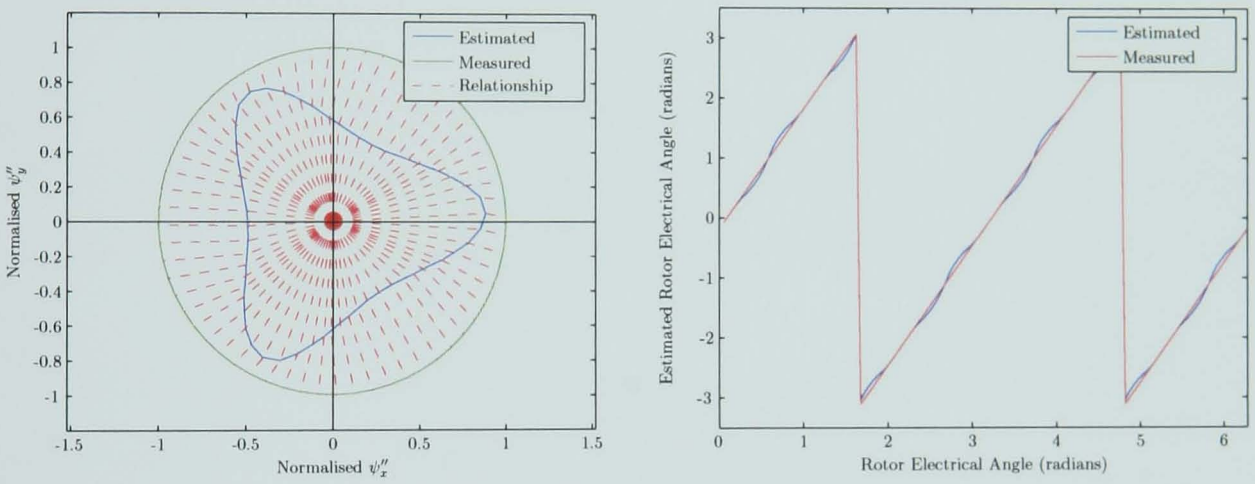

(a) (b)

Figure 6.15: Results for 'Kart' Motor Version 03
(a) Fingerprint, (b) Estimation Results

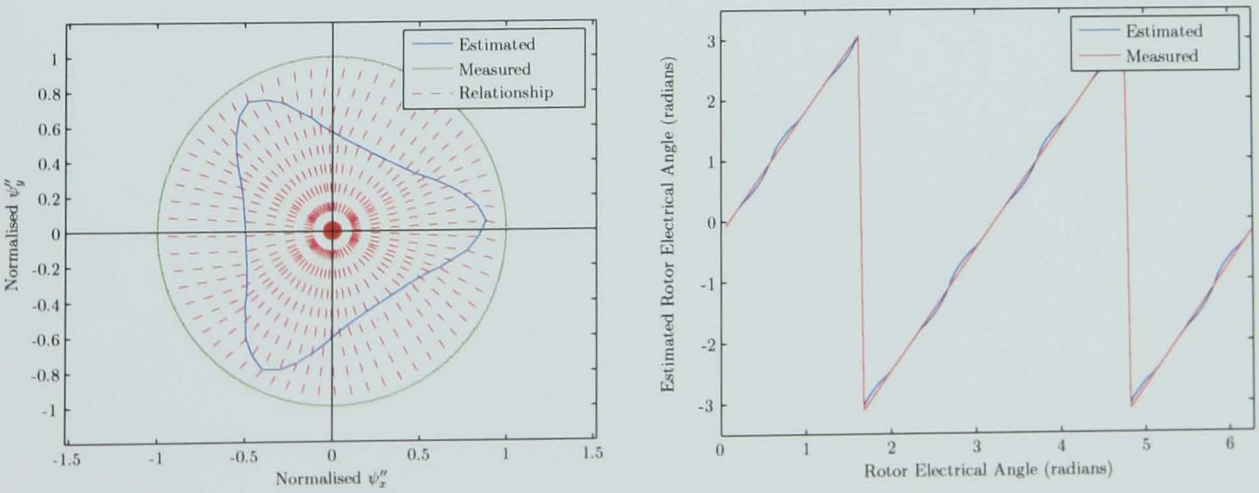

(a) (b)

Figure 6.16: Results for 'Kart' Motor Version 04
(a) Fingerprint, (b) Estimation Results

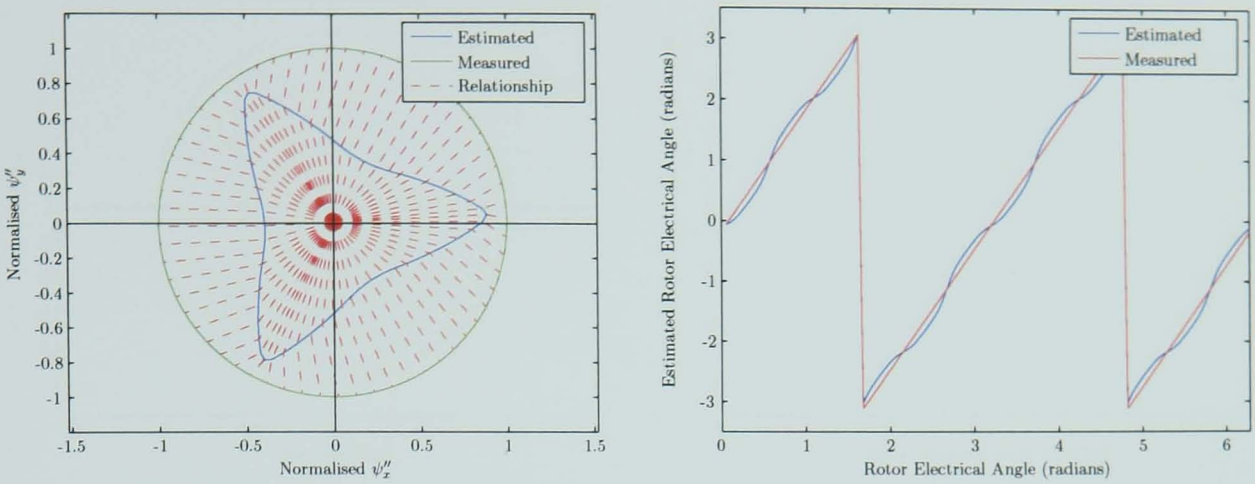

(a) (b)

Figure 6.17: Results for 'Kart' Motor Version 01
(a) Fingerprint, (b) Estimation Results

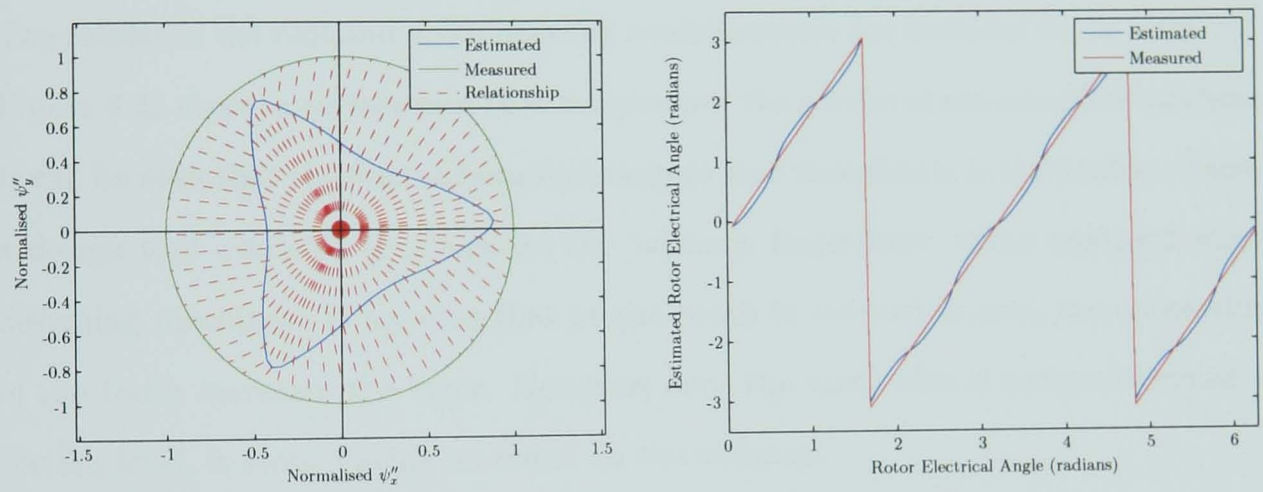

(a) (b)

Figure 6.18: Results for 'Kart' Motor Version 05
(a) Fingerprint, (b) Estimation Results

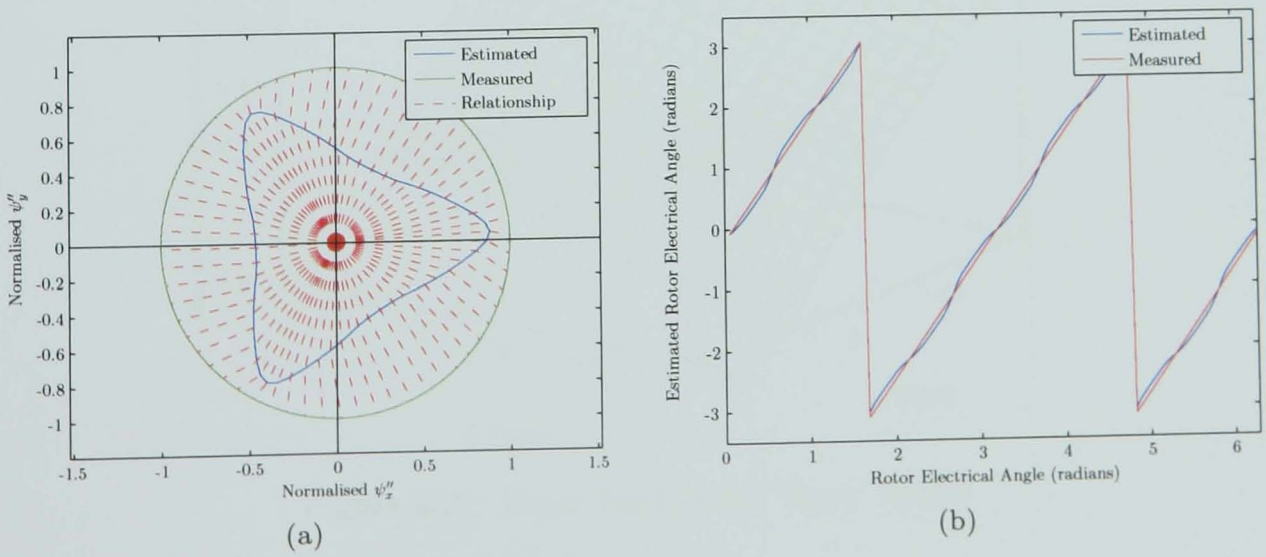

(a) (b)

Figure 6.19: Results for 'Kart' Motor Version 09
(a) Fingerprint, (b) Estimation Results

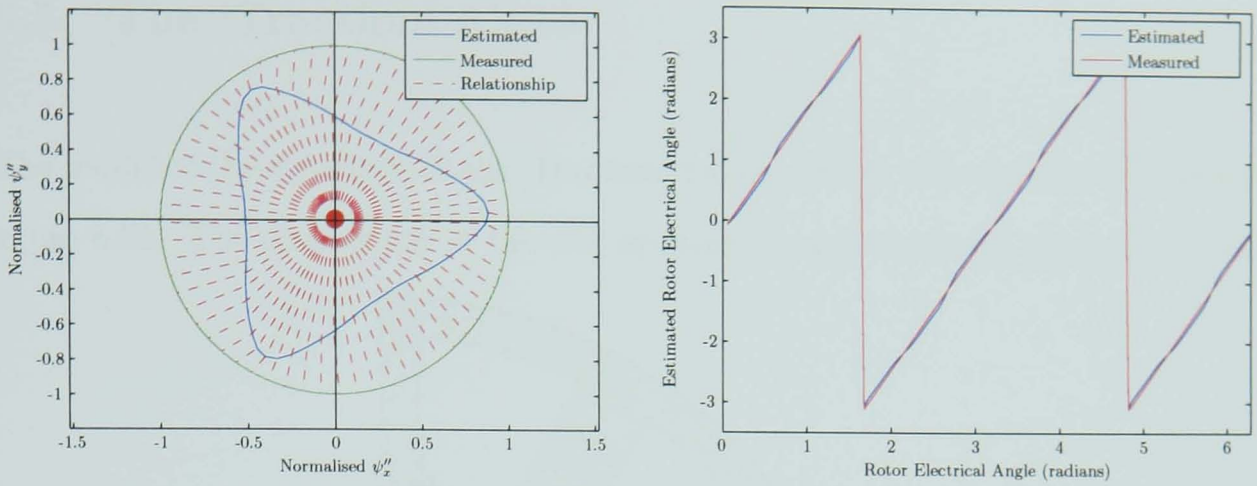

(a) (b)

Figure 6.20: Results for 'Kart' Motor Version 13
(a) Fingerprint, (b) Estimation Results

The results of the remaining slot opening configurations are included in Appendix C. Figure 6.21 shows a surface plot that summarises the results of the complete analysis. It can be seen that the fluctuations are complex and therefore it is invaluable to have a design tool available that enables the 'saliency fingerprint' to be analysed when designing machines. It appears that as the tooth is reduced in size, the saturation of the tooth increases the error. However, once the tooth size is reduced beyond a certain level, it stops having an effect on the saliency.

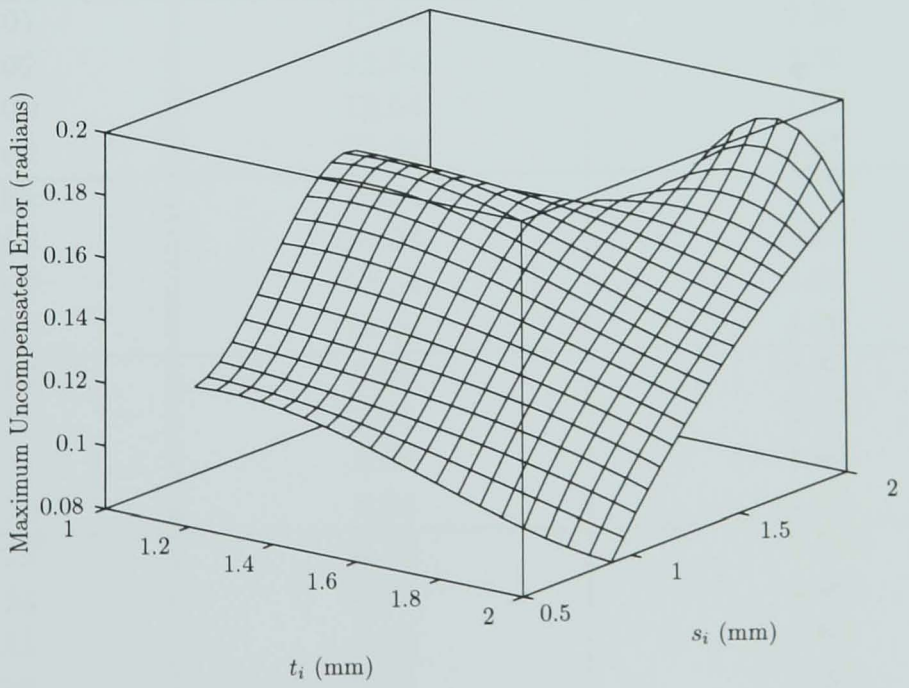

Figure 6.21: Error Surface for 'Kart' Motor

6.5 The 'Traction' Motor

The model of the structure of the 'Traction' motor used in this analysis is shown in figure 6.22. The dimensions of the slot opening, s, and tooth tip thickness, t, are

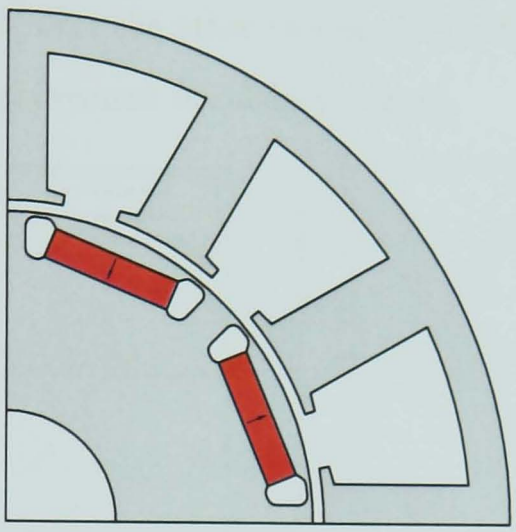

Figure 6.22: Model of 'Traction' Motor

12.64 mm and 2.3 mm respectively. Combining these with table 6.1 results in the simulation set shown in table 6.4. For each slot opening size, every tooth tip size is assessed and thus the trends can be properly assessed.

Machine Version	Slot Opening Size (mm)	Tooth Tip Thickness (mm)
01	12.64	2.30
02	12.64	2.00
03	12.64	1.60
04	12.64	1.20
05	10.34	2.30
06	10.34	2.00
07	10.34	1.60
08	10.34	1.20
09	8.04	2.30
10	8.04	2.00
11	8.04	1.60
12	8.04	1.20
13	5.75	2.30
14	5.75	2.00
15	5.75	1.60
16	5.75	1.20

Table 6.4: 'Traction' Motor Alterations for Slotting Analysis

Figure 6.23 shows the results of the finite element analysis of the original machine.

It can be seen that the segmented approach to modelling produces results that are identical to those produced by the full model. Figures 6.24–6.26 show the effect of reducing the size of the tooth tip whilst maintaining a constant slot opening size. It can be seen that the size of the tooth tip has little effect on the magnitude of the distorting components. Unlike the other two machines, the reduction in tooth tip size produces a small improvement in saliency quality.

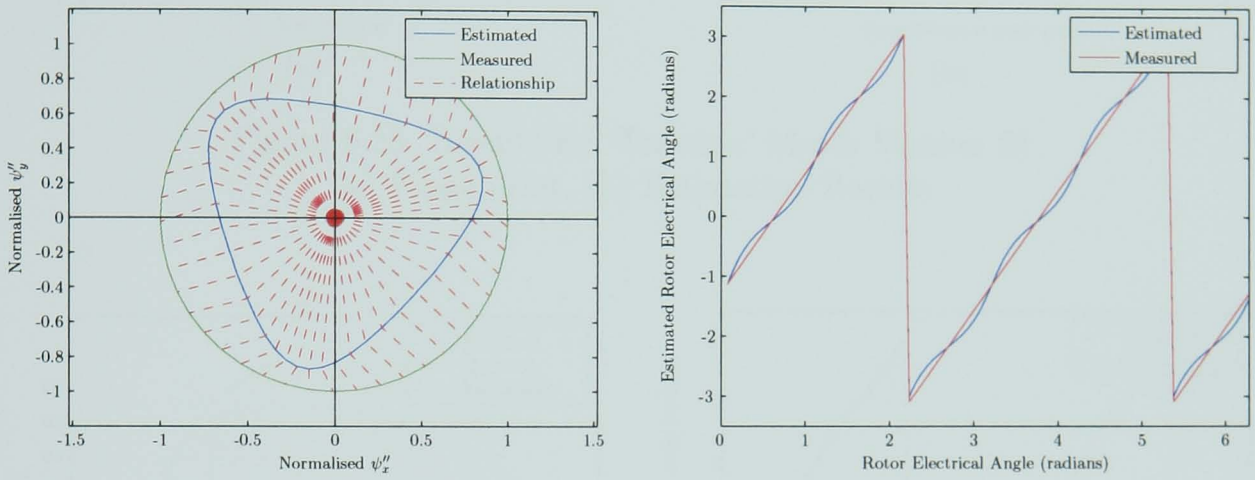

(a) (b)

Figure 6.23: Results for 'Traction' Motor Version 01
(a) Fingerprint, (b) Estimation Results

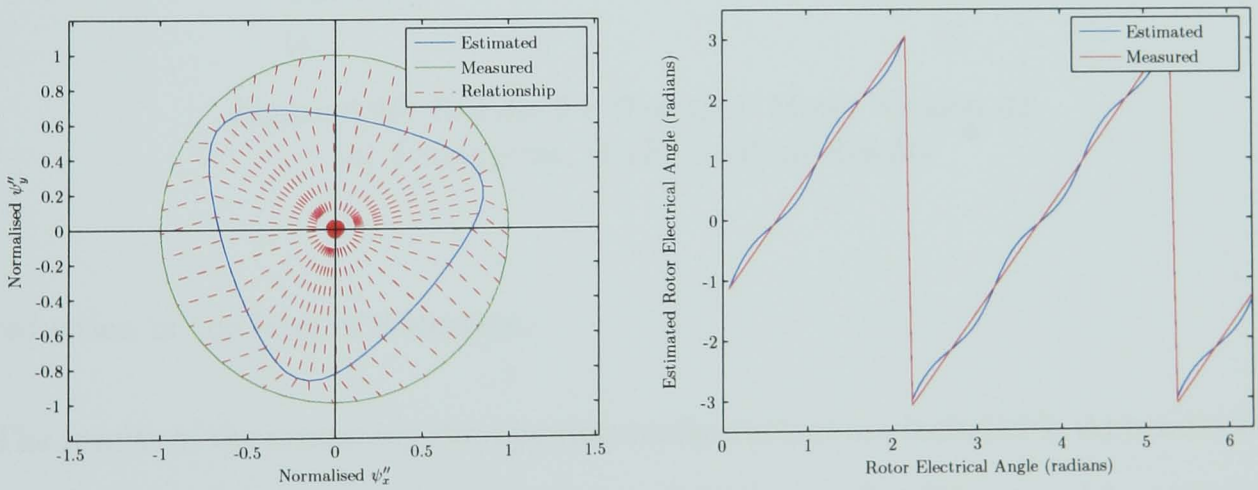

(a) (b)

Figure 6.24: Results for 'Traction' Motor Version 02
(a) Fingerprint, (b) Estimation Results

The results from the original machine are reproduced as figure 6.27. Figures 6.28–6.30 show the effect of reducing the size of the slot opening whilst maintaining the thickness of the tooth tip. It can be seen that the size reduction again produces a

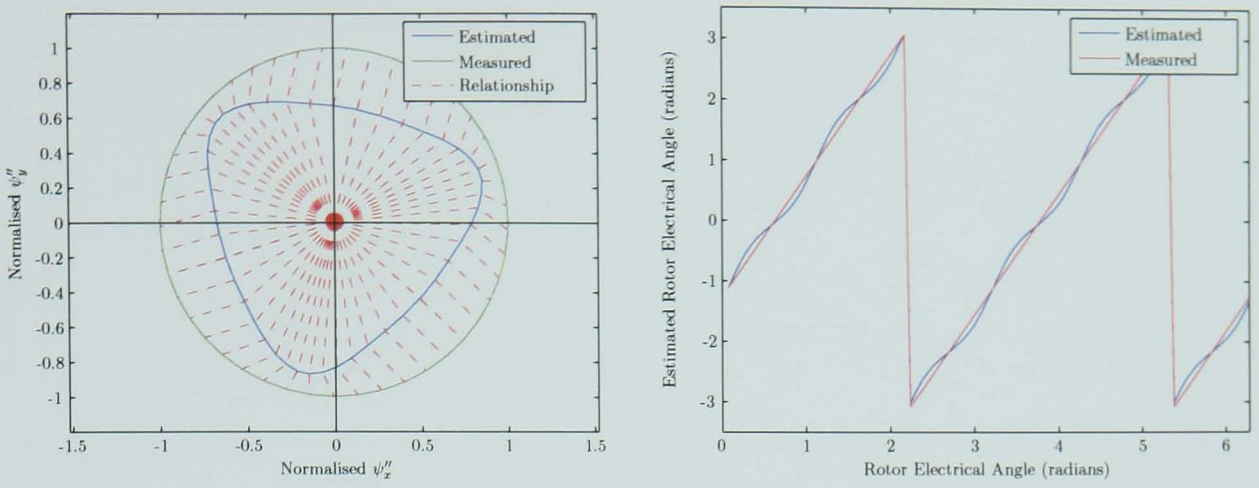

(a) (b)

Figure 6.25: Results for 'Traction' Motor Version 03
(a) Fingerprint, (b) Estimation Results

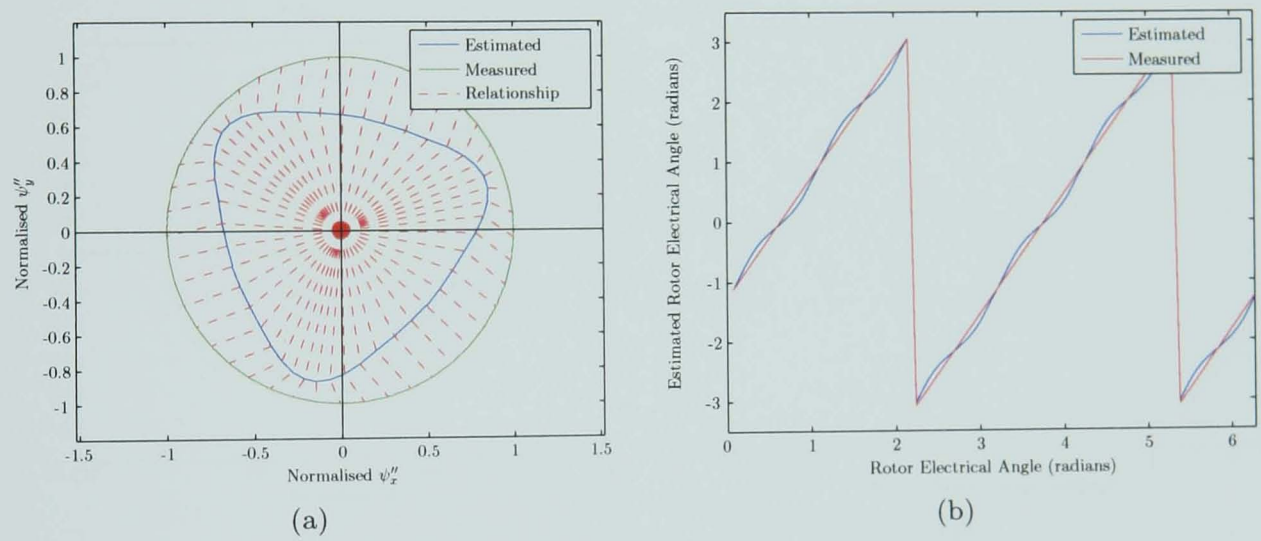

(a) (b)

Figure 6.26: Results for 'Traction' Motor Version 04
(a) Fingerprint, (b) Estimation Results

reduction in the level of distortion.

The results of the remaining slot opening configurations are included in Appendix D. Figure 6.31 shows a surface plot that summarises the results of the complete analysis. The effect of the slot shape variation on the saliency distortion is considerably less than with the other two machines. This is likely to be due to the increased size of the air gap[1], which reduces the sensitivity of the magnetic circuit to variations in the stator structure.

[1]For the 'Traction' motor, the ratio of air gap to stator outer diameter is $\approx \frac{1}{46}$, whilst for the other two motors it is $\approx \frac{1}{64}$.

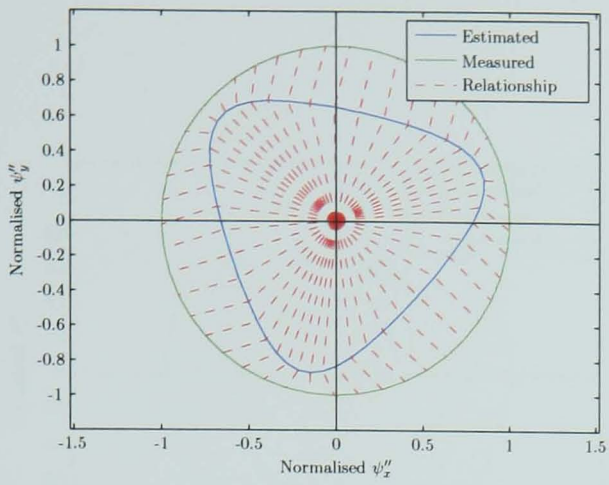

(a)

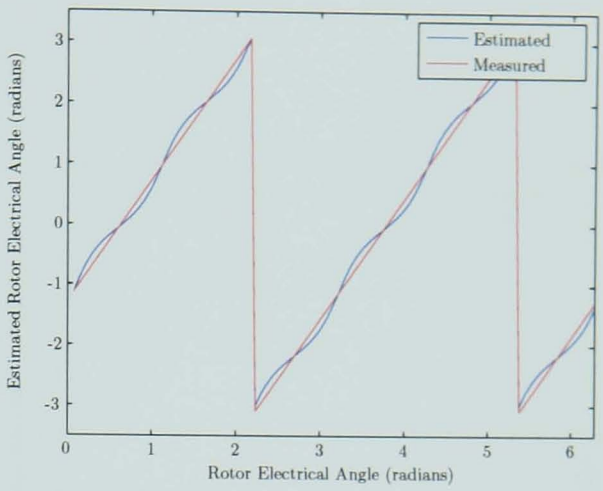

(b)

Figure 6.27: Results for 'Traction' Motor Version 01
(a) Fingerprint, (b) Estimation Results

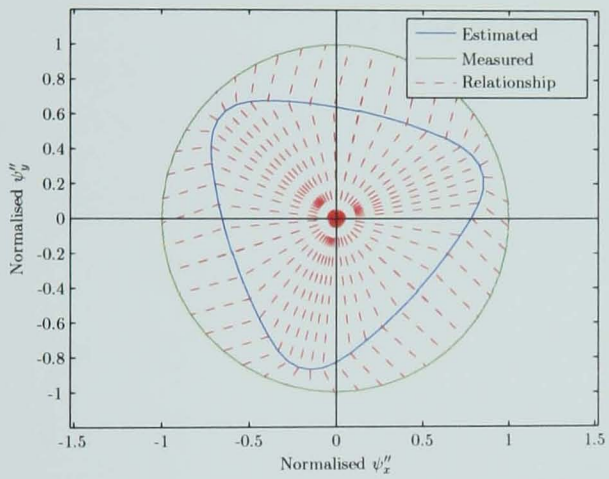

(a)

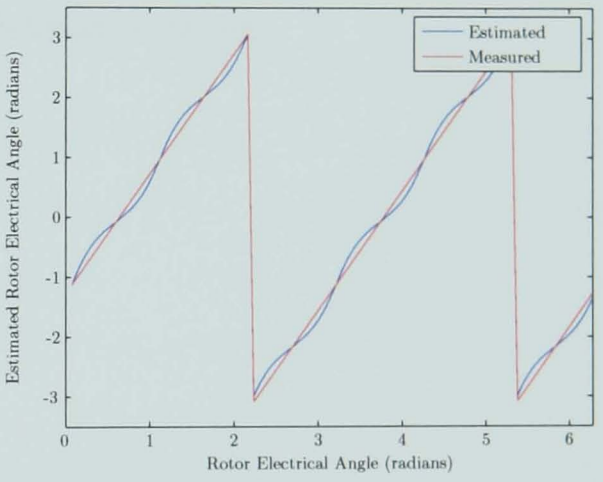

(b)

Figure 6.28: Results for 'Traction' Motor Version 05
(a) Fingerprint, (b) Estimation Results

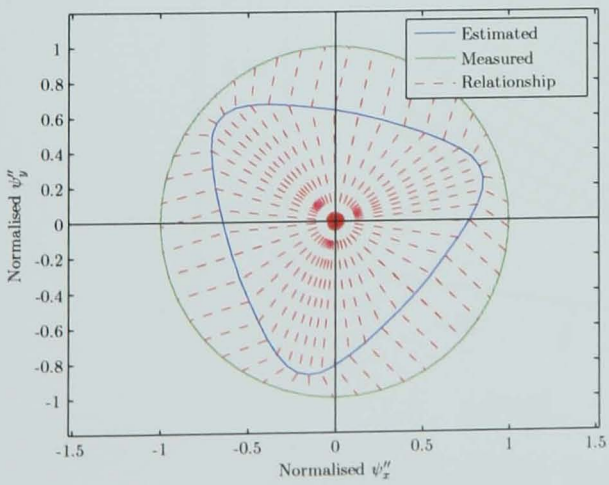

(a)

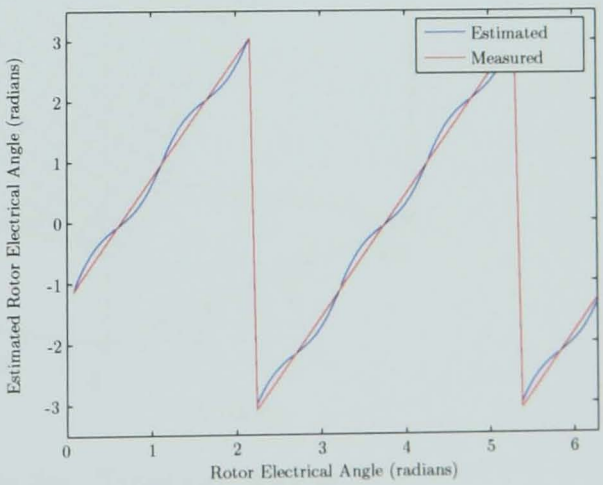

(b)

Figure 6.29: Results for 'Traction' Motor Version 09
(a) Fingerprint, (b) Estimation Results

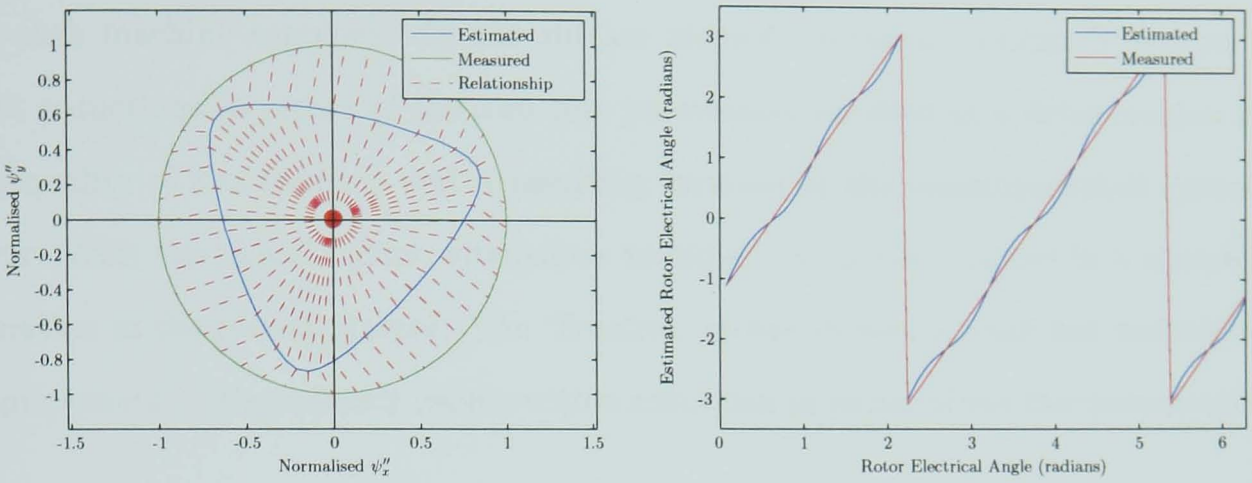

(a) (b)

Figure 6.30: Results for 'Traction' Motor Version 13
(a) Fingerprint, (b) Estimation Results

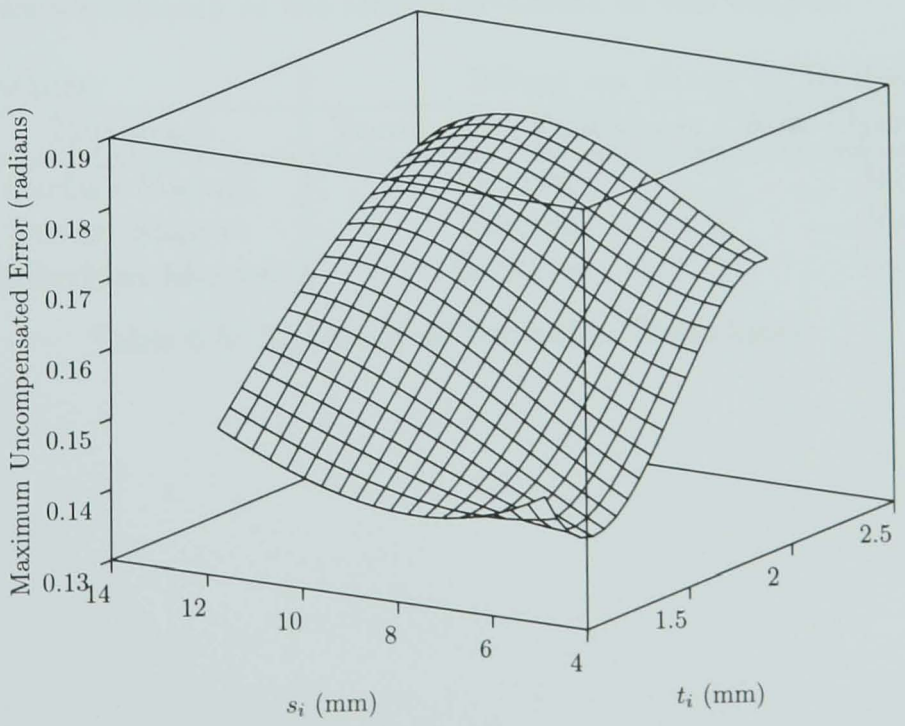

Figure 6.31: Error Surface for 'Traction' Motor

6.6 Conclusions

It has been shown in this chapter that the effects of slot shape variations are different for each machine topology. In the surface magnet 'Actuator' motor, it was seen that reductions in either of the two test parameters resulted in a deterioration in the quality of the saliency and a resulting increase in the uncompensated system error. With the 'Kart' motor, alterations to either parameter resulted in a complex variation in the resulting error. The 'Traction' motor showed a small but noticeable improvement in the saliency profile with a reduction in either of the two parameters.

It is clear that the effect of tooth tip size variation is considerably more complex than anticipated and that there is no general principle for optimisation of machine structure for zero speed sensorless position estimation. Many factors (including rotor structure and size of air gap as well as slot shape) will affect the form of the saliency. It is therefore invaluable to have a design tool available that enables analysis of the 'saliency fingerprint' and the effects of variations in structural dimensions for a given machine design prior to construction.

Table 6.5 shows a summary of the results presented in this chapter.

Machine		**Effect on Error of Reducing**	
Name	**Topology**	**Tooth Tip Thickness**	**Slot Opening Width**
'Actuator'	Surface Magnet	Increase	Increase
'Kart'	Buried Magnet	Varying	Varying
'Traction'	Embedded Magnet	Decrease	Decrease

Table 6.5: Summary of Sensorless Techniques

Chapter 7

Full System Implementation

7.1 Introduction

In order to fully validate the sensorless strategy documented in this thesis, an experimental platform has been developed. Section 7.2 provides details of the platform and the interface with the other components of the system. Section 7.3 discusses the practical implementation of the uncompensated system and presents results for all three test machines. Section 7.4 provides a similar discussion and set of results for the compensated system.

7.2 Implementation of the Final Test Rig

The test platform is based on the Spectrum Digital DSP starter kit for the Texas Instruments TMS320C6713 DSP in combination with a Xilinx Spartan XC2S300E Field Programmable Gate Array (FPGA) development board and an interface board to provide interconnection and additional I/O capability.

7.2.1 Digital Signal Processor

The TMS320C6713 is a floating-point DSP operating at a clock speed of 225 MHz. The processor has limited built-in I/O capabilities, but includes an External Memory Interface (EMIF) that allows external digital circuitry to provide additional functionality. In the experimental platform detailed in this chapter, the DSP performs the generation of the sinusoidal injection signals as well as performing the demodulation of the captured outputs in order to derive the position of the rotor. A photo of the DSP starter kit (disconnected from the remainder of the platform) is shown in figure 7.1.

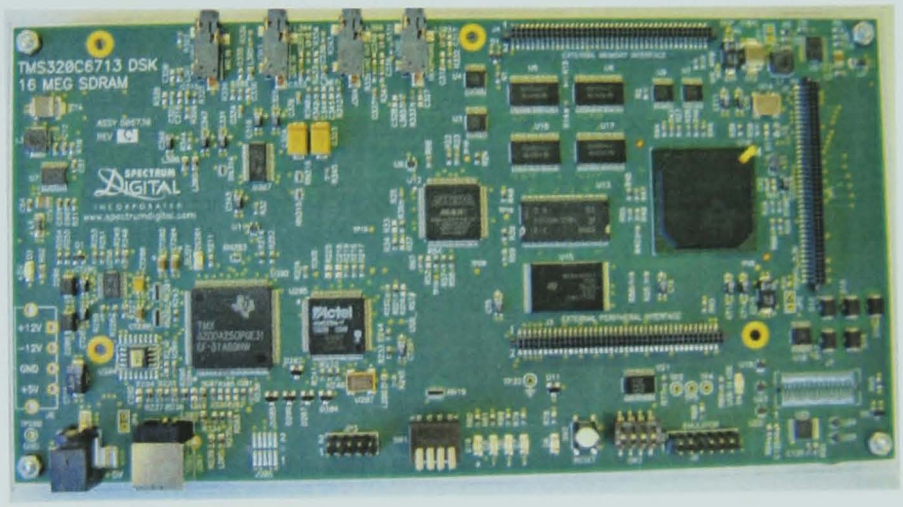

Figure 7.1: Digital Signal Processor Starter Kit

7.2.2 Interface Board

The interface used in the test platform is the Goodrich Control Systems generic controller board. This board provides interconnections between the DSP and FPGA and also provides external I/O functionality for the FPGA. This functionality includes ADCs (used for current sampling), Digital-to-Analogue Converters (DACs) (used for debugging and visualising results), isolated digital outputs (for connection to the inverter) and a Resolver-to-Digital Converter (for accuracy checking). A photograph of the controller board is shown in figure 7.2.

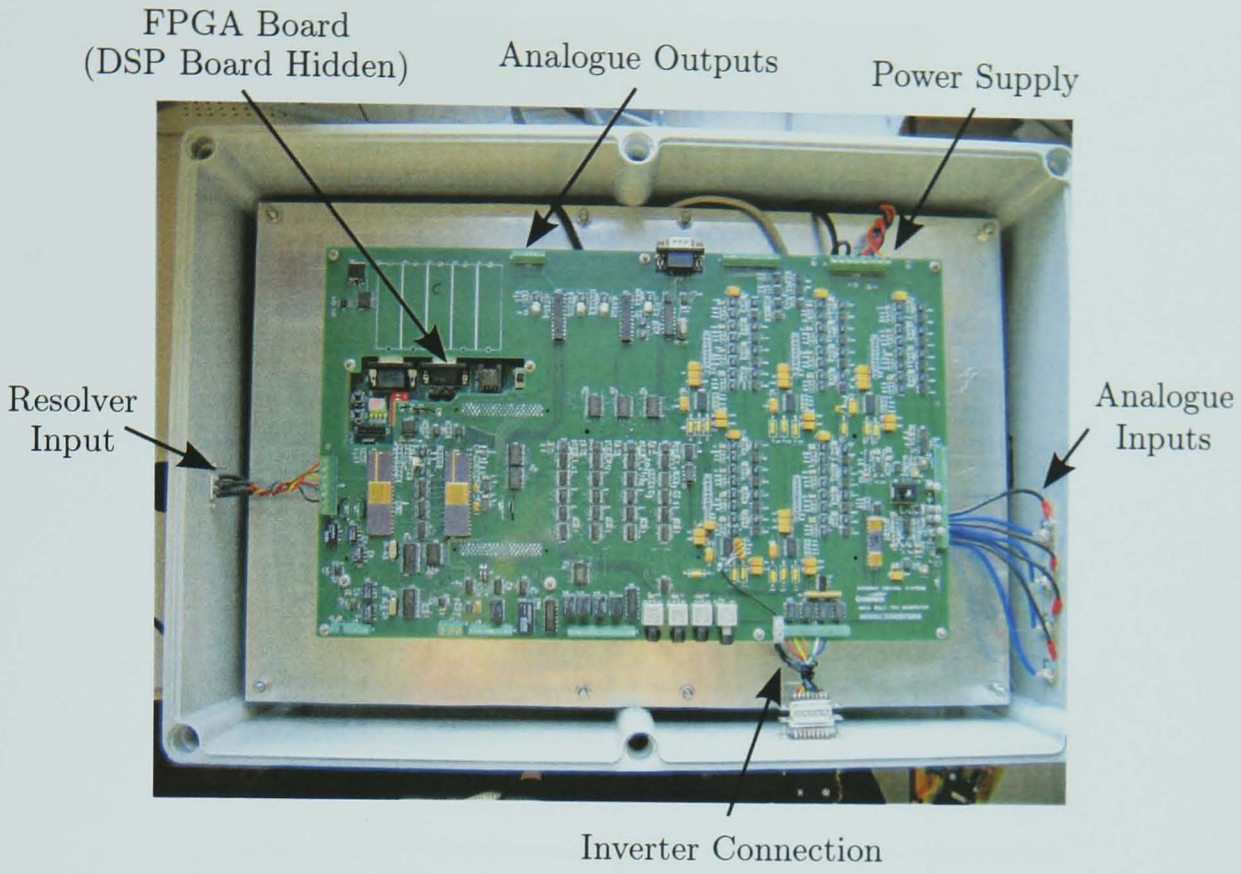

Figure 7.2: Interface Board

7.2.3 Field Programmable Gate Array

The FPGA (shown in figure 7.3) is used to provide 'glue logic' between the external I/O devices and also to generate PWM signals based on instructions from the DSP. The PWM generation is internally achieved using an up-down counter, three comparators and three dead-band generation units, all implemented using the Very High Speed Integrated Circuit Hardware Description Language (VHDL).

The comparators compare the output of the counter with a reference value provided by the DSP. This produces a PWM reference for the dead-band generators. The dead-band generators produce the controlling signals for the top and bottom switches of the inverter. The top switch is controlled by delaying the rising edge of the PWM reference and the bottom switch by delaying the rising edge of an inverted version of it. This principle is shown in figure 7.4.

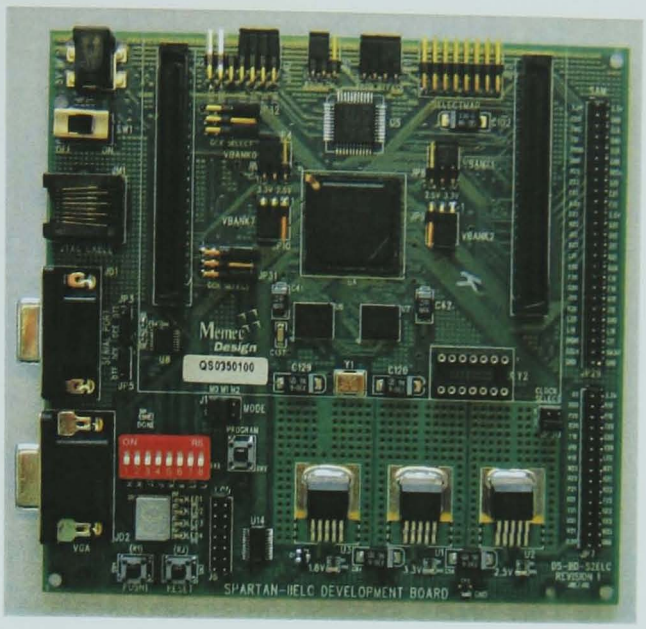

Figure 7.3: Field Programmable Gate Array Development Board

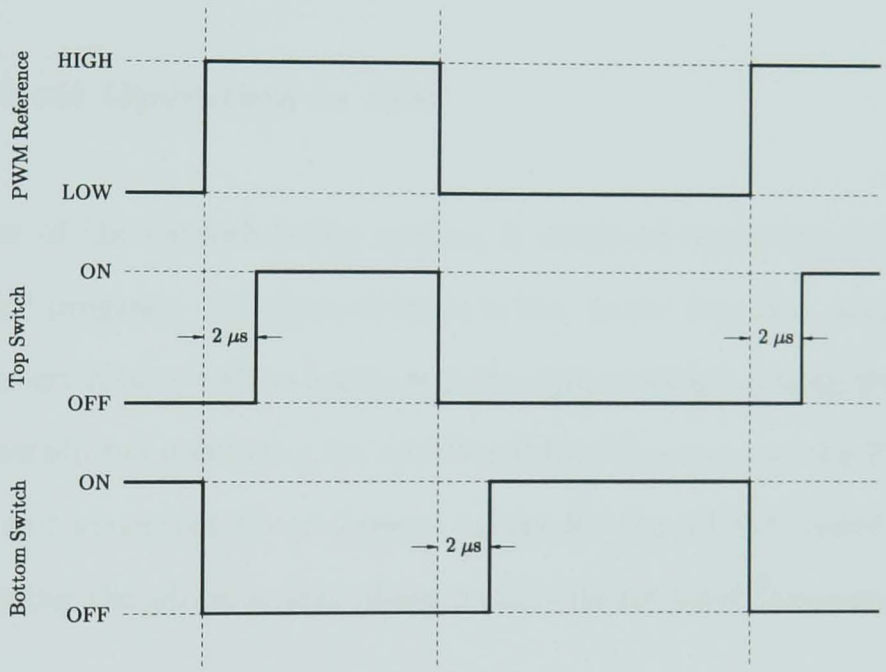

Figure 7.4: Operation of Dead-Band Generators

7.2.4 Other Components

In addition to the controller platform, the test system also includes a gate drive interface, CTs and an IPM. These components are identical to those discussed in chapter 4 and therefore the details have been omitted from this section. A block diagram of the complete system is shown in figure 7.5.

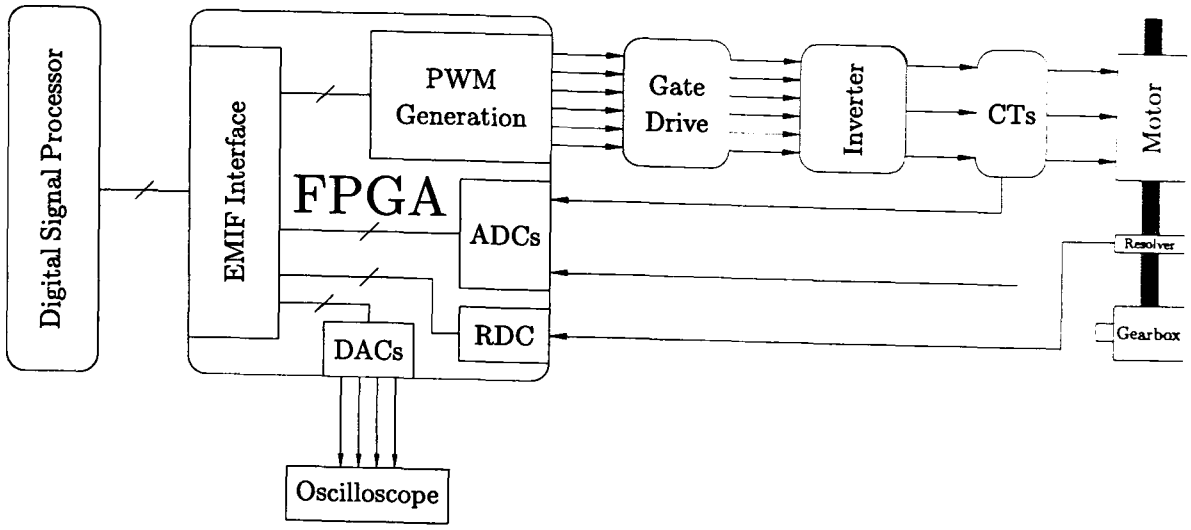

Figure 7.5: System Block Diagram

7.3 Implementation of Uncompensated System

7.3.1 Practical Operation in DSP

Implementation of the demodulation system is achieved using three main subroutines in the DSP program. The first of these is the 'main' function, which initialises variables and interrupts as well as setting up the communication with the FPGA and checking for operational conflicts. An additional function runs at the PWM switching frequency and generates the reference values for the FPGA based comparator as well as sampling the phase a and phase b currents for later processing.

The final primary subroutine in the system performs all of the processing of the captured currents necessary for position estimation. This involves a Clarke transform (to convert to the $\alpha\beta$ reference frame), a Park transform (to convert to the injection-synchronous reference frame), a synchronous reference frame high-pass filter, a second Park transform (to convert to the inverse injection-synchronous reference frame) and finally the angle calculation and polarity tracking. A rolling average is used in the inverse injection-synchronous reference frame to promote noise immunity. In addition, the i'' currents, the estimated electrical position and the measured electrical position (from the shaft-mounted resolver) are copied to the DACs on the interface board to enable visualisation of the results.

An execution flow diagram for the uncompensated system is shown in figure 7.6. The algorithm completes in under 40 μs.

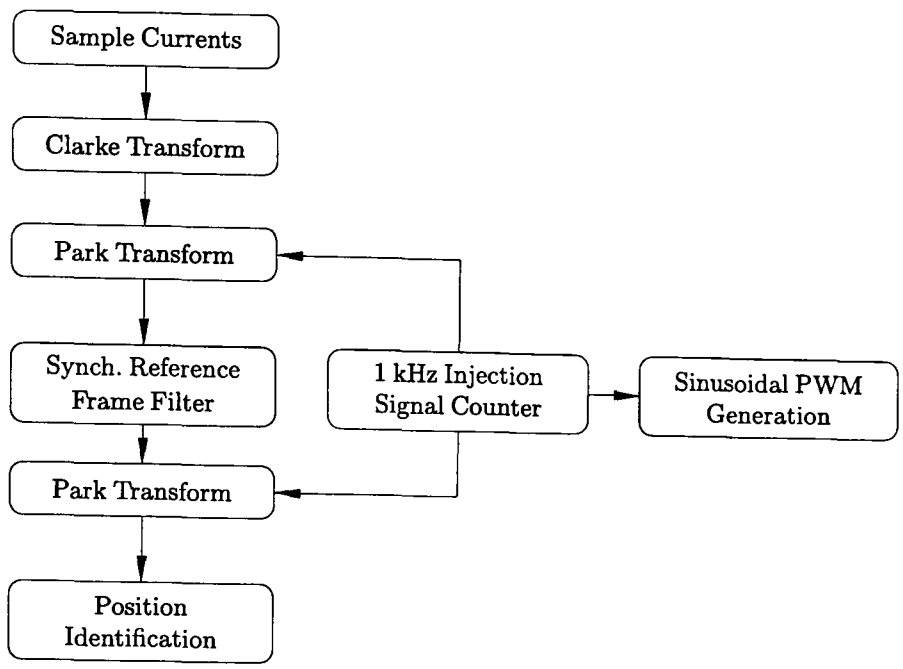

Figure 7.6: Execution Flow Diagram

7.3.2 Results for 'Actuator' Motor

The test procedure adopted was similar to that used in chapter 4. The controller board was used to generate the switching signals and to process the line currents. The results produced by the DSP were captured directly from the on-board memory by the DSP interface software. In addition, an oscilloscope (connected to the DACs on the controller board) was used to produce 'live' results with the shaft being manually rotated.

Figure 7.7 shows the captured 'saliency fingerprint' for the 'Actuator' motor using the final development system. As expected, the 'fingerprint' is of the same form as that seen in chapter 5. The uncompensated results are shown over several electrical cycles in figure 7.8[1]. The distortion in the estimated position can be clearly seen, thus confirming the need for compensation with this machine.

[1]No attempt has been made to align the resolver with the a axis for this system.

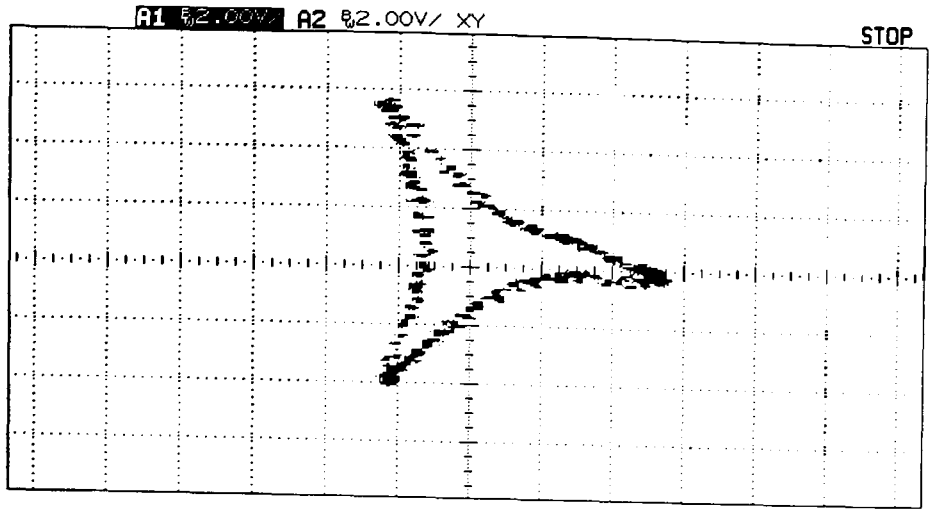

Figure 7.7: Captured 'Saliency Fingerprint' for 'Actuator' Motor

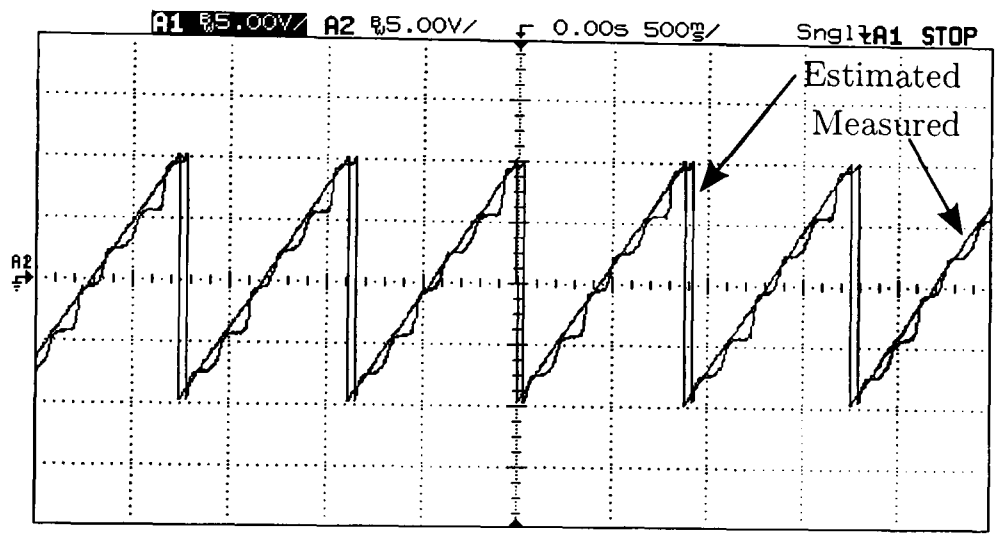

Figure 7.8: Captured Uncompensated Results for 'Actuator' Motor

7.3.3 Results for 'Kart' Motor

The same test procedure was used to analyse the operation of the system with the 'Kart' motor. Figure 7.9 shows the 'saliency fingerprint' produced by the controller board for a large sample of rotor positions. The shape of the 'fingerprint' matches that seen in chapter 5, again confirming the operation of the system. The final uncompensated angle estimation results are shown in figure 7.10[2]. The distortion of the estimated position can again be clearly seen and it is evident that compensation is required for this machine.

[2]The small fluctuations in the *measured* position are due to imperfections in the locking gearbox, which affect the uniformity of rotation required for oscilloscope capture.

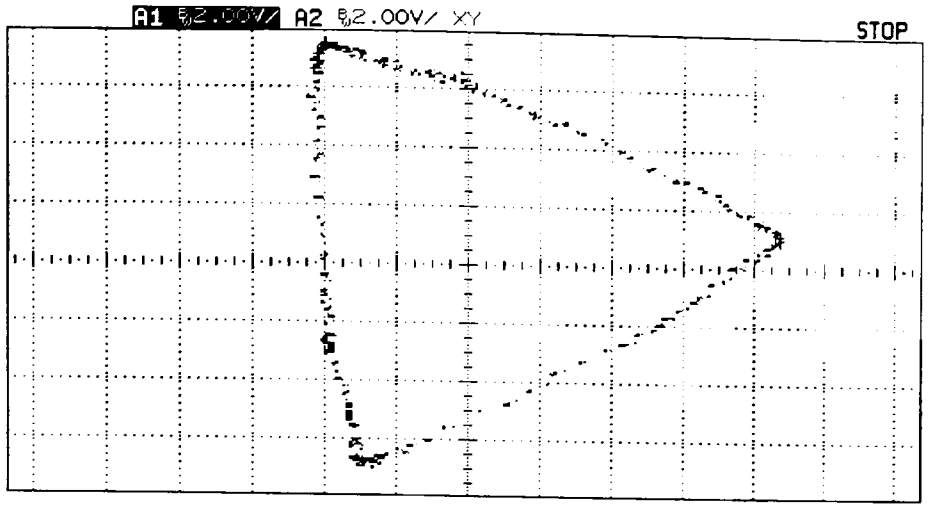

Figure 7.9: Captured 'Saliency Fingerprint' for 'Kart' Motor

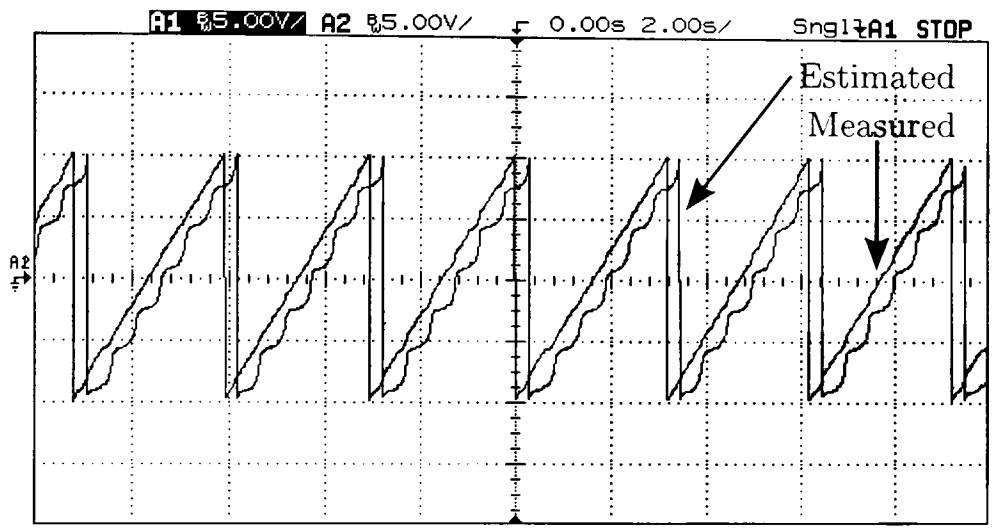

Figure 7.10: Captured Uncompensated Results for 'Kart' Motor

7.3.4 Results for 'Traction' Motor

Figure 7.11 shows the experimentally captured 'saliency fingerprint' for the 'Traction' motor. The shape of the 'fingerprint' again closely matches that seen in chapter 5. The final uncompensated angle estimation results are shown in figure 7.12. It can be seen that the level of distortion is, as expected, much lower than with the other two machines and the accuracy may be sufficient for use without compensation.

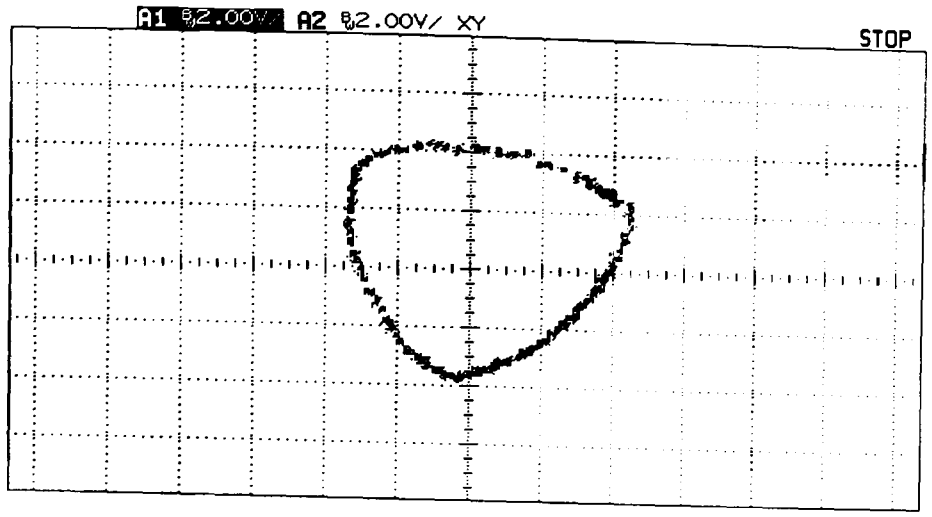

Figure 7.11: Captured 'Saliency Fingerprint' for 'Traction' Motor

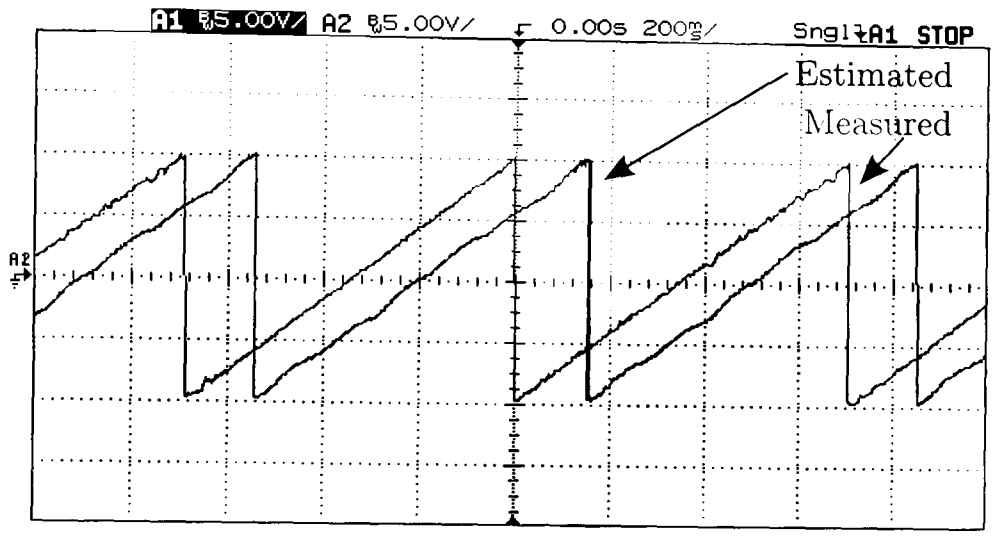

Figure 7.12: Captured Uncompensated Results for 'Traction' Motor

7.4 Implementation of Compensated System

7.4.1 Practical Operation in DSP

The compensated system is heavily based on the uncompensated one discussed in section 7.3.1. All additional functionality is included in the post-processing part of the program. There are two operating modes that can be used. The first of these uses the uncompensated system to generate the correction table for compensation and can also be used to quickly create a set of compensated (or uncompensated) results for further examination[3]. The second operating mode uses the generated table to dynamically produce compensated estimation results.

[3]This was used for generation of all MATLAB based results in this section.

7.4.2 Results for 'Actuator' Motor

Figure 7.13 shows the final compensated estimation results captured with the oscilloscope.

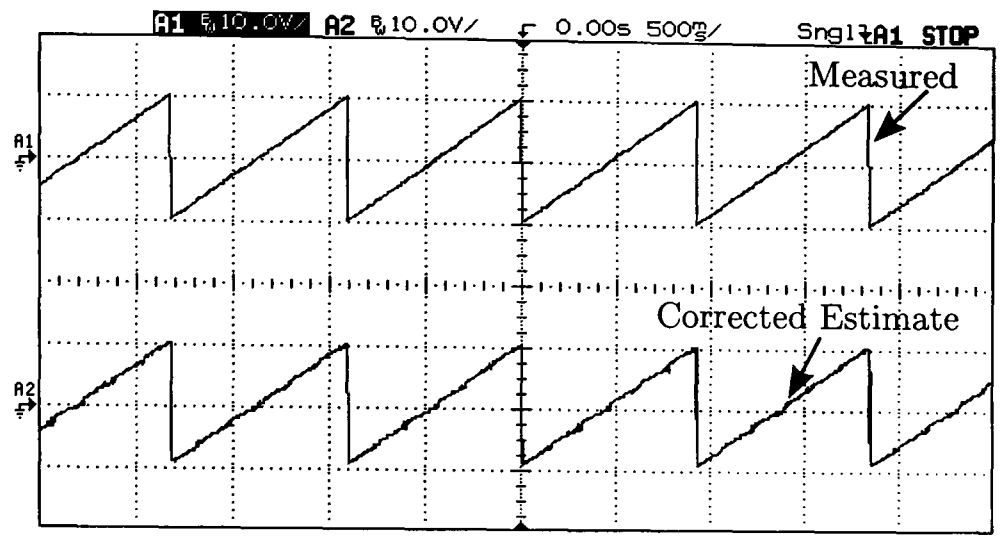

Figure 7.13: Captured Compensated Results for 'Actuator' Motor

It can be seen that the compensation system has reduced the distortion considerably; however, there is still a detectable error due to the high level of distortion present in the surface magnet machine. The results and error (captured directly from the DSP memory) over one electrical cycle are shown in figures 7.14 and 7.15 respectively and it can be seen that the maximum error is 2.65° mechanical (0.14 rad electrical).

7.4.3 Results for 'Kart' Motor

Figure 7.16 shows the final compensated estimation results captured with the oscilloscope.

It can be seen that the compensation has virtually removed the distorting component and thus improved the quality of the overall system. The results captured directly from the DSP over one electrical cycle are shown in figure 7.17.

Figure 7.18 shows that the maximum error is less than 2.3° mechanical (0.12 rad electrical) and that in almost all positions is less than 1° mechanical (0.05 rad electrical).

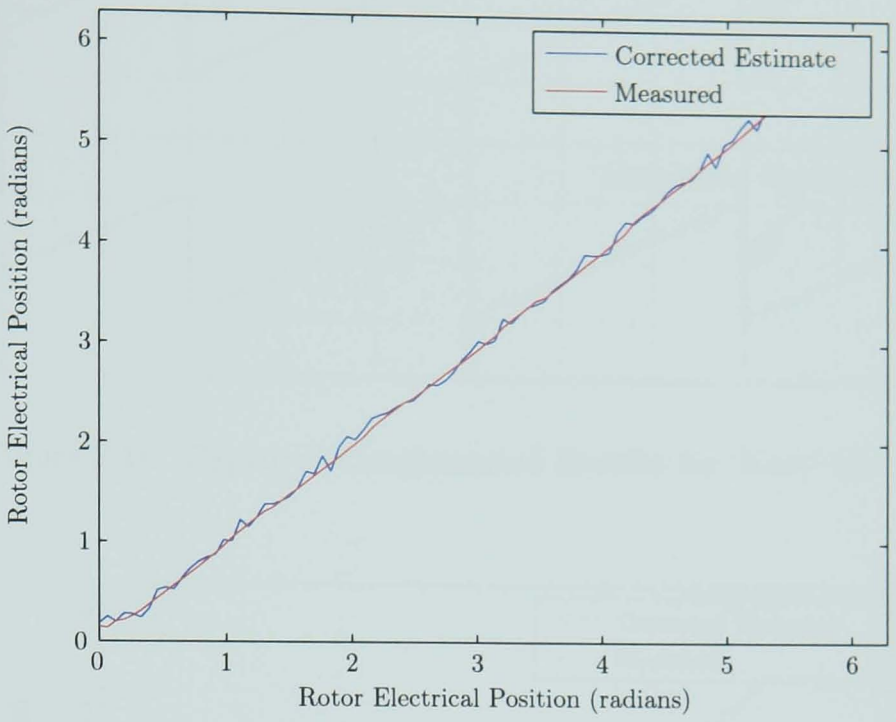

Figure 7.14: Compensated Results for 'Actuator' Motor

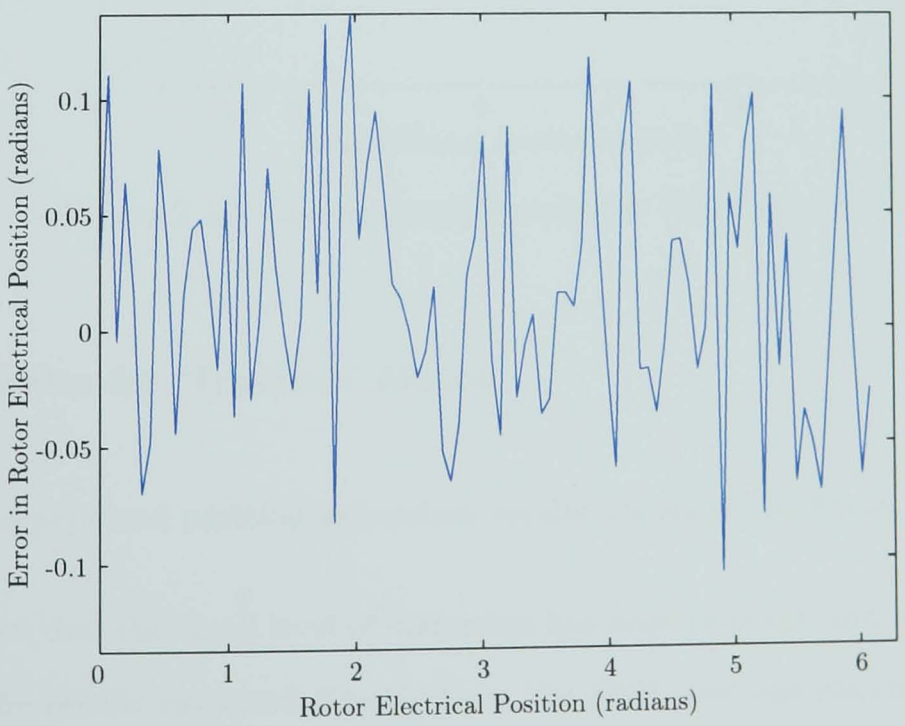

Figure 7.15: Compensated Error for 'Actuator' Motor

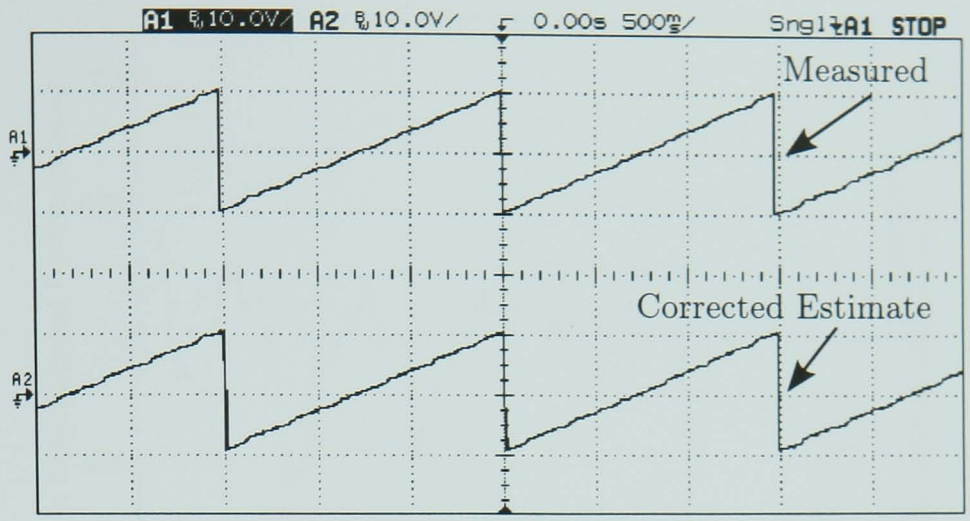

Figure 7.16: Captured Compensated Results for 'Kart' Motor

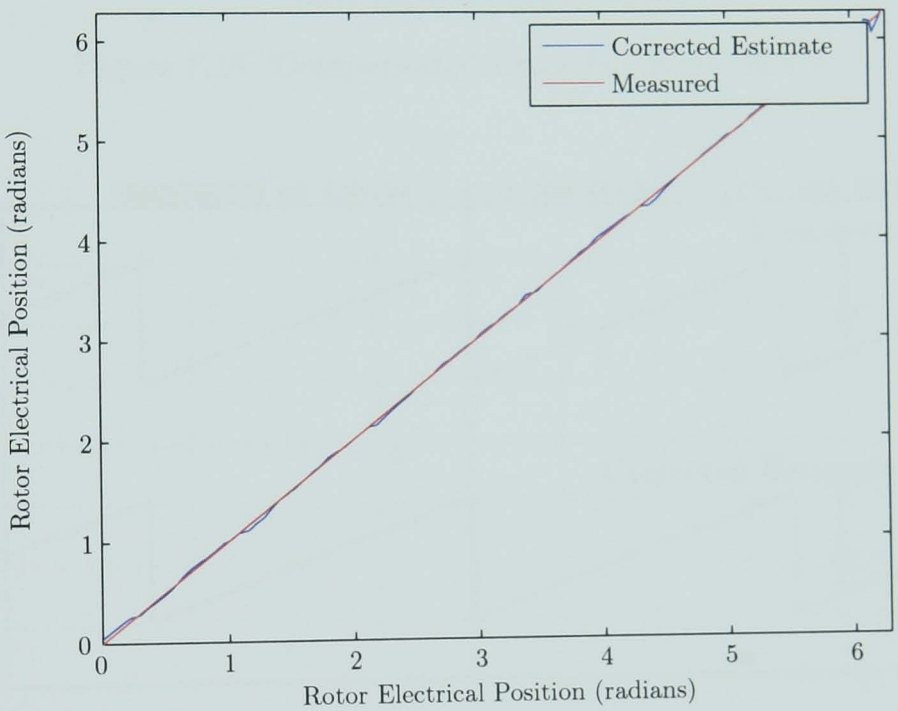

Figure 7.17: Compensated Results for 'Kart' Motor

7.4.4 Results for 'Traction' Motor

The final compensated position estimation results are shown in figure 7.19.

It can be seen that the small level of distortion has been removed and thus the error reduced. The results captured directly from the DSP over one electrical cycle are shown in figure 7.20.

As can be seen in figure 7.21, the maximum error is less than 1° mechanical (0.07 rad electrical).

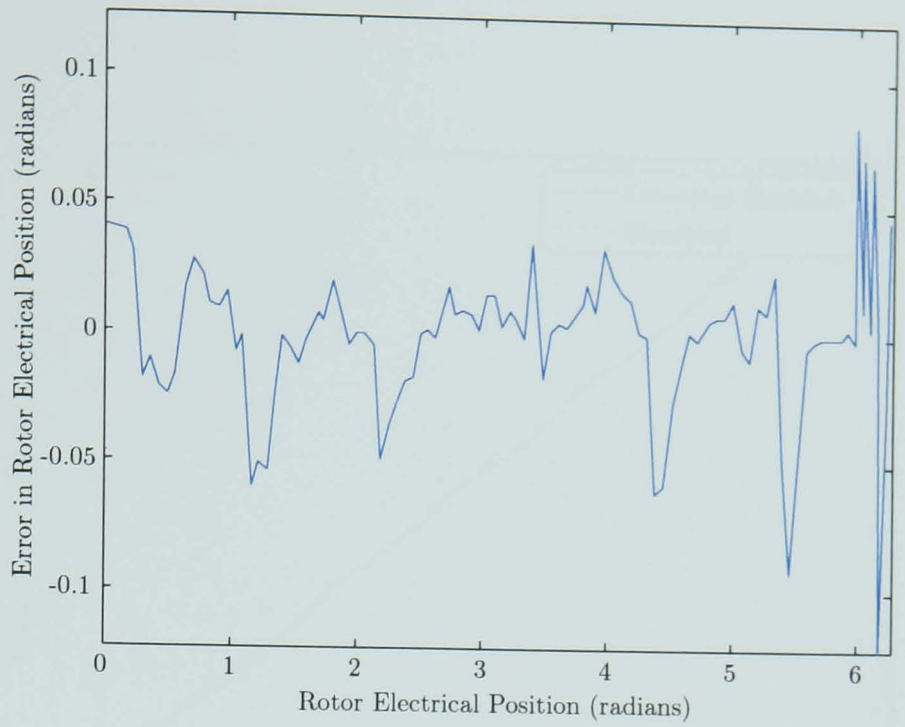

Figure 7.18: Compensated Error for 'Kart' Motor

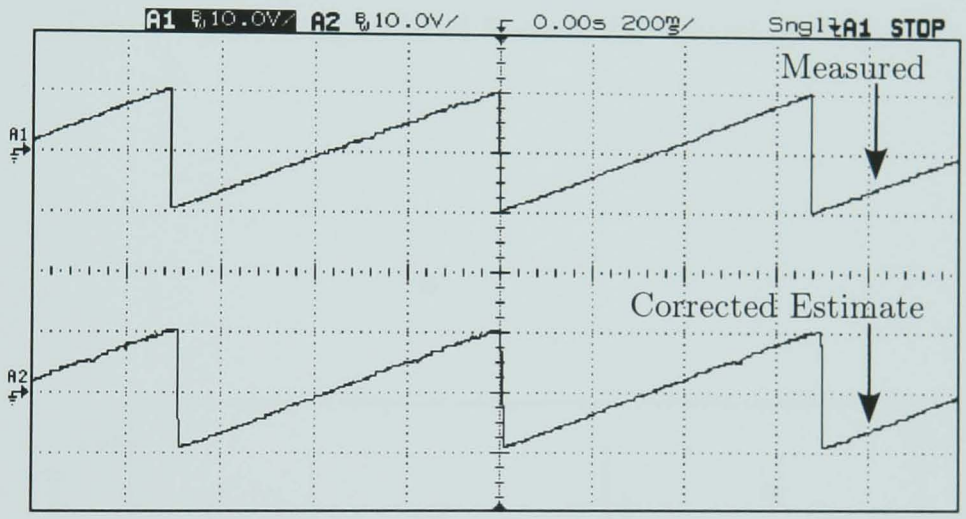

Figure 7.19: Captured Compensated Results for 'Traction' Motor

7.5 Summary

The experimental test system has shown that the zero speed sensorless position detection algorithm is capable of producing accurate results for all three test machines. With machines that exhibit highly distorted saliencies, there is a significant reduction in the uncompensated accuracy. However, the compensation scheme is capable of correcting these results to a sufficient accuracy for brushless AC operation. The remaining errors can be attributed to measurement noise from the CTs and interconnections, sampling errors from the ADCs, inaccuracies in the injected

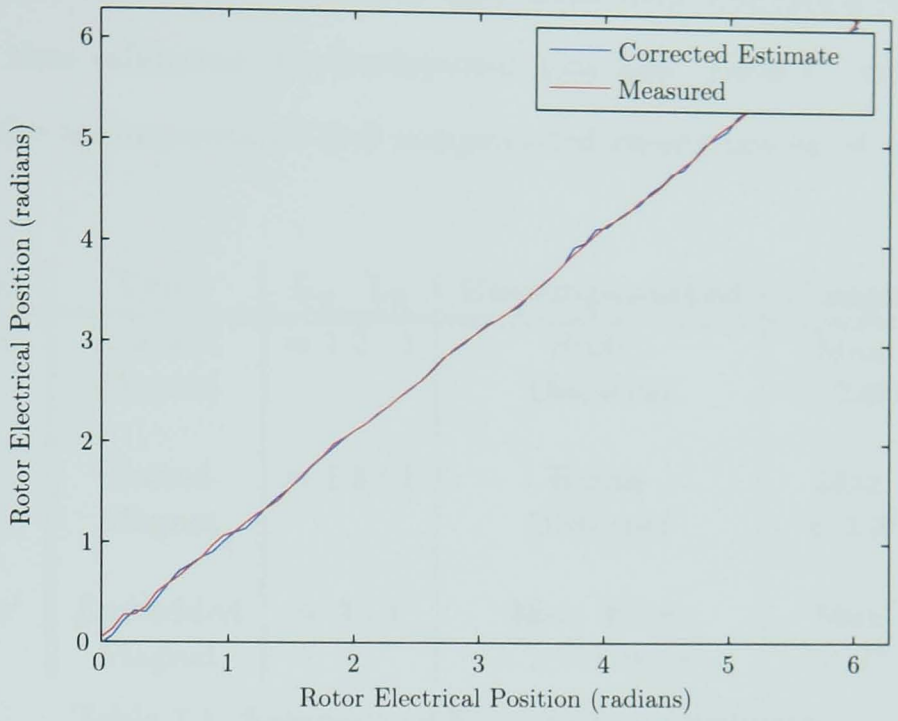

Figure 7.20: Compensated Results for 'Traction' Motor

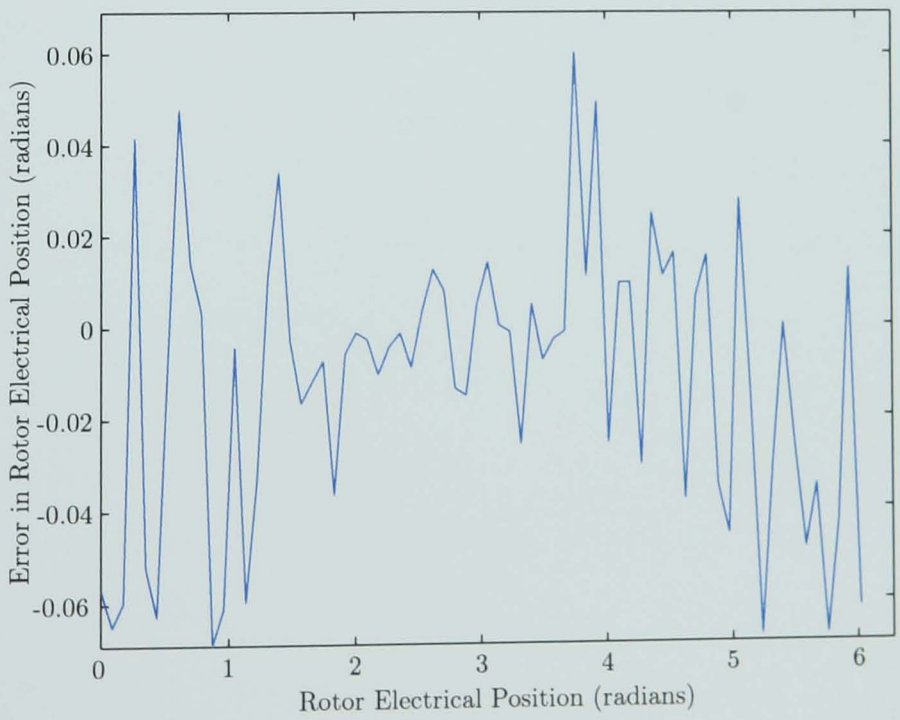

Figure 7.21: Compensated Error for 'Traction' Motor

voltages due to dead-band and the limited resolution of the PWM generation, and the possibility of lamination chatter in the machine itself. It can also be seen that the experimental results show excellent agreement with simulation and finite element results, thus validating the development approach. Table 7.1 presents a brief summary of the uncompensated and compensated results produced with the final system.

Machine	**Type**	$\mathbf{L_q : L_d}$	**Uncompensated**	**Compensated**
'Actuator' Motor	Surface Magnet	$\approx 1.2 : 1$	Highly Distorted	Max. Error $< 2.65°$ mech.
'Kart' Motor	Buried Magnet	$\approx 1.5 : 1$	Highly Distorted	Max. Error $< 2.3°$ mech.
'Traction' Motor	Embedded Magnet	$\approx 2 : 1$	Max. Error $< 2.75°$ mech.	Max. Error $< 1°$ mech.

Table 7.1: Summary of Final System Operation

Chapter 8

Conclusions

8.1 The State of The Art

In the published literature, there are a wide number of different approaches to sensorless rotor position estimation for brushless permanent magnet machines. The earliest paper on sensorless position estimation for brushless permanent magnet machines found by the author was Iizuka *et al.* [5], who focused on the zero crossing point approach to 'at speed' position estimation for brushless DC machines. Since the publication of this paper, there have been many different approaches to addressing the problem. As described in chapter 2, these fall into two broad categories: back EMF based techniques and saliency based techniques. The former group, which encompasses observers, machine models and most artificial intelligence systems as well as the original zero crossing approach, is only applicable when the shaft is rotating at sufficient speed to overcome measurement noise issues. Saliency based techniques are theoretically applicable over the whole speed range; however, computational demands, possible torque ripple issues and available DC link voltage shift the focus of these techniques towards the stationary end of the speed range. In practice, therefore, it is desirable to combine the two groups and produce a dual mode system. The practical implications of this are beyond the scope of this thesis; however, the reader is directed to [72] for further information on the subject.

Due to the greater degree of understanding of high speed position sensing techniques and the increased complexity of zero speed estimation, this thesis has concentrated on implementation at zero speed; the integration of the two groups is left as an obvious avenue for further development.

8.2 Applications of Sensorless Control

Despite a continuing interest in sensorless position estimation techniques both in industry and academia, there are no commercially available sensorless position estimators that operate over the full speed range. Many back EMF based estimators are available, but these are very limited, in terms of both speed range and accuracy.

It is suggested that the lack of availability is due to the difficulty in detecting rotor position at zero speed, particularly with the predominance of surface magnet topology machines. In addition, the majority of zero speed sensorless techniques are highly computationally intensive and therefore not applicable to the low-cost market to which the concept of sensorless rotor position estimation appeals. In many applications with less stringent cost limitations, there is a desire to implement additional functionality beyond the basic drive system. In these applications, a computationally simple sensorless position estimator is desirable as the micro- or digital signal processor is expected to have processing capacity available after the position computation.

The aim of this thesis has been to address both of the main situations: when cost is critical, a simple estimator can be used with or without compensation and, when less so, bespoke machine design enables highly accurate position estimation without the need for compensation.

8.3 Theoretical Analysis

In chapter 3, a derivation of the mathematical model of a permanent magnet synchronous machine is presented. This idealised model was used as a basis for a detailed analysis of the stationary system and the effect of applying measurement signals to the windings of the machine. This enabled the development of the base (uncompensated) system, which was implemented without the considerable complexity of tracking observers.

The idealised model made the assumption that slotting effects could be ignored. This is a standard approach to machine model derivation. It has been shown throughout this thesis, however, that slotting effects are of significance and cannot be safely omitted when dealing with saliency based estimation. The theoretical analysis of chapter 3 thus continues with a compensation approach that allows the system to overcome slotting effects.

8.4 Machine Analysis

In validating any machine control technique, whether it be sensorless position estimation, direct torque control or any other drive system, it is essential that it can be demonstrated to work on a range of different machines. Without this, it is impossible to assess the wider viability of the approach. For example, the operation of a saliency based sensorless position estimator would be significantly different with a wide air gap embedded magnet IPMSM with 1.5 slots per pole compared to its operation with a narrow air gap surface magnet machine with 3 slots per pole. It is thus instructive to perform a detailed analysis of the effect of injected measurement signals on a variety of topologies. This experimental analysis is presented in chapter 4 and the variations in saliency magnitude are clearly manifested in the varying shapes of the current locus presented therein.

8.5 System Modelling and Simulation

For most engineering design applications, simulation tools are readily available for testing systems prior to final implementation. These tools have been used throughout this thesis to continually verify each stage of the development. In chapter 3, modelling was carried out primarily based on the idealised model. This enabled an initial system to be developed for successful operation in the ideal environment. This theme continues in chapter 4, where finite element analysis techniques were used to model the test machines and to explore the effect of saliency distortion on the accuracy of the technique. This is an important tool as it enables machine designers developing bespoke machines for applications involving sensorless position estimation to assess the likely accuracy of saliency based techniques prior to machine construction.

Chapter 6 extends the finite element analysis discussed in chapter 4 by demonstrating the effect of small variations in slot shape on the different topologies. It was shown that the size of the stator teeth (and thus the level of saturation in those teeth) has a significant effect on the shape of the saliency, especially when the magnitude of the saliency in the machine is low. This information can be used by machine designers to enable them to adjust the saliency ratio and slot shape in order to optimise for sensorless position estimation as well as for machine performance. It is important to note that the design suggestions provided by this analysis may contradict normal machine design rules; in this circumstance, some form of compromise would be necessary.

The mathematical modelling approach to system verification was further extended to include experimental data for realistic validation. In chapter 4, a basic test platform was used to capture the currents induced by voltage injection for further analysis. The MATLAB environment was then used in chapter 5 to study the captured currents. A simulated implementation of the demodulation approaches provided valuable confirmation of the accuracy of the finite element simulations. In addition, it clearly demonstrated the validity of the position estimation method, in

particular the computationally simple compensation method.

8.6 Experimental Verification

To be certain that any system is genuinely valid, it is essential that it is demonstrated in a practical environment. This ensures that computational requirements are not excessive and that the levels of noise present in the measurements do not overwhelm the required information and result in a reduction of accuracy. A discussion of the implementation is presented in chapter 7, along with experimental results for all three test machines. The system was demonstrated to be valid for all three machines and it was seen that the accuracy with the 'Traction' motor was extremely good even without compensation.

With the highly distorted saliency present in the 'Actuator' motor, the accuracy of the uncompensated system is very poor; however, the compensation approach is able to substantially improve this. The small level of saliency in surface magnet machines does limit their applicability to high accuracy zero speed sensorless position estimation; however, it can be seen that the approach is still valid.

For the 'Kart' motor, the uncompensated accuracy is again very poor. However, the distortion was found to be very consistent, making it ideally suited to the compensation approach. In the tests, the maximum observed error in the estimation results is only 2.3° mechanical with this machine.

The 'Traction' motor shows good accuracy without compensation; however, an improvement is still possible if desired. The maximum observed error in the estimation results for the compensated system with this machine is only 1° mechanical.

8.7 Further Work

Although it has been demonstrated that the sensorless approach discussed herein is applicable to a number of different machine topologies, it would be desirable

to extend this analysis to include further structures. In particular, it would be valuable to individually assess the effect of changes to rotor and stator structure by constructing different rotors for one or more existing stators and vice versa. To some extent this could also be achieved through finite element analysis.

The finite element analysis of slotting effects discussed in chapter 6 has been limited to variations of only two parameters. Clearly this could be extended to produce a comprehensive summary of the optimum approach to machine design for sensorless position estimation. Continuing with the simulation and modelling theme, it would be valuable to modify the original machine model to incorporate slotting effects.

In order to produce a comprehensive sensorless approach, it is necessary to operate over the whole speed range. Therefore, combining this work with a similar investigation into high speed position estimation (both above and below base speed) would be useful.

Finally, it would be desirable to investigate the applicability of the technique discussed in this thesis to other machine types, such as synchronous reluctance machines and machines with either a skewed rotor or a skewed stator.

Appendix A

Reference Frames

The reference frames used in this report are shown diagrammatically in figure A.1.

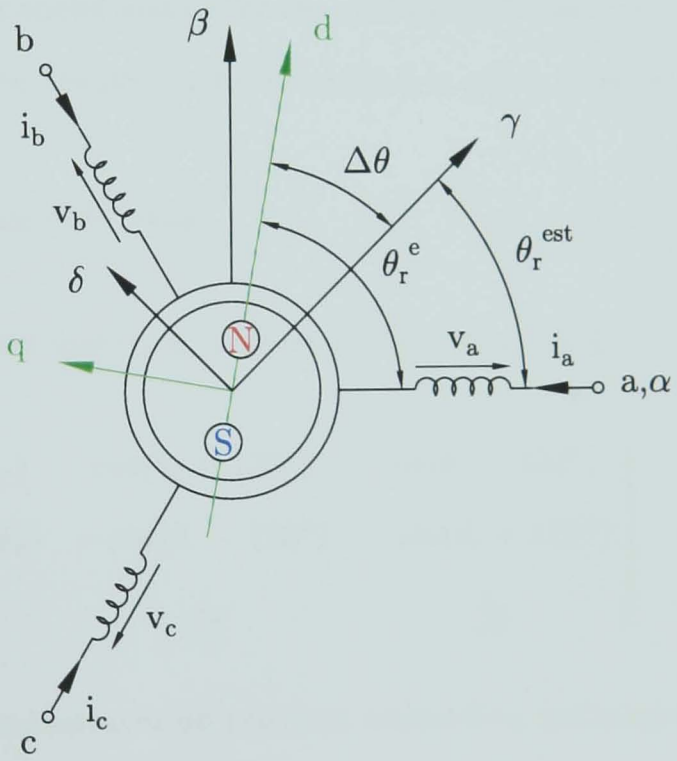

Figure A.1: Reference Frames for Modelling

The *abc* reference frame is referred to as the three axis stationary reference frame. Quantities expressed in this frame directly relate to the physical properties of the three-phase windings in the machine. To simplify the equations, this is often trans-

formed into a two axis stationary reference frame ($\alpha\beta$), using equation (A.1) [87].

$$X_{\alpha\beta 0} = BX_{abc}; X_{abc} = B^T X_{\alpha\beta 0} \tag{A.1}$$

where X is the voltage, current or flux space vector and B is defined in equation (A.2).

$$B = \sqrt{\frac{2}{3}} \begin{pmatrix} 1 & -\frac{1}{2} & -\frac{1}{2} \\ 0 & \frac{\sqrt{3}}{2} & -\frac{\sqrt{3}}{2} \\ \frac{1}{\sqrt{2}} & \frac{1}{\sqrt{2}} & \frac{1}{\sqrt{2}} \end{pmatrix} \tag{A.2}$$

In addition to the reference frames attached to the stationary part of the machine, it is useful to consider what is happening in the machine relative to the rotor. For this purpose, the synchronous reference frame (dq) is used. This is a reference frame rotating at the synchronous speed of the machine. For a synchronous machine, this corresponds to the rotor speed and hence the synchronous and rotor reference frames are interchangeable. The transformation required is given in equation (A.3) [87],

$$X_{dq0} = CX_{abc}; X_{abc} = C^T X_{dq0} \tag{A.3}$$

where the transformation matrix C is given by equation (A.4).

$$C = \sqrt{\frac{2}{3}} \begin{pmatrix} \cos(\theta_r) & \cos(\theta_r - 120°) & \cos(\theta_r + 120°) \\ -\sin(\theta_r) & -\sin(\theta_r - 120°) & -\sin(\theta_r + 120°) \\ \frac{1}{\sqrt{2}} & \frac{1}{\sqrt{2}} & \frac{1}{\sqrt{2}} \end{pmatrix} \tag{A.4}$$

Since this document concentrates on position estimation techniques, it is important to note that the position considered by the system will not correspond exactly to the position of the rotor. Therefore, an additional rotating reference frame ($\gamma\delta$) attached to the estimated position of the rotor is utilised.

Appendix B

'Actuator' Motor FEA Results

Table B.1 summarises the machine versions used in the finite element analysis. The full results are included in figures B.1–B.16.

Machine Version	$\frac{s_i}{s}$	s_i (mm)	$\frac{t_i}{t}$	t_i (mm)
01	11/11	2.75	6/6	1.50
02	11/11	2.75	5/6	1.25
03	11/11	2.75	4/6	1.00
04	11/11	2.75	3/6	0.75
05	9/11	2.25	6/6	1.50
06	9/11	2.25	5/6	1.25
07	9/11	2.25	4/6	1.00
08	9/11	2.25	3/6	0.75
09	7/11	1.75	6/6	1.50
10	7/11	1.75	5/6	1.25
11	7/11	1.75	4/6	1.00
12	7/11	1.75	3/6	0.75
13	5/11	1.25	6/6	1.50
14	5/11	1.25	5/6	1.25
15	5/11	1.25	4/6	1.00
16	5/11	1.25	3/6	0.75

Table B.1: 'Actuator' Motor Alterations for Slotting Analysis

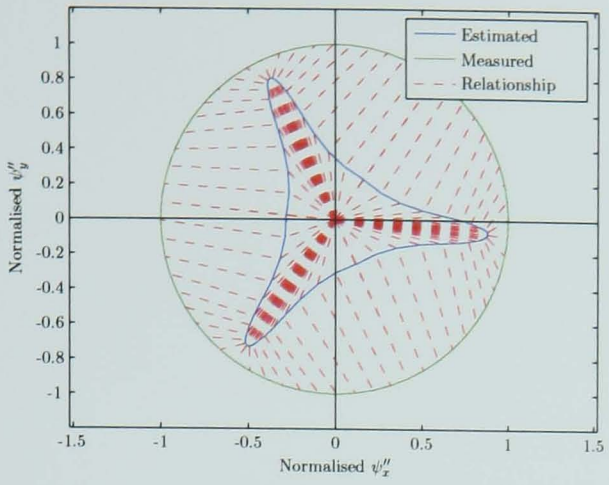

(a)

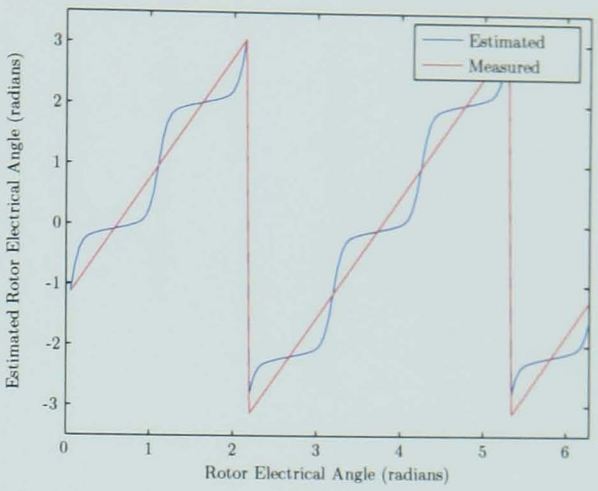

(b)

Figure B.1: Results for 'Actuator' Motor Version 01
(a) Fingerprint, (b) Estimation Results

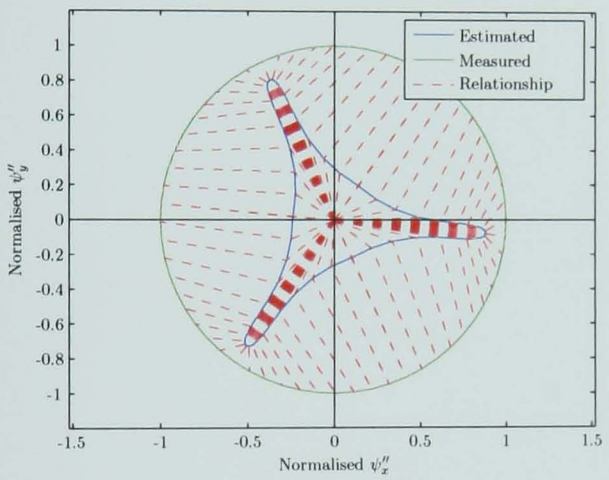

(a)

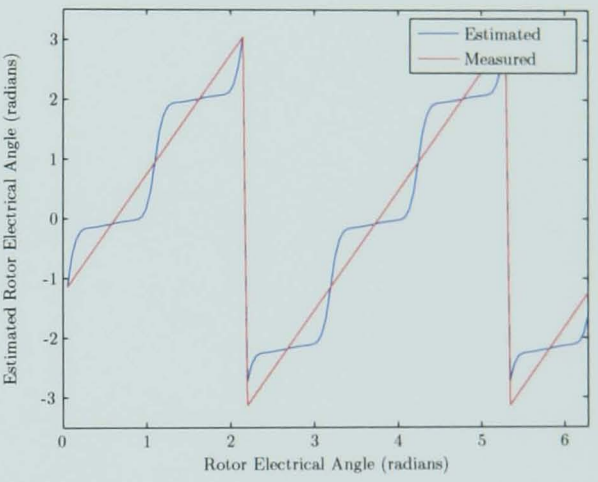

(b)

Figure B.2: Results for 'Actuator' Motor Version 02
(a) Fingerprint, (b) Estimation Results

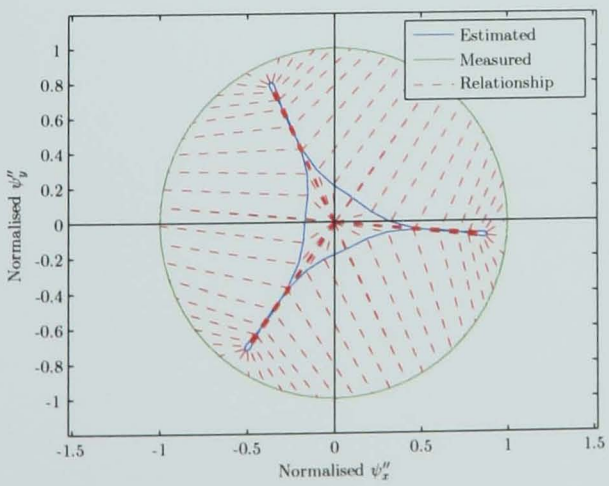

(a)

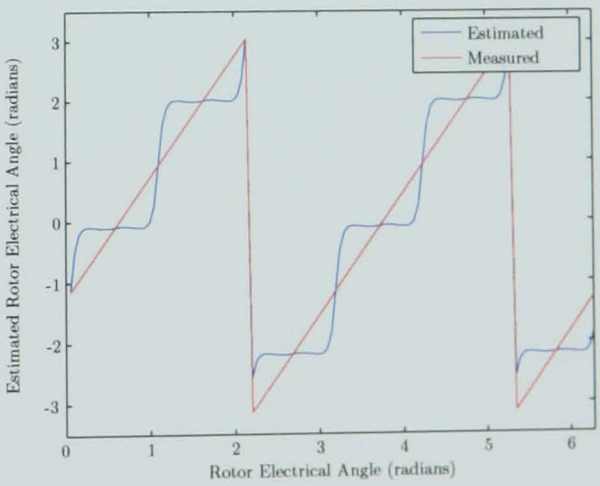

(b)

Figure B.3: Results for 'Actuator' Motor Version 03
(a) Fingerprint, (b) Estimation Results

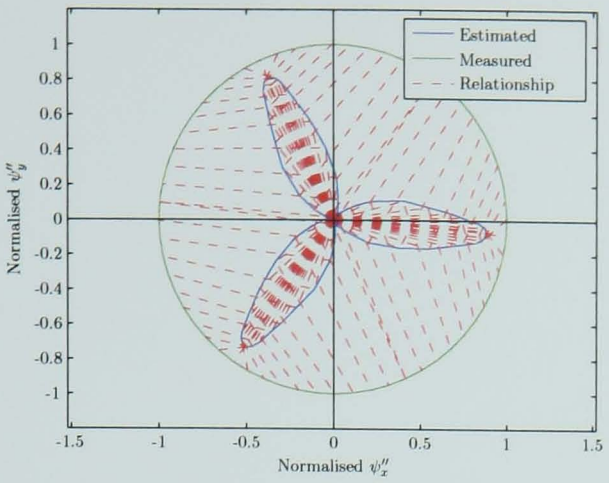

(a)

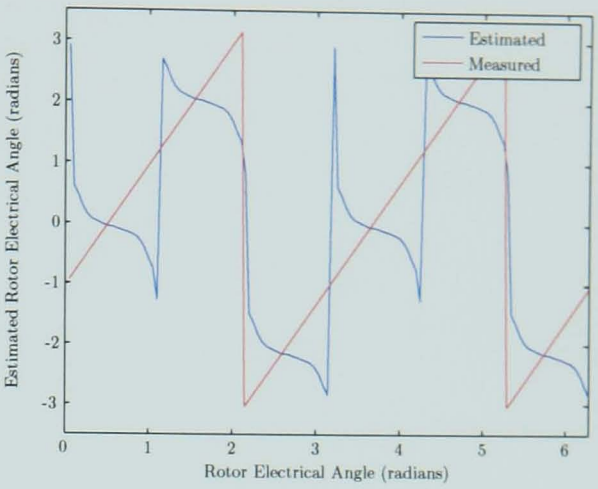

(b)

Figure B.4: Results for 'Actuator' Motor Version 04
(a) Fingerprint, (b) Estimation Results

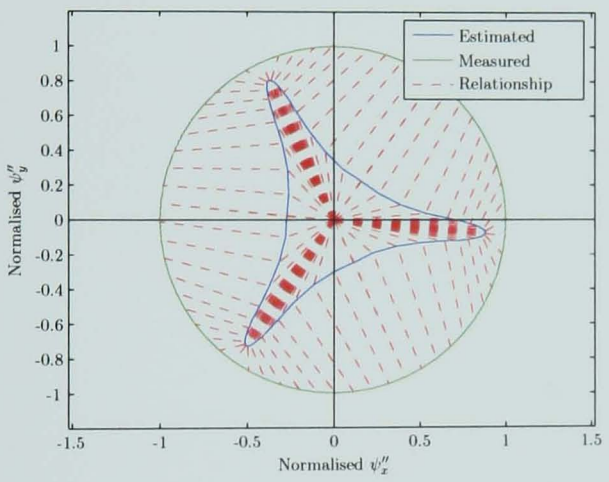

(a)

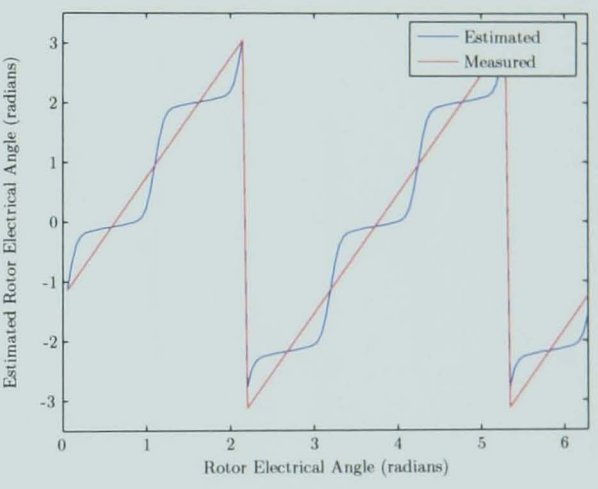

(b)

Figure B.5: Results for 'Actuator' Motor Version 05
(a) Fingerprint, (b) Estimation Results

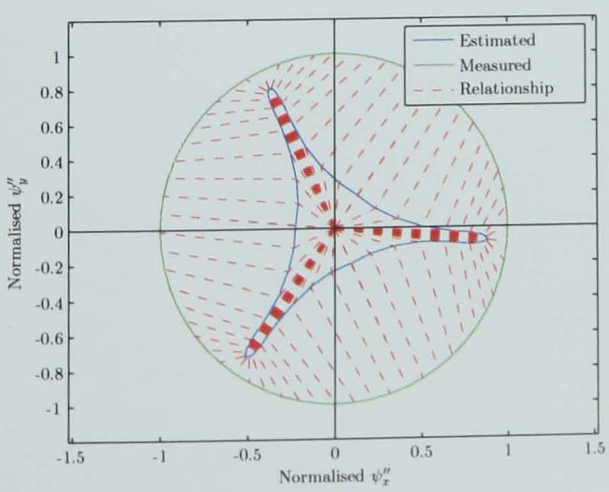

(a)

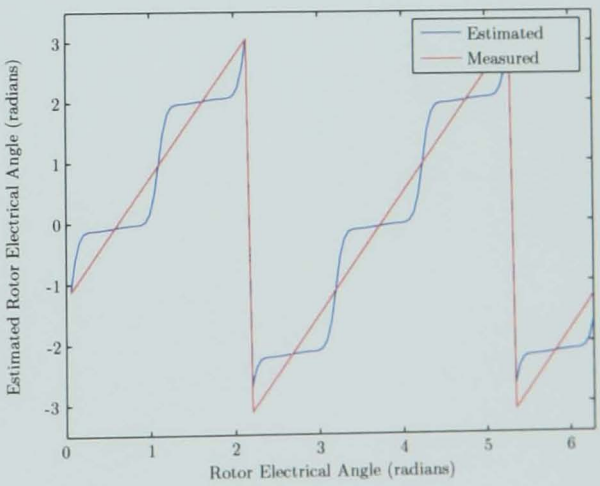

(b)

Figure B.6: Results for 'Actuator' Motor Version 06
(a) Fingerprint, (b) Estimation Results

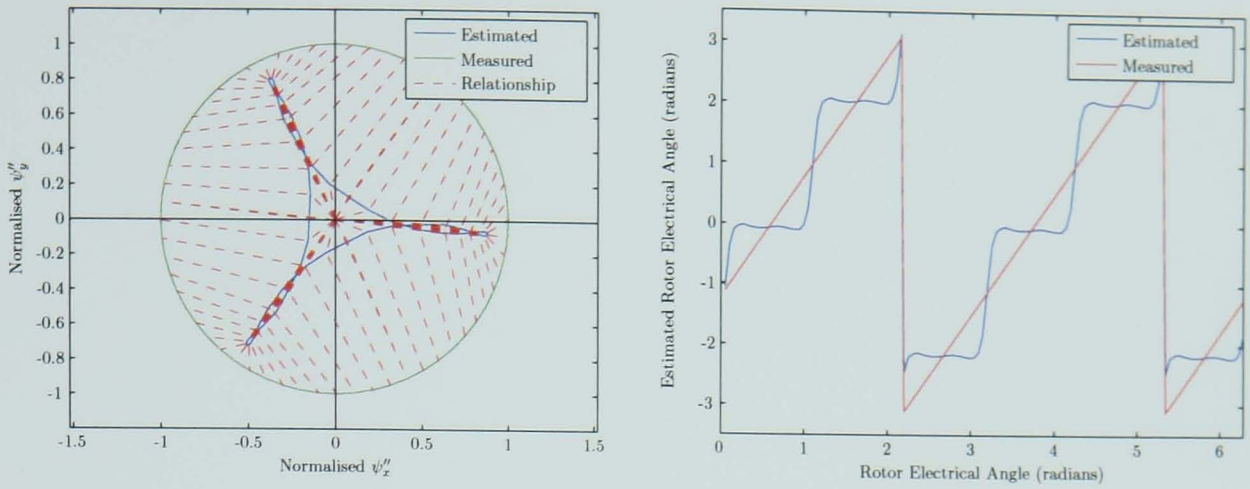

(a) (b)

Figure B.7: Results for 'Actuator' Motor Version 07
(a) Fingerprint, (b) Estimation Results

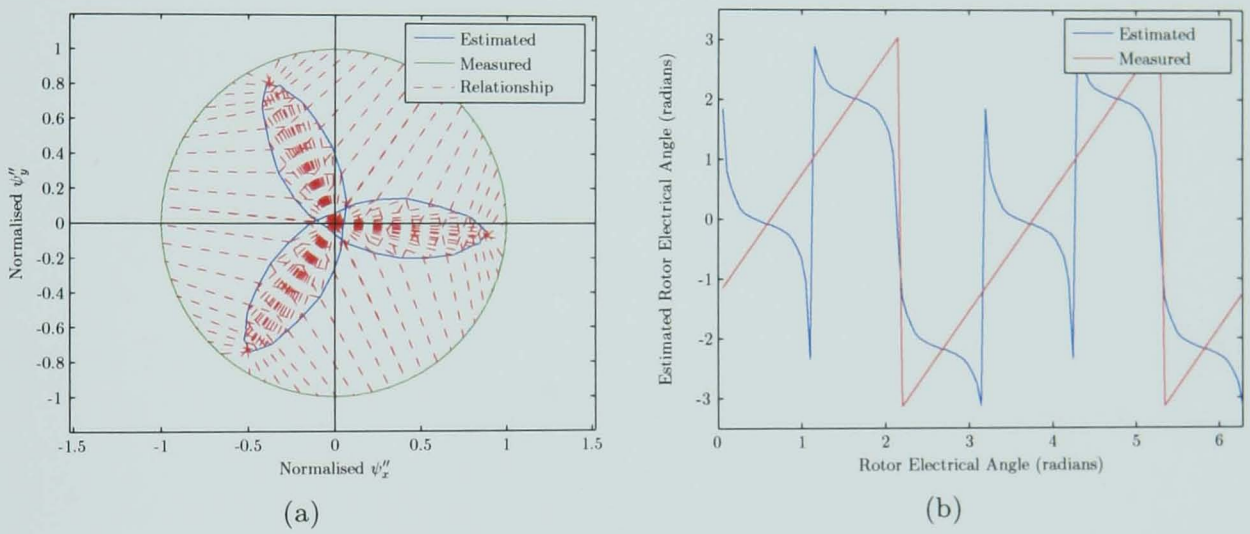

(a) (b)

Figure B.8: Results for 'Actuator' Motor Version 08
(a) Fingerprint, (b) Estimation Results

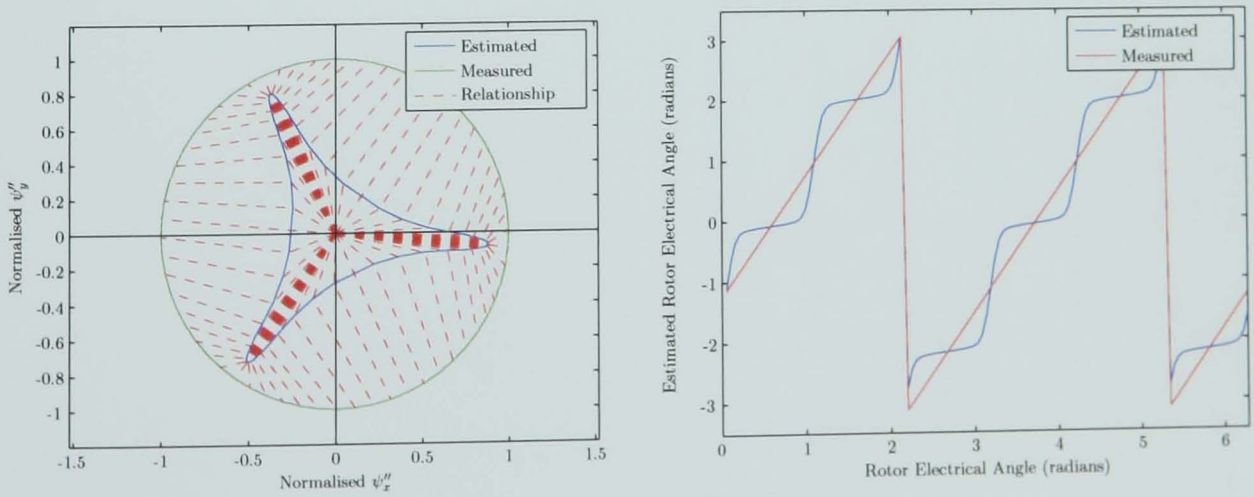

(a) (b)

Figure B.9: Results for 'Actuator' Motor Version 09
(a) Fingerprint, (b) Estimation Results

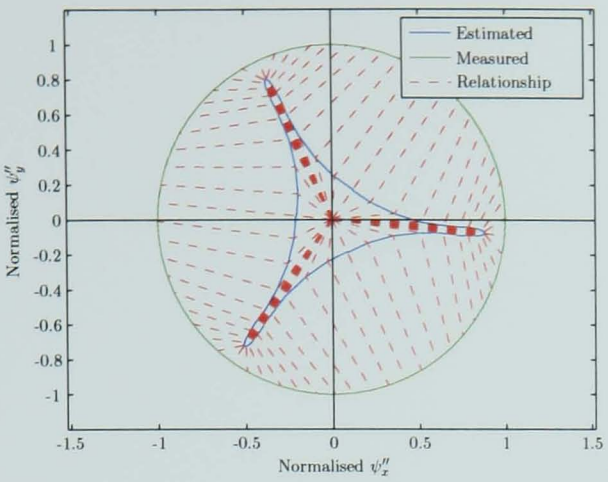

(a)

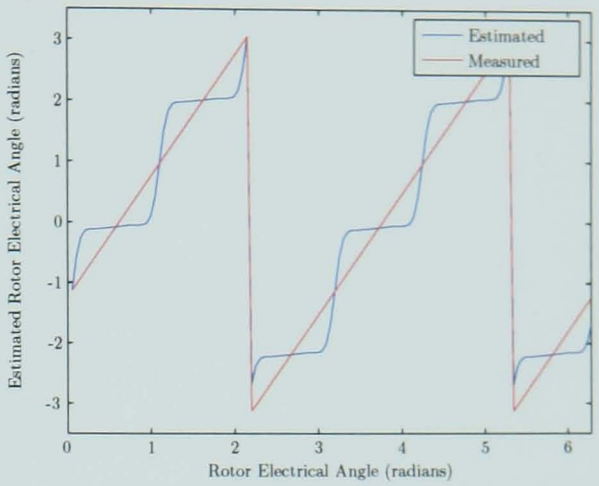

(b)

Figure B.10: Results for 'Actuator' Motor Version 10
(a) Fingerprint, (b) Estimation Results

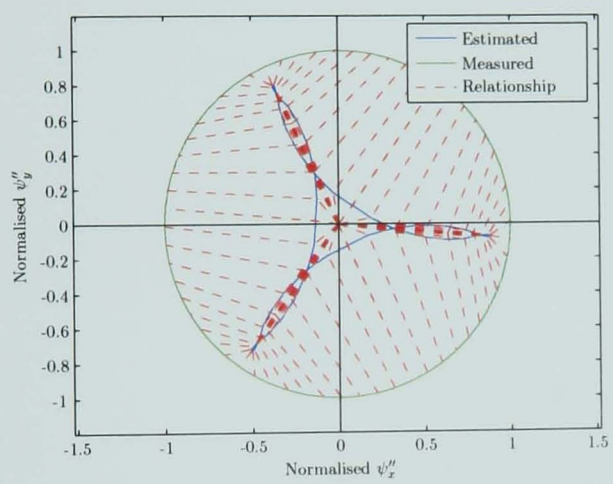

(a)

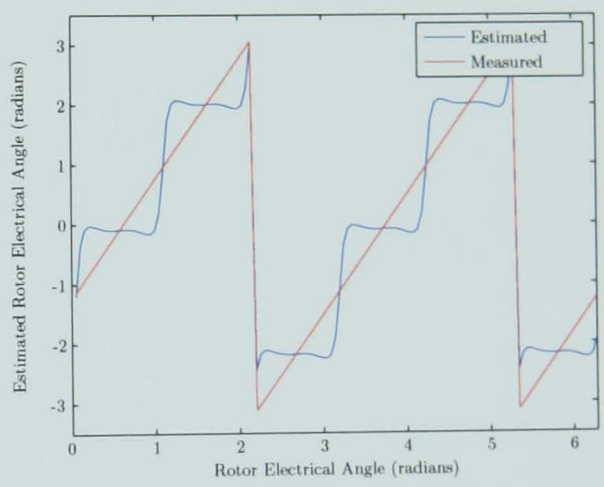

(b)

Figure B.11: Results for 'Actuator' Motor Version 11
(a) Fingerprint, (b) Estimation Results

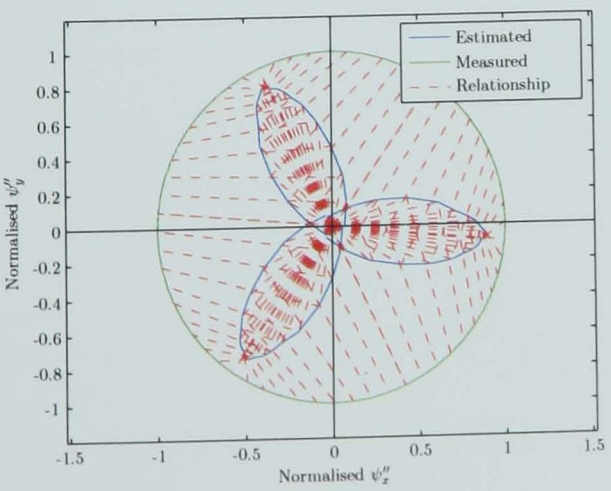

(a)

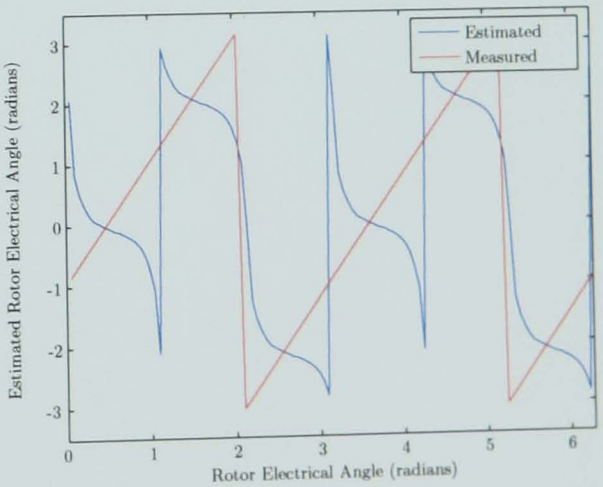

(b)

Figure B.12: Results for 'Actuator' Motor Version 12
(a) Fingerprint, (b) Estimation Results

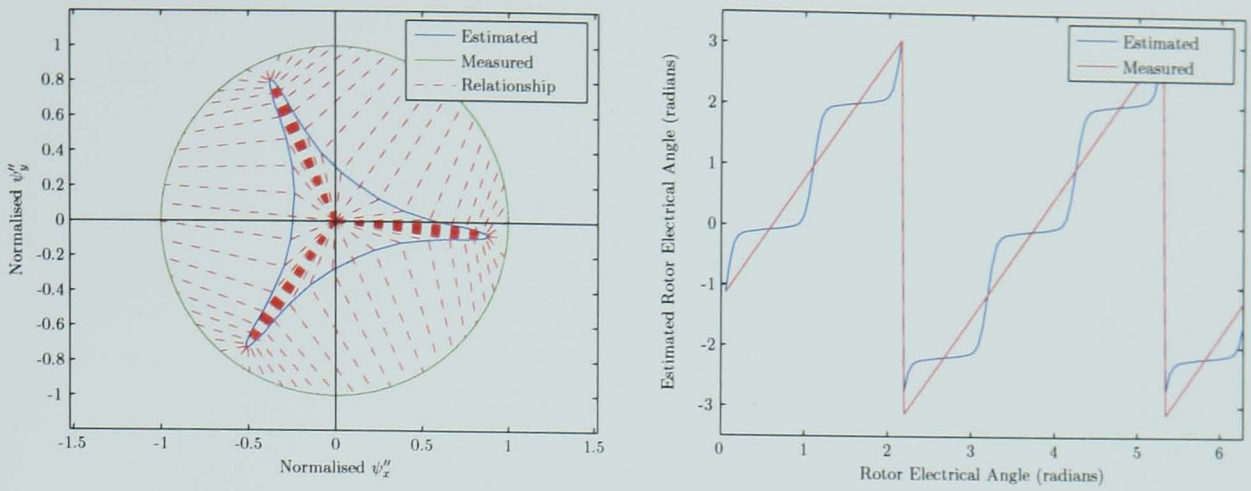

(a) (b)

Figure B.13: Results for 'Actuator' Motor Version 13
(a) Fingerprint, (b) Estimation Results

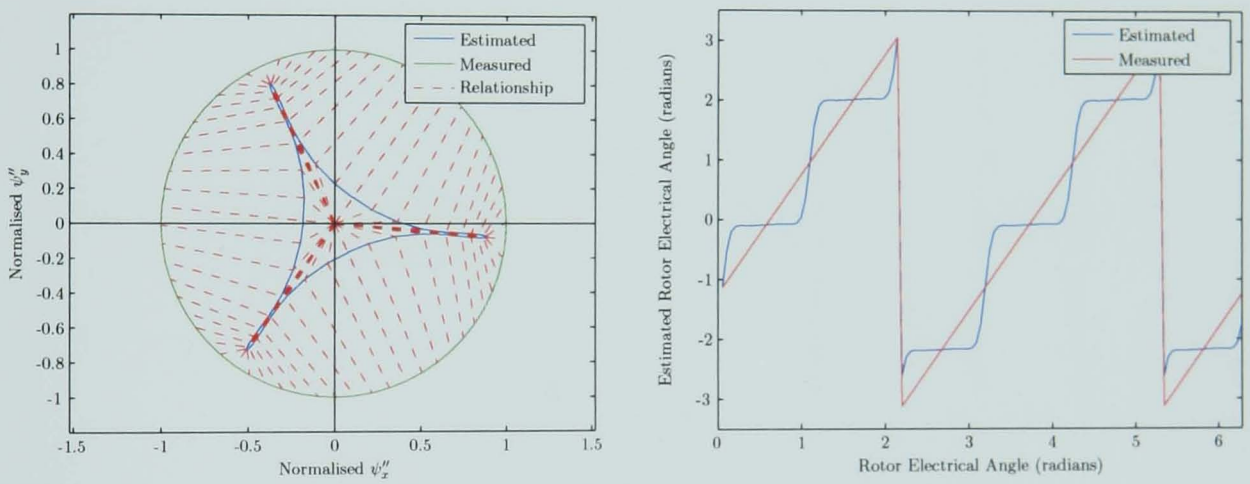

(a) (b)

Figure B.14: Results for 'Actuator' Motor Version 14
(a) Fingerprint, (b) Estimation Results

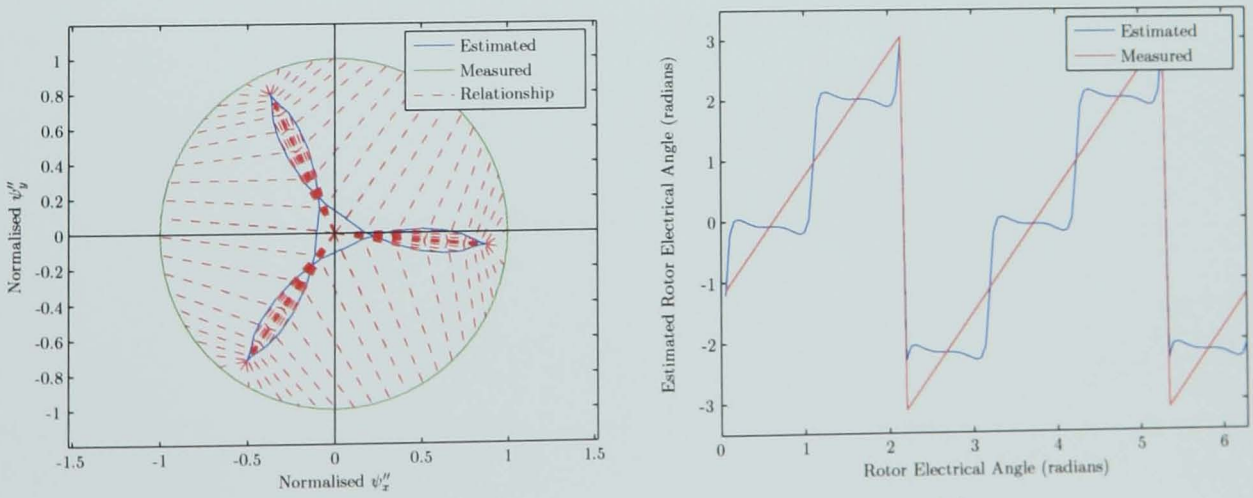

(a) (b)

Figure B.15: Results for 'Actuator' Motor Version 15
(a) Fingerprint, (b) Estimation Results

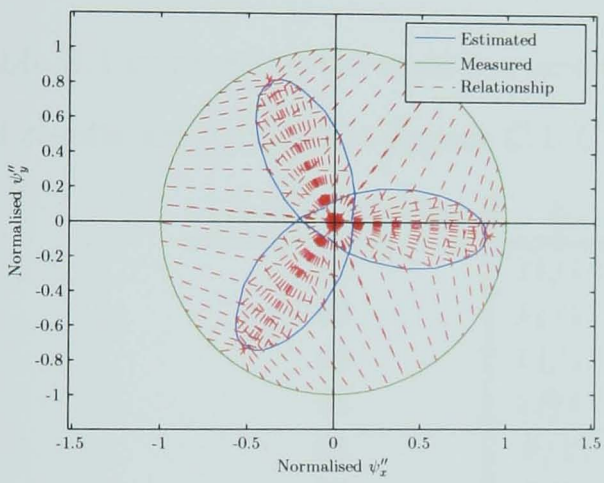

(a)

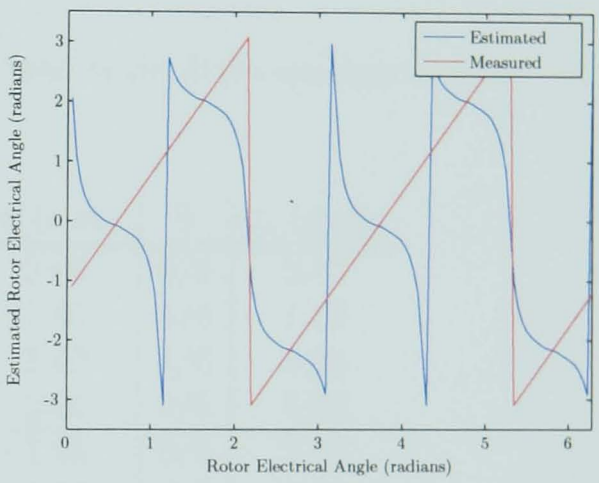

(b)

Figure B.16: Results for 'Actuator' Motor Version 16
(a) Fingerprint, (b) Estimation Results

Appendix C

'Kart' Motor FEA Results

Table C.1 summarises the machine versions used in the finite element analysis. The full results are included in figures C.1–C.16.

Machine Version	$\frac{s_i}{s}$	s_i (mm)	$\frac{t_i}{t}$	t_i (mm)
01	11/11	2.00	6/6	2.00
02	11/11	2.00	5/6	1.66
03	11/11	2.00	4/6	1.33
04	11/11	2.00	3/6	1.00
05	9/11	1.64	6/6	2.00
06	9/11	1.64	5/6	1.66
07	9/11	1.64	4/6	1.33
08	9/11	1.64	3/6	1.00
09	7/11	1.27	6/6	2.00
10	7/11	1.27	5/6	1.66
11	7/11	1.27	4/6	1.33
12	7/11	1.27	3/6	1.00
13	5/11	0.91	6/6	2.00
14	5/11	0.91	5/6	1.66
15	5/11	0.91	4/6	1.33
16	5/11	0.91	3/6	1.00

Table C.1: 'Kart' Motor Alterations for Slotting Analysis

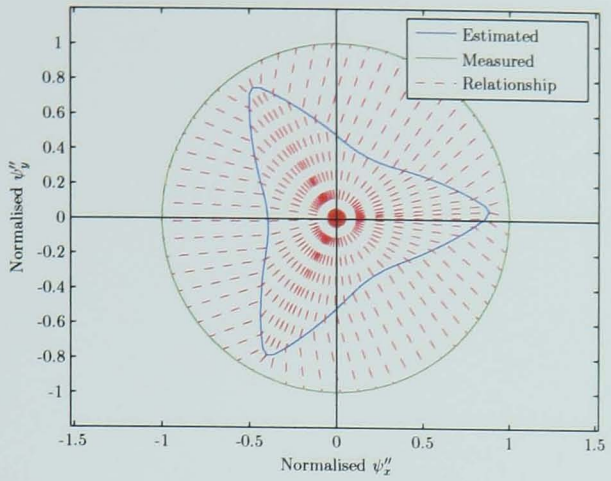

(a)

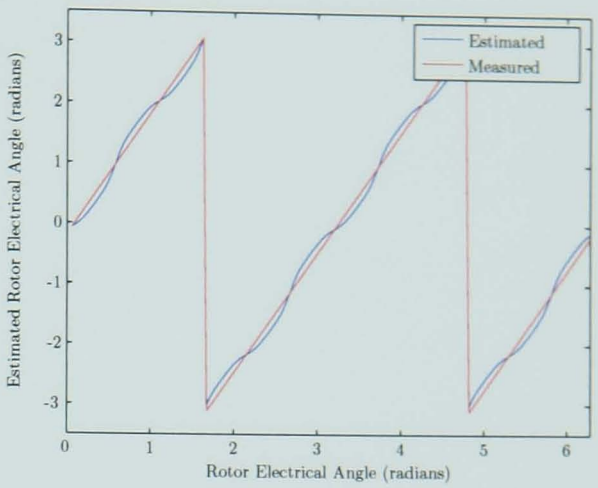

(b)

Figure C.1: Results for 'Kart' Motor Version 01
(a) Fingerprint, (b) Estimation Results

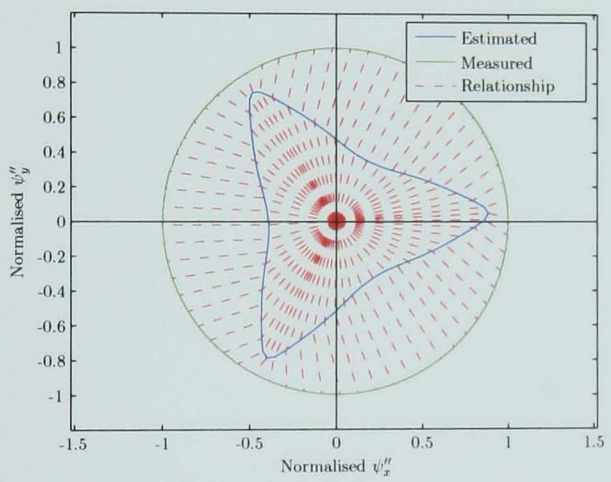

(a)

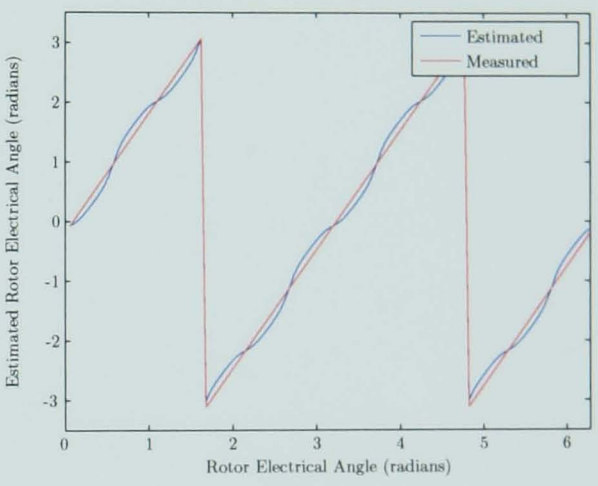

(b)

Figure C.2: Results for 'Kart' Motor Version 02
(a) Fingerprint, (b) Estimation Results

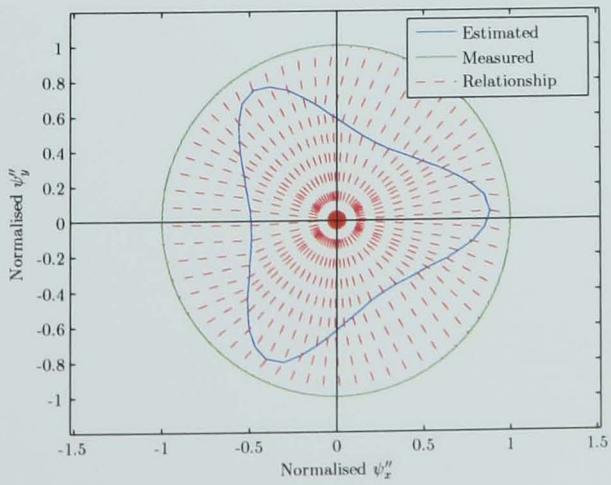

(a)

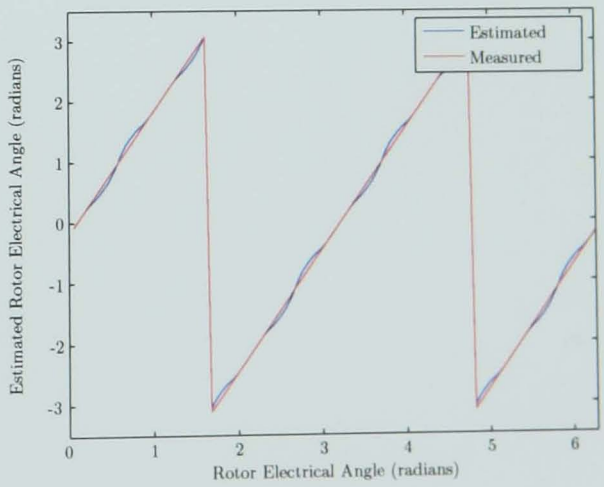

(b)

Figure C.3: Results for 'Kart' Motor Version 03
(a) Fingerprint, (b) Estimation Results

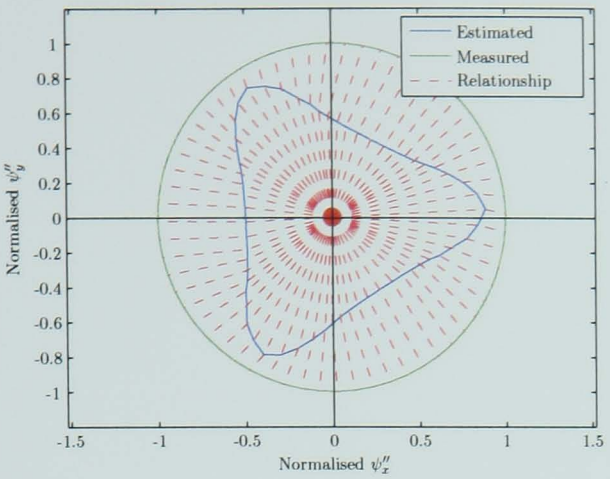

(a)

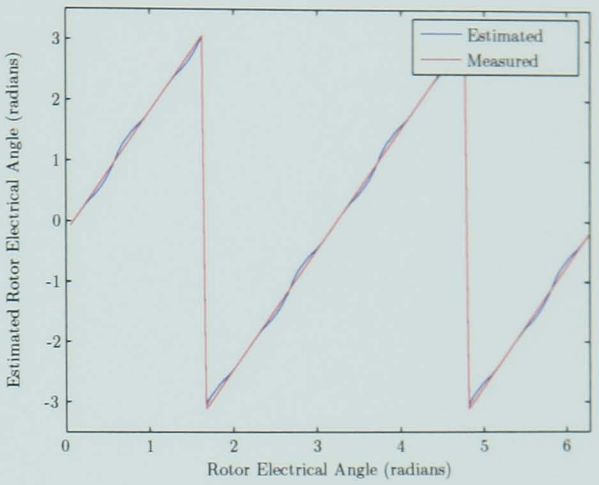

(b)

Figure C.4: Results for 'Kart' Motor Version 04
(a) Fingerprint, (b) Estimation Results

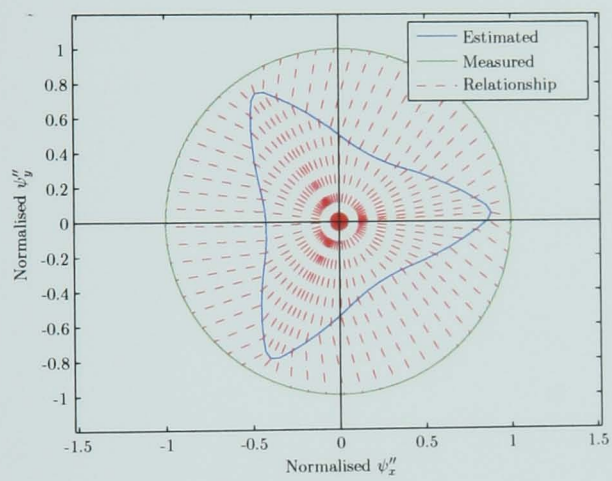

(a)

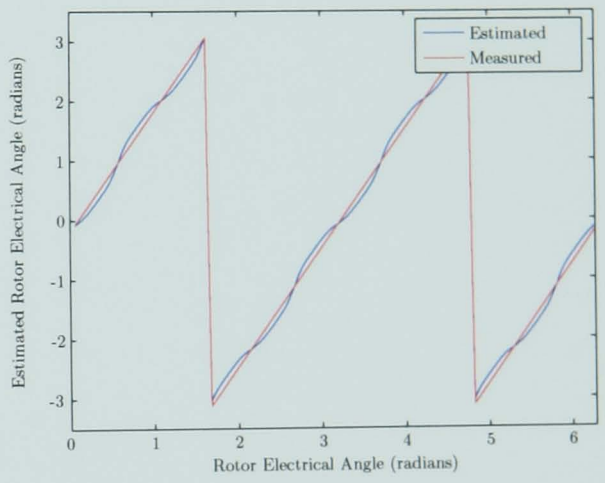

(b)

Figure C.5: Results for 'Kart' Motor Version 05
(a) Fingerprint, (b) Estimation Results

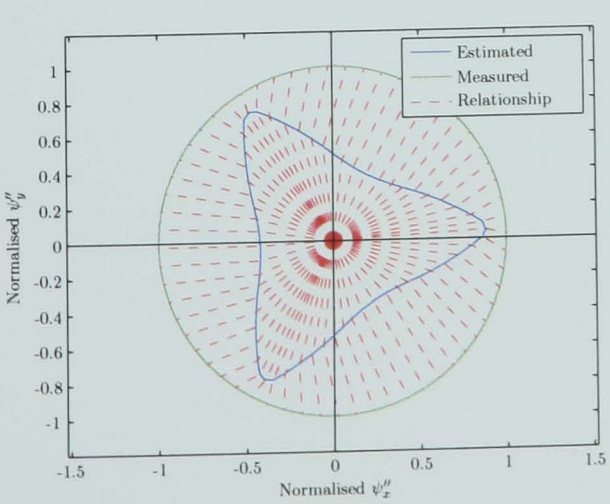

(a)

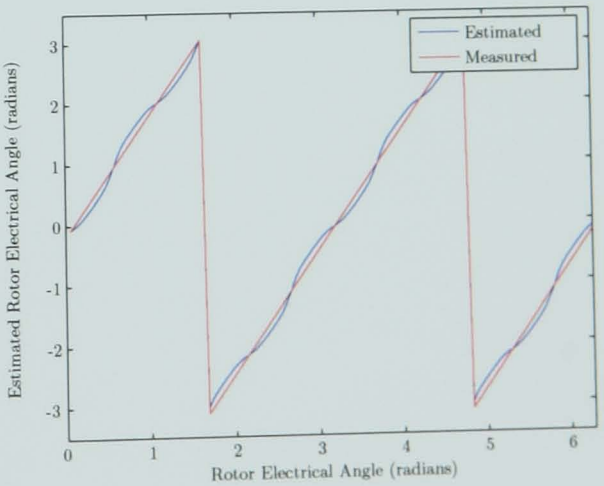

(b)

Figure C.6: Results for 'Kart' Motor Version 06
(a) Fingerprint, (b) Estimation Results

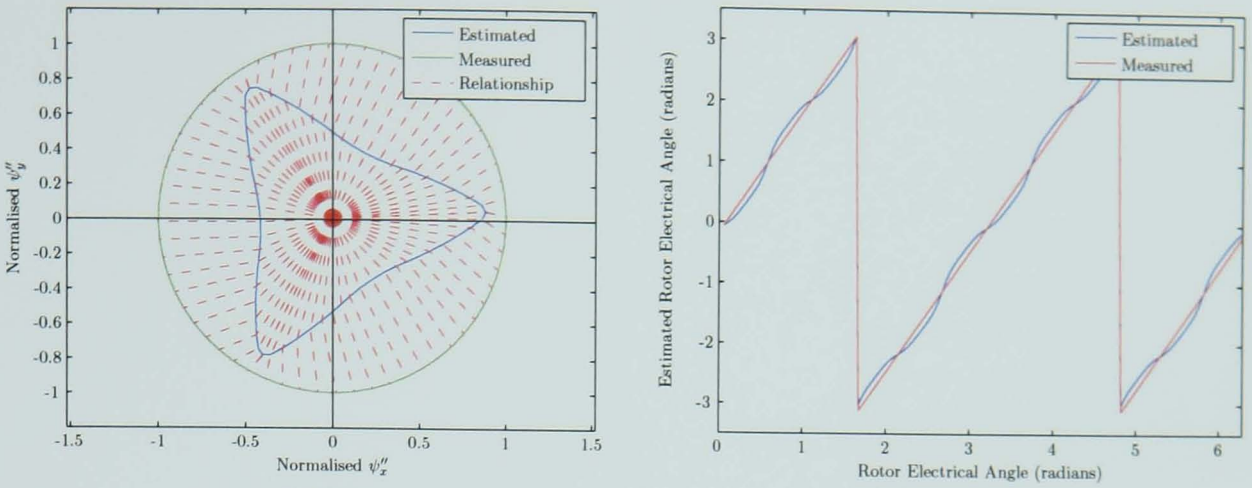

(a) (b)

Figure C.7: Results for 'Kart' Motor Version 07
(a) Fingerprint, (b) Estimation Results

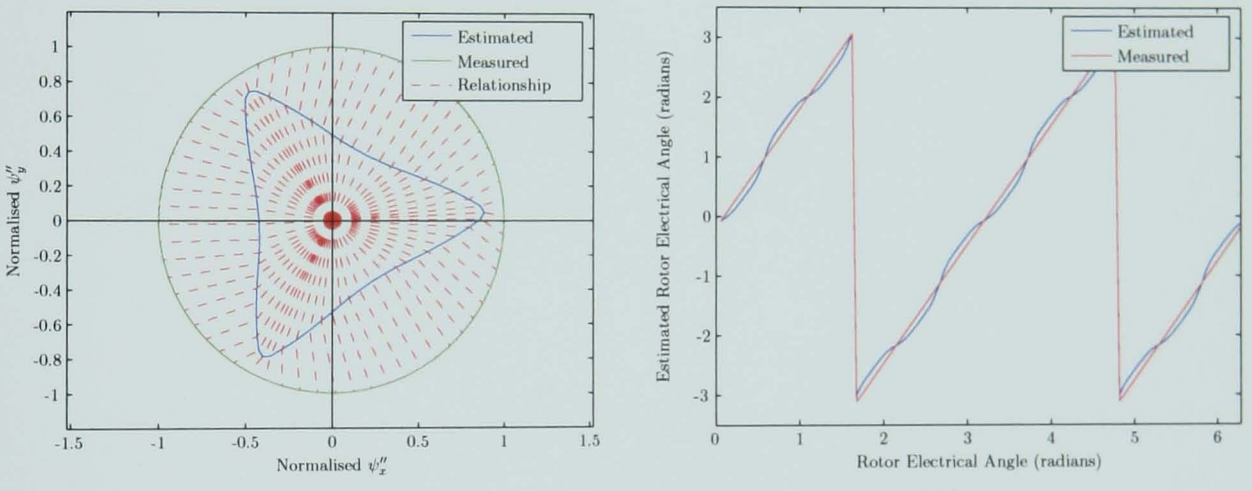

(a) (b)

Figure C.8: Results for 'Kart' Motor Version 08
(a) Fingerprint, (b) Estimation Results

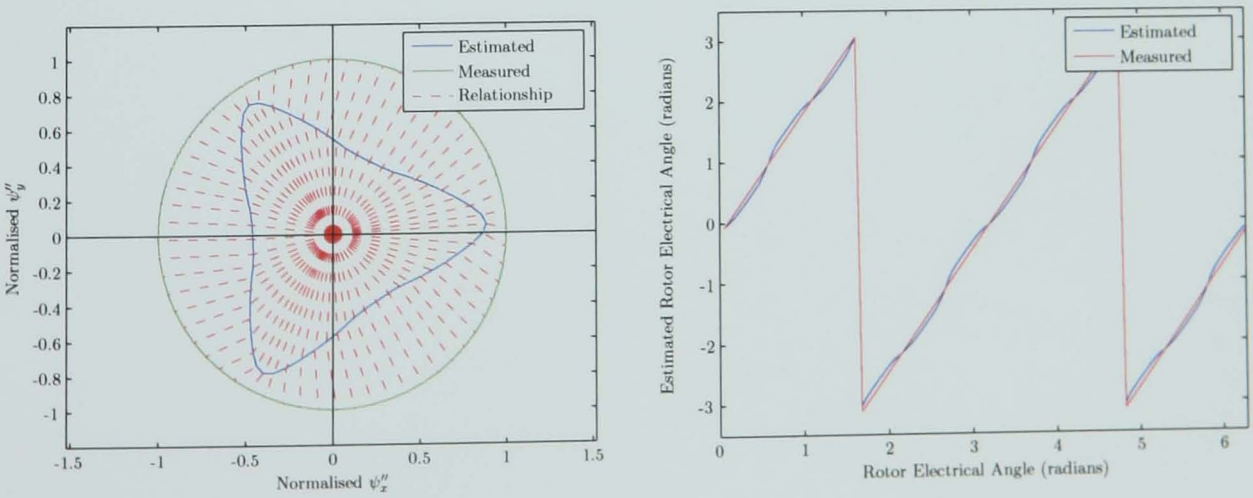

(a) (b)

Figure C.9: Results for 'Kart' Motor Version 09
(a) Fingerprint, (b) Estimation Results

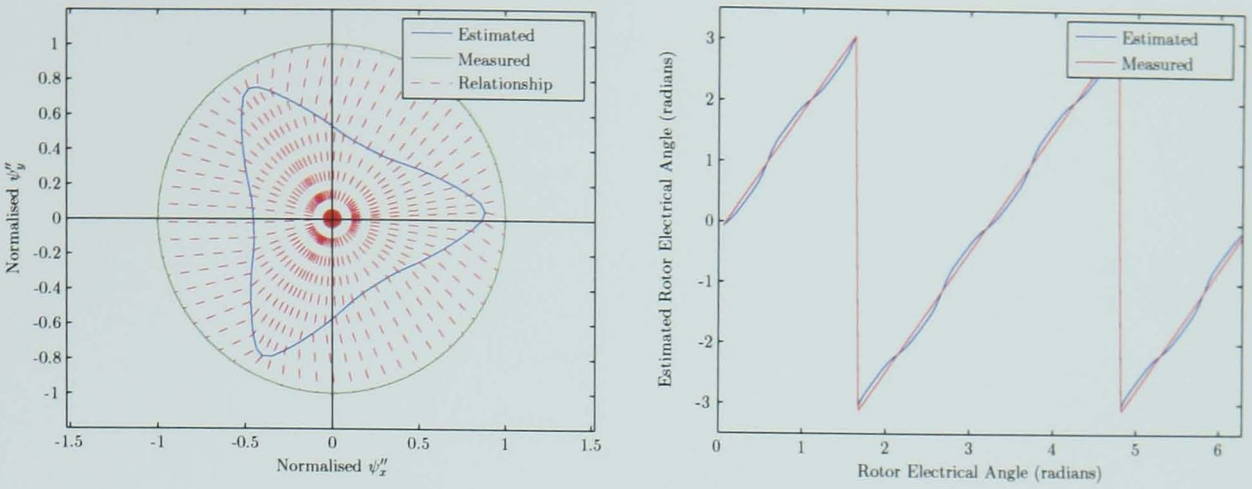

(a) (b)

Figure C.10: Results for 'Kart' Motor Version 10
(a) Fingerprint, (b) Estimation Results

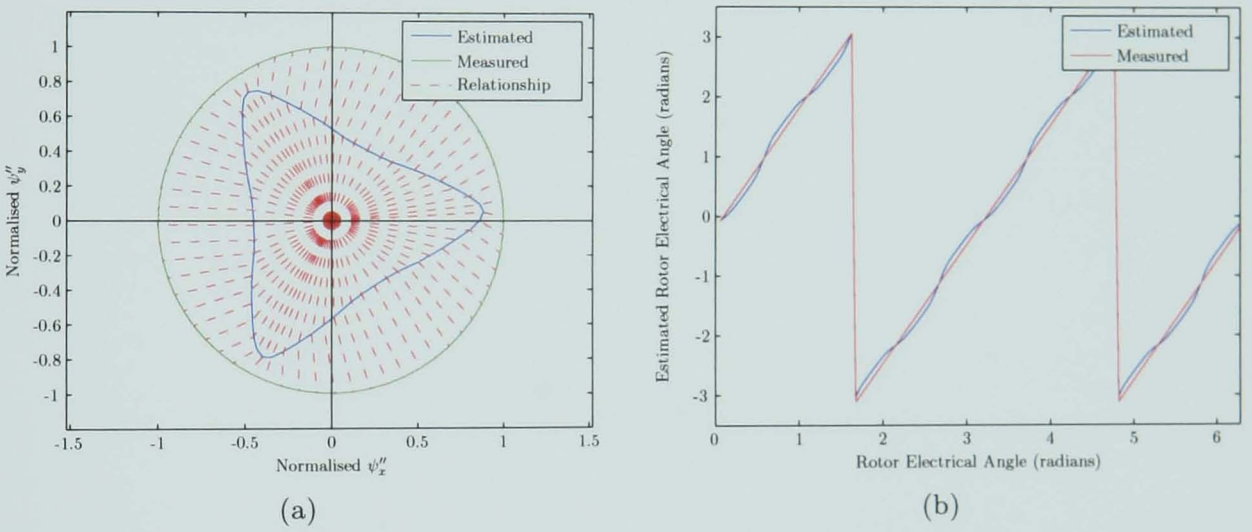

(a) (b)

Figure C.11: Results for 'Kart' Motor Version 11
(a) Fingerprint, (b) Estimation Results

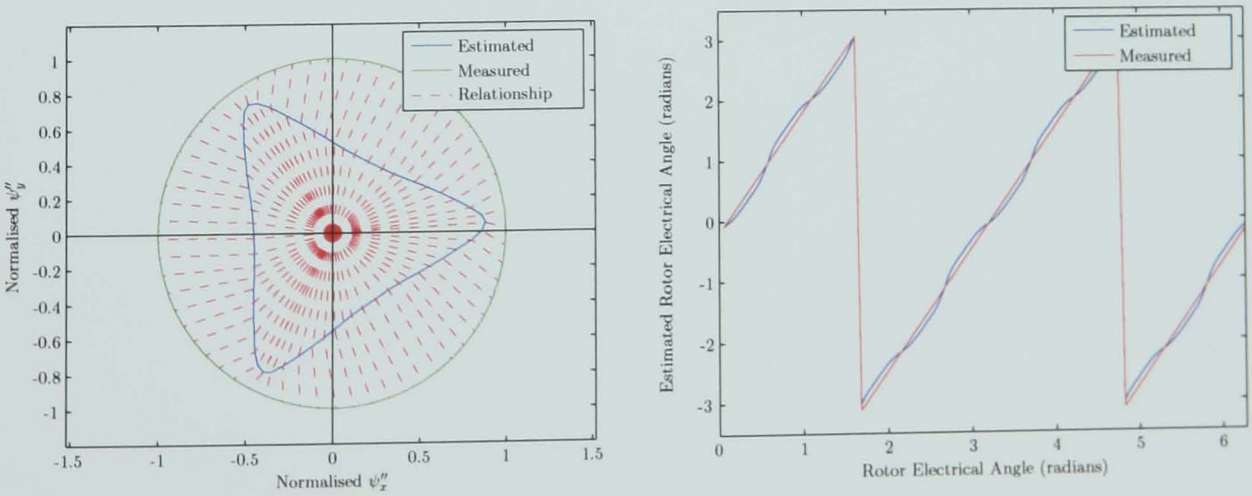

(a) (b)

Figure C.12: Results for 'Kart' Motor Version 12
(a) Fingerprint, (b) Estimation Results

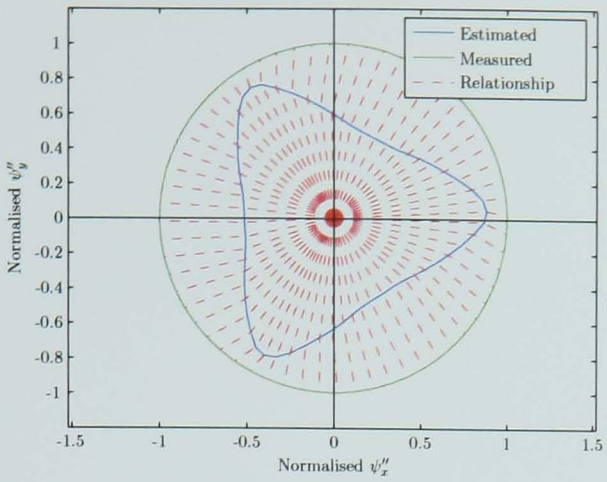

(a)

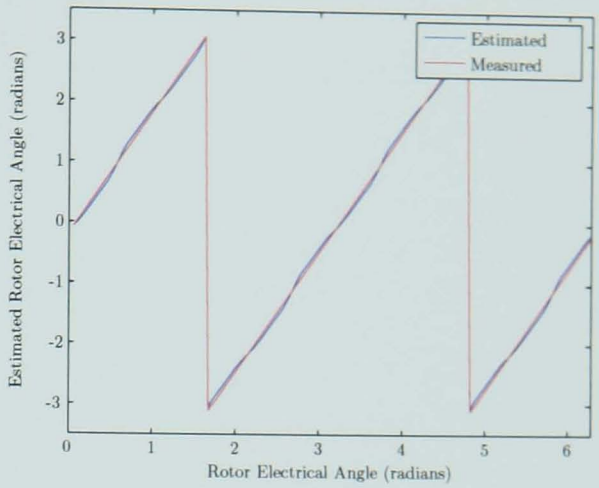

(b)

Figure C.13: Results for 'Kart' Motor Version 13
(a) Fingerprint, (b) Estimation Results

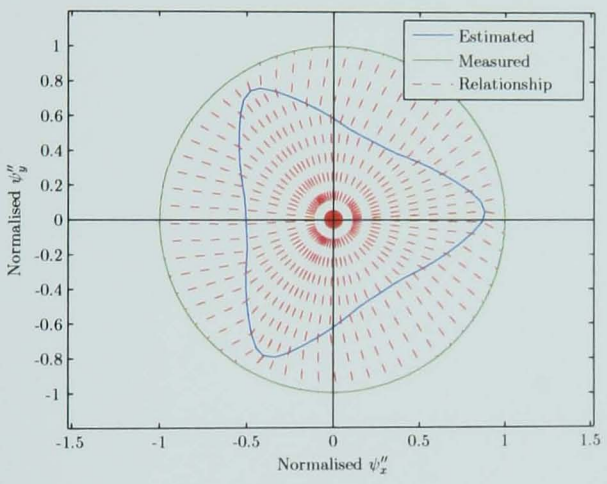

(a)

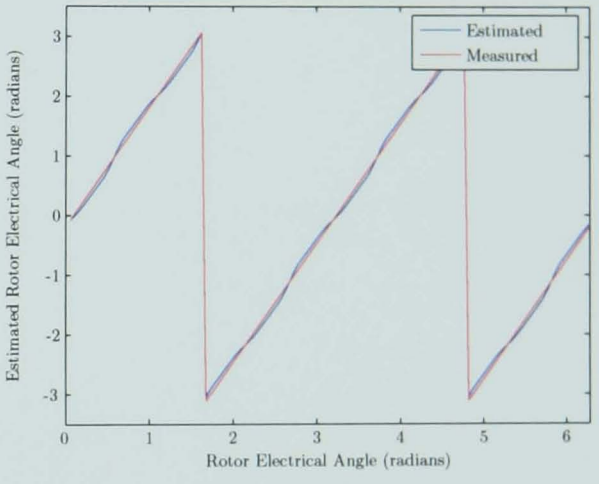

(b)

Figure C.14: Results for 'Kart' Motor Version 14
(a) Fingerprint, (b) Estimation Results

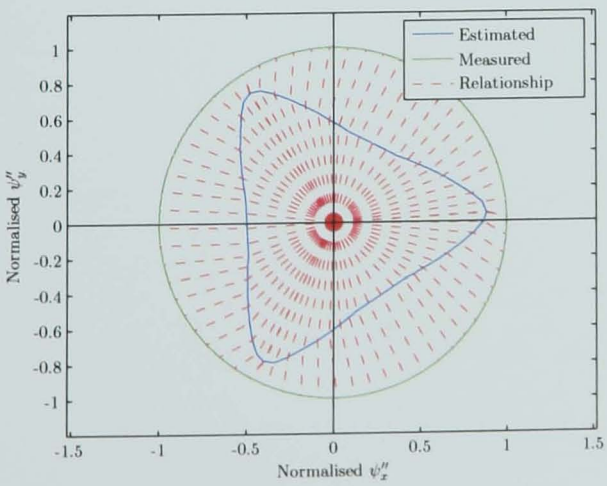

(a)

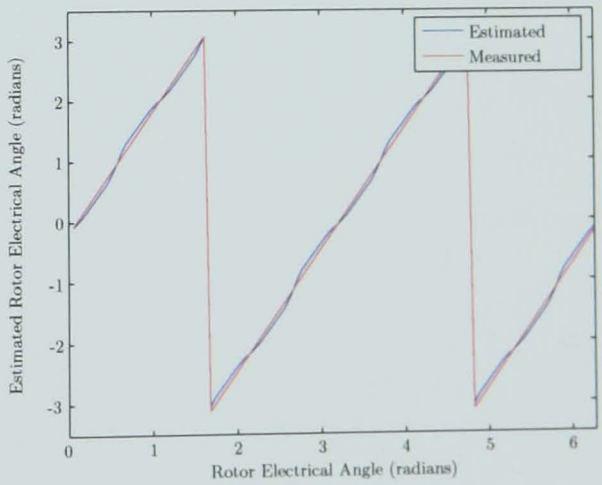

(b)

Figure C.15: Results for 'Kart' Motor Version 15
(a) Fingerprint, (b) Estimation Results

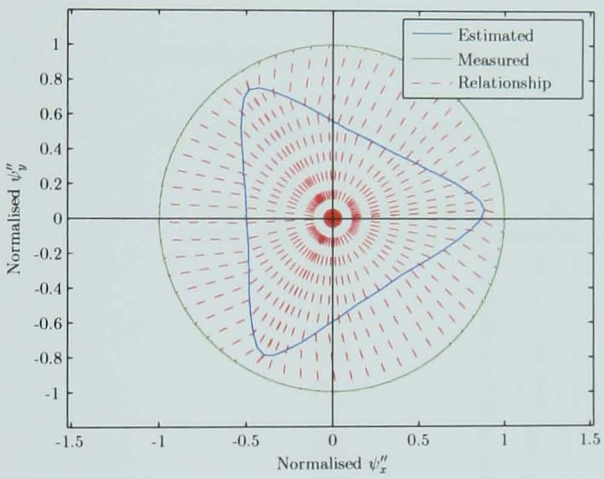

(a)

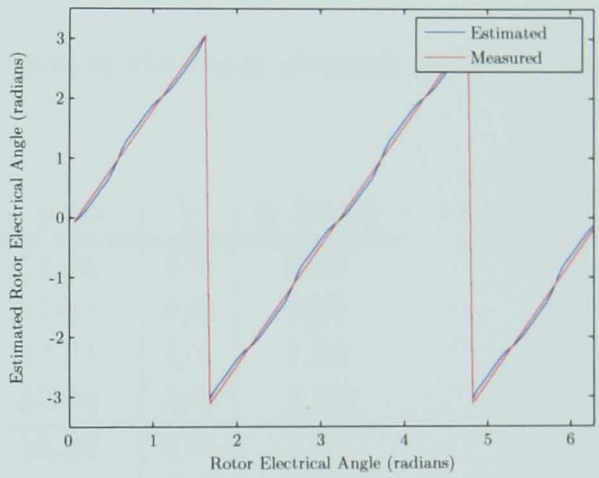

(b)

Figure C.16: Results for 'Kart' Motor Version 16
(a) Fingerprint, (b) Estimation Results

Appendix D

'Traction' Motor FEA Results

Table D.1 summarises the machine versions used in the finite element analysis. The full results are included in figures D.1–D.16.

Machine Version	$\frac{s_i}{s}$	s_i (mm)	$\frac{t_i}{t}$	t_i (mm)
01	11/11	12.64	6/6	2.30
02	11/11	12.64	5/6	2.00
03	11/11	12.64	4/6	1.60
04	11/11	12.64	3/6	1.20
05	9/11	10.34	6/6	2.30
06	9/11	10.34	5/6	2.00
07	9/11	10.34	4/6	1.60
08	9/11	10.34	3/6	1.20
09	7/11	8.04	6/6	2.30
10	7/11	8.04	5/6	2.00
11	7/11	8.04	4/6	1.60
12	7/11	8.04	3/6	1.20
13	5/11	5.75	6/6	2.30
14	5/11	5.75	5/6	2.00
15	5/11	5.75	4/6	1.60
16	5/11	5.75	3/6	1.20

Table D.1: 'Traction' Motor Alterations for Slotting Analysis

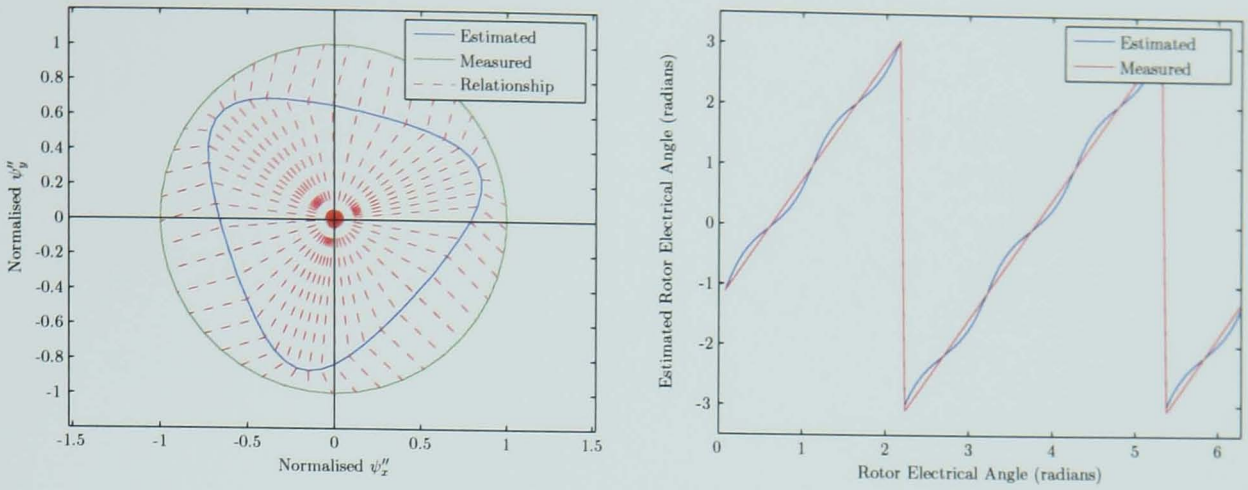

(a) (b)

Figure D.1: Results for 'Traction' Motor Version 01
(a) Fingerprint, (b) Estimation Results

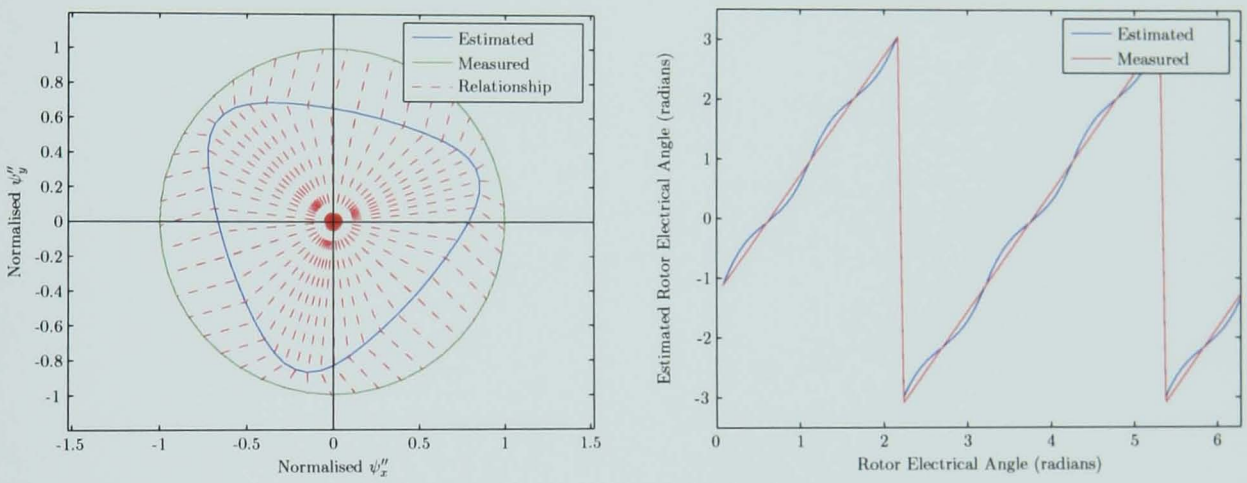

(a) (b)

Figure D.2: Results for 'Traction' Motor Version 02
(a) Fingerprint, (b) Estimation Results

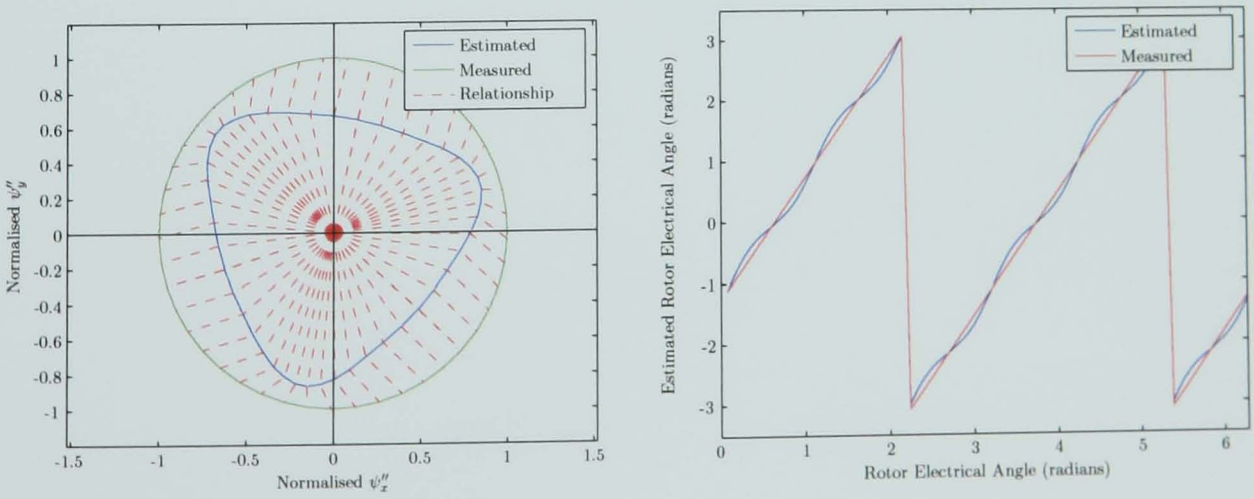

(a) (b)

Figure D.3: Results for 'Traction' Motor Version 03
(a) Fingerprint, (b) Estimation Results

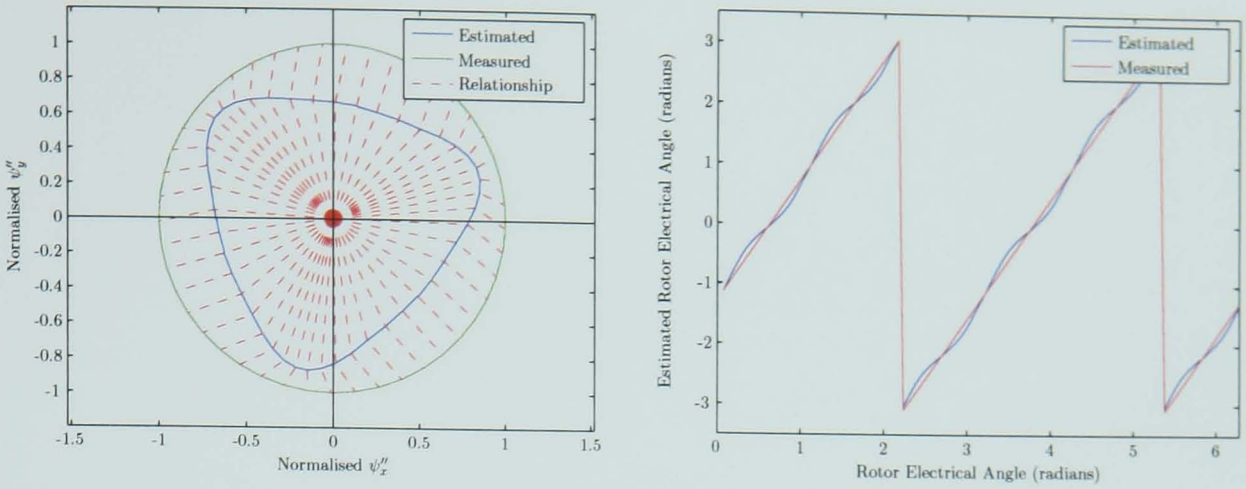

(a) (b)

Figure D.4: Results for 'Traction' Motor Version 04
(a) Fingerprint, (b) Estimation Results

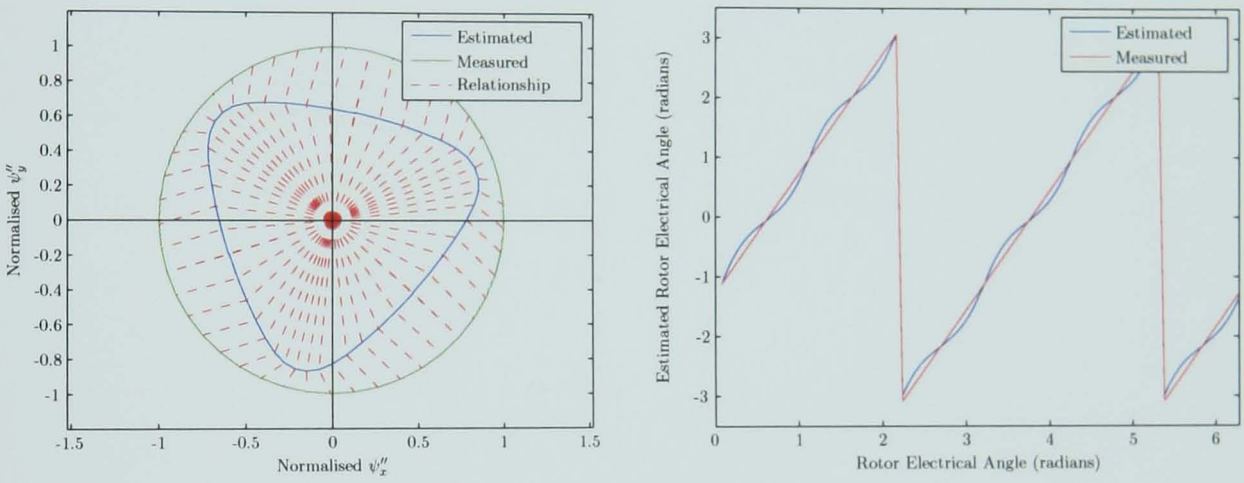

(a) (b)

Figure D.5: Results for 'Traction' Motor Version 05
(a) Fingerprint, (b) Estimation Results

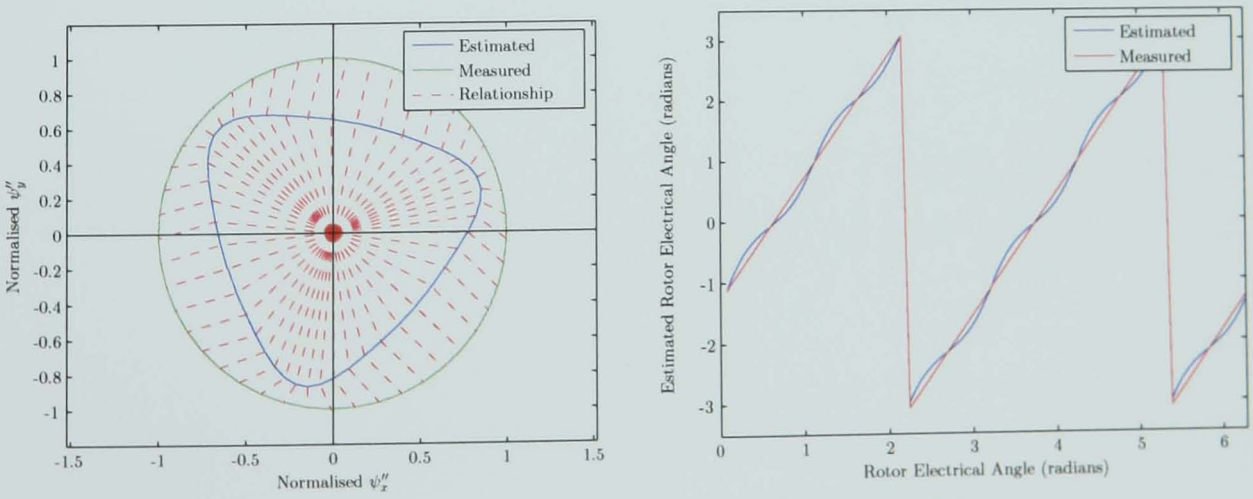

(a) (b)

Figure D.6: Results for 'Traction' Motor Version 06
(a) Fingerprint, (b) Estimation Results

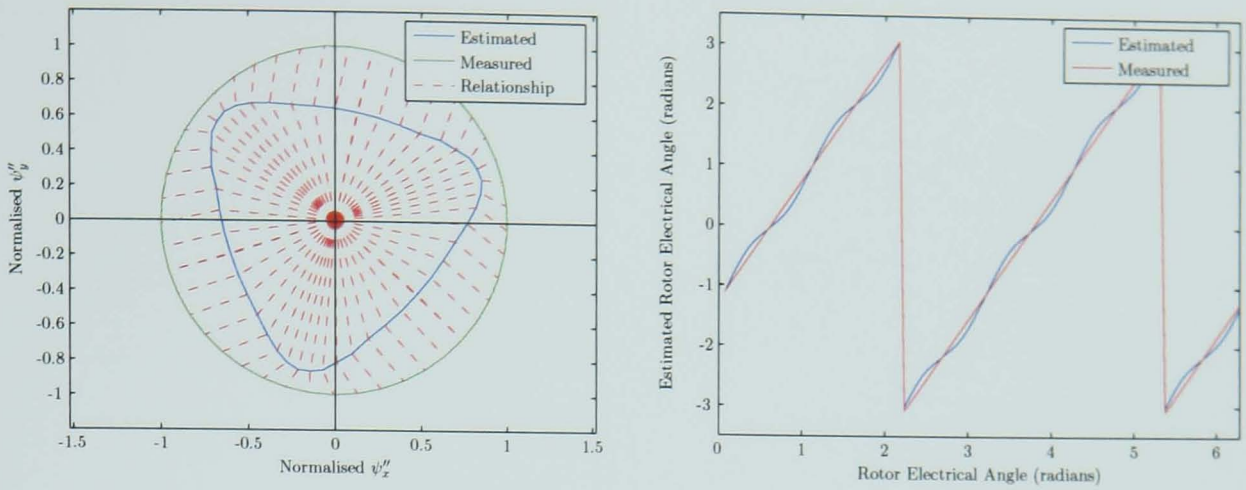

(a) (b)

Figure D.7: Results for 'Traction' Motor Version 07
(a) Fingerprint, (b) Estimation Results

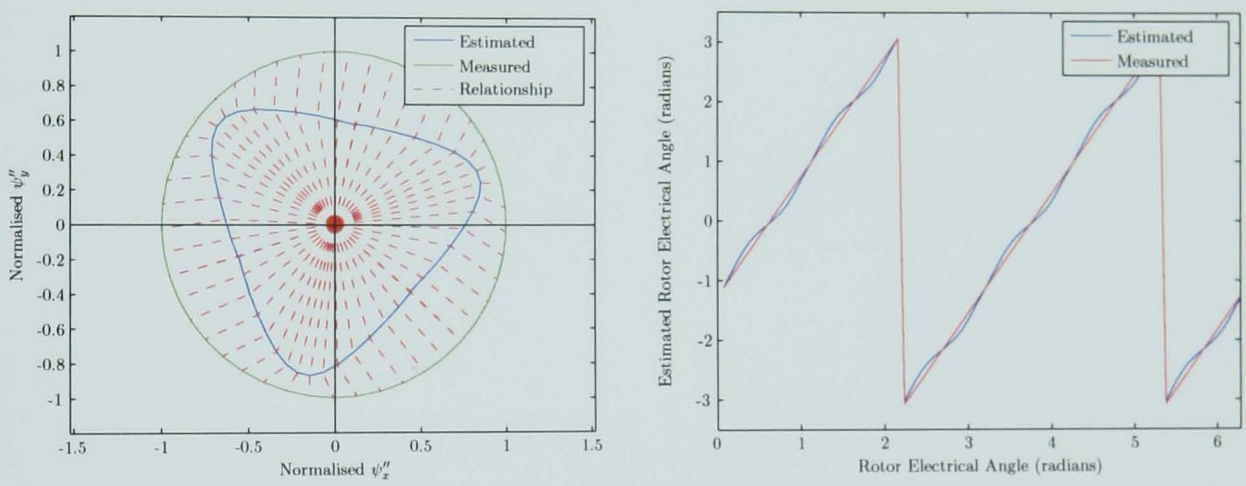

(a) (b)

Figure D.8: Results for 'Traction' Motor Version 08
(a) Fingerprint, (b) Estimation Results

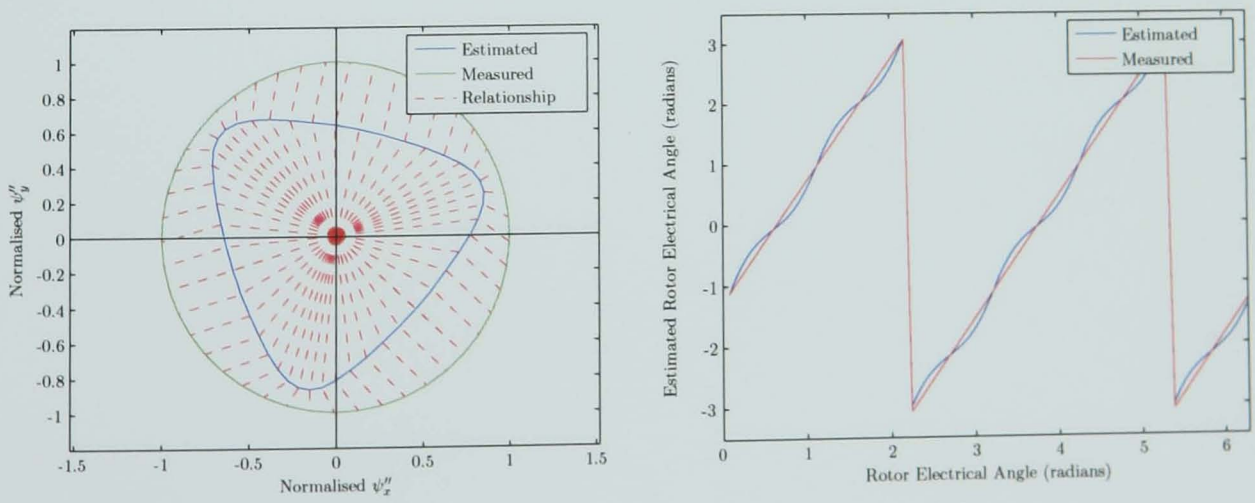

(a) (b)

Figure D.9: Results for 'Traction' Motor Version 09
(a) Fingerprint, (b) Estimation Results

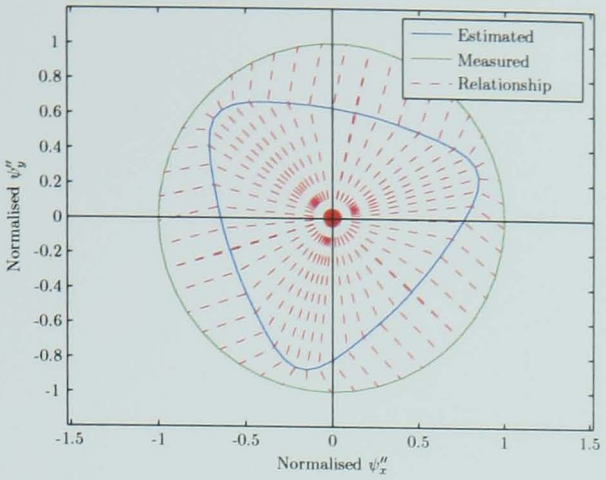

(a)

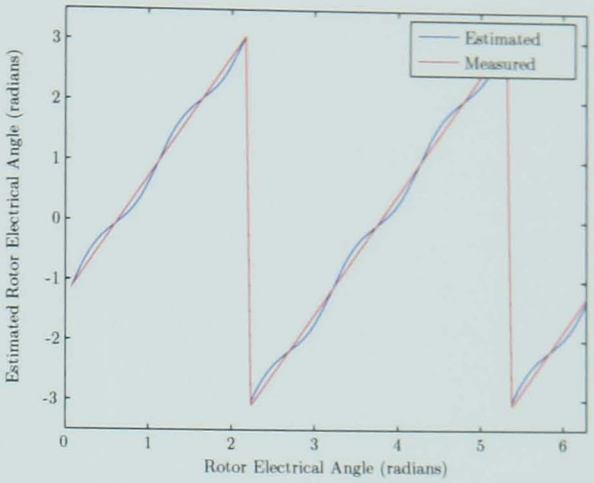

(b)

Figure D.10: Results for 'Traction' Motor Version 10
(a) Fingerprint, (b) Estimation Results

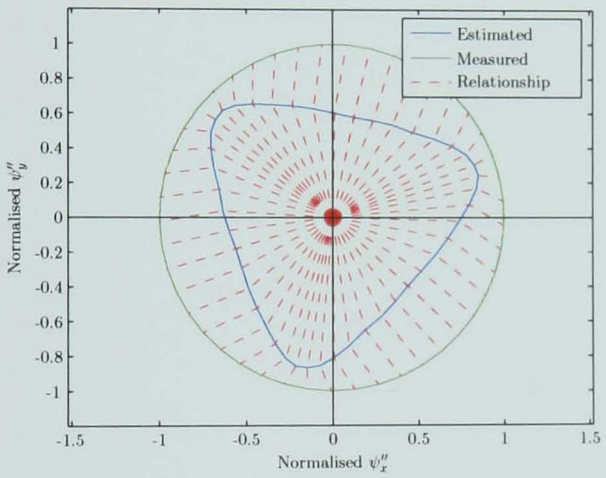

(a)

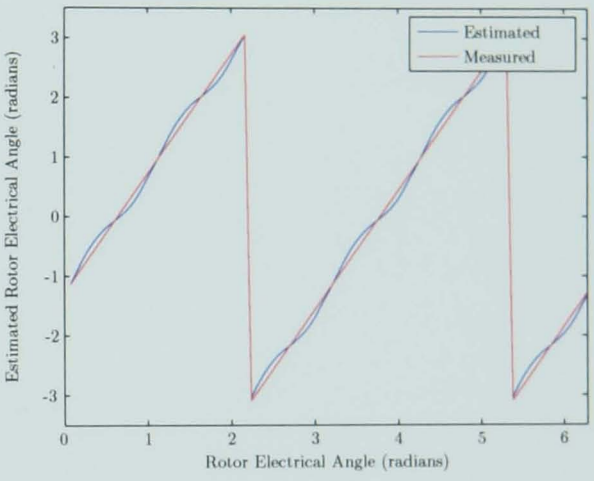

(b)

Figure D.11: Results for 'Traction' Motor Version 11
(a) Fingerprint, (b) Estimation Results

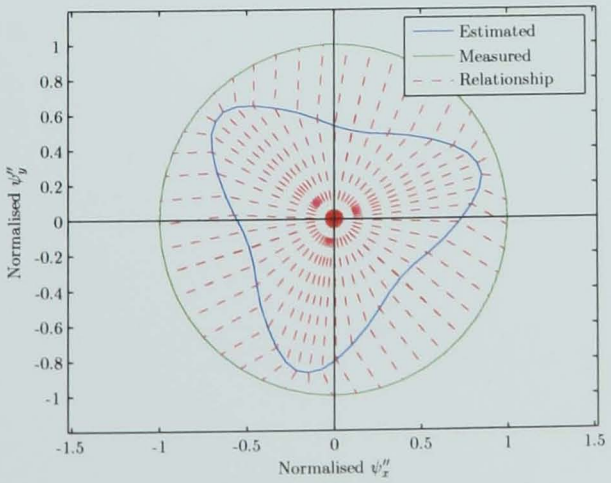

(a)

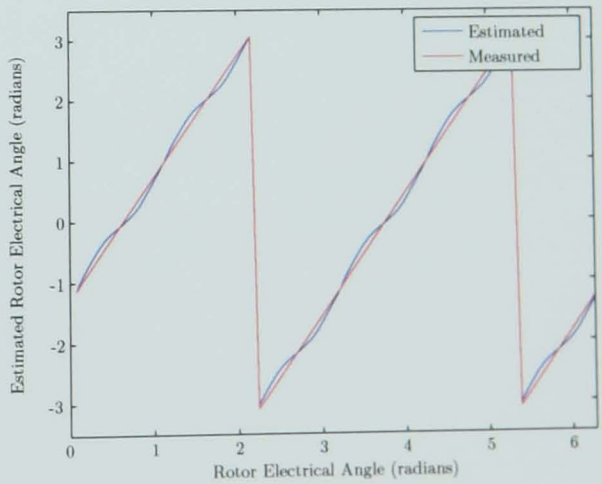

(b)

Figure D.12: Results for 'Traction' Motor Version 12
(a) Fingerprint, (b) Estimation Results

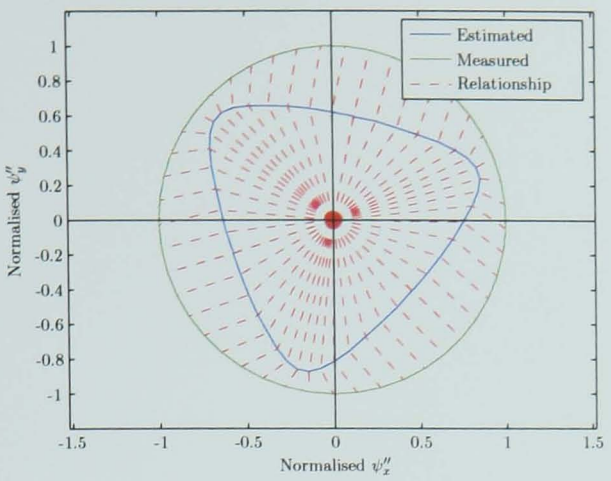

(a)

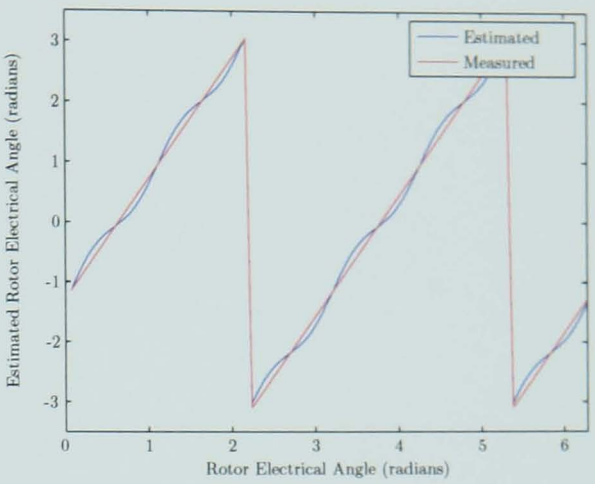

(b)

Figure D.13: Results for 'Traction' Motor Version 13
(a) Fingerprint, (b) Estimation Results

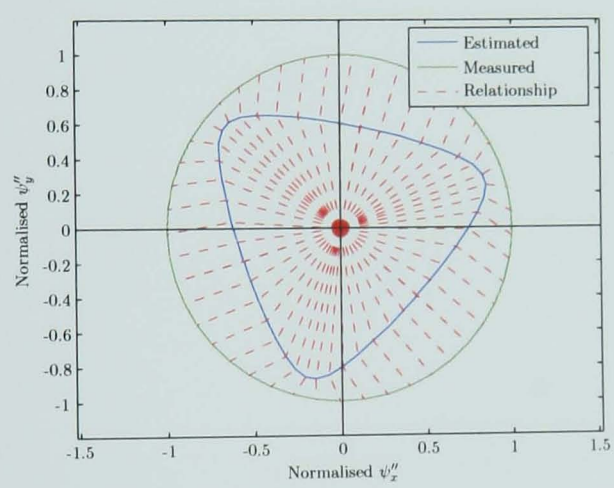

(a)

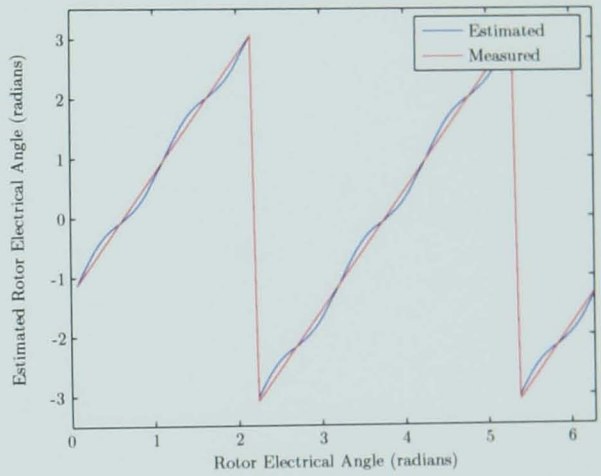

(b)

Figure D.14: Results for 'Traction' Motor Version 14
(a) Fingerprint, (b) Estimation Results

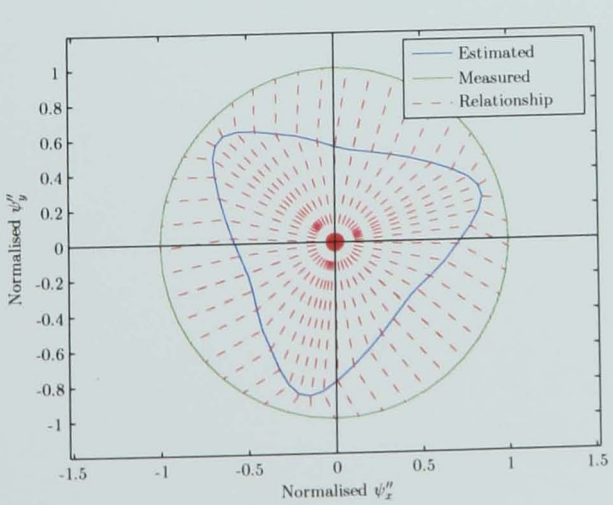

(a)

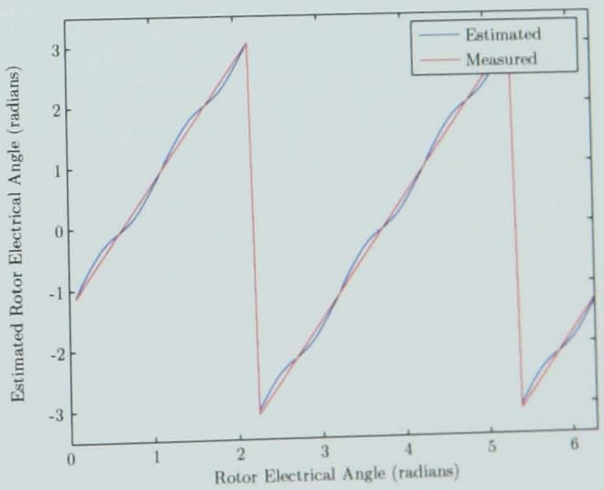

(b)

Figure D.15: Results for 'Traction' Motor Version 15
(a) Fingerprint, (b) Estimation Results

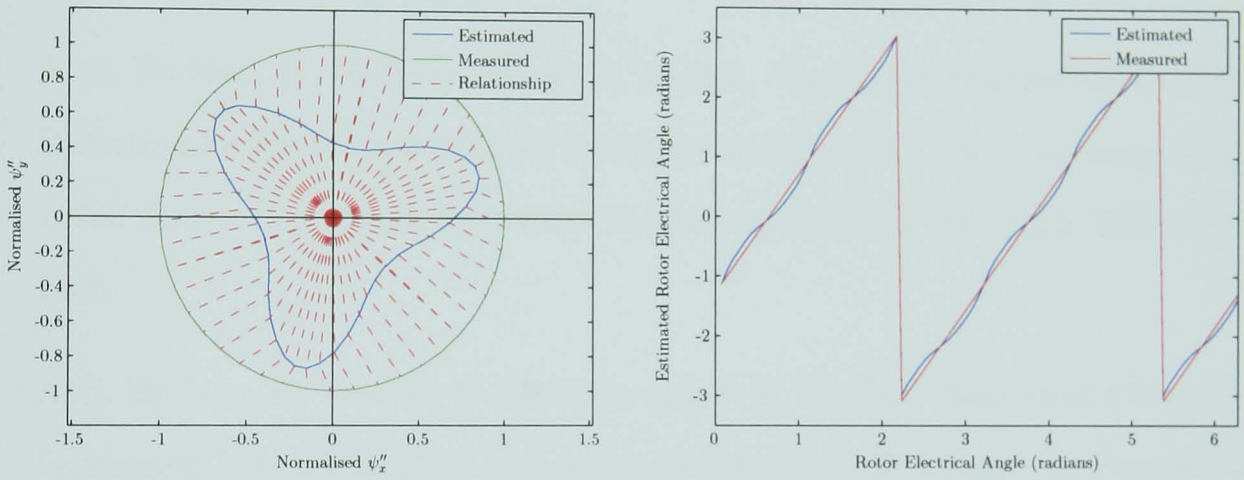

(a) (b)

Figure D.16: Results for 'Traction' Motor Version 16
(a) Fingerprint, (b) Estimation Results

Bibliography

[1] M. Vilathgamuwa, M. A. Rahman and K. J. Tseng, "Nonlinear Control of Interior Permanent Magnet Synchronous Motor", in *Proceedings of the Industry Applications Society (IAS)*, vol. 2, pp. 1115–1120, 2000.

[2] A. S. Budden, D. Holliday and P. H. Mellor, "Zero Speed Sensorless Position Detection for Permanent Magnet Synchronous Machines", in *Proceedings of the IEEE Power Electronics Specialists Conference (PESC)*, vol. 1, pp. 2436–2441, 2005.

[3] A. S. Budden, R. Wrobel, D. Holliday and P. H. Mellor, "Sensorless Control of Permanent Magnet Machine Drives for Aerospace Applications", in *Proceedings of the IEEE International Conference on Power Electronics and Drive Systems (PEDS)*, 2005.

[4] R. Wu and G. R. Slemon, "A Permanent Magnet Motor Drive without a Shaft Sensor", in *Proceedings of the Industry Applications Society (IAS)*, vol. 1, pp. 553–558, 1990.

[5] K. Iizuka, H. Uzuhashi, M. Kano, T. Endo and K. Mohri, "Microcomputer Control for Sensorless Brushless Motor", *IEEE Transactions on Industry Applications*, vol. IA-21, no. 3, pp. 595–601, 1985.

[6] S. Saha, T. Tazawa, T. Iijima, K. Narasaki, H. Murakami and Y. Honda, "A Novel Sensorless Control Drive for an Interior Permanent Magnet Motor", in *Proceedings of the International Conference on Industrial Electronics, Control and Instrumentation (IECON)*, vol. 3, pp. 1655–1660, 2001.

[7] N. Matsui and M. Shigyo, "Brushless DC Motor Control without Position and Speed Sensors", in *Proceedings of the Industry Applications Society (IAS)*, vol. 1, pp. 448–453, 1990.

[8] N. Matsui and M. Shigyo, "Brushless DC Motor Control without Position and Speed Sensors", *IEEE Transactions on Industry Applications*, vol. 28, no. 1, pp. 120–127, 1992.

[9] N. Matsui, "Sensorless PM Brushless DC Motor Drives", *IEEE Transactions on Industrial Electronics*, vol. 43, no. 2, pp. 300–308, 1996.

[10] S. Bolognani, R. Oboe and M. Zigliotto, "Sensorless full-digital PMSM drive with EKF estimation of speed and rotor position", *IEEE Transactions on Industrial Electronics*, vol. 46, no. 1, pp. 184–191, 1999.

[11] R. Dhaouadi, N. Mohan and L. Norum, "Design and Implementation of an Extended Kalman Filter for the State Estimation of a Permanent Magnet Synchronous Motor", *IEEE Transactions on Power Electronics*, vol. 6, no. 3, pp. 491–497, 1991.

[12] A. Germano, F. Parasiliti and M. Tursini, "Sensorless Speed Control of a PM Synchronous Motor Drive by Kalman Filter", in *Proceedings of the International Conference on Electrical Machines (ICEM)*, vol. 2, pp. 540–544, Paris, France, 1994.

[13] S. Bolognani, R. Oboe and M. Zigliotto, "DSP-Based Extended Kalman Filter Estimation of Speed and Rotor Position of a PM Synchronous Motor", in *Proceedings of the International Conference on Industrial Electronics, Control and Instrumentation (IECON)*, vol. 3, pp. 2097–2102, New York, NY, USA, 1994.

[14] S. Bolognani and M. Zigliotto, "Parameter Sensitivity of the Kalman Filter Applied to a Sensorless Synchronous Motor Drive", in *Proceedings of the European Conference on Power Electronics and Applications (EPE)*, vol. 3, pp. 375–380, Brussels, Belgium, 1995.

[15] P. Vas, *Sensorless Vector and Direct Torque Control*, Oxford University Press, New York, 1998.

[16] S. Bolognani, L. Tubiana and M. Zigliotto, "Extended Kalman Filter Tuning in Sensorless PMSM Drives", in *Proceedings of the IEEE Power Conversion Conference*, vol. 1, pp. 276–281, 2002.

[17] B. Terzic and M. Jadric, "Design and Implementation of the Extended Kalman Filter for the Speed and Rotor Estimation of Brushless DC Motor". *IEEE Transactions on Industrial Electronics*, vol. 48, no. 6, pp. 1065–1072, 2001.

[18] R. Tarantino, F. Szigeti and E. Colina-Morles, "Generalized Luenberger Observer-Based Fault-Detection Filter Design: An Industrial Application", *Control Engineering Practice*, vol. 8, no. 6, pp. 665–671, 2000.

[19] Z. Chen, M. Tomita, S. Doki and S. Okuma, "New Adaptive Sliding Observer for Sensorless Control of Surface Permanent Magnet Synchronous Motor", in *Proceedings of the Power Electronics and Motion Control Conference (PEMC)*, vol. 1, pp. 180–185, 2000.

[20] Z. Chen, M. Tomita, S. Doki and S. Okuma, "New Adaptive Sliding Observers for Position- and Velocity-Sensorless Controls of Brushless DC Motors", *IEEE Transactions on Industrial Electronics*, vol. 47, no. 3, pp. 582–591, 2000.

[21] M. Tursini, R. Petrella and F. Parasiliti, "Adaptive Sliding-Mode Observer for Speed-Sensorless Control of Induction Motors", *IEEE Transactions on Industry Applications*, vol. 36, no. 5, pp. 1380–1387, 2000.

[22] K. W. Lim, K. S. Low, M. F. Rahman and R. Mayebo, "Observers for Sensorless Control of Permanent Magnet Synchronous Motor Drive", in *Proceedings of the 12th Triennial World Congress of the International Federation of Automatic Control*, vol. 3, pp. 367–370, Oxford, UK, 1994.

[23] P. B. Schmidt and A. H. Wijenayake, "Sensorless Control of a Permanent Magnet Synchronous Machine Down to Near Zero Speed Applied to Position Motion Control", in *Proceedings of the Industry Applications Society (IAS)*, vol. 1, pp. 21–28, 1996.

[24] M. Jovanović, R. E. Betz and D. Platt, "Sensorless Vector Controller for a Synchronous Reluctance Motor", in *Proceedings of the Industry Applications Society (IAS)*, vol. 1, pp. 122–129, 1996.

[25] T. Song, M. F. Rahman and K. W. Lim, "A Singular Perturbation Approach to Sensorless Control of a Permanent Magnet Synchronous Motor", in *Proceedings of the IEEE International Electric Machines and Drives Conference (IEMDC)*, pp. MC3–7.1–3, 1997.

[26] K. Tatematsu, D. Hamada, K. Uchida, S. Wakao and T. Onuki, "Sensorless Control for Permanent Magnet Synchronous Motor with Reduced Order Observer", in *Proceedings of the IEEE Power Electronics Specialists Conference (PESC)*, vol. 1, pp. 125–131, New York, NY, USA, 1998.

[27] T. D. Batzel and K. Y. Lee, "Slotless Permanent Magnet Synchronous Motor Operation without a High Resolution Rotor Angle Sensor", *IEEE Transactions on Energy Conversion*, vol. 15, no. 4, pp. 366–371, 2000.

[28] K. R. Thompson, P. P. Acarnley and C. French, "Rotor Position Estimation in a Switched Reluctance Drive Using Recursive Least Squares", *IEEE Transactions on Industrial Electronics*, vol. 47, no. 2, pp. 368–379, 2000.

[29] L. Ying and N. Ertugrul, "A Novel Position Sensorless Control for Permanent Magnet AC Motors", in *Proceedings of the Power Electronics and Motion Control Conference (PEMC)*, vol. 1, pp. 169–174, 2000.

[30] S. Ichikawa, Z. Chen, M. Tomita, S. Doki and S. Okuma, "Sensorless Control of an Interior Permanent Magnet Synchronous Motor on the Rotating Coordinate Using an Extended Electromotive Force", in *Proceedings of the International Conference on Industrial Electronics, Control and Instrumentation (IECON)*, vol. 3, pp. 1667–1672, 2001.

[31] A. Bellini, F. Filippetti, G. Franceschini, C. Tassoni and P. Vas, "Position Sensorless Control of a SRM Drive using ANN-techniques", in *Proceedings of the Industry Applications Society (IAS)*, vol. 1, pp. 709–714, New York, NY, USA, 1998.

[32] H. S. Ooi and T. C. Green, "Simulation of Neural Networks to Sensorless Control of Switched Reluctance Motor", in *Proceedings of the Power Electronics and Variable Speed Drives Conference (PEVSD)*, pp. 281–286, London, UK. 1998.

[33] H. S. Ooi and T. C. Green, "Sensorless Switched Reluctance Motor Drive With Torque Ripple Minimization", in *Proceedings of the IEEE Power Electronics Specialists Conference (PESC)*, pp. 1538–1543, 2000.

[34] P. Vas, J. Chen and A. F. Stronach, "Fuzzy Control of AC Drives", in *Proceedings of the Power Electronics and Variable Speed Drives Conference (PEVSD)*, pp. 113–118, London, UK, 1994.

[35] Z. Chen, S. A. Gómez and M. McCormick, "A Fuzzy Logic Controlled Power Electronic System for Variable Speed Wind Energy Conversion Systems", in *Proceedings of the Power Electronics and Variable Speed Drives Conference (PEVSD)*, pp. 114–119, 2000.

[36] P. Vas, A. F. Stronach and M. Neuroth, "Application of Conventional and AI-Based Techniques in Sensorless High-Performance Torque-Controlled Induction Motor Drives", in *IEE Colloquium on Vector Control Revisited*, pp. 8/1–7, London, UK, 1998.

[37] P. Vas, A. F. Stronach and M. Neuroth, "A Fuzzy-Controlled Speed-Sensorless Induction Motor Drive with Flux Estimators", in *Proceedings of the International Conference on Electrical Machines and Drives*, pp. 315–319, London, UK, 1995.

[38] S. Ogasawara and H. Akagi, "An Approach to Position Sensorless Drive for Brushless DC Motors", in *Proceedings of the Industry Applications Society (IAS)*, vol. 1, pp. 443–447, 1990.

[39] S. Ogasawara and H. Akagi, "An Approach to Position Sensorless Drive for Brushless DC Motors", *IEEE Transactions on Industry Applications*, vol. 27, no. 5, pp. 928–933, 1991.

[40] S. Kondo, A. Takahashi and T. Nishida, "Armature Current Locus Based Estimation Method of Rotor Position of Permanent Magnet Synchronous Motor without Mechanical Sensor", in *Proceedings of the Industry Applications Society (IAS)*, vol. 1, pp. 55–60, 1995.

[41] W. D. Harris and J. H. Lang, "A Simple Motion Estimator for Variable-Reluctance Motors", *IEEE Transactions on Industry Applications*, vol. 26, no. 2, pp. 237–243, 1990.

[42] P. L. Jansen and R. D. Lorenz, "Transducerless Position and Velocity Estimation in Induction and Salient AC Machines", in *Proceedings of the Industry Applications Society (IAS)*, vol. 1, pp. 488–495, 1994.

[43] P. L. Jansen and R. D. Lorenz, "Transducerless Position and Velocity Estimation in Induction and Salient AC machines", *IEEE Transactions on Industry Applications*, vol. 31, no. 2, pp. 240–247, 1995.

[44] M. J. Corley and R. D. Lorenz, "Rotor Position and Velocity Estimation for a Permanent Magnet Synchronous Machine at Standstill and High Speeds", in *Proceedings of the Industry Applications Society (IAS)*, vol. 1, pp. 36–41, New York, NY, USA, 1996.

[45] T. Noguchi, K. Yamada, S. Kondo and I. Takahashi, "Rotor Position Estimation of Sensorless PM Motor at Rest with No Sensitivity to Armature Resistance", in *Proceedings of the International Conference on Industrial Electronics, Control and Instrumentation (IECON)*, vol. 2, pp. 1171–1176, 1996.

[46] S. Östlund and M. Brokemper, "Sensorless Rotor-Position Detection from Zero to Rated Speed for an Integrated PM Synchronous Motor Drive", *IEEE Transactions on Industry Applications*, vol. 32, no. 5, pp. 1158–1165, 1996.

[47] M. W. Degner and R. D. Lorenz, "Using Multiple Saliencies for the Estimation of Flux, Position, and Velocity in AC machines", in *Proceedings of the Industry Applications Society (IAS)*, vol. 1, pp. 760–767, New Orleans, Louisiana, 1997.

[48] M. A. Jabbar, M. A. Hoque and M. A. Rahman, "Sensorless Permanent Magnet Synchronous Motor Drives", in *Canadian Conference on Electrical and Computer Engineering*, vol. 2, pp. 878–883, 1997.

[49] K. Seog-Joo, K. Jamg-Mok and S. Seung-Ki, "Position Sensorless Control of Synchronous Reluctance Motor using High Frequency Current Injection". *Transactions of the Korean Institute of Electrical Engineers*, vol. 46, no. 10, pp. 1486–1489, 1997.

[50] M. J. Corley and R. D. Lorenz, "Rotor Position And Velocity Estimation for a Salient-Pole Permanent Magnet Synchronous Machine at Standstill and High Speeds", *IEEE Transactions on Industry Applications*, vol. 34, no. 4, pp. 784–789, 1998.

[51] M. L. Aime, M. W. Degner, N. Tice and R. D. Lorenz, "Measuring the Location of Saliencies in AC MAchines", in *Proceedings of the International Conference on Industrial Electronics, Control and Instrumentation (IECON)*, vol. 1, pp. 286–291, 1998.

[52] M. W. Degner and R. D. Lorenz, "Using Multiple Saliencies for the Estimation of Flux, Position, and Velocity in AC Machines", *IEEE Transactions on Industry Applications*, vol. 34, no. 5, pp. 1097–1104, 1998.

[53] R. Mizutani, T. Takeshita and N. Matsui, "Current Model-Based Sensorless Drives of Salient-Pole PMSM at Low Speed and Standstill", *IEEE Transactions on Industry Applications*, vol. 34, no. 4, pp. 841–846, 1998.

[54] T. Noguchi, K. Yamada, S. Kondo and I. Takahashi, "Initial Rotor Position Estimation Method of Sensorless PM Synchronous Motor with No Sensitivity to Armature Resistance", *IEEE Transactions on Industrial Electronics*, vol. 45, no. 1, pp. 118–125, 1998.

[55] C. Spiteri Staines, G. M. Asher and K. J. Bradley, "A Periodic Burst Injection Method for Deriving Rotor Position in Saturated Cage-Salient Induction Motors without a Shaft Encoder", in *Proceedings of the Industry Applications Society (IAS)*, vol. 1, pp. 617–624, 1998.

[56] M. L. Aime, M. W. Degner, N. Tice and R. D. Lorenz, "The Effects of Saturation on Flux Angle Estimation for Sensorless, Direct Field Oriented Control of Induction Machines", in *Proceedings of the European Conference on Power Electronics and Applications (EPE)*, p. 8 pages, 1999.

[57] A. Consoli, G. Scarcella and A. Testa, "Sensorless Control of AC Motors at Zero Speed", in *Proceedings of the IEEE International Symposium on Industrial Electronics (ISIE)*, vol. 1, pp. 373–379, 1999.

[58] P. L. Jansen, M. J. Corley and R. D. Lorenz, "Flux, Position, and Velocity Estimation in AC Machines at Zero and Low Speed via Tracking of High Frequency Saliencies", in *Proceedings of the European Conference on Power Electronics and Applications (EPE)*, vol. 9, pp. 45–50, 1999.

[59] F. Briz, M. W. Degner, A. Diez and R. D. Lorenz, "Measuring, Modeling and Decoupling of Saturation-Induced Saliencies in Carrier Signal Injection-Based Sensorless AC Drives", in *Proceedings of the Industry Applications Society (IAS)*, vol. 3, pp. 1842–1849, 2000.

[60] M. W. Degner and R. D. Lorenz, "Position Estimation in Induction Machines Utilizing Rotor Bar Slot Harmonics and Carrier-Frequency Signal Injection", *IEEE Transactions on Industry Applications*, vol. 36, no. 3, pp. 736–742, 2000.

[61] L. Wang and R. D. Lorenz, "Rotor Position Estimation for Permanent Magnet Synchronous Motor Using Saliency-Tracking Self Sensing Method", in *Proceedings of the Industry Applications Society (IAS)*, vol. 1, pp. 445–450, 2000.

[62] L. Wang, G. Qingding and R. D. Lorenz, "Sensorless Control of Permanent Magnet Synchronous Motor", in *Proceedings of the Power Electronics and Motion Control Conference (PEMC)*, vol. 1, pp. 186–190, 2000.

[63] F. Briz, M. W. Degner, J. M. Guerrero, A. Zammarón and R. D. Lorenz, "Implementation Issues Affecting the Performance of Carrier Signal Injection Based Sensorless Controlled AC Drives", in *Proceedings of the Industry Applications Society (IAS)*, vol. 4, pp. 2645–2652, 2001.

[64] F. Briz, M. W. Degner, A. Diez and R. D. Lorenz, "Measuring, Modeling, and Decoupling of Saturation-Induced Saliencies in Carrier-Signal Injection-Based Sensorless AC Drives", *IEEE Transactions on Industry Applications*, vol. 37. no. 5, pp. 1356–1364, 2001.

[65] F. Briz, M. W. Degner, A. Diez and R. D. Lorenz, "Static and Dynamic Behaviour of Saturation-Induced Saliencies and Their Effect on Carrier-Signal-Based Sensorless AC Drives", in *Proceedings of the Industry Applications Society (IAS)*, vol. 2, pp. 1210–1217, 2001.

[66] R. D. Lorenz, "Practical Issues and Research Opportunities when Implementing Zero Speed Sensorless Control", in *ICEMS 2001, Conference Record of the Fifth International Conference on Electrical Machines and Systems*, vol. 1, pp. 1–10, 2001.

[67] J. Oyama, K. Ogawa, T. Higuchi, E. Rashad, M. Mamo and M. Sawamura, "Sensorless Vector-Control of IPM Motors Over Whole Speed Range", in *Proceedings of the IEEE International Conference on Power Electronics and Drive Systems (PEDS)*, vol. 2, pp. 448–451, 2001.

[68] F. Briz, M. W. Degner, A. Diez and R. D. Lorenz, "Static and Dynamic Behaviour of Saturation-Induced Saliencies and Their Effect on Carrier-Signal-Based Sensorless AC Drives", *IEEE Transactions on Industry Applications*, vol. 38, no. 3, pp. 670–678, 2002.

[69] C. Spiteri Staines, J. Cilia, B. Micallef and M. Apap, "Sensorless Vector Control of a Surface Mount PMSM Using High Frequency Injection", in *Proceedings of the IEE Power Electronics, Machines and Drives Conference (PEMD)*, pp. 44 48, 2002.

[70] J.-H. Jang, S.-K. Sul, J.-I. Ha, K. Ide and M. Sawamura, "Sensorless Drive of Surface-Mounted Permanent-Magnet Motor by High-Frequency Signal Injection Based on Magnetic Saliency", *IEEE Transactions on Industry Applications*, vol. 39, no. 4, pp. 1031–1039, 2003.

[71] P. L. Jansen, M. J. Corley and R. D. Lorenz, "Flux, Position, and Velocity Estimation in AC Machines at Zero and Low Speed via Tracking of High Frequency Saliencies", in *Proceedings of the European Conference on Power Electronics and Applications (EPE)*, vol. 3, pp. 154–159, Brussels, Belgium, 1995.

[72] N. Patel, T. O'Meara, J. Nagashima and R. Lorenz, "Encoderless IPM Traction Drive for EV/HEV's", in *Proceedings of the Industry Applications Society (IAS)*, pp. 1703–1707, 2001.

[73] R. Mizutani, T. Takeshita and N. Matsui, "Current Model-Based Sensorless Drives of Salient-Pole PMSM at Low Speed and Standstill", in *Proceedings of the Industry Applications Society (IAS)*, pp. 445–450, New Orleans, Louisiana, 1997.

[74] A. B. Kulkarni and M. Ehsani, "A Novel Position Sensor Elimination Technique for The Interior Permanent-Magnet Synchronous Motor Drive", in *Proceedings of the Industry Applications Society (IAS)*, vol. 1, pp. 773–779, 1989.

[75] S. Ogasawara and H. Akagi, "An Approach to Real-Time Position Estimation at Zero and Low Speed for a PM Motor Based on Saliency", in *Proceedings of the Industry Applications Society (IAS)*, vol. 1, pp. 29–35, 1996.

[76] S. Ogasawara and H. Akagi, "Implementation and Position Control Performance of a Position-Sensorless IPM Motor Drive System Based on Magnetic Saliency", in *Proceedings of the Industry Applications Society (IAS)*, vol. 1, pp. 464–470, 1997.

[77] M. G. Jovanović, R. E. Betz and D. Platt, "Sensorless Vector Controller for a Synchronous Reluctance Motor", *IEEE Transactions on Industry Applications*, vol. 34, no. 2, pp. 346–354, 1998.

[78] S. Ogasawara and H. Akagi, "An Approach to Real-Time Position Estimation at Zero and Low Speed for a PM Motor Based on Saliency", *IEEE Transactions on Industry Applications*, vol. 34, no. 1, pp. 163–168, 1998.

[79] S. Ogasawara and H. Akagi, "Implementation and Position Control Performance of a Position-Sensorless IPM Motor Drive System based on Magnetic Saliency", *IEEE Transactions on Industry Applications*, vol. 34, no. 4, pp. 806–812, 1998.

[80] S. Ogasawara and H. Akagi, "Rotor Position Estimation Based on Magnetic Saliency of an IPM Motor", in *Proceedings of the Industry Applications Society (IAS)*, vol. 1, pp. 460–466, 1998.

[81] N. Kobayashi, K. Choeisai and S. Kondo, "Walsh Function Based Position Sensorless Drive of Salient Pole PM Motor", in *Proceedings of the IEEE Power Conversion Conference*, vol. 1, pp. 270–275, 2002.

[82] H. S. Patel and R. G. Hoft, "Generalized Techniques for Harmonic Elimination and Voltage Control in Thyristor Inverters; Part I: Harmonic Elimination", *IEEE Transactions on Industry Applications*, vol. 9, no. 3, pp. 310–317, 1973.

[83] M. Schroedl, "Operation of the Permanent Magnet Synchronous Machine without a Mechanical Sensor", in *Proceedings of the Power Electronics and Variable Speed Drives Conference (PEVSD)*, pp. 51–56, London, UK, 1990.

[84] P. B. Schmidt, M. L. Gasperi, G. Ray and A. H. Wijenayake, "Initial Rotor Angle Detection of a Nonsalient Pole Permanent Magnet Synchronous Machine", in *Proceedings of the Industry Applications Society (IAS)*, vol. 1, pp. 459–463, New York, NY, USA, 1997.

[85] S. Nakashima, Y. Inagaki and I. Miki, "Sensorless Initial Rotor Position Estimation of Surface Permanent Magnet Synchronous Motor", in *Proceedings of the IEEE International Electric Machines and Drives Conference (IEMDC)*, pp. 525–527, Piscataway, NJ, USA, 1999.

[86] S. Nakashima, Y. Inagaki and I. Miki, "Sensorless Initial Rotor Position Estimation of Surface Permanent-Magnet Synchronous Motor", *IEEE Transactions on Industry Applications*, vol. 36, no. 6, pp. 1598–1603, 2000.

[87] D. O'Kelly and S. Simmons, *Introduction to Generalized Electrical Machine Theory*, McGraw-Hill Publishing Company Limited, Maidenhead, 1968.

[88] D. Y. Ohm, "Dynamic Model of PM Synchronous Motors", , 2000, accessed 14/07/2005.
URL: http://www.drivetechinc.com/articles/IM97PM%5FRev1forPDF.pdf

[89] Wikipedia, "Conic Section", , 2005, accessed 14/07/2005.
URL: http://en.wikipedia.org/wiki/Conic%20section

[90] F. L. Bookstein, "Fitting Conic Sections to Scattered Data", *Computer Graphics and Image Processing*, , no. 9, pp. 56–71, 1979.

[91] A. W. Fitzgibbon, M. Pilu and R. B. Fisher, "Direct Least Squares Fitting Of Ellipses", in *ICPR '96, Proceedings of the of the 13th International Conference on Pattern Recognition*, vol. 1, pp. 253–257, 1996.

[92] K. Hyunbae, H. Kum-Kang, R. Lorenz and T. Jahns, "A Novel Method for Initial Rotor Position Estimation for IPM Synchronous Machine Drives", *IEEE Transactions on Industry Applications*, vol. 40, no. 5, pp. 1369–1378, 2004.

[93] A. S. Budden, D. M. J. Holliday and P. H. Mellor, "Effects of Non-Sinusoidal Inductance Variation on Saliency Based Position Detection Techniques in Interior Permanent Magnet Synchronous Machines", in *Proceedings of the IEE Power Electronics, Machines and Drives Conference (PEMD)*, vol. 1, pp. 308–313, 2004.